A two-wire antenna system

for detecting objects

in a homogeneous dielectric half space

A two-wire antenna system

for detecting objects

in a homogeneous dielectric half space

PROEFSCHRIFT

ter verkrijging van de graad van doctor aan de
Technische Universiteit Eindhoven, op gezag van de
Rector Magnificus, prof.dr. R.A. van Santen, voor een
commissie aangewezen door het College voor
Promoties in het openbaar te verdedigen
op woensdag 23 april 2003 om 16.00 uur

door

Stefan Henri Jean Antoin Vossen

geboren te Nederweert

Dit proefschrift is goedgekeurd door de promotoren:

prof.dr. A.G. Tijhuis,
en
prof.dr.ir. H. Blok

Copromotor:
dr.ir. E.S.A.M. Lepelaars

Aan mijn moeder
A Rosmary

Contents

Chapter 1

Introduction

1.1 Detection of buried objects

Over the last decades, the detection and clearing of land mines has been of growing concern. The number of land mines being laid yearly exceeds the clearing rate by far [1, 2]. In the early 1930's, land mines consisted for a considerable part of metallic parts. Nowadays, land mines are constructed from a variety of materials. These materials are chosen such that the electromagnetic properties do not differ much from their surroundings. The metallic content of a land mine is intentionally reduced to a minimum.

The main reason for depositing land mines is the low cost versus effectiveness. Large pieces of land can be made unusable for both vehicles and man in a period of war. Two main categories can be distinguished, namely, anti-personnel mines (AP) and anti-tank mines (AT). The first type of mine is usually buried close to the surface and the latter type is located at greater depths. A quick but most of all cheap and secure detection device is needed for clearing these grounds after a period of war.

The demand for the detection of land mines exists ever since they were invented around the American civil war. The very first antenna system for the detection of buried objects consisted of two dipole antennas and the objects to be detected were also treated as dipoles [3]. During the years, the antenna systems became more and more advanced because the metallic content of a land mine decreased significantly. The near absence of metallic parts in modern land mines demands the generalization to a dielectric object. In addition to the detection of land mines, all kinds of buried objects can be detected with the same antenna system. Other applications vary from the detection of pipes to applications in archeology [4, 5, 6].

The advantages of such high-tech antenna systems lie in the field of extended penetration

depth of the electromagnetic waves, higher resolution, power of the waves coupled into the ground, discrimination of buried objects versus clutter, width of the pulsed signal, etc. All these enhancements are serving the purpose of a better detection of buried objects. However, these enhancements raise the cost of the detection system.

The use of electromagnetic signals for the detection of buried objects is an old technique which has proven itself to be extremely usable [7, 8, 9]. Lately, new techniques that measure the nuclear spin resonance of nitrogen molecules are being developed. Land mines with a very low metallic content but with an explosive containing a reasonable amount of nitrogen bonds can be detected and positively discriminated from its surroundings [10, 11].

The first use of electromagnetic signals to determine the presence and features of metallic objects is generally attributed to Hülsmeyer in 1904 [3]. The first use of pulsed techniques was introduced by Húlsenbeck in 1926 [12]. From that time on, different pulsed techniques have been developed for numerous kinds of ground studies.

In the early 1960's, several authors [13, 14, 15, 16, 17] have investigated the short-pulse behavior of dipole antennas with a resistive coating. These short pulses are important because they have a very broad frequency spectrum. Detection is primarily based on exciting certain natural frequencies in the spectrum of the material to be detected. The more frequencies present in the spectrum of the source, the greater the chance that a natural mode in an object is excited.

A major problem in the detection of a buried object is the ground in which it is buried. Generally, the ground is highly inhomogeneous and dispersive. Not only do the electromagnetic material parameters of the ground as such depend on frequency, these parameters vary as well with the water content of the ground. The dependence of the material parameters on both water content and frequency has been investigated by numerous authors, see e.g. [18, 19, 20].

Although the research in dipole antennas has been ongoing ever since, more advanced antenna systems were studied for detection purposes. In the early 1990's, the resistively loaded dipole for constructing broadband systems was rediscovered by several authors [20, 21, 22, 23, 24, 25, 26] in both theory and measurements. The results obtained by Rubio Bretones and Tijhuis [25, 27] inspired the present thesis.

1.2   The scope of the thesis

The search for a low-cost and effective antenna system for the detection of a buried object is very important. One way to reduce the cost is to minimize the post-processing of the

received signal. Ideally, detection takes place by merely observing the received signal of the antenna system directly. Therefore, a number of techniques will be studied in this thesis to enhance the received signal in such a way that detection becomes possible from that signal without post processing.

As stated above, resistively loaded dipoles exhibit good broadband characteristics. In addition they are rather cheap. Several authors have shown the broadband qualities of resistively loaded dipole antennas with theoretically obtained results [23, 28, 29, 30]. Measurements with such antennas by several authors [15, 23, 29] showed that the theoretical results are accurate. The broadband qualities of resistively loaded dipoles make them highly suitable for the detection of buried objects [20, 31] since a vast number of natural modes of the object are excited.

Before the dipoles with a resistive profile are studied, a bi-static set up consisting of two dipole antennas for the detection of a buried object is investigated numerically. In this bi-static set up, one wire serves as a transmitter while the other wire is the receiver. As a case study, a wire antenna is used as a buried object. The modeling of a buried wire is fairly easy when compared to that of realistic buried dielectric objects. The "ground" is modeled as a homogeneous half space. Following [20], the averages of the electromagnetic properties of two types of soil over a certain frequency range are used for numerical computations. The detection capabilities are studied with a minimum of post-processing techniques.

It will be demonstrated that, along the receiving wire, a difference in the current distribution can be noticed when the buried wire is present. The time-domain response to the presence of a buried wire is better observable in the current along the resistively loaded receiving wire. Even when the ground is lossy, a characteristic waveform can be observed. It turned out that buried objects near the interface are more difficult to detect directly from the received signal. Therefore the buried wire will be mainly located near the interface.

The single disadvantage of a resistively loaded dipole is the power loss due to the coating. From literature it is known that only between 10% and 30% of the input power is transmitted by the antenna [17, 23]. To generate an adequate signal into the ground would require a battery with a large capacity. This automatically means a bigger and heavier battery which in its turn makes it less suitable for mobile use.

In this thesis, a novel technique, called "pulse compensation", is presented which is inspired by the results of the resistively loaded dipoles. The blurring of the received antenna signals is mainly caused by repeated reflections of the current at the end faces of the wire. The resistive profile along the wire compensates these repeated reflections. Therefore, the resistive profile is a passive compensation. Pulse compensation, on the other hand, is an active way of compensating the repeated reflections at the end faces of the wire. A second

voltage pulse is generated from the initial voltage pulse. This additional voltage pulse serves as a second input signal at the center of the wire. Combining the responses to both voltage pulses results in a suppression of the late-time ringing of the current along the wire. The total current is actively attenuated at later times. Broadband characteristics similar to those of the resistively loaded wire can be expected from such a wire antenna. Furthermore, the technique can be used as a post or pre processing technique. The major advantage is that the power consumption is comparable to that of regular dipoles.

1.3   Organization of this thesis

In Chapter 2, reflected and transmitted field terms due to a dipole point source are derived. The derivation is based on earlier work by Rubio Bretones *et al.* [24]. The respective terms are extended to a situation with multiple layers to show that the derivation is a general one for layered media [32].

Chapter 3 is concerned with the derivation of the integral equation for the current along a single thin wire. The well known expressions given by Pocklington [33] and Hallén [14, 34] are addressed. To demonstrate the behavior of the current along a thin-wire antenna, a traveling-wave model according to [35] is introduced as well. Some representative results will be shown and compared to results found in the literature. These results will be obtained with the aid of Hallén's equation.

In Chapter 4, the results from Chapters 2 and 3 will be used to construct the final configuration of three wires in a half-space configuration in a few consecutive steps. The results of each individual step will be compared to results from the literature. In the final configuration, a transmitting and receiving wire in the upper half space form a detection set up, and a buried wire in the lower half space is the object to be detected. The examples will illustrate some characteristic effects of the lower half space with the buried wire on the current along the receiving wire. The effects of different material properties of the lower half space in combination with the effects of the buried wire on the current along the receiving wire will be studied as well.

Chapter 5 demonstrates how Hallén's equation for the current along a wire which is described in a certain coordinate system can be transformed to describe that current in terms of another coordinate system. In the literature, simplified formulations have been found in the case of coupled dipoles. In this case, the formal derivation will be given. The results are then used to form a set of coupled integral equations that describe the current along a number of arbitrarily oriented wires. Some representative results are compared to reference

results obtained with the Numerical Electromagnetics Code (NEC) [36].

In Chapter 6, the resistive profile as well as pulse compensation are introduced. Both ideas are then used to study several configurations in Chapter 7. In Chapter 8, some synthetic seismograms are calculated with the final configuration from Chapter 4. Both the resistive profile and pulse compensation are used on the wires of the detection set up. From the synthetic seismograms certain features of the buried wire can be extracted.

Chapter 9 shows results of the pulse compensated and resistively loaded antennas above an inhomogeneous slab.

In Chapter 10, a summary is given of the main results reported in this thesis. Based on these results, some general conclusions are drawn and recommendations for future research are given.

Chapter 2

Electromagnetic field equations for stratified media

In this chapter, Maxwell's equations to describe an electromagnetic field will be discussed. Maxwell unified previous work from other scientists to arrive at a set of equations that describe the behavior of electromagnetic fields.

These equations serve as the basis for this chapter and Chapter 3. Maxwell's equations are rewritten in a convenient form to describe the electric and magnetic field in a homogeneous space. With the definition of a current density, the rewritten form of Maxwell's equations is solved for a homogeneous space.

The space is divided into two homogeneous half spaces with different electromagnetic material parameters. Because of the abrupt change of medium parameters at the interface between the two half spaces, part of the radiated electromagnetic field is reflected at that interface and part is transmitted into the other half space. With the aid of a set of boundary conditions and the definition of a current density in one of the half spaces, terms to describe the transmitted and reflected field are found.

The procedure to find the reflected and transmitted fields is generalized to a slab configuration.

The obtained reflected and transmitted fields can no longer be evaluated analytically. Therefore, these fields are evaluated numerically. The composite Gaussian quadrature rule involved with this evaluation is addressed at the end of this chapter.

2.1   Basic relations

In this section, Maxwell's equations are introduced for an isotropic medium with space varying permittivity $\epsilon(\mathbf{r})$, permeability $\mu(\mathbf{r})$ and conductivity $\sigma(\mathbf{r})$. From these general relations, basic relations for free space and for a homogeneous medium will be derived. The basic mathematical tools to derive suitable expressions from Maxwell's equations will be introduced.

2.1.1   Maxwell's equations in the time domain

In a medium where the material parameters vary in time and space, Maxwell's equations can be written in the following special form

$$\nabla \times \boldsymbol{\mathcal{E}} + \partial_t \boldsymbol{\mathcal{B}} = -\boldsymbol{\mathcal{K}}_0, \tag{2.1}$$

$$\nabla \times \boldsymbol{\mathcal{H}} - \partial_t \boldsymbol{\mathcal{D}} - \boldsymbol{\mathcal{J}} = \boldsymbol{\mathcal{J}}_0. \tag{2.2}$$

In this notation, bold script letters indicate vector quantities in the space-time domain $(\mathbf{r}, t)$. Unless indicated otherwise, these arguments are omitted. The vector fields in the right-hand of the equations above are known excitations where $\boldsymbol{\mathcal{K}}_0$ is an external magnetic current density and $\boldsymbol{\mathcal{J}}_0$ is an external electric current density. The components on the left-hand side represent the responses to these excitations. The electric and magnetic field strengths and the electric and magnetic flux densities, as well as an induced electric current density, are denoted by $\boldsymbol{\mathcal{E}}$, $\boldsymbol{\mathcal{H}}$, $\boldsymbol{\mathcal{D}}$, $\boldsymbol{\mathcal{B}}$ and $\boldsymbol{\mathcal{J}}$, respectively. All responses are supposed to be causal functions. In other words, if a source starts at an instant $t = t_0$ it is clear that $\boldsymbol{\mathcal{E}}, \boldsymbol{\mathcal{H}} = \mathbf{0}$, for $t \leq t_0$.

Between the electric flux density and the electric field, as well as between the magnetic flux density and the magnetic field, an interrelationship exists that depends on the type of medium under consideration. These interrelationships are known as the constitutive relations. For instance, in free space, the flux densities differ only by a constant factor from the field intensities as follows

$$\boldsymbol{\mathcal{D}} = \epsilon_0 \boldsymbol{\mathcal{E}}, \qquad \boldsymbol{\mathcal{B}} = \mu_0 \boldsymbol{\mathcal{H}}, \tag{2.3}$$

where μ_0 and ϵ_0 are the free-space permeability and the free-space permittivity, respectively. A general formulation of the constitutive relations is found by using the properties of the medium. In the formulation of the general case, it proves convenient to introduce two additional vectors, namely the electric and magnetic polarization vectors,

$$\boldsymbol{\mathcal{P}} = \boldsymbol{\mathcal{D}} - \epsilon_0 \boldsymbol{\mathcal{E}}, \qquad \boldsymbol{\mathcal{M}} = \frac{1}{\mu_0} \boldsymbol{\mathcal{B}} - \boldsymbol{\mathcal{H}}. \tag{2.4}$$

The polarization vectors are thus associated with the medium and vanish in free space. In demonstrating the effect of the medium parameters on the polarization vectors, the electric polarization vector will be used as an example. For a linear and time-invariant medium, the electric polarization vector is written as

$$\boldsymbol{\mathcal{P}}(\mathbf{r},t) = \epsilon_0 \int_0^\infty \underline{\underline{\chi}}_e(\mathbf{r},\tau)\boldsymbol{\mathcal{E}}(\mathbf{r},t-\tau)d\tau, \tag{2.5}$$

where $\underline{\underline{\chi}}_e(\mathbf{r},t)$ is the electric susceptibility which is a 2-tensor. If the medium is isotropic, the electric susceptibility can be written as

$$\underline{\underline{\chi}}_e(\mathbf{r},t) = \chi_e(\mathbf{r},t)\cdot\mathbf{I}, \tag{2.6}$$

where $\mathbf{I}$ is the identity matrix. In addition, the medium is assumed to react instantaneously and the electric susceptibility can thus be simplified to

$$\chi_e(\mathbf{r},t) = \chi_e(\mathbf{r})\delta(t), \tag{2.7}$$

where $\delta(t)$ is the Dirac delta distribution. With this definition of $\chi_e(\mathbf{r},t)$, the expression for the electric polarization vector assumes the simplified form

$$\boldsymbol{\mathcal{P}} = \epsilon_0\chi_e(\mathbf{r})\boldsymbol{\mathcal{E}}. \tag{2.8}$$

The magnetic polarization vector can be found in a similar way as

$$\boldsymbol{\mathcal{M}} = \chi_m(\mathbf{r})\boldsymbol{\mathcal{H}}, \tag{2.9}$$

where $\chi_m(\mathbf{r})$ is the magnetic susceptibility. The induced current density is found as

$$\boldsymbol{\mathcal{J}} = \sigma(\mathbf{r})\boldsymbol{\mathcal{E}}, \tag{2.10}$$

where $\sigma(\mathbf{r})$ is the conductivity. Both susceptibilities and the conductivity are scalar functions that depend only on the position $\mathbf{r}$. Combining (2.8) – (2.10) with (2.1) and (2.2) leads to

$$\nabla \times \boldsymbol{\mathcal{E}} + \mu_0\mu_r(\mathbf{r})\partial_t\boldsymbol{\mathcal{H}} = -\boldsymbol{\mathcal{K}}_0, \tag{2.11}$$

$$\nabla \times \boldsymbol{\mathcal{H}} - \epsilon_0\epsilon_r(\mathbf{r})\partial_t\boldsymbol{\mathcal{E}} - \sigma(\mathbf{r})\boldsymbol{\mathcal{E}} = \boldsymbol{\mathcal{J}}_0, \tag{2.12}$$

where $\epsilon_r(\mathbf{r}) = 1 + \chi_e(\mathbf{r})$ is the relative permittivity and $\mu_r(\mathbf{r}) = 1 + \chi_m(\mathbf{r})$ is the relative permeability, which both depend solely on the position $\mathbf{r}$. With these definitions, the flux densities can also be written as

$$\boldsymbol{\mathcal{D}} = \epsilon(\mathbf{r})\boldsymbol{\mathcal{E}}, \qquad \boldsymbol{\mathcal{B}} = \mu(\mathbf{r})\boldsymbol{\mathcal{H}}, \tag{2.13}$$

where $\epsilon(\mathbf{r}) = \epsilon_0\epsilon_r(\mathbf{r})$ is the permittivity and $\mu(\mathbf{r}) = \mu_0\mu_r(\mathbf{r})$ is the permeability.

2.1.2   Maxwell's equations in the frequency domain

Since, later on in this thesis, a so-called "marching-on-in-frequency" technique [37] is used to obtain time-domain results for the quantities under investigation, a temporal Fourier transformation is used to facilitate the necessary conversions to the frequency domain. This mathematical tool transforms the space-time equations into space-frequency equations. In this thesis, the temporal Fourier transformation and its inverse are defined as

$$F(\omega) = \int_{-\infty}^{\infty} \mathcal{F}(t) \exp(i\omega t) dt, \tag{2.14}$$

$$\mathcal{F}(t) = \frac{1}{2\pi} \int_{-\infty}^{\infty} F(\omega) \exp(-i\omega t) d\omega. \tag{2.15}$$

As can be seen, the time-domain quantities are represented by a script symbol and the frequency-domain quantities are represented by a roman symbol. Since, in the time domain, only causal and real-valued quantities are considered, the temporal Fourier transformation and its inverse can be written as

$$F(\omega) = \int_{0}^{\infty} \mathcal{F}(t) \exp(i\omega t) dt, \tag{2.16}$$

$$\mathcal{F}(t) = \frac{1}{\pi} \mathrm{Re} \int_{0}^{\infty} F(\omega) \exp(-i\omega t) d\omega, \tag{2.17}$$

where it is noted that the frequency-domain quantities are complex-valued. Applying the temporal Fourier transformation to the time-domain Maxwell's equations results in

$$\nabla \times \mathbf{E} - i\omega\mu(\mathbf{r})\mathbf{H} = -\mathbf{K}_0, \tag{2.18}$$

$$\nabla \times \mathbf{H} + i\omega\epsilon(\mathbf{r})\mathbf{E} - \sigma(\mathbf{r})\mathbf{E} = \mathbf{J}_0, \tag{2.19}$$

which are Maxwell's equations in the frequency domain. Note that the constitutive parameters ϵ, μ and σ depend on position $\mathbf{r}$.

Usually the conductivity is incorporated in the complex permittivity. To this end, the relative permittivity is redefined as

$$\varepsilon_r(\mathbf{r}) = \frac{\varepsilon(\mathbf{r})}{\epsilon_0} = \epsilon_r(\mathbf{r}) - \frac{\sigma(\mathbf{r})}{i\omega\epsilon_0}, \tag{2.20}$$

also often referred to as the complex relative permittivity. The frequency dependence in the argument of the complex permittivity is omitted. Substitution of this definition in the frequency-domain Maxwell's equations results in

$$\nabla \times \mathbf{E} - i\omega\mu(\mathbf{r})\mathbf{H} = \mathbf{0}, \tag{2.21}$$

$$\nabla \times \mathbf{H} + i\omega\varepsilon(\mathbf{r})\mathbf{E} = \mathbf{J}_0, \tag{2.22}$$

where $\mathbf{K}_0 = \mathbf{0}$ since no magnetic current sources are considered.

2.2 Current sources in layered media

In this section, the solution for the electric and magnetic field quantities excited by an external source will be given for a planarly layered structure. To facilitate this, Maxwell's equations will be rewritten as a suitable set of equations to account for a dielectric, lossy medium. In principle, the set of equations is also applicable to dispersive media.

As an example, this set of equations will be solved for a homogeneous medium. This example is extended to two half spaces and finally a solution for a three-layer configuration (slab) will be given.

An impressed current source is located in a three-dimensional space where the appropriate material parameters vary in the z-direction only. In view of the layered configuration to be studied at a later stage, Maxwell's equations are decomposed into longitudinal and transverse components. This is done as follows

$$
\begin{aligned}
\mathbf{E} &= \mathbf{E}_T + E_z \mathbf{u}_z, \\
\mathbf{r} &= \mathbf{r}_T + z \mathbf{u}_z,
\end{aligned}
\tag{2.23}
$$

where the subscript T refers to the two-dimensional transverse vector and where the subscript z is the longitudinal direction. Similar definitions apply to the other physical quantities and coordinates. A solution to Maxwell's equations in the spatial domain can be found with the aid of a two-dimensional spatial Fourier transformation. After this transformation, propagation in the z-direction remains, therefore, the longitudinal components are taken in that direction. This spatial Fourier transformation is defined in this thesis as

$$
\hat{\mathbf{E}}(\mathbf{k}_T, z, \omega) = \int_{-\infty}^{\infty} \int_{-\infty}^{\infty} \mathbf{E}(\mathbf{r}, \omega) \exp(-i\mathbf{k}_T \cdot \mathbf{r}_T) dx dy,
\tag{2.24}
$$

where $\mathbf{k}_T = k_x \mathbf{u}_x + k_y \mathbf{u}_y$. Note that the circumflex ˆ represents a spatially transformed quantity. The corresponding inverse transformation is given by

$$
\mathbf{E}(\mathbf{r}, \omega) = \frac{1}{4\pi^2} \int_{-\infty}^{\infty} \int_{-\infty}^{\infty} \hat{\mathbf{E}}(\mathbf{k}_T, z, \omega) \exp(i\mathbf{k}_T \cdot \mathbf{r}_T) dk_x dk_y.
\tag{2.25}
$$

Applying the decomposition into transverse and longitudinal components and the spatial Fourier transformation to the frequency-domain Maxwell's equations results in

$$
(i\mathbf{k}_T + \partial_z \mathbf{u}_z) \times \left[\hat{\mathbf{E}}_T + \hat{E}_z \mathbf{u}_z \right] - i\omega\mu(z) \left[\hat{\mathbf{H}}_T + \hat{H}_z \mathbf{u}_z \right] = \mathbf{0},
\tag{2.26}
$$

$$
(i\mathbf{k}_T + \partial_z \mathbf{u}_z) \times \left[\hat{\mathbf{H}}_T + \hat{H}_z \mathbf{u}_z \right] + i\omega\varepsilon(z) \left[\hat{\mathbf{E}}_T + \hat{E}_z \mathbf{u}_z \right] = \hat{\mathbf{J}}_T + \hat{J}_z \mathbf{u}_z,
\tag{2.27}
$$

where the arguments $(\mathbf{k}_T, z, \omega)$ are omitted. Note that the subscript 0 of the current source is omitted.

It is possible to derive a scalar ordinary differential equation for the longitudinal (z-) components and to express the transverse field components in terms of $\hat{E}_z$ and $\hat{H}_z$. The field components can thus be evaluated.

To this end, equations (2.26) and (2.27) are decomposed into the three directions $\mathbf{u}_z$, $i\mathbf{k}_T$ and ($\mathbf{u}_z \times i\mathbf{k}_T$). Figure 2.1 shows these components in the (k_x, k_y) plane. The procedure
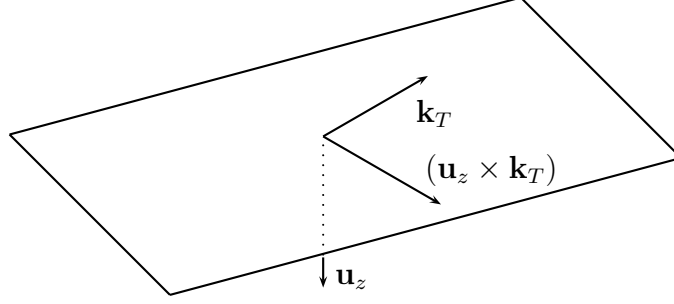
Figure 2.1: *Alternative coordinates for a point in the (k_x, k_y) plane.*

to find the different electromagnetic field components is carried out by taking the inner products of (2.26) and (2.27) with $\mathbf{u}_z$, $i\mathbf{k}_T$ and ($\mathbf{u}_z \times i\mathbf{k}_T$), respectively. These inner products result in six equations which, combined, give the desired set to solve Maxwell's equations.

Since the derivation is completely analogous for (2.26) and (2.27), the procedure is outlined only for (2.27). For (2.26) merely the results are given.

First, the inner product of (2.27) with $\mathbf{u}_z$ is taken. This gives

$$\mathbf{u}_z \cdot \left[(i\mathbf{k}_T + \partial_z \mathbf{u}_z) \times \left(\hat{\mathbf{H}}_T + \hat{H}_z \mathbf{u}_z \right) \right] + i\omega \varepsilon(z) \hat{E}_z = \hat{J}_z, \tag{2.28}$$

which simplifies to

$$(\mathbf{u}_z \times i\mathbf{k}_T) \cdot \hat{\mathbf{H}}_T + i\omega \varepsilon(z) \hat{E}_z = \hat{J}_z. \tag{2.29}$$

The same procedure for (2.26) gives

$$(\mathbf{u}_z \times i\mathbf{k}_T) \cdot \hat{\mathbf{E}}_T - i\omega \mu(z) \hat{H}_z = 0. \tag{2.30}$$

Next, the inner product of (2.27) with $i\mathbf{k}_T$ is taken. This gives

$$i\mathbf{k}_T \cdot \left[(i\mathbf{k}_T + \partial_z \mathbf{u}_z) \times \left(\hat{\mathbf{H}}_T + \hat{H}_z \mathbf{u}_z \right) \right] + i\omega \varepsilon(z) \hat{\mathbf{E}}_T \cdot i\mathbf{k}_T = \hat{\mathbf{J}}_T \cdot i\mathbf{k}_T \tag{2.31}$$

which simplifies to

$$-\partial_z (\mathbf{u}_z \times i\mathbf{k}_T) \cdot \hat{\mathbf{H}}_T + i\omega \varepsilon(z) \hat{\mathbf{E}}_T \cdot i\mathbf{k}_T = \hat{\mathbf{J}}_T \cdot i\mathbf{k}_T. \tag{2.32}$$

When (2.32) is combined with (2.29), the latter equation can be written as

$$\hat{\mathbf{E}}_T \cdot i\mathbf{k}_T = \frac{1}{i\omega\varepsilon(z)}\left(\hat{\mathbf{J}}_T \cdot i\mathbf{k}_T + \partial_z \hat{J}_z\right) - \frac{1}{\varepsilon(z)}\partial_z\left(\varepsilon(z)\hat{E}_z\right), \tag{2.33}$$

and analogously for (2.26)

$$\hat{\mathbf{H}}_T \cdot i\mathbf{k}_T = -\frac{1}{\mu(z)}\partial_z\left(\mu(z)\hat{H}_z\right). \tag{2.34}$$

Finally, the inner product of (2.27) with $(\mathbf{u}_z \times i\mathbf{k}_T)$ is taken. This gives

$$(\mathbf{u}_z \times i\mathbf{k}_T) \cdot \left[(i\mathbf{k}_T + \partial_z\mathbf{u}_z) \times \left(\hat{\mathbf{H}}_T + \hat{H}_z\mathbf{u}_z\right)\right] + i\omega\varepsilon(z)(\mathbf{u}_z \times i\mathbf{k}_T) \cdot \hat{\mathbf{E}}_T =$$
$$(\mathbf{u}_z \times i\mathbf{k}_T) \cdot \hat{\mathbf{J}}_T. \tag{2.35}$$

With the aid of the following identities

$$(\mathbf{u}_z \times i\mathbf{k}_T) \cdot (i\mathbf{k}_T \times \hat{H}_z\mathbf{u}_z) = -(i\mathbf{k}_T \cdot i\mathbf{k}_T)\hat{H}_z = k_T^2\hat{H}_z, \tag{2.36}$$

$$(\mathbf{u}_z \times i\mathbf{k}_T) \cdot (\partial_z\mathbf{u}_z \times \hat{\mathbf{H}}_T) = \partial_z(i\mathbf{k}_T \cdot \hat{\mathbf{H}}_T), \tag{2.37}$$

where $k_T^2 = |\mathbf{k}_T|^2 = k_x^2 + k_y^2$, the latter equation is rewritten as

$$k_T^2\hat{H}_z + \partial_z(i\mathbf{k}_T \cdot \hat{\mathbf{H}}_T) + i\omega\varepsilon(z)(\mathbf{u}_z \times i\mathbf{k}_T) \cdot \hat{\mathbf{E}}_T = (\mathbf{u}_z \times i\mathbf{k}_T) \cdot \hat{\mathbf{J}}_T. \tag{2.38}$$

Substituting (2.34) and (2.30) in (2.38) results in the desired ordinary differential equation for $\hat{H}_z$:

$$\left[k_T^2 - \omega^2\varepsilon(z)\mu(z)\right]\hat{H}_z - \partial_z\left[\frac{1}{\mu(z)}\partial_z\left(\mu(z)\hat{H}_z\right)\right] = (\mathbf{u}_z \times i\mathbf{k}_T) \cdot \hat{\mathbf{J}}_T. \tag{2.39}$$

The counterpart of (2.39) is found as

$$\left[k_T^2 - \omega^2\varepsilon(z)\mu(z)\right]\hat{E}_z - \partial_z\left[\frac{1}{\varepsilon(z)}\partial_z\left(\varepsilon(z)\hat{E}_z\right)\right] = i\omega\mu(z)\hat{J}_z - \partial_z\left(\frac{\hat{\mathbf{J}}_T \cdot i\mathbf{k}_T + \partial_z\hat{J}_z}{i\omega\varepsilon(z)}\right). \tag{2.40}$$

In the next step, the transverse field components are expressed in terms of the longitudinal field components. The expressions for the transverse field components follow directly from decomposing them into the directions depicted in Figure 2.1. Doing so results in the following decomposition for the transverse electric field component

$$\hat{\mathbf{E}}_T = -\frac{1}{k_T^2}\left[\left(\hat{\mathbf{E}}_T \cdot i\mathbf{k}_T\right)i\mathbf{k}_T + \left(\hat{\mathbf{E}}_T \cdot (\mathbf{u}_z \times i\mathbf{k}_T)\right)(\mathbf{u}_z \times i\mathbf{k}_T)\right], \tag{2.41}$$

where both inner product terms can immediately be recognized in (2.33) and (2.30), respectively. For the transverse magnetic field component, the same procedure applies. Substitution of these expressions in (2.41) yields

$$\hat{\mathbf{E}}_T = \frac{1}{k_T^2}\left[\frac{1}{\varepsilon(z)}\left[\partial_z\left(\varepsilon(z)\hat{E}_z\right) + \frac{i}{\omega}\left(\hat{\mathbf{J}}_T \cdot i\mathbf{k}_T + \partial_z\hat{J}_z\right)\right]i\mathbf{k}_T - i\omega\mu(z)\hat{H}_z(\mathbf{u}_z \times i\mathbf{k}_T)\right]. \tag{2.42}$$

The counterpart for $\hat{\mathbf{H}}_T$ is given by

$$\hat{\mathbf{H}}_T = \frac{1}{k_T^2} \left[\frac{1}{\mu(z)} \partial_z \left(\mu(z) \hat{H}_z \right) i\mathbf{k}_T - \left(\hat{J}_z - i\omega\varepsilon(z)\hat{E}_z \right) (\mathbf{u}_z \times i\mathbf{k}_T) \right]. \tag{2.43}$$

The result of the derivation described above is the following set of equations

$$\left(k_T^2 - \omega^2\varepsilon(z)\mu(z) \right) \hat{E}_z - \partial_z \left[\frac{1}{\varepsilon(z)} \partial_z \left(\varepsilon(z)\hat{E}_z \right) \right] = i\omega\mu(z)\hat{J}_z - \partial_z \left(\frac{\hat{\mathbf{J}}_T \cdot i\mathbf{k}_T + \partial_z \hat{J}_z}{i\omega\varepsilon(z)} \right), \tag{2.44}$$

$$\left(k_T^2 - \omega^2\varepsilon(z)\mu(z) \right) \hat{H}_z - \partial_z \left[\frac{1}{\mu(z)} \partial_z \left(\mu(z)\hat{H}_z \right) \right] = (\mathbf{u}_z \times i\mathbf{k}_T) \cdot \hat{\mathbf{J}}_T, \tag{2.45}$$

$$\hat{\mathbf{E}}_T = \frac{1}{k_T^2} \left[\frac{1}{\varepsilon(z)} \left[\partial_z \left(\varepsilon(z)\hat{E}_z \right) + \frac{i}{\omega} \left(\hat{\mathbf{J}}_T \cdot i\mathbf{k}_T + \partial_z \hat{J}_z \right) \right] i\mathbf{k}_T - i\omega\mu(z)\hat{H}_z \left(\mathbf{u}_z \times i\mathbf{k}_T \right) \right], \tag{2.46}$$

$$\hat{\mathbf{H}}_T = \frac{1}{k_T^2} \left[\frac{1}{\mu(z)} \partial_z \left(\mu(z)\hat{H}_z \right) i\mathbf{k}_T - \left(\hat{J}_z - i\omega\varepsilon(z)\hat{E}_z \right) (\mathbf{u}_z \times i\mathbf{k}_T) \right], \tag{2.47}$$

which is a generalization of the result found in [38, Chapter 6.1]. This result is analogous to the transmission-line solution for (I, V) derived by Felsen and Marcuvitz [39].

Once the solutions for $\hat{E}_z$ and $\hat{H}_z$ are obtained, the expressions for the transverse field components can be easily obtained. The set of equations will be solved for three different media configurations. First a current point source in a homogeneous medium will be addressed.

2.2.1   Solution for a homogeneous medium

The easiest solution to the differential equations (2.44) – (2.45) is found for a homogeneous medium. For a homogeneous medium the material parameters do not depend on z. Therefore, the complex permittivity and permeability can be written as $\varepsilon(z) = \varepsilon_1$ and $\mu(z) = \mu_1$ and the set of equations (2.44) – (2.47) becomes much easier to work with.

As stated earlier, the electromagnetic field is excited by an external source. In view of the configurations to be investigated later, the external source is a current point source located at $(x = 0, y = 0, z = z_1)$ pointing into the x-direction and is defined as

$$\boldsymbol{\mathcal{J}}_0(\mathbf{r}, t) = d_t \mathcal{F}(t)\delta_3(\mathbf{r} - z_1\mathbf{u}_z)\mathbf{u}_x, \tag{2.48}$$

where $\mathcal{F}(t)$ is a pulse of finite duration that starts at time instant t_0 and $\mathbf{u}_x$ is a unit vector in the x-direction. Note that δ_3 is the three-dimensional Dirac delta distribution. The derivative with respect to time has been included to ensure that no static charge stays behind as $t \to \infty$. After transformation to the frequency and spatial Fourier domain, the current density is written as

$$\hat{\mathbf{J}}_0 \left(\mathbf{k}_T, z, \omega \right) = -i\omega F(\omega)\delta(z - z_1)\mathbf{u}_x, \tag{2.49}$$

where δ is the Dirac delta distribution. As an example, the differential equation for the longitudinal electric field will be solved. At the end of this section, the results for the other field components will be given as well.

With the definitions of the material parameters and the current density (2.49), (2.44) reduces to

$$\partial_z^2 \hat{E}_z - (k_T^2 - \omega^2 \varepsilon_1 \mu_1)\hat{E}_z = -\frac{ik_x F(\omega)}{\varepsilon_1}\delta'(z - z_1), \tag{2.50}$$

where the prime denotes the derivative with respect to z. To find a solution of this differential equation, it is convenient to first look at the fundamental, one-dimensional wave equation

$$\partial_z^2 \hat{G}_z - \gamma_1^2 \hat{G}_z = -\delta(z - z_1), \tag{2.51}$$

where $\gamma_1^2 = k_T^2 - \omega^2 \varepsilon_1 \mu_1$ is the square of the axial wavenumber. The general solution of (2.51) is found as

$$\hat{G}_z = \frac{1}{2\gamma_1}\exp(-\gamma_1|z - z_1|) + P\exp(-\gamma_1 z) + Q\exp(\gamma_1 z). \tag{2.52}$$

This solution must satisfy the radiation conditions, which imply that the solution must remain bounded or represent outgoing waves as $z \to \pm\infty$. Therefore, the unknown constants must be $P = Q = 0$ and the particular solution to the one-dimensional wave equation remains. This particular solution is referred to as Green's function which is defined as

$$\hat{G}_z = \frac{1}{2\gamma_1}\exp(-\gamma_1|z - z_1|). \tag{2.53}$$

The evaluation of the complex root for γ_1 requires special attention. When the inverse temporal Fourier transformation (2.17) is carried out for (2.53), the following integrand is found

$$\hat{G}_z \exp(-i\omega t) = \frac{1}{2\gamma_1}\exp\left[-i\left(\omega t + \mathrm{Im}(\gamma_1)|z - z_1|\right) - \mathrm{Re}(\gamma_1)|z - z_1|\right] \tag{2.54}$$

To ensure a decaying wave for large $|z - z_1|$, the real part of the axial wavenumber must be non-negative. To ensure a radiating solution, it is required that $(\omega t + \mathrm{Im}(\gamma_1)|z - z_1|)$ is constant for $t \to \infty$ and $|z - z_1| \to \infty$, therefore the imaginary part of γ_1 is non-positive. With the solution of (2.51), the solution of (2.50) is readily found as

$$\begin{aligned}
\hat{E}_z &= \frac{ik_x}{2\gamma_1 \varepsilon_1}F(\omega)\partial_z\left[\exp(-\gamma_1|z - z_1|)\right] \\
&= -\frac{ik_x}{2\varepsilon_1}F(\omega)\mathrm{sgn}(z - z_1)\exp(-\gamma_1|z - z_1|),
\end{aligned} \tag{2.55}$$

and the other field components can easily be found as

$$\hat{H}_z = -\frac{k_y\omega}{2\gamma_1}F(\omega)\exp(-\gamma_1|z-z_1|), \tag{2.56}$$

$$\hat{\mathbf{E}}_T = \frac{F(\omega)}{2\gamma_1\varepsilon_1}\exp(-\gamma_1|z-z_1|)\left[(\omega^2\varepsilon_1\mu_1 - k_x^2)\mathbf{u}_x - k_xk_y\mathbf{u}_y\right], \tag{2.57}$$

$$\hat{\mathbf{H}}_T = \frac{i\omega F(\omega)}{2}\mathrm{sgn}(z-z_1)\exp(-\gamma_1|z-z_1|)\mathbf{u}_y. \tag{2.58}$$

2.2.2   Solution for two homogeneous half spaces

In this section, the homogeneous space, as described in the previous section, will be extended to the configuration depicted in Figure 2.2. The appropriate material parameters
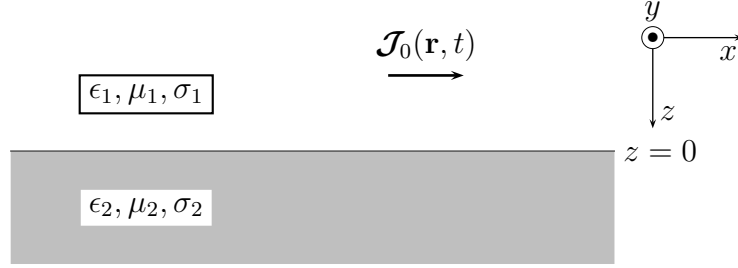
Figure 2.2: *The location of the current point source $\boldsymbol{\mathcal{J}}_0(\mathbf{r},t)$ in a half space.*

in the upper medium will be denoted with subscript 1 and in the lower medium with subscript 2. The positive z-direction points downwards. A current point source is located at $(x=0,\ y=0,\ z=z_1 < 0)$ above the interface $z=0$ between the two media and has been introduced in (2.48).

Since there are two regions with different material properties, boundary conditions are needed to ensure a correct representation of the field values in both regions. In this section, a general derivation of these conditions will be given for the longitudinal field components because these are the field components that will be solved first from the appropriate differential equations. The expressions for the longitudinal components will be used to derive representations for the total field in the half spaces.

The first two boundary conditions follow directly from (2.29) and (2.30)

$$\left.\begin{array}{l}\hat{D}_z = \varepsilon(z)\hat{E}_z \text{ is continuous} \\ \hat{B}_z = \mu(z)\hat{H}_z \text{ is continuous}\end{array}\right\} \text{ for } z = 0. \tag{2.59}$$

The third boundary condition is obtained by integrating (2.44) over a small interval

$[-\Delta z, \Delta z]$ surrounding the interface. This yields

$$\left[\frac{1}{\varepsilon(z)}\partial_z\left(\varepsilon(z)\hat{E}_z\right)\right]\Bigg|_{z=-\Delta z}^{z=\Delta z} + \int_{-\Delta z}^{\Delta z}[\omega^2\varepsilon(z)\mu(z) - k_T^2]\hat{E}_z dz = 0. \tag{2.60}$$

If the limit for $\Delta z \downarrow 0$ is taken, it follows that $\left[\partial_z(\varepsilon(z)\hat{E}_z)\right]/\varepsilon(z)$ must be continuous because the integral in the second term of (2.60) vanishes. From (2.45), it follows in the same way that $\left[\partial_z(\mu(z)\hat{H}_z)\right]/\mu(z)$ must be continuous. This leads to a second set of boundary conditions:

$$\left.\begin{array}{l} \dfrac{1}{\varepsilon(z)}\partial_z\left(\varepsilon(z)\hat{E}_z\right) \text{ is continuous} \\[2mm] \dfrac{1}{\mu(z)}\partial_z\left(\mu(z)\hat{H}_z\right) \text{ is continuous} \end{array}\right\} \text{ for } z = 0. \tag{2.61}$$

Since both half spaces are homogeneous, the latter set of boundary conditions reduces to

$$\left.\begin{array}{l} \partial_z\hat{E}_z \text{ is continuous} \\[2mm] \partial_z\hat{H}_z \text{ is continuous} \end{array}\right\} \text{ for } z = 0. \tag{2.62}$$

The longitudinal electric field component for a homogeneous space was found in the previous section. Since there is an interface in the present configuration, a wave reflected at the interface propagating in the negative z-direction in the first medium will occur. This reflected wave is accounted for by a coefficient Q and an appropriate propagation factor $\exp(\gamma_1 z)$ which follows immediately from the general solution for the one-dimensional wave equation (2.51). Again the general solution must satisfy the radiation conditions and therefore $P = 0$. For the first medium the longitudinal field can be written as

$$\hat{E}_z = \frac{-ik_x}{2\varepsilon_1}F(\omega)\text{sgn}(z - z_1)\exp(-\gamma_1|z - z_1|) + Q\exp(\gamma_1 z), \text{ for } z < 0, \tag{2.63}$$

which is similar to the generalized solution (2.52). In the second medium, there is no source and only a downward propagating wave can be present ($Q = 0$) and therefore the longitudinal field in the second medium is written as

$$\hat{E}_z = P\exp(-\gamma_2 z), \text{ for } z > 0, \tag{2.64}$$

with $\gamma_n^2 = k_T^2 - \omega^2\varepsilon_n\mu_n$, $n = 1, 2$. The coefficients P and Q are still undetermined. To find an expression for these coefficients, the boundary conditions (2.59) and (2.62) are applied to (2.63) and (2.64), which gives the following system of linear equations

$$\frac{-ik_x}{2}F(\omega)\exp(\gamma_1 z_1) + \varepsilon_1 Q = \varepsilon_2 P, \tag{2.65}$$

$$\frac{ik_x\gamma_1}{2\varepsilon_1}F(\omega)\exp(\gamma_1 z_1) + \gamma_1 Q = -\gamma_2 P. \tag{2.66}$$

Solving this system of equations yields

$$Q = \frac{-ik_x}{2\varepsilon_1} F(\omega) \exp(\gamma_1 z_1) \frac{\varepsilon_2\gamma_1 - \varepsilon_1\gamma_2}{\varepsilon_2\gamma_1 + \varepsilon_1\gamma_2} = \frac{-ik_x}{2\varepsilon_1} F(\omega) \exp(\gamma_1 z_1) R_{12}^E, \tag{2.67}$$

$$P = \frac{-ik_x}{2\varepsilon_2} F(\omega) \exp(\gamma_1 z_1) \frac{2\varepsilon_2\gamma_1}{\varepsilon_2\gamma_1 + \varepsilon_1\gamma_2} = \frac{-ik_x}{2\varepsilon_2} F(\omega) \exp(\gamma_1 z_1) T_{12}^E, \tag{2.68}$$

where

$$R_{12}^E = \frac{\varepsilon_2\gamma_1 - \varepsilon_1\gamma_2}{\varepsilon_2\gamma_1 + \varepsilon_1\gamma_2}, \qquad \text{and} \qquad T_{12}^E = \frac{2\varepsilon_2\gamma_1}{\varepsilon_2\gamma_1 + \varepsilon_1\gamma_2}, \tag{2.69}$$

are the electric Fresnel reflection and transmission coefficient, respectively. The subscript 12 in the reflection and transmission coefficient denotes the reflection in medium 1 at the interface with medium 2 and the transmission from medium 1 to 2, respectively. With these definitions, (2.63) and (2.64) finally assume the form

$$\hat{E}_z = \frac{-ik_x}{2\varepsilon_1} F(\omega) \left\{ \text{sgn}(z - z_1) \exp(-\gamma_1|z - z_1|) + R_{12}^E \exp[\gamma_1(z + z_1)] \right\}, \text{ for } z < 0, \tag{2.70}$$

$$\hat{E}_z = \frac{-ik_x}{2\varepsilon_2} F(\omega) T_{12}^E \exp(\gamma_1 z_1 - \gamma_2 z), \text{ for } z > 0. \tag{2.71}$$

The longitudinal component of the magnetic field is derived in a similar way and looks as follows

$$\hat{H}_z = \frac{-k_y\omega}{2\gamma_1} F(\omega) \left\{ \exp(-\gamma_1|z - z_1|) + R_{12}^H \exp[\gamma_1(z + z_1)] \right\}, \text{ for } z < 0, \tag{2.72}$$

$$\hat{H}_z = \frac{-k_y\omega\mu_1}{2\gamma_1\mu_2} F(\omega) T_{12}^H \exp(\gamma_1 z_1 - \gamma_2 z), \text{ for } z > 0, \tag{2.73}$$

where the magnetic reflection and transmission coefficients are defined as

$$R_{12}^H = \frac{\mu_2\gamma_1 - \mu_1\gamma_2}{\mu_2\gamma_1 + \mu_1\gamma_2}, \qquad \text{and} \qquad T_{12}^H = \frac{2\mu_2\gamma_1}{\mu_2\gamma_1 + \mu_1\gamma_2}. \tag{2.74}$$

Now that the expressions for the longitudinal field components are known, the spectral transverse electric field can easily be found from (2.46) as

$$\hat{\mathbf{E}}_T = \frac{F(\omega)}{2\varepsilon_1\gamma_1} \exp(-\gamma_1|z - z_1|) \left\{ (\omega^2\varepsilon_1\mu_1 - k_x^2)\mathbf{u}_x - k_xk_y\mathbf{u}_y \right\}$$
$$+ \frac{F(\omega)}{2\varepsilon_1\gamma_1} \exp[\gamma_1(z + z_1)] \left\{ \gamma_1^2 R_{12}^E \frac{k_x^2\mathbf{u}_x + k_xk_y\mathbf{u}_y}{k_T^2} + \omega^2\varepsilon_1\mu_1 R_{12}^H \frac{k_y^2\mathbf{u}_x - k_xk_y\mathbf{u}_y}{k_T^2} \right\},$$
$$\text{for } z < 0, \tag{2.75}$$

$$\hat{\mathbf{E}}_T = \frac{F(\omega)}{2\varepsilon_2\gamma_1} \exp(\gamma_1 z_1 - \gamma_2 z) \left\{ \omega^2\varepsilon_2\mu_1 \frac{k_y^2\mathbf{u}_x - k_xk_y\mathbf{u}_y}{k_T^2} T_{12}^H - \gamma_1\gamma_2 \frac{k_x^2\mathbf{u}_x + k_xk_y\mathbf{u}_y}{k_T^2} T_{12}^E \right\},$$
$$\text{for } z > 0. \tag{2.76}$$

For the transverse magnetic field, similar expressions can be found. The transverse components of the electric field can be broken up into x and y-components. Furthermore, a reflected and transmitted field component can be recognized by comparing the latter expressions to the results found for a homogenous medium as found in the previous section. As an example, the x-components of the reflected and transmitted electric field are extracted

$$\hat{E}_x^r = \frac{F(\omega)}{2\varepsilon_1\gamma_1} \exp\left[\gamma_1(z + z_1)\right] \left\{ \gamma_1^2 R_{12}^E \frac{k_x^2}{k_T^2} + \omega^2 \varepsilon_1 \mu_1 \frac{k_y^2}{k_T^2} R_{12}^H \right\}, \qquad (2.77)$$

$$\hat{E}_x^t = \frac{F(\omega)}{2\varepsilon_2\gamma_1} \exp(\gamma_1 z_1 - \gamma_2 z) \left\{ \omega^2 \varepsilon_2 \mu_1 \frac{k_y^2}{k_T^2} T_{12}^H - \gamma_1 \gamma_2 \frac{k_x^2}{k_T^2} T_{12}^E \right\}, \qquad (2.78)$$

which is the same result that was found in [24, 25]. With these expressions, the reflected and the transmitted field are known and the total electromagnetic field can be determined for any $z < 0$ and $z > 0$, respectively.

2.2.3 Solution for a homogeneous slab configuration

In this section, a generalized reflection coefficient for the medium above a homogeneous slab will be derived. The situation as depicted in Figure 2.3 will be considered. A homogeneous slab with thickness d_s of medium 2 is flanked by two half spaces consisting of medium 1 and 3, respectively. In this configuration, medium 2 may act as a waveguide. Therefore, the inverse spatial Fourier transformation needs special attention. The material parameters
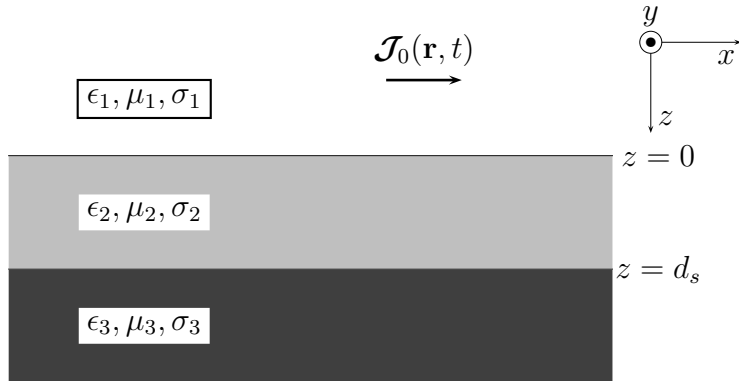
Figure 2.3: *The location of the current point source $\mathcal{J}_0(\mathbf{r}, t)$ in a slab configuration.*

inside the slab are homogeneous. Following the same procedure as in the previous section for a configuration with two half spaces, the longitudinal electric field for the three regions

can be written as follows:

$$\hat{E}_z = -\frac{ik_x}{2\varepsilon_1}F(\omega)\mathrm{sgn}(z - z_1)\exp\left(-\gamma_1|z - z_1|\right) + Q\exp(\gamma_1 z), \text{ for } z < 0, \tag{2.79}$$

$$\hat{E}_z = A\exp(-\gamma_2 z) + B\exp(\gamma_2 z), \text{ for } 0 < z < d_s, \tag{2.80}$$

$$\hat{E}_z = P\exp(-\gamma_3 z), \text{ for } z > d_s. \tag{2.81}$$

Applying the boundary conditions (2.59) and (2.62) to the longitudinal field components at $z = 0$ and $z = d_s$ results in the following system of equations:

$$-\frac{ik_x}{2}F(\omega)\exp(\gamma_1 z_1) + \varepsilon_1 Q = \varepsilon_2(A + B), \tag{2.82}$$

$$\frac{ik_x}{2\varepsilon_1}\gamma_1 F(\omega)\exp(\gamma_1 z_1) + \gamma_1 Q = \gamma_2(B - A), \tag{2.83}$$

$$\varepsilon_2 B\exp(\gamma_2 d_s) + \varepsilon_2 A\exp(-\gamma_2 d_s) = \varepsilon_3 P\exp(-\gamma_3 d_s), \tag{2.84}$$

$$\gamma_2 B\exp(\gamma_2 d_s) - \gamma_2 A\exp(-\gamma_2 d_s) = -\gamma_3 P\exp(-\gamma_3 d_s). \tag{2.85}$$

Solving this system of equations yields

$$Q = -\frac{ik_x}{2\varepsilon_1}F(\omega)\exp(\gamma_1 z_1)\tilde{R}_{12}^E, \tag{2.86}$$

$$A = -\frac{ik_x}{2\varepsilon_2}F(\omega)\exp(\gamma_1 z_1)\tilde{T}_{12}^E, \tag{2.87}$$

$$B = -\frac{ik_x}{2\varepsilon_2}F(\omega)\exp(\gamma_1 z_1)\tilde{R}_{23}^E, \tag{2.88}$$

$$P = -\frac{ik_x}{2\varepsilon_3}F(\omega)\exp(\gamma_1 z_1)\tilde{T}_{13}^E, \tag{2.89}$$

with

$$\tilde{R}_{12}^E = R_{12}^E + \frac{T_{12}^E R_{23}^E T_{21}^E \exp(-2\gamma_2 d)}{1 - R_{21}^E R_{23}^E \exp(-2\gamma_2 d_s)}, \quad \tilde{R}_{23}^E = \frac{T_{12}^E R_{23}^E \exp(-2\gamma_2 d_s)}{1 - R_{21}^E R_{23}^E \exp(-2\gamma_2 d_s)},$$

$$\tilde{T}_{12}^E = \frac{T_{12}^E}{1 - R_{21}^E R_{23}^E \exp(-2\gamma_2 d_s)}, \quad \tilde{T}_{13}^E = \frac{T_{12}^E T_{23}^E \exp(-(\gamma_2 - \gamma_3)d_s)}{1 - R_{21}^E R_{23}^E \exp(-2\gamma_2 d)},$$

$$R_{12}^E = \frac{\varepsilon_2\gamma_1 - \varepsilon_1\gamma_2}{\varepsilon_2\gamma_1 + \varepsilon_1\gamma_2}, \quad R_{21}^E = \frac{\varepsilon_1\gamma_2 - \varepsilon_2\gamma_1}{\varepsilon_2\gamma_1 + \varepsilon_1\gamma_2}, \quad R_{23}^E = \frac{\varepsilon_3\gamma_2 - \varepsilon_2\gamma_3}{\varepsilon_3\gamma_2 + \varepsilon_2\gamma_3}$$

$$T_{12}^E = \frac{2\varepsilon_2\gamma_1}{\varepsilon_2\gamma_1 + \varepsilon_1\gamma_2}, \quad T_{21}^E = \frac{2\varepsilon_1\gamma_2}{\varepsilon_2\gamma_1 + \varepsilon_1\gamma_2}, \quad T_{23}^E = \frac{2\varepsilon_3\gamma_2}{\varepsilon_3\gamma_2 + \varepsilon_2\gamma_3},$$

where the tildes ˜ indicate that the respective coefficients now refer to the complete slab configuration. With these definitions, (2.79) – (2.81) assume the form

$$\hat{E}_z = -\frac{ik_x}{2\varepsilon_1}F(\omega)\left\{\mathrm{sgn}(z-z_1)\exp\left(-\gamma_1|z-z_1|\right) + \tilde{R}_{12}^E\exp(\gamma_1(z+z_1))\right\},$$
$$\text{for } z < 0, \tag{2.90}$$

$$\hat{E}_z = -\frac{ik_x}{2\varepsilon_2}F(\omega)\exp(\gamma_1 z_1)\left\{\tilde{T}_{12}^E\exp(-\gamma_2 z) + \tilde{R}_{23}^E\exp(\gamma_2 z)\right\}, \text{ for } 0 < z < d_s, \tag{2.91}$$

$$\hat{E}_z = -\frac{ik_x}{2\varepsilon_3}F(\omega)\tilde{T}_{13}^E\exp(\gamma_1 z_1 - \gamma_3 z), \text{ for } z > d_s. \tag{2.92}$$

For the longitudinal components of the magnetic field, similar expressions apply. With the expressions for the longitudinal field components, the transverse electric field can easily be found from (2.46) as

$$\mathbf{E}_T = \frac{F(\omega)}{2\varepsilon_1\gamma_1}\exp\left(\gamma_1(z+z_1)\right)\left\{\tilde{R}_{12}^E\gamma_1^2\frac{k_x^2\mathbf{u}_x + k_xk_y\mathbf{u}_y}{k_T^2} + \omega^2\varepsilon_1\mu_1\tilde{R}_{12}^H\frac{k_y^2\mathbf{u}_x - k_xk_y\mathbf{u}_y}{k_T^2}\right\}$$
$$+\frac{F(\omega)}{2\varepsilon_1\gamma_1}\exp\left(-\gamma_1|z-z_1|\right)\left\{(\omega^2\varepsilon_1\mu_1 - k_x^2)\mathbf{u}_x - k_xk_y\mathbf{u}_y\right\}, \text{ for } z < 0, \tag{2.93}$$

$$\mathbf{E}_T = \frac{F(\omega)}{2\varepsilon_2\gamma_1}\exp(\gamma_1 z - 1)\left\{\gamma_1\gamma_2\left(\tilde{T}_{12}^E\exp(-\gamma_2 z) + \tilde{R}_{23}^E\exp(\gamma_2 z)\right)\frac{k_x^2\mathbf{u}_x + k_xk_y\mathbf{u}_y}{k_T^2}\right.$$
$$+\omega^2\varepsilon_2\mu_1\left(\tilde{T}_{12}^H\exp(-\gamma_2 z) + \tilde{R}_{23}^H\exp(\gamma_2 z)\right)\Bigg\}, \text{ for } 0 < z < d_s, \tag{2.94}$$

$$\mathbf{E}_T = \frac{F(\omega)}{2\varepsilon_3\gamma_1}\exp(\gamma_1 z_1 - \gamma_3 z)\left\{\gamma_1\gamma_3\tilde{T}_{13}^E\frac{k_x^2\mathbf{u}_x + k_xk_y\mathbf{u}_y}{k_T^2} + \omega^2\varepsilon_3\mu_2\tilde{T}_{12}^H\frac{k_y^2\mathbf{u}_x - k_xk_y\mathbf{u}_y}{k_T^2}\right\},$$
$$\text{for } z > d_s, \tag{2.95}$$

where the magnetic reflection and transmission coefficients with superscripts H differ from their electric counterparts, with superscripts E, by interchanging ε and μ.

In the case that there are more layers, the reflection and transmission coefficients can again be generalized per medium, but in this thesis, no more than three layers will be considered. A good description of this generalization can be found in e.g. [40, pages 52-53].

An elegant solution for an inhomogeneous slab configuration can be found in [27, 32, 38].

2.3 Transformation to the spatial domain

In this section, the inverse Fourier transformation to the spatial domain, which is defined as,

$$\mathbf{E}(\mathbf{r}, \omega) = \frac{1}{4\pi^2}\int_{-\infty}^{\infty}\int_{-\infty}^{\infty}\hat{\mathbf{E}}(\mathbf{k}_T, z, \omega)\exp(i\mathbf{k}_T \cdot \mathbf{r}_T)dk_x dk_y, \tag{2.96}$$

will be elaborated. To this end, cylindrical coordinates are introduced as follows

$$k_x = k_T \cos \phi_k,$$
$$k_y = k_T \sin \phi_k,$$
$$x = \rho \cos \phi,$$
$$y = \rho \sin \phi,$$

and thus

$$\mathbf{k}_T \cdot \mathbf{r}_T = k_T \rho \cos(\phi_k - \phi). \tag{2.97}$$

After substitution of the cylindrical coordinates, (2.96) becomes

$$\mathbf{E}(\mathbf{r}, \omega) = \frac{1}{4\pi^2} \int_0^\infty k_T dk_T \int_{-\pi}^\pi \hat{\mathbf{E}}\big(k_T(\cos \phi_k \mathbf{u}_x + \sin \phi_k \mathbf{u}_y), z, \omega\big) \cdot$$
$$\exp\big(ik_T \rho \cos(\phi_k - \phi)\big) d\phi_k. \tag{2.98}$$

Later on in this thesis, the x-components of the electric field are used to solve a number of problems involving thin wires. Therefore, the x-components of the reflected and transmitted fields as described by (2.77) and (2.78) are used to demonstrate the inverse Fourier transformation in the k-domain. After carrying out the inverse Fourier transformation (2.25) and expressing (2.77) and (2.78) in terms of cylindrical coordinates, the following expressions for the x-component of the reflected and transmitted electric field are obtained:

$$E_x^r(\mathbf{r}, \omega) = \frac{F(\omega)}{8\varepsilon_1 \pi^2} \int_0^\infty k_0^3 \frac{\nu \, d\nu}{u_1} \exp\big(k_0 u_1(z + z_1)\big) \cdot$$
$$\left\{ u_1^2 R_{12}^E \int_{-\pi}^\pi \cos^2(\phi_k) \exp\big(ik_0 \nu \rho \cos(\phi_k - \phi)\big) \, d\phi_k \right.$$
$$\left. + R_{12}^H \varepsilon_{1r} \mu_{1r} \int_{-\pi}^\pi \sin^2(\phi_k) \exp\big(ik_0 \nu \rho \cos(\phi_k - \phi)\big) \, d\phi_k \right\}, \tag{2.99}$$

$$E_x^t(\mathbf{r}, \omega) = \frac{F(\omega)}{8\varepsilon_2 \pi^2} \int_0^\infty k_0^3 \frac{\nu \, d\nu}{u_1} \exp\big(k_0(u_1 z_1 - u_2 z)\big) \cdot$$
$$\left\{ T_{12}^H \varepsilon_{2r} \mu_{1r} \int_{-\pi}^\pi \sin^2(\phi_k) \exp\big(ik_0 \nu \rho \cos(\phi_k - \phi)\big) \, d\phi_k \right.$$
$$\left. - T_{12}^E u_1 u_2 \int_{-\pi}^\pi \cos^2(\phi_k) \exp\big(ik_0 \nu \rho \cos(\phi_k - \phi)\big) \, d\phi_k \right\}, \tag{2.100}$$

where the normalized quantities $\nu = k_T/k_0$ and $u_n = \sqrt{\nu^2 - \varepsilon_{r,n} \mu_{r,n}} = \gamma_n/k_0$ have been introduced and where $k_0 = \omega/c_0$. The integrals over ϕ_k can be evaluated in closed form. In both field quantities these integrals are the same. The integral containing the squared

cosine will be used to demonstrate the integration over ϕ_k. The integral with the squared sine is evaluated in a similar way.

First, the identity

$$\cos^2(\phi_k) = \frac{1}{2} + \frac{1}{2}\cos(2\phi_k), \tag{2.101}$$

and $\phi'_k = \phi_k - \phi$ are substituted in

$$\int_{-\pi}^{\pi} \cos^2(\phi_k) \exp\left[ik_0\nu\rho\cos(\phi_k - \phi)\right] d\phi_k. \tag{2.102}$$

This results in the following integral

$$2\int_0^{\pi} \left(\frac{1}{2} + \frac{1}{2}\cos(2\phi'_k)\cos(2\phi)\right) \exp\left(ik_0\nu\rho\cos(\phi'_k)\right) d\phi'_k. \tag{2.103}$$

Now, the identity [41, (9.1.21)]

$$\frac{1}{\pi}\int_0^{\pi} \exp\left(iz\cos(\theta)\right)\cos(n\theta)\, d\theta = i^n J_n(z), \tag{2.104}$$

can be used, where J_n is the Bessel function of the first kind of order n. With this identity, (2.103) is reduced to

$$\int_{-\pi}^{\pi} \cos^2(\phi_k) \exp\left(ik_0\nu\rho\cos(\phi_k - \phi)\right) d\phi_k = \pi J_0(k_0\nu\rho) - \pi J_2(k_0\nu\rho)\cos(2\phi), \tag{2.105}$$

which is the desired analytical expression for the integral containing the squared cosine. The result for the integral containing the squared sine follows in an analogous way as

$$\int_{-\pi}^{\pi} \sin^2(\phi_k) \exp\left(ik_0\nu\rho\cos(\phi_k - \phi)\right) d\phi_k = \pi J_0(k_0\nu\rho) + \pi J_2(k_0\nu\rho)\cos(2\phi). \tag{2.106}$$

Substitution of both results in the reflected and transmitted electric field expressions under consideration gives

$$E_x^r(\mathbf{r}, \omega) = \frac{\omega^3 F(\omega)\mu_0}{8\pi c_0} \int_0^{\infty} \nu\, d\nu \exp\left(k_0 u_1(z + z_1)\right) \left\{ J_0(k_0\nu\rho)\left[\frac{u_1}{\varepsilon_{1r}}R_{12}^E + \frac{\mu_{1r}}{u_1}R_{12}^H\right] \right.$$
$$\left. + J_2(k_0\nu\rho)\cos(2\phi)\left[\frac{\mu_{1r}}{u_1}R_{12}^H - \frac{u_1}{\varepsilon_{1r}}R_{12}^E\right]\right\}, \tag{2.107}$$

$$E_x^t(\mathbf{r}, \omega) = \frac{\omega^3 F(\omega)\mu_0}{8\pi c_0} \int_0^{\infty} \nu\, d\nu \exp\left(k_0(u_1 z_1 - u_2 z)\right) \left\{ J_0(k_0\nu\rho)\left[\frac{\mu_{1r}}{u_1}T_{12}^H - \frac{u_2}{\varepsilon_{2r}}T_{12}^E\right] \right.$$
$$\left. + J_2(k_0\nu\rho)\cos(2\phi)\left[\frac{\mu_{1r}}{u_1}T_{12}^H + \frac{u_2}{\varepsilon_{2r}}T_{12}^E\right]\right\}. \tag{2.108}$$

which is the same result as was found by Rubio Bretones *et al.* [24].

It is clear that the integral over ν in the expressions above cannot be evaluated in closed form. Therefore that integral is evaluated numerically with the aid of a composite Gaussian quadrature rule. The challenge is to find a fixed quadrature rule that may be applied for all frequencies and nevertheless produces a correct time-domain result.

The first problem in the integration over ν finds its origin in the $1/u_n$ root singularity. In fact the integrand has two branch points at $\nu_j = \sqrt{\epsilon_{jr}\mu_{jr}}$ with $j = 1, 2$. The integration needs special attention at these points.

Secondly, in the interval $\nu \in [\nu_2, \infty)$, the asymptotic behavior of the integrand plays an important role. In [24], the analysis of this behavior takes place in the time domain. It turns out that the integrand is of the order $\mathcal{O}(\nu^{-2})$ and converges uniformly in the space and the frequency domain as $\nu \to \infty$. The integration contour runs along the real ν axis in the fourth quadrant, see Figure 2.4. Following [24], the branch points are $n_1 = \min\{\nu_1, \nu_2\}$
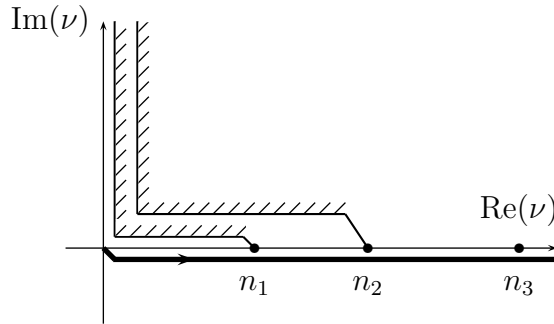
Figure 2.4: *Integration contour in the complex ν-plane with the branch points $n_1 = \min\{\nu_1, \nu_2\}$ and $n_2 = \max\{\nu_1, \nu_2\}$.*

and $n_2 = \max\{\nu_1, \nu_2\}$.

Before the substitution that governs the asymptotic behavior of the integrand can be carried out, an intermediate point n_3 where the integrand is sufficiently small is introduced. Now, the integration contour is divided into 5 intervals. In each interval, a suitable substitution of the integrand is chosen to handle the problematic behavior near the end points of the interval. For the choices of $n_{1,2}$ as described above, the substitution for ν is chosen according to Table 2.1. In addition to the choice of the substitution for ν per interval, the integration boundaries for the new integration variable β are tabulated. The boundaries of β are necessary to determine the appropriate parameters for the quadrature rule. Each of the subintegrals is evaluated with a Gauss-Legendre rule with the exception of the last interval, which is evaluated with a Gauss-Laguerre rule with a weighting function $\exp(-2\beta)$ [24]. The latter rule governs the asymptotic behavior of the integrand [24]. Note that in the last interval, the substitution contains n_1 instead of n_3. This choice is based on the presence

Interval	ν substitutes	boundaries
$0 < \nu < n_1$	$n_1 \sin\beta$	$0 < \beta < \dfrac{\pi}{2}$
$n_1 < \nu < \dfrac{n_1 + n_2}{2}$	$n_1 \cosh\beta$	$0 < \beta < \cosh^{-1}\left(\dfrac{n_1 + n_2}{2n_1}\right)$
$\dfrac{n_1 + n_2}{2} < \nu < n_2$	$n_2 \sin\beta$	$\arcsin\left(\dfrac{n_1 + n_2}{2n_2}\right) < \beta < \dfrac{\pi}{2}$
$n_2 < \nu < n_3$	$n_2 \cosh\beta$	$0 < \beta < \cosh^{-1}\left(\dfrac{n_3}{n_2}\right)$
$n_3 < \nu < \infty$	$n_1 \cosh\beta$	$\cosh^{-1}\left(\dfrac{n_3}{n_1}\right) < \beta < 2$

Table 2.1: *Substitutions for ν for each interval of the integration and the boundaries for the new integration variable β.*

of u_1 in the field expressions.

The point n_3 needs to be carefully chosen for a correct calculation of the ν integral. When the shape of the input voltage is considered in the determination of the point n_3, a lower value of n_3 will suffice to produce accurate results.

To demonstrate the effects of the choice of n_3 in the frequency domain, the reflected and transmitted fields due to a point source are evaluated with a composite Gaussian quadrature rule. The fields in (2.107) and (2.108) are approximated according to

$$E_x^{r,t}(\mathbf{r},\omega) \approx \sum_{k=1}^{K} \alpha_k \zeta^{r,t}(\mathbf{r},\nu_k,\omega), \tag{2.109}$$

where

$$\zeta^r(\mathbf{r},\nu_k,\omega) = \frac{i\mu_0}{8\pi c_0}\omega^2\nu_k \exp\left[k_0 u_1(z + z_1)\right] \left\{ J_0\left(k_0\nu_k\rho\right)\left[\frac{u_1}{\varepsilon_{1r}}R_{12}^E + \frac{\mu_{1r}}{u_1}R_{12}^H\right] \right.$$
$$\left. + J_2\left(k_0\nu_k\rho\right)\cos(2\phi)\left[\frac{\mu_{1r}}{u_1}R_{12}^H - \frac{u_1}{\varepsilon_{1r}}R_{12}^E\right] \right\}, \tag{2.110}$$

$$\zeta^t(\mathbf{r},\nu_k,\omega) = \frac{i\mu_0}{8\pi c_0}\omega^2\nu_k \exp\left[k_0(u_1 z_1 - u_2 z)\right] \left\{ J_0\left(k_0\nu_k\rho\right)\left[\frac{\mu_{1r}}{u_1}T_{12}^H - \frac{u_2}{\varepsilon_{2r}}T_{12}^E\right] \right.$$
$$\left. + J_2\left(k_0\nu_k\rho\right)\cos(2\phi)\left[\frac{\mu_{1r}}{u_1}T_{12}^H + \frac{u_2}{\varepsilon_{2r}}T_{12}^E\right] \right\}, \tag{2.111}$$

and where K is the number of points needed for the composite Gaussian quadrature rule.

The weights $\{\alpha_k\}$ and abscissa $\{\nu_k\}$ with index k are calculated with the aid of the sub-routine `D01BCF` of the NAG numerical library. Note that the weights $\{\alpha_k\}$ do not depend on the frequency.

In all examples, the point source is located at $\mathbf{r} = 0.5\mathbf{u}_x - 0.1\mathbf{u}_z$. With the exception of the permittivity of the lower half space ϵ_{2r}, the medium properties of both half spaces equal the ones for vacuum. The points of observation are chosen at $\mathbf{r} = 0.5\mathbf{u}_x + \mathbf{u}_y - 0.1\mathbf{u}_z$ and $\mathbf{r} = 0.5\mathbf{u}_x + 0.5\mathbf{u}_y + 0.1\mathbf{u}_z$ for the reflected and transmitted field expressions, respectively. The first example considers a lower half space with $\epsilon_{2r} = 3$. In Figure 2.5, the real and
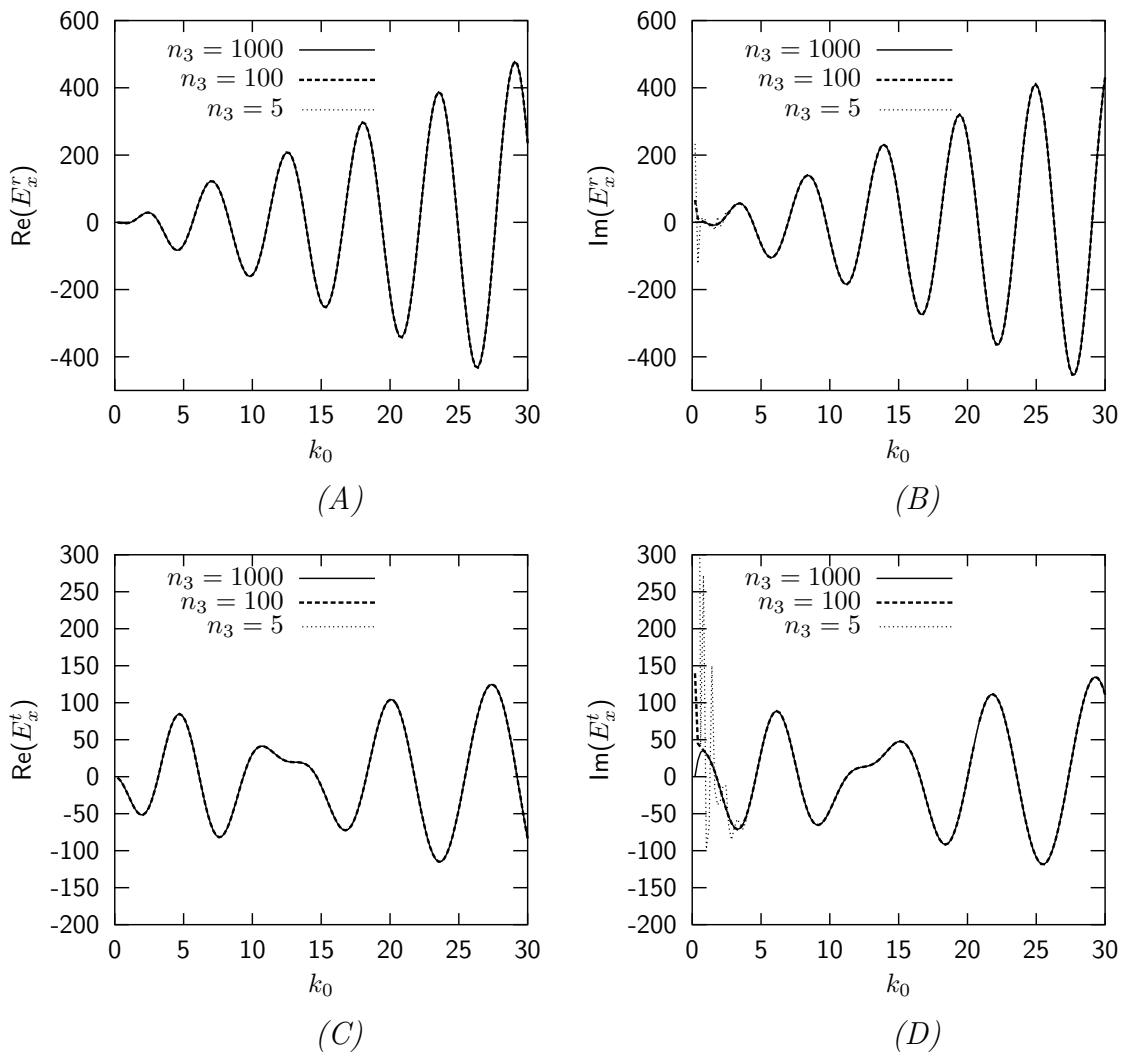
Figure 2.5: *Real and imaginary part of the reflected (A,B) and transmitted electric field(C,D) at $\mathbf{r} = 0.5\mathbf{u}_x + 0.5\mathbf{u}_y + 0.1\mathbf{u}_z$ generated by a point source at $\mathbf{r} = 0.5\mathbf{u}_x - 0.1\mathbf{u}_z$ for different values of n_3. The material parameters of both half spaces are equal to the ones from vacuum except $\epsilon_{2r} = 3$.*
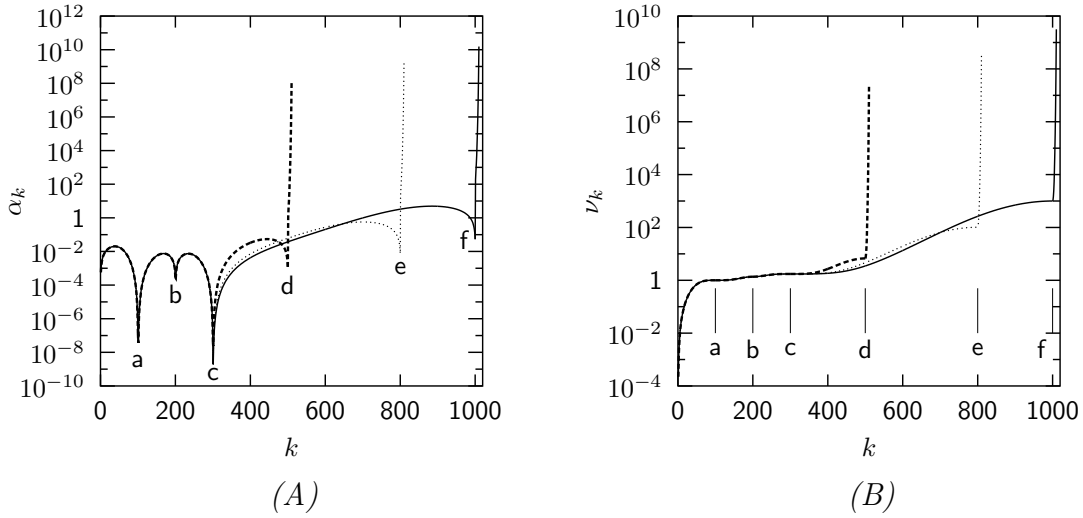
Figure 2.6: *Weights α_k (A) and abscissa ν_k (B) as a function of index k. The material parameters of both half spaces are equal to the ones from vacuum except $\epsilon_{2r} = 3$. The letters denote* a $= \nu_{100} = n_1$, b $= \nu_{200} = (n_1 + n_2)/2$, c $= \nu_{300} = n_2$, d $= \nu_{500} = n_3 = 5$, e $= \nu_{800} = n_3 = 100$, f $= \nu_{1000} = n_3 = 1000$, *respectively.*

imaginary parts of the reflected and transmitted electric fields are plotted as a function of frequency for various values of n_3. The value $n_3 = 1000$ is chosen as a reference value for the calculation of the field expressions. It is observed that the results for the real parts of the reflected and transmitted fields are stable over the entire frequency range. The imaginary parts of both fields on the other hand show numerical errors for lower values of n_3. For $n_3 \approx 145$, the imaginary parts of both fields are calculated accurately. For $\epsilon_{2r} = 3$, the weights and abscissa are plotted as a function of the index k in Figure 2.6. The points $n_{1,2,3}$ are indicated in both plots. The number of points for the first three intervals is 100 and 10 for the last interval. The number of points for the fourth interval is 200, 500 and 700 for the values 5, 100 and 1000 of n_3, respectively.

In Figure 2.5, it was observed that the real parts of both electric fields are stable. Therefore, only the imaginary parts of the reflected and transmitted electric fields will be plotted in the remainder of this section.

The next example concerns lower half spaces with $\epsilon_{2r} = 9$ and $\epsilon_{2r} = 16$, respectively. In Figure 2.7, the imaginary parts of the reflected and transmitted electric fields are plotted for two values of n_3. For one value of n_3, the calculations are unstable and the other value of n_3 is taken at the point where the calculations become stable. Comparing Figures 2.5 and 2.7 shows that the values of n_3 where the field calculations are accurate is proportional to the square root of the permittivity. The value for n_3 is approximately given by $n_3 = Cn_2$,
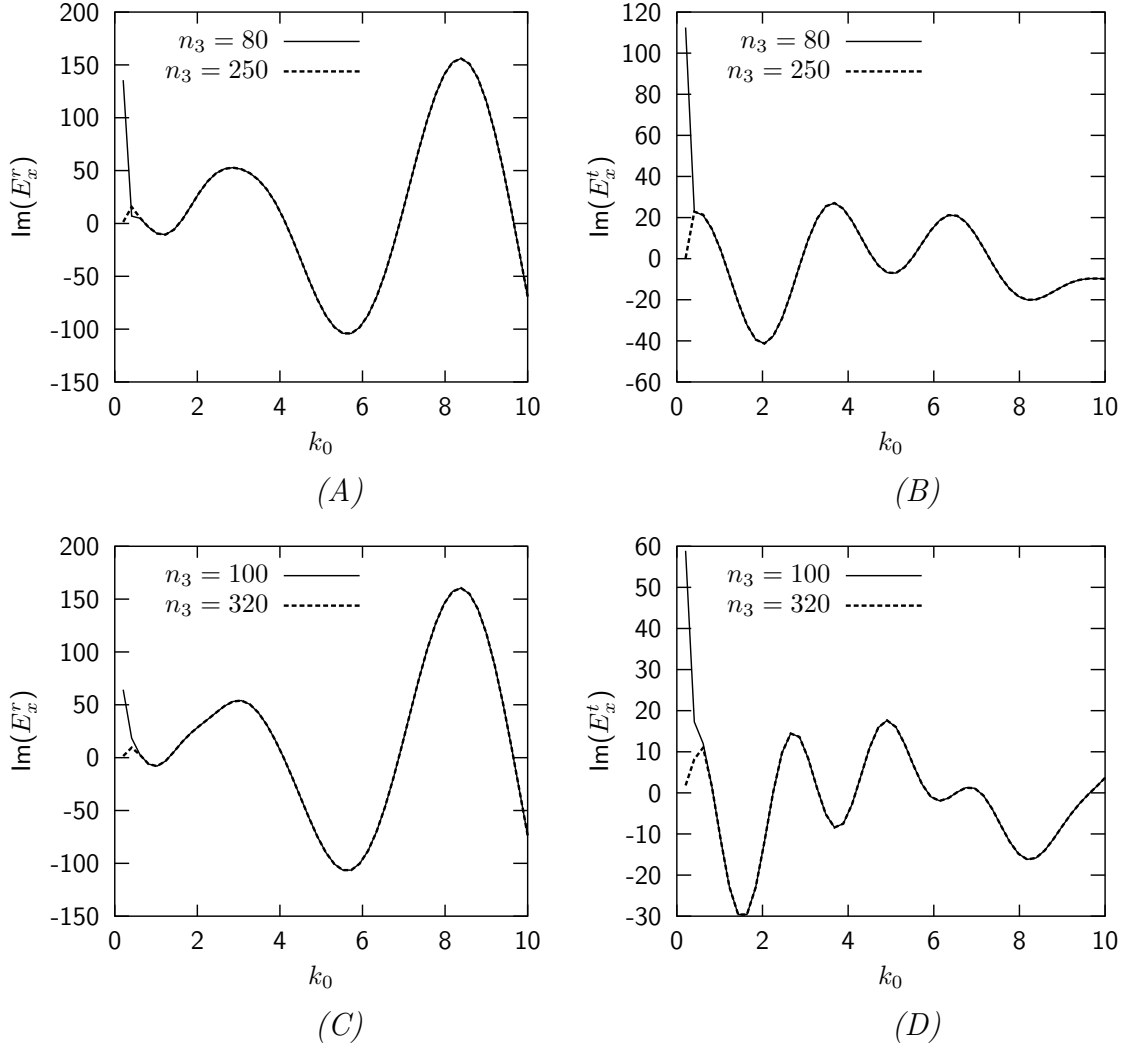
Figure 2.7: *Imaginary parts of the reflected and transmitted electric fields at* $\mathbf{r} = 0.5\mathbf{u}_x + 0.5\mathbf{u}_y + 0.1\mathbf{u}_z$ *generated by a point source at* $\mathbf{r} = 0.5\mathbf{u}_x - 0.1\mathbf{u}_z$ *for different values of* n_3. *The permittivity of the lower half space is* $\epsilon_{2r} = 9$ *(A,B) and* $\epsilon_{2r} = 16$ *(C,D), respectively. The other material parameters equal the ones from vacuum.*

where C is a constant. From the calculations, it follows that $C \approx 85$ results in an accurate calculation of the reflected and transmitted fields in the frequency domain. For the input voltage considered in later chapters, it follows that $C \approx 16$ produces accurate results.

For the slab configuration, the integration contour has to be deformed differently. In the slab region, guided-wave poles may occur. This complicates the numerical calculation of the ν integral significantly [27, 42]. An extensive analysis of how to handle the ν integral in case of a slab configuration can be found in [42] and in less detail in [27].

Chapter 3

The current along a single straight thin wire

The current along a single thin wire can be described by an integral equation. To find this equation, first two integral equations are derived for the scattering by an electrically impenetrable object in three dimensions. These equations are the well-known electric and magnetic field integral equations, in the literature often abbreviated as EFIE and MFIE [43].

The frequency-domain EFIE is then cast into a special form which is also known as the integral equation of Pocklington [37]. From this equation, the current along a wire antenna can be obtained for a given voltage source and/or an external incident electric field. A disadvantage of Pocklington's equation is the presence of a second-order partial derivative. In an attempt to find an analytical expression for the current along a wire, Hallén eliminated the second-order partial derivative. The equation to describe the current along a wire that was found by Hallén is referred to as Hallén's equation.

Hallén's equation is discretized and solved numerically. In this chapter, the excitation is a delta-gap voltage source. The results are compared to results from the literature.

At the end of this chapter, a traveling-wave model of the current is presented. This model gives some insight into the actual behavior of the current. The traveling wave model is adopted from a first-order approximate solution of Hallén's equation [44]. The current is described as a sum of traveling waves with the velocity of the exterior medium which are repeatedly reflected at the end faces of the wire [35]. The parameters involved are a reflection coefficient and an admittance which determines the amplitude of the traveling waves at various locations along the wire.

In the first-order approximation, the reflection coefficient at the end faces of the wire equals

-1. The higher-order approximation [35] uses the generalized reflection coefficient found by Ufimtsev [45] and the generalized admittance found by Shen *et al.* [46].

3.1   Scattering by an electrically impenetrable object

In this section the integral equation for scattering by an electrically impenetrable object will be derived following [47]. The entire derivation is carried out in the frequency domain. The object and the domain definitions involved with the derivation of the integral equation are depicted in Figure 3.1. A perfectly conducting scatterer which comprises the domain
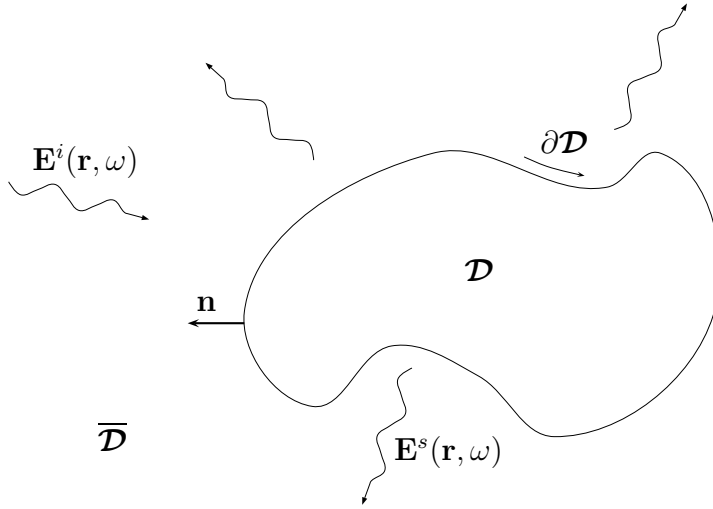
Figure 3.1: *Domain definitions for the derivation of the integral equations.*

$\mathcal{D}$ is embedded in a homogeneous dielectric medium. The homogeneous medium will be denoted as medium 1 with material parameters $\mu_1(\mathbf{r}) = \mu_1$ and $\varepsilon_1(\mathbf{r}) = \varepsilon_1$. The scatterer is bounded by $\partial\mathcal{D}$. The embedding extends over an infinite domain denoted by $\overline{\mathcal{D}}$ and is exterior to $\partial\mathcal{D}$. The normal $\mathbf{n}$ on the surface of $\mathcal{D}$ points into $\overline{\mathcal{D}}$ and is assumed to be piecewise continuous. The incident field that illuminates the object is generated by an external electric current density.

3.1.1   The incident field

First, the incident field in the interior domain $\mathcal{D}$ is considered. This is the field that would be present in absence of the scatterer. The incident field has its sources in $\overline{\mathcal{D}}$ and therefore

satisfies

$$\nabla \times \mathbf{H}^i(\mathbf{r}, \omega) + i\omega\varepsilon_1 \mathbf{E}^i(\mathbf{r}, \omega) = \mathbf{0}, \tag{3.1}$$

$$\nabla \times \mathbf{E}^i(\mathbf{r}, \omega) - i\omega\mu_1 \mathbf{H}^i(\mathbf{r}, \omega) = \mathbf{0}, \tag{3.2}$$

for $\mathbf{r} \in \mathcal{D}$. It is seen that the trivial solution to this system of homogeneous differential equations would be $\mathbf{E}^i = \mathbf{0}$ and $\mathbf{H}^i = \mathbf{0}$. However, non-trivial solutions exist in $\mathcal{D}$ and can be expressed in terms of an electric and magnetic surface current density along $\partial\mathcal{D}$. To find these expressions, the three-dimensional spatial Fourier transformation will be used. The 3D spatial Fourier transform $\hat{\mathbf{V}}(\mathbf{k}, \omega)$ of a vector field $\mathbf{V}(\mathbf{r}, \omega)$ over the finite domain $\mathcal{D}$ with boundary $\partial\mathcal{D}$ is defined as

$$\hat{\mathbf{V}}(\mathbf{k}, \omega) = \int_{\mathbf{r} \in \mathcal{D}} \mathbf{V}(\mathbf{r}, \omega) \exp(-i\mathbf{k} \cdot \mathbf{r}) \, d\mathbf{r}, \tag{3.3}$$

where $\mathbf{k} = k_x\mathbf{u}_x + k_y\mathbf{u}_y + k_z\mathbf{u}_z$. Since the vector field $\mathbf{V}(\mathbf{r}, \omega)$ is restricted to the domain $\mathcal{D}$, it is extended to an infinite domain by introducing a shape function [48, Appendix B2] which is defined as

$$\mathcal{S}_{\mathcal{D}}(\mathbf{r}) = \begin{cases} 1 & \text{for } \mathbf{r} \in \mathcal{D} \\ \frac{1}{2} & \text{for } \mathbf{r} \in \partial\mathcal{D} \\ 0 & \text{for } \mathbf{r} \in \overline{\mathcal{D}} \end{cases}. \tag{3.4}$$

The choice of this particular shape function follows directly by treating the integral in (3.3) as a Cauchy principal value integral around "infinity". The spatial Fourier transformation can then be written in a general form as

$$\hat{\mathbf{V}}(\mathbf{k}, \omega) = \int_{\mathbf{r} \in \mathbb{R}^3} \mathbf{V}(\mathbf{r}, \omega) \mathcal{S}_{\mathcal{D}}(\mathbf{r}) \exp(-i\mathbf{k} \cdot \mathbf{r}) \, d\mathbf{r}. \tag{3.5}$$

Note that the hat ˆ now represents a Fourier transformation of a spatially filtered function over the entire domain $\mathbb{R}^3$. To apply this transformation to Maxwell's equations in the frequency domain, (2.21) and (2.22), the corresponding transform of $\nabla \times \mathbf{V}(\mathbf{r}, \omega)$ has to be derived. By using Gauss' theorem, this transform is found as:

$$\begin{aligned}
(\widehat{\nabla \times \mathbf{V}})(\mathbf{k}, \omega) &= \int_{\mathbf{r} \in \mathcal{D}} (\nabla \times \mathbf{V})(\mathbf{r}, \omega) \exp(-i\mathbf{k} \cdot \mathbf{r}) d\mathbf{r} \\
&= \int_{\mathbf{r} \in \mathcal{D}} \nabla \times [\mathbf{V}(\mathbf{r}, \omega) \exp(-i\mathbf{k}\cdot\mathbf{r})] \, d\mathbf{r} + \int_{\mathbf{r} \in \mathcal{D}} \mathbf{V}(\mathbf{r}, \omega) \times [\nabla \exp(-i\mathbf{k}\cdot\mathbf{r})] \, d\mathbf{r} \\
&= \oint_{\mathbf{r} \in \partial\mathcal{D}} \mathbf{n}(\mathbf{r}) \times \mathbf{V}(\mathbf{r}, \omega) \exp(-i\mathbf{k} \cdot \mathbf{r}) d\mathbf{r} + i\mathbf{k} \times \hat{\mathbf{V}}(\mathbf{k}, \omega),
\end{aligned} \tag{3.6}$$

where $\mathbf{n}(\mathbf{r}) \times \mathbf{V}(\mathbf{r}, \omega)$ is identified as a surface current density. The forward 3D spatial Fourier transformation as given in (3.5) has an inverse counterpart, which is defined as

$$\mathcal{S}_{\mathcal{D}}(\mathbf{r})\mathbf{V}(\mathbf{r}, \omega) = \frac{1}{8\pi^3} \int_{\mathbf{k} \in \mathbb{R}^3} \hat{\mathbf{V}}(\mathbf{k}, \omega) \exp(i\mathbf{k} \cdot \mathbf{r}) d\mathbf{k}. \tag{3.7}$$

Applying the 3D spatial Fourier transformation to (3.1) and (3.2) yields

$$i\mathbf{k} \times \hat{\mathbf{H}}^i(\mathbf{k}, \omega) + i\omega\varepsilon_1 \hat{\mathbf{E}}^i(\mathbf{k}, \omega) = \hat{\mathbf{J}}_B^{e,i}(\mathbf{k}, \omega), \tag{3.8}$$

$$i\mathbf{k} \times \hat{\mathbf{E}}^i(\mathbf{k}, \omega) - i\omega\mu_1 \hat{\mathbf{H}}^i(\mathbf{k}, \omega) = -\hat{\mathbf{J}}_B^{m,i}(\mathbf{k}, \omega), \tag{3.9}$$

in which $\hat{\mathbf{J}}_B^{e,i}(\mathbf{k}, \omega)$ and $\hat{\mathbf{J}}_B^{m,i}(\mathbf{k}, \omega)$ are the spatial transforms over the boundary $\partial\mathcal{D}$ of the quantities

$$\mathbf{J}_B^{e,i}(\mathbf{r}, \omega) = -\mathbf{n}(\mathbf{r}) \times \mathbf{H}^i(\mathbf{r}, \omega), \tag{3.10}$$

$$\mathbf{J}_B^{m,i}(\mathbf{r}, \omega) = \mathbf{n}(\mathbf{r}) \times \mathbf{E}^i(\mathbf{r}, \omega), \tag{3.11}$$

where the subscript B stands for "boundary". Equations (3.8) and (3.9) are now of an algebraic form, from which analytic expressions for the electric and magnetic field can be found in terms of the surface current densities. As an example, an expression for $\hat{\mathbf{H}}^i$ will be derived.

First, the cross product of $i\mathbf{k}$ with (3.8) is taken as follows

$$i\mathbf{k} \times \left(i\mathbf{k} \times \hat{\mathbf{H}}^i(\mathbf{k}, \omega) \right) + i\omega\varepsilon_1 \left(i\mathbf{k} \times \hat{\mathbf{E}}^i(\mathbf{k}, \omega) \right)$$
$$= i\mathbf{k}\left(i\mathbf{k} \cdot \hat{\mathbf{H}}^i(\mathbf{k}, \omega) \right) + k^2 \hat{\mathbf{H}}^i(\mathbf{k}, \omega) + i\omega\varepsilon_1 \left(i\mathbf{k} \times \hat{\mathbf{E}}^i(\mathbf{k}, \omega) \right) = i\mathbf{k} \times \hat{\mathbf{J}}_B^{e,i}(\mathbf{k}, \omega), \tag{3.12}$$

with $k = |\mathbf{k}| = (\mathbf{k} \cdot \mathbf{k})^{\frac{1}{2}}$. The next step is to take the inner product of $i\mathbf{k}$ and (3.9) as

$$-\frac{1}{i\omega\mu_1} \underbrace{i\mathbf{k} \cdot \left(i\mathbf{k} \times \hat{\mathbf{E}}^i(\mathbf{k}, \omega) \right)}_{=0} + i\mathbf{k} \cdot \hat{\mathbf{H}}^i(\mathbf{k}, \omega) = \frac{i\mathbf{k}}{i\omega\mu_1} \cdot \hat{\mathbf{J}}_B^{m,i}(\mathbf{k}, \omega). \tag{3.13}$$

After rewriting (3.9) as

$$i\mathbf{k} \times \hat{\mathbf{E}}^i(\mathbf{k}, \omega) = i\omega\mu_1 \hat{\mathbf{H}}^i(\mathbf{k}, \omega) - \hat{\mathbf{J}}_B^{m,i}(\mathbf{k}, \omega), \tag{3.14}$$

and substituting this result together with (3.13) in (3.12), the following expression is obtained

$$\hat{\mathbf{H}}^i(\mathbf{k}, \omega) = \frac{1}{k^2 - k_1^2} \left\{ i\mathbf{k} \times \hat{\mathbf{J}}_B^{e,i}(\mathbf{k}, \omega) + i\omega\varepsilon_1 \hat{\mathbf{J}}_B^{m,i}(\mathbf{k}, \omega) - \frac{i\mathbf{k}}{i\omega\mu_1} \left(i\mathbf{k} \cdot \hat{\mathbf{J}}_B^{m,i}(\mathbf{k}, \omega) \right) \right\}, \tag{3.15}$$

where $k_1 = \omega\sqrt{\varepsilon_1\mu_1}$. An expression for $\hat{\mathbf{E}}^i(\mathbf{k}, \omega)$ follows analogously as:

$$\hat{\mathbf{E}}^i(\mathbf{k}, \omega) = \frac{1}{k^2 - k_1^2}\left\{-i\mathbf{k} \times \hat{\mathbf{J}}_B^{m,i}(\mathbf{k}, \omega) + i\omega\mu_1\hat{\mathbf{J}}_B^{e,i}(\mathbf{k}, \omega) - \frac{i\mathbf{k}}{i\omega\varepsilon_1}\left(i\mathbf{k} \cdot \hat{\mathbf{J}}_B^{e,i}(\mathbf{k}, \omega)\right)\right\}. \quad (3.16)$$

At this point, the inverse 3D spatial Fourier transformation is applied to obtain an integral relation in the space-frequency domain. To perform this inverse transformation, it is convenient to first look at the solution of the three-dimensional time-domain Helmholtz equation

$$\left(\nabla^2 - \frac{1}{c_1^2}\partial_t^2\right)\mathcal{G}(\mathbf{r}, t) = -\delta(\mathbf{r})\delta(t), \quad (3.17)$$

in which c_1 denotes the constant propagation velocity in medium 1 and $\delta(\mathbf{r})$ is the three-dimensional Dirac distribution. By subjecting (3.17) to a temporal Fourier and spatial Fourier transformation over $\mathbb{R}^3$, the following result is obtained

$$\hat{G}(\mathbf{k}, \omega) = \frac{1}{k^2 - k_1^2}, \quad (3.18)$$

which is referred to as the 3D Green's function for an infinite homogeneous space in the $(\mathbf{k}, \omega)$ domain. The right-hand side of (3.18) is the same multiplicative factor that occurs in (3.15) and (3.16). Therefore $\hat{\mathbf{H}}^i(\mathbf{k}, \omega)$ in (3.15) and $\hat{\mathbf{E}}^i(\mathbf{k}, \omega)$ in (3.16) can be regarded as the spatial Fourier transforms of a convolution involving the Green's function $G(\mathbf{r}, \omega)$ in the spatial domain. The fact that k_1 depends on ω has no consequences for the convolution mentioned above because it concerns a convolution in the $\mathbf{k}$-domain and not in the ω-domain. The 3D Green's function in the spatial domain is obtained by carrying out the inversion integral over the domain $\mathbb{R}^3$ as follows

$$G(\mathbf{r}, \omega) = \frac{1}{8\pi^3}\int_{\mathbf{k}\in\mathbb{R}^3}\hat{G}(\mathbf{k}, \omega)\exp(i\mathbf{k}\cdot\mathbf{r})d\mathbf{k},$$
$$= \frac{1}{8\pi^3}\int_0^\infty dk \int_0^\pi d\theta_k \int_0^{2\pi} d\phi_k \frac{k^2\sin\theta_k}{k^2 - k_1^2}\exp\left(ikr\cos\theta_k\right), \quad (3.19)$$

where spherical coordinates (k, θ_k, ϕ_k) have been introduced to describe the $\mathbf{k}$-domain and $r = |\mathbf{r}|$. This spherical coordinate system is chosen such that the direction $\theta_k = 0$ coincides with the direction of the position vector $\mathbf{r}$. With this particular choice, it follows that $\mathbf{k}\cdot\mathbf{r} = kr\cos\theta_k$. Since the result (3.19) only depends on the length r of $\mathbf{r}$, Green's function will be denoted as $G(r, \omega)$. In (3.19), the integrals over ϕ_k and θ_k are elementary and result in

$$G(r, \omega) = \frac{1}{4i\pi^2 r}\int_0^\infty \frac{k}{k^2 - k_1^2}\left[\exp(ikr) - \exp(-ikr)\right]\,dk$$
$$= -\frac{1}{4i\pi^2 r}\int_{-\infty}^\infty \frac{\exp(-ikr)}{k^2 - k_1^2}k\,dk. \quad (3.20)$$

Consider medium 1 to be lossy and choose a fixed real and positive frequency ω. Since $\operatorname{Re} \varepsilon_1 > 0$, $\operatorname{Im} \varepsilon_1 \geq 0$ and $\mu_1 \in \mathbb{R}$, it follows that $\operatorname{Im} k_1 > 0$. Hence, the poles in the complex k-plane are as indicated in Figure 3.2 by the crosses. By integrating along the contour of
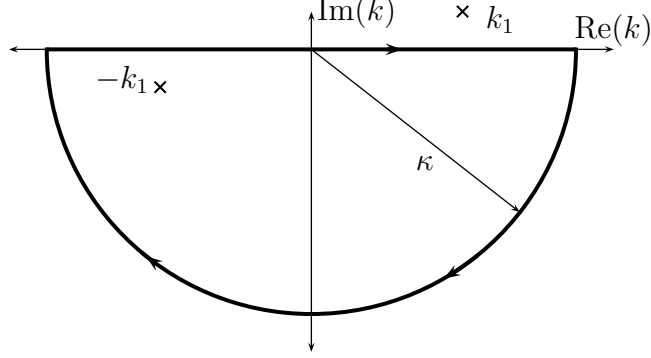
Figure 3.2: *Chosen contour in the complex k-plane for evaluation of the integral (3.20).*

Figure 3.2 and by applying Jordan's lemma, it follows that in the limit of $\kappa \to \infty$:

$$G(r,\omega) = -\frac{1}{4i\pi^2 r} \int_{-\infty}^{\infty} \frac{\exp(-ikr)}{k^2 - k_1^2} k \, dk = \frac{2\pi i}{4i\pi^2 r} \operatorname*{Res}_{k=-k_1} \frac{\exp(-ikr)}{k^2 - k_1^2} k = \frac{\exp(ik_1 r)}{4\pi r}. \quad (3.21)$$

For a lossless medium, the limit for $\operatorname{Im} \varepsilon_1 \downarrow 0$ is to be taken, which does not affect the obtained result (3.21). In the more general case of a point source in $\mathbf{r} = \mathbf{r}'$, the Fourier transformed Green's function is found by using translation symmetry as

$$G(R,\omega) = \frac{\exp(ik_1 R)}{4\pi R}, \quad (3.22)$$

where $R = |\mathbf{r} - \mathbf{r}'|$.

Now, $\mathbf{H}^i(\mathbf{r},\omega)$ and $\mathbf{E}^i(\mathbf{r},\omega)$ can be written as space convolution integrals

$$\mathcal{S}_{\mathcal{D}}(\mathbf{r})\,\mathbf{H}^i(\mathbf{r},\omega) = \nabla \times \boldsymbol{A}_B^{e,i}(\mathbf{r},\omega) - \left(\frac{1}{i\omega\mu_1}\nabla\nabla \cdot -i\omega\varepsilon_1\right)\boldsymbol{A}_B^{m,i}(\mathbf{r},\omega), \quad (3.23)$$

$$\mathcal{S}_{\mathcal{D}}(\mathbf{r})\,\mathbf{E}^i(\mathbf{r},\omega) = -\nabla \times \boldsymbol{A}_B^{m,i}(\mathbf{r},\omega) - \left(\frac{1}{i\omega\varepsilon_1}\nabla\nabla \cdot -i\omega\mu_1\right)\boldsymbol{A}_B^{e,i}(\mathbf{r},\omega), \quad (3.24)$$

with

$$\boldsymbol{A}_B^{e,i}(\mathbf{r},\omega) = \oint_{\mathbf{r}'\in\partial\mathcal{D}} G(R,\omega)\mathbf{J}_B^{e,i}(\mathbf{r}',\omega)d\mathbf{r}' \quad (3.25)$$

$$\boldsymbol{A}_B^{m,i}(\mathbf{r},\omega) = \oint_{\mathbf{r}'\in\partial\mathcal{D}} G(R,\omega)\mathbf{J}_B^{m,i}(\mathbf{r}',\omega)d\mathbf{r}', \quad (3.26)$$

where $R = |\mathbf{r} - \mathbf{r}'|$ and where $\mathbf{r}$ is the point of observation.

3.1.2 The scattered field

Next, the scattered field in the exterior domain $\overline{\mathcal{D}}$ is considered. The scattered field in $\overline{\mathcal{D}}$ satisfies

$$\nabla \times \mathbf{H}^s(\mathbf{r}, \omega) + i\omega\varepsilon_1 \mathbf{E}^s(\mathbf{r}, \omega) = \mathbf{0}, \tag{3.27}$$

$$\nabla \times \mathbf{E}^s(\mathbf{r}, \omega) - i\omega\mu_1 \mathbf{H}^s(\mathbf{r}, \omega) = \mathbf{0}, \tag{3.28}$$

for $\mathbf{r} \in \overline{\mathcal{D}}$. Again, no sources are found in the right-hand sides of the latter equations because the sources are located in the interior domain $\mathcal{D}$. Analogous to the integral relations for the incident field, the integral relations for the scattered field are found as

$$-\nabla \times \boldsymbol{A}_B^{e,s}(\mathbf{r}, \omega) + \left(\frac{1}{i\omega\mu_1}\nabla\nabla \cdot -i\omega\varepsilon_1\right) \boldsymbol{A}_B^{m,s}(\mathbf{r}, \omega) = \mathcal{S}_{\overline{\mathcal{D}}}(\mathbf{r})\, \mathbf{H}^s(\mathbf{r}, \omega), \tag{3.29}$$

$$\nabla \times \boldsymbol{A}_B^{m,s}(\mathbf{r}, \omega) + \left(\frac{1}{i\omega\varepsilon_1}\nabla\nabla \cdot -i\omega\mu_1\right) \boldsymbol{A}_B^{e,s}(\mathbf{r}, \omega) = \mathcal{S}_{\overline{\mathcal{D}}}(\mathbf{r})\, \mathbf{E}^s(\mathbf{r}, \omega). \tag{3.30}$$

The opposite signs in the right-hand sides of the latter integral relations originate from the fact that $\mathbf{n}(\mathbf{r})$ points into $\overline{\mathcal{D}}$. In writing down (3.29) and (3.30), the integral relations given by (3.23) and (3.24) have been applied to an infinite domain. Strictly speaking, this is not allowed, since this relation was derived for a finite domain only. However, (3.29) and (3.30) can also be found by considering the domain between $\partial\mathcal{D}$ and a second boundary at $r = r_\infty$. From the radiation condition that the scattered field must represent an outgoing wave as $r \to \infty$.

Subtracting (3.30) from (3.24) yields

$$\mathcal{S}_{\mathcal{D}}(\mathbf{r})\mathbf{E}^i(\mathbf{r}, \omega) - \mathcal{S}_{\overline{\mathcal{D}}}(\mathbf{r})\mathbf{E}^s(\mathbf{r}, \omega) = -\nabla \times \boldsymbol{A}_B^m(\mathbf{r}, \omega) - \frac{1}{i\omega\varepsilon_1}\left(\nabla\nabla \cdot + k_1^2\right) \boldsymbol{A}_B^e(\mathbf{r}, \omega), \tag{3.31}$$

with

$$\boldsymbol{A}_B^m(\mathbf{r}, \omega) = \oint_{\mathbf{r}' \in \partial\mathcal{D}} \frac{\exp(ik_1 R)}{4\pi R}\, \mathbf{J}_B^m(\mathbf{r}', \omega)d\mathbf{r}',$$

$$\boldsymbol{A}_B^e(\mathbf{r}, \omega) = \oint_{\mathbf{r}' \in \partial\mathcal{D}} \frac{\exp(ik_1 R)}{4\pi R}\, \mathbf{J}_B^e(\mathbf{r}', \omega)d\mathbf{r}'.$$

The fact that the object is electrically impenetrable provides the extra boundary condition

$$\mathbf{J}_B^{m,i} + \mathbf{J}_B^{m,s} = \mathbf{J}_B^m = \mathbf{n}(\mathbf{r}) \times \mathbf{E} = \mathbf{0}, \tag{3.32}$$

for $\mathbf{r} \in \partial\mathcal{D}$. After substitution of the extra boundary condition and replacing the scattered electric field with $\mathbf{E}^s = \mathbf{E} - \mathbf{E}^i$, an integral relation for the total electric field remains

$$\mathcal{S}_{\overline{\mathcal{D}}}(\mathbf{r})\mathbf{E}(\mathbf{r}, \omega) = \mathbf{E}^i(\mathbf{r}, \omega) + \frac{1}{i\omega\varepsilon_1}\left(\nabla\nabla \cdot + k_1^2\right) \boldsymbol{A}(\mathbf{r}, \omega), \tag{3.33}$$

where

$$\boldsymbol{A}(\mathbf{r}, \omega) = \oint_{\mathbf{r}' \in \partial \boldsymbol{\mathcal{D}}} \frac{\exp(ik_1 R)}{4\pi R} \mathbf{J}(\mathbf{r}', \omega) d\mathbf{r}'. \tag{3.34}$$

The electric vector potential and the electric current density have been replaced with $\boldsymbol{A}_B^e = \boldsymbol{A}$ and $\mathbf{J}_B^e = \mathbf{J}$, respectively. In the remainder of this thesis, $\boldsymbol{A}$ and $\mathbf{J}$ will be referred to as the vector potential and the current density, respectively.

For the magnetic field strength a similar relation is found:

$$\mathcal{S}_{\overline{\boldsymbol{\mathcal{D}}}}(\mathbf{r}) \, \mathbf{H}(\mathbf{r}, \omega) = \mathbf{H}^i(\mathbf{r}, \omega) - \nabla \times \boldsymbol{A}(\mathbf{r}, \omega). \tag{3.35}$$

To make (3.33) and (3.35) suitable for numerical procedures, the tangential field component on $\partial \boldsymbol{\mathcal{D}}$ must be selected and the curl operator in (3.35) must be evaluated. To this end, the cross product with $\mathbf{n}(\mathbf{r})$ is taken and the resulting integral equation is solved for the electric current density. Analogous to (3.32), the electric current density is given by

$$\mathbf{J}(\mathbf{r}, \omega) = -\mathbf{n}(\mathbf{r}) \times \mathbf{H}(\mathbf{r}, \omega). \tag{3.36}$$

With this definition, (3.35) can be rewritten as

$$\mathbf{J}(\mathbf{r}, \omega) = 2\mathbf{J}_B^{e,i} - 2\mathbf{n}(\mathbf{r}) \times \nabla \times \mathbf{A}(\mathbf{r}, \omega), \tag{3.37}$$

with $\mathbf{r} \in \partial \boldsymbol{\mathcal{D}}$. In the literature [43], this equation is known as the magnetic-field integral equation (MFIE). Since the MFIE pertains to field values on $\partial \boldsymbol{\mathcal{D}}$, it is of the boundary type. A similar equation can be obtained by considering the electric-field strength $\mathbf{E}(\mathbf{r}, \omega)$ for $\partial \boldsymbol{\mathcal{D}}$, and is known as the electric field integral equation (EFIE)

$$i\omega \varepsilon_1 \mathbf{J}_B^{e,i}(\mathbf{r}, \omega) + k_1^2 \left(\mathbf{n}(\mathbf{r}) \times \mathbf{A}(\mathbf{r}, \omega) \right) + \left(\mathbf{n}(\mathbf{r}) \times \nabla \right) \nabla \cdot \mathbf{A}(\mathbf{r}, \omega) = \mathbf{0}, \tag{3.38}$$

with $\mathbf{r} \in \partial \boldsymbol{\mathcal{D}}$.

Now that the general integral equations for the magnetic and electric field are known, an integral equation to describe the current along the surface of a thin-wire antenna can be derived.

3.2   The integral equation of Pocklington

In this section, an integral equation to describe the current along the surface $\partial \boldsymbol{\mathcal{D}}$ of a perfectly conducting, straight thin-wire antenna will be derived. This equation is referred to as Pocklington's equation.
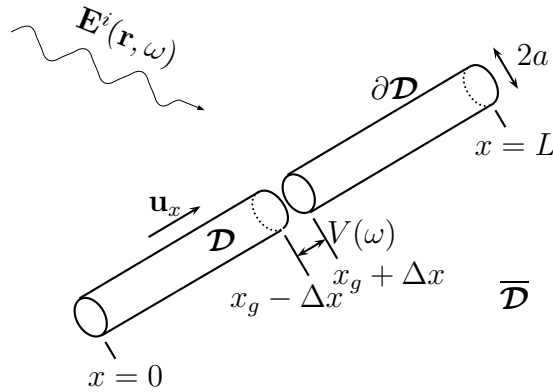
Figure 3.3: *Wire geometry.*

A wire antenna of length L and radius a positioned along the x-axis will be considered, see Figure 3.3. The wire is embedded in a homogeneous medium with the material parameters $\varepsilon(\mathbf{r}) = \varepsilon_1$ and $\mu(\mathbf{r}) = \mu_1$, which is located in the domain $\overline{\mathcal{D}}$. The wire antenna can act as a receiver or as a transmitter. When the wire acts as a receiver, the external source is an incident electric field $\mathbf{E}^i(\mathbf{r}, \omega)$ which induces a current along the wire. When the wire acts as a transmitter, the current along the wire is driven by a voltage $V(\omega)$ across a small gap with vanishing dimension $2\Delta x$ which is located at $x = x_g$. The voltage excitation is referred to as a delta-gap voltage when $\Delta x \downarrow 0$. In (3.33), $\mathbf{A}(\mathbf{r}, \omega)$ denotes the vector potential which is used to interrelate the electric field with the current density $\mathbf{J}(\mathbf{r}, \omega)$ along the wire. The vector potential was defined as

$$\mathbf{A}(\mathbf{r}, \omega) = \oint_{\mathbf{r}' \in \partial \mathcal{D}} G(R, \omega) \mathbf{J}(\mathbf{r}', \omega) d\mathbf{r}',$$

with

$$G(R, \omega) = \frac{\exp(ikR)}{4\pi R}, \tag{3.39}$$

and again $R = |\mathbf{r} - \mathbf{r}'|$ for all source points $\mathbf{r}'$ along the wire. To facilitate the formulation, cylindrical coordinates (ρ, ϕ, x) are introduced. Note that this not the standard form of the cylindrical coordinate system, where the z-direction is used instead of the x-direction. The vectors $\mathbf{r}$ and $\mathbf{r}'$ may now be written as $\mathbf{r}' = \rho' \mathbf{u}_{\rho'}(\phi') + x' \mathbf{u}_x$ and $\mathbf{r} = \rho \mathbf{u}_\rho(\phi) + x \mathbf{u}_x$. The unit vectors are defined according to Figure 3.4 where a small part of the wire has been magnified. It is observed that the unit vector $\mathbf{u}_\rho(\phi)$ can also be regarded as the normal on the surface of the wire, with the exception of the end faces of the wire. The derivation of Pocklington's integral equation is carried out in several steps, see also [37].
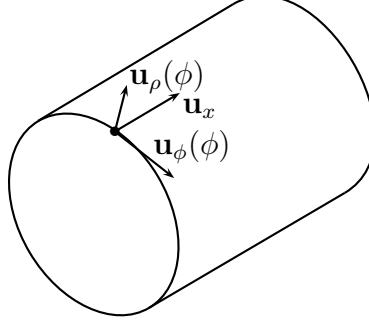
Figure 3.4: *Definition of the unit vectors $\mathbf{u}_\rho(\phi)$, $\mathbf{u}_\phi(\phi)$ and $\mathbf{u}_x$.*

First, the x-component of (3.33) is chosen according to

$$
i\omega\varepsilon_1\mathbf{u}_x \cdot \left(\mathcal{S}_{\overline{\mathcal{D}}}\left(\mathbf{r}\right)\mathbf{E}(\mathbf{r},\omega) - \mathbf{E}^i(\mathbf{r},\omega)\right) = \mathbf{u}_x \cdot \left(\nabla\nabla \cdot +k_1^2\right)\boldsymbol{A}(\mathbf{r},\omega)
$$
$$
= \partial_x \nabla \cdot \boldsymbol{A}(\mathbf{r},\omega) + k_1^2 \mathbf{u}_x \cdot \boldsymbol{A}(\mathbf{r},\omega). \tag{3.40}
$$

With the definition of the vector potential, this equation can be further simplified as

$$
i\omega\varepsilon_1 \cdot \left(\mathcal{S}_{\overline{\mathcal{D}}}\left(\mathbf{r}\right)E_x(\mathbf{r},\omega) - E_x^i(\mathbf{r},\omega)\right)
$$
$$
= \partial_x \nabla \cdot \boldsymbol{A}(\mathbf{r},\omega) + k_1^2 \oint_{\mathbf{r}'\in\partial\mathcal{D}} G(R,\omega)J_x(\mathbf{r}',\omega)d\mathbf{r}'. \tag{3.41}
$$

Next, the remaining ∇ operator is split up according to

$$
\nabla = \partial_x \mathbf{u}_x + \nabla_T, \tag{3.42}
$$

where the subscript T stands for transverse. Substituting (3.42) in the pertaining part of (3.41) gives

$$
\partial_x \nabla \cdot \boldsymbol{A}(\mathbf{r},\omega) = \partial_x^2 \oint_{\mathbf{r}'\in\partial\mathcal{D}} G(R,\omega)J_x(\mathbf{r}',\omega)d\mathbf{r}' + \partial_x \oint_{\mathbf{r}'\in\partial\mathcal{D}} \nabla_T \cdot \left(G(R,\omega)\mathbf{J}(\mathbf{r}',\omega)\right)d\mathbf{r}'.
$$

The integrand containing the $\nabla_T\cdot$ operator in the right-hand side of the latter equation can be written as

$$
\nabla_T \cdot \left(G(R,\omega)\mathbf{J}(\mathbf{r}',\omega)\right) = G(R,\omega)\underbrace{\nabla_T \cdot \mathbf{J}(\mathbf{r}',\omega)}_{=0} + \mathbf{J}(\mathbf{r}',\omega) \cdot \nabla_T G(R,\omega)
$$
$$
= \mathbf{J}(\mathbf{r}',\omega) \cdot \frac{\rho\mathbf{u}_\rho(\phi) - \rho'\mathbf{u}_{\rho'}(\phi')}{R}\partial_R G(R,\omega). \tag{3.43}
$$

When the point of observation is chosen on the central axis of the wire, i.e., $\mathbf{r} = x\mathbf{u}_x$, and the source point on the surface of the wire, it follows that $\rho = 0$ and $\rho' = a$. Along the

surface of the wire, except for the end faces, the inner product $\mathbf{J}(\mathbf{r}', \omega) \cdot \mathbf{u}_{\rho'}(\phi') = 0$ and consequently $\nabla_T \cdot (G(R, \omega)\mathbf{J}(\mathbf{r}', \omega)) = 0$. If the currents at the end faces of the wire are neglected, (3.40) can therefore be written as

$$
\begin{aligned}
i\omega\varepsilon_1 \cdot \left(\mathcal{S}_{\overline{\mathcal{D}}} \left(x\mathbf{u}_x \right) E_x(x\mathbf{u}_x, \omega) - E_x^i(x\mathbf{u}_x, \omega) \right) \\
= \left(\partial_x^2 + k_1^2 \right) \oint_{\mathbf{r}' \in \partial\mathcal{D}} G(R_a, \omega) J_x(\mathbf{r}', \omega) d\mathbf{r}',
\end{aligned}
\tag{3.44}
$$

with $R_a = \sqrt{(x - x')^2 + a^2}$. Because $G(R_a, \omega)$ does not depend on ϕ', the latter integral may be written as

$$
\begin{aligned}
\oint_{\mathbf{r}' \in \partial\mathcal{D}} G(R_a, \omega) J_x(\mathbf{r}', \omega) d\mathbf{r}' &= \int_0^L G(R_a, \omega) \left\{ a \int_{-\pi}^{\pi} J_x(x'\mathbf{u}_x + a\mathbf{u}_{\rho'}(\phi'), \omega) d\phi' \right\} dx' \\
&= \int_0^L G(R_a, \omega) I(x', \omega) dx',
\end{aligned}
\tag{3.45}
$$

where the definition of the total current

$$
I(x', \omega) = a \int_{-\pi}^{\pi} J_x(x'\mathbf{u}_x + a\mathbf{u}_{\rho'}(\phi'), \omega) d\phi'
\tag{3.46}
$$

flowing along the wire at position $x = x'$ now follows naturally from the derivation. The electric field in the gap at $x = x_g$ satisfies

$$
\int_{x_g - \Delta x}^{x_g + \Delta x} E_x(x\mathbf{u}_x, \omega) dx = -V(\omega),
\tag{3.47}
$$

where $V(\omega)$ is a known impressed voltage across the gap. By taking the limit $\Delta x \downarrow 0$, the electric-field strength inside the delta gap can be written as $E_x(x\mathbf{u}_x, \omega) = -\delta(x - x_g)V(\omega)$, where $\delta(x - x_g)$ denotes the Dirac delta distribution. Substitution of this result in the left-hand side of (3.44) gives the integro-differential equation of Pocklington:

$$
(\partial_x^2 + k_1^2) \int_0^L G(R_a, \omega) I(x', \omega) dx' = -i\omega\varepsilon_1 \left[V(\omega)\delta(x - x_g) + E_x^i(x\mathbf{u}_x, \omega) \right].
\tag{3.48}
$$

From the above derivation, which was first given in [37], it follows that this integral equation is almost exact. In fact, the only approximation amounts to neglecting the radial currents on the end faces.

Pocklington's equation can easily be solved numerically. However, the differentiations with respect to x can cause problems in the numerical evaluation of (3.48), especially near $x = x'$, where $1/R_a$ becomes almost singular.

3.3   Hallén's equation

In 1938, Hallén [34] derived a simple approximation for describing the current along a thin wire with the intention to find an analytical expression. In addition, this new equation is more convenient for a numerical computation of the current along a wire.

In this section, a brief description of the derivation of Hallén's equation will be given. After writing the incident electric field as a superposition of delta distributions as follows

$$E_x^i(x\mathbf{u}_x, \omega) = \int_0^L E_x^i(x'\mathbf{u}_x, \omega)\delta(x - x')dx', \tag{3.49}$$

the differential operator $(\partial_x^2 + k_1^2)$ in (3.48) can be handled in an elegant manner.

As a first step, (3.49) is substituted in (3.48) which yields the following result:

$$(\partial_x^2 + k_1^2) \int_0^L G(R_a, \omega)I(x', \omega)dx'$$
$$= -i\omega\varepsilon_1 \left[V(\omega)\delta(x - x_g) + \int_0^L E_x^i(x'\mathbf{u}_x, \omega)\delta(x - x')dx' \right], \tag{3.50}$$

for $0 \leq x \leq L$. A closer look at the latter equation shows that the structure of (3.50) again resembles the structure of the one-dimensional wave equation. Therefore the solution to the one-dimensional wave equation (2.51) can be used to rewrite (3.50) as

$$\int_0^L \frac{I(x', \omega)\exp(ik_1 R_a)}{4\pi R_a}dx' - F_0(\omega)\exp(ik_1 x) - F_L(\omega)\exp(ik_1(L - x))$$
$$= \frac{Y_1}{2} \left[V(\omega)\exp(ik_1|x - x_g|) + \int_0^L E_x^i(x'\mathbf{u}_x, \omega)\exp(ik_1|x - x'|)dx' \right], \tag{3.51}$$

for $0 \leq x \leq L$ and where $Y_1 = \sqrt{\varepsilon_1/\mu_1}$ is the complex admittance of the medium. The terms containing $F_0(\omega)$ and $F_L(\omega)$ are the homogeneous solutions of the one-dimensional wave equation. The factors $F_0(\omega)$ and $F_L(\omega)$ can be found as a combination of source terms with the aid of the boundary conditions $I(0, \omega) = I(L, \omega) = 0$. In the present derivation these factors are solved numerically as extra unknowns. It is, however, necessary to explicitly account for the boundary conditions given $I(0, \omega) = I(L, \omega) = 0$. Equation (3.51) is known as Hallén's equation.

3.3.1   Discretization of Hallén's equation

In the previous paragraph, Hallén's equation for the current along a straight thin wire with a circular cross section was derived. This equation cannot be solved analytically and is therefore solved numerically.

To this end, Hallén's equation will be discretized. Following [37], the wire is divided in M subintervals with mesh size $\Delta x = L/M$ where M is chosen as a fixed value which does not depend on the frequency. Now x is chosen fixed as $x = x_m = m\Delta x$, with $m = 0, \ldots, M$. If the numerator containing the current in (3.51) is approximated piecewise linearly, the following expression is obtained

$$I(x',\omega)\exp(ik_1 R_a) \approx \sum_{m'=1}^{M-1} I_{m'}(\omega)\exp(ik_1 R_{m-m'}^a)\phi_{m'}(x'), \qquad (3.52)$$

with $R_m^a = \sqrt{m^2\Delta x^2 + a^2}$ and where $\phi_{m'}(x)$ is the triangular expansion function which is defined as

$$\phi_{m'}(x) = \begin{cases} 1 - |x - x_{m'}|/\Delta x & \text{for } |x - x_{m'}| \leq \Delta x \\ 0 & \text{otherwise} \end{cases}, \qquad (3.53)$$

for $m' = 1, \ldots, M - 1$. This approximation implicitly accounts for the boundary conditions $I(0,\omega) = I(L,\omega) = 0$. The first term on the left-hand side of (3.51) can now be approximated by

$$\int_0^L \sum_{m'=1}^{M-1} \frac{I_{m'}(\omega)\exp(ik_1 R_{m-m'}^a)\phi_{m'}(x')}{4\pi R_a} dx'$$

$$\approx \sum_{m'=1}^{M-1} I(x_{m'},\omega)\exp(ik_1 R_{m-m'}^a) \int_0^L \frac{\phi_{m'}(x')}{4\pi R_a} dx', \quad m = 0, \ldots, M. \qquad (3.54)$$

The integral in the right-hand side of the latter equation is rewritten as

$$\int_0^L \frac{\phi_{m'}(x')}{4\pi R_a} dx' = \int_{x_{m'}-\Delta x}^{x_{m'}+\Delta x} \frac{\phi_{m'}(x')}{4\pi\sqrt{(m\Delta x - x')^2 + a^2}} dx', \quad m = 1 - M, \ldots, M - 1. \quad (3.55)$$

The weighting coefficients w_m are defined as

$$w_m = \frac{1}{4\pi} \int_{x_m-\Delta x}^{x_m+\Delta x} \frac{\phi_m(x)}{\sqrt{x^2 + a^2}} dx \qquad (3.56)$$

The integrals in the definition of the weighting coefficients w_m are split up as

$$w_m = \frac{1}{4\pi} \left(\int_{x_m-\Delta x}^{x_m} \frac{\Delta x - x_m + x}{\Delta x\sqrt{x^2 + a^2}} dx + \int_{x_m}^{x_m+\Delta x} \frac{\Delta x + x_m - x}{\Delta x\sqrt{x^2 + a^2}} dx \right). \qquad (3.57)$$

The first integral is calculated in closed form as

$$\int_{x_m-\Delta x}^{x_m} \frac{\Delta x - x_m + x}{\Delta x \sqrt{x^2 + a^2}} dx = \int_{x_m-\Delta x}^{x_m} \frac{1-m}{\sqrt{x^2+a^2}} dx + \frac{1}{\Delta x}\int_{x_m-\Delta x}^{x_m} \frac{x}{\sqrt{x^2+a^2}} dx$$

$$= (1-m)\log\left(\frac{m\Delta x + R_m^a}{(m-1)\Delta x + R_{m-1}^a}\right) + \frac{1}{\Delta x}\left(R_m^a - R_{m-1}^a\right), \tag{3.58}$$

where log is the natural logarithm. The second integral of (3.57) is found analogously. The closed-form expression for the weighting coefficient w_m is thus found as

$$w_m = \frac{1}{4\pi}\left\{\left[(m-1)\log\left(\frac{R_{m-1}^a + (m-1)\Delta x}{R_m^a + m\Delta x}\right) + (m+1)\log\left(\frac{R_{m+1}^a + (m+1)\Delta x}{R_m^a + m\Delta x}\right)\right]\right.$$

$$\left. - \frac{1}{\Delta x}\left[R_{m+1}^a - 2R_m^a + R_{m-1}^a\right]\right\}, \tag{3.59}$$

for $m = 1 - M, \ldots, M - 1$. The remaining integrals in (3.51) can be approximated by a straightforward trapezoidal rule. The discretized Hallén equation can thus be written as

$$\sum_{m'=1}^{M-1} w_{m-m'}\exp\left(ik_1 R_{m-m'}^a\right) I_{m'}(\omega) - \exp\left(ik_1 x_m\right) F_0(\omega) - \exp\left(ik_1(L-x_m)\right)F_L(\omega)$$

$$= \frac{Y_1}{2}\left[\exp\left(ik_1|x_m - x_g|\right) V(\omega) + \sum_{m'=0}^{M} v_{m'}\exp\left(ik_1|x_m - x_{m'}|\right) E_x^i(x_{m'}\mathbf{u}_x, \omega)\right], \tag{3.60}$$

for $m = 0, \ldots, M$. The weighting coefficients v_m are defined as

$$v_m = \begin{cases} \Delta x, & \text{for } m = 1, \ldots, M-1, \\ \frac{\Delta x}{2} & \text{for } m = 0, M. \end{cases} \tag{3.61}$$

Now, all coefficients, except the current along the wire, are known and (3.60) is a linear system of equations of fixed dimension $(M + 1)$. The $M + 1$ unknowns are F_0, F_L and $\{I_m|m = 1, \ldots, M - 1\}$.

The system of equations is solved numerically with the aid of a conjugate-gradient fast-Fourier transformation (CGFFT) method [49]. When this system has been solved for N_f frequencies, the inverse Fourier transformation (2.17) can be applied to obtain the time-domain current.

3.3.2 Results

A single thin wire is excited by a Gaussian voltage pulse which in the time domain is defined as

$$\mathcal{V}(t) = \exp\left[-\left(\frac{t - t_1}{\tau}\right)^2\right], \tag{3.62}$$

where τ corresponds to the pulse duration and t_1 the time instant where the amplitude reaches its maximum (see Figure 3.5). The frequency-domain voltage pulse is given by

$$V(\omega) = \tau\sqrt{\pi}\exp\left(-\left(\frac{\omega\tau}{2}\right)^2 + i\omega t_1\right), \tag{3.63}$$

and is also displayed in Figure 3.5. In the remainder of this chapter, this Gaussian pulse
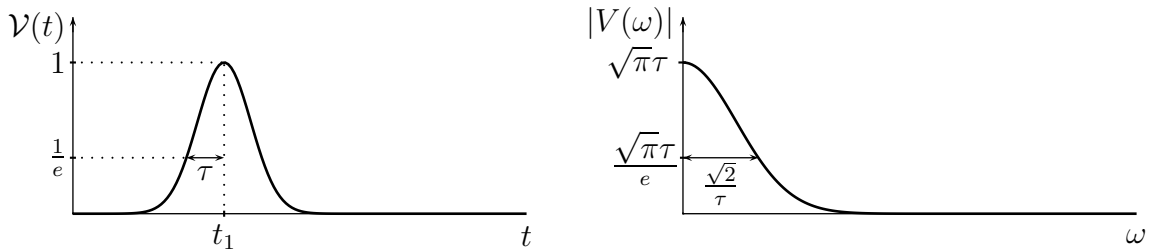
Figure 3.5: *The shape of the Gaussian excitation in time and frequency domain.*

will be used with $\tau = 0.5$ ns and $t_1 = 4\tau$. This particular choice of t_1 ensures that the magnitude of the voltage pulse is negligible for $t \leq 0$. Therefore, the Gaussian voltage pulse may be regarded as a causal signal and is thus a correct input signal for the numerical procedure. The maximum frequency in the spectrum of the Gaussian excitation is 2 GHz. An external incident field is not considered here, i.e., $E_x^i = 0$.

The wire is located along the x-axis, see Figure 3.3. The points of excitation and observation are chosen at the center of the wire ($x_g = x = L/2$). The current along the wire has been calculated using the parameters $L = 1$ m and $a = 0.002$ m. The spatial discretization is given by $M = 30$ and the number of time steps is $N = 1024$. The current at the center of the wire is calculated for four different embeddings. The results have been compared with results from a time-domain numerical code for thin-wire structures "DOTIG1"[50]. Both results are visualized in Figure 3.6. The present frequency-domain Hallén method is referred to as "FDH". At a first glance, it is observed that the presented results from the frequency domain Hallén method are in perfect agreement with the time-domain results from DOTIG1. The difference in relative permittivity between (A) and (C) and between (B) and (D) results in a difference in travel time of the current along the wires. For (A)
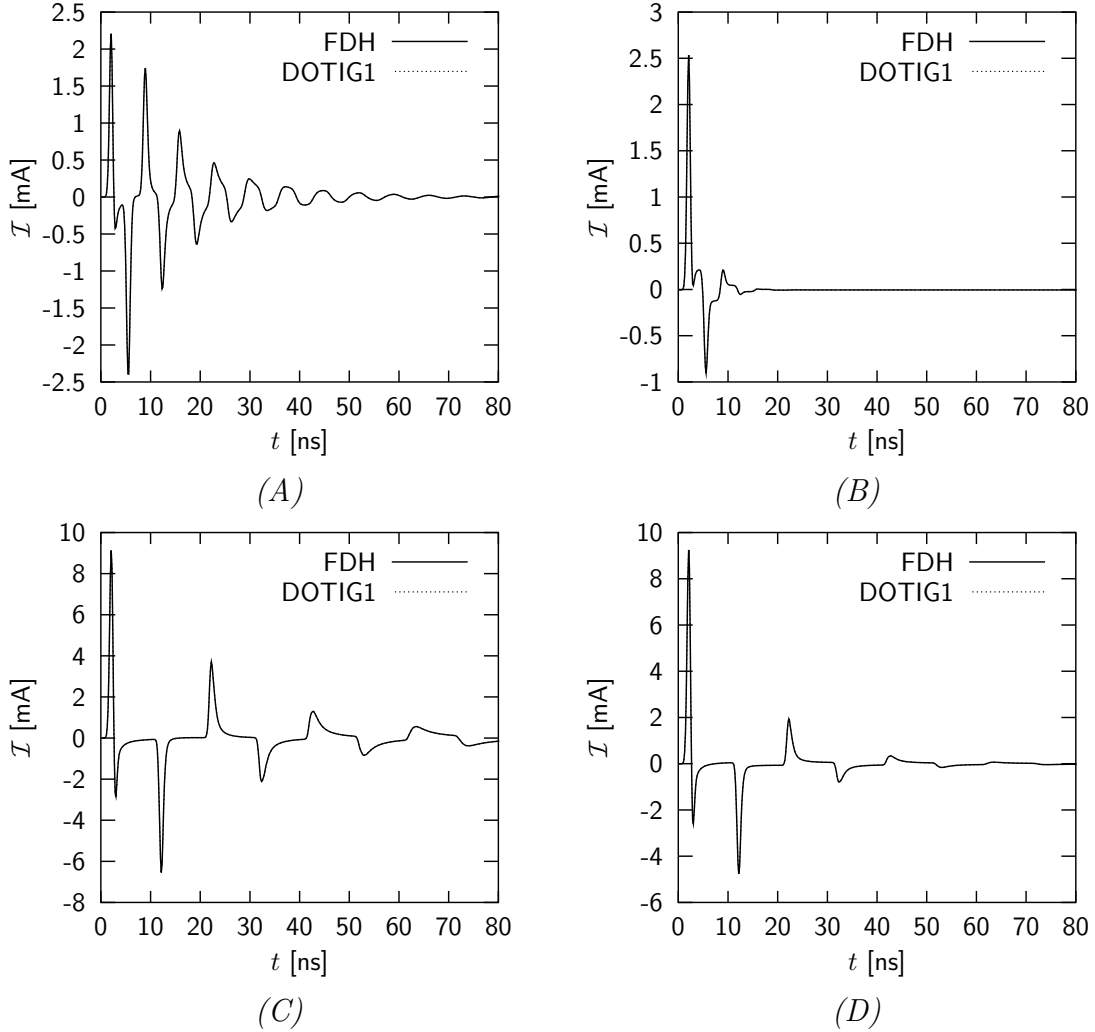
Figure 3.6: *The induced current at the center of a wire with length $L = 1$ m, radius $a = 0.002$ m, $M = 30$ and $N = 1024$ for an embedding with $\epsilon_1 = 1$, $\sigma_1 = 0$ (A), $\epsilon_1 = 1$, $\sigma_1 = 0.005$ S/m (B), $\epsilon_1 = 9$, $\sigma_1 = 0$ (C) and $\epsilon_1 = 9$, $\sigma_1 = 0.005$ S/m (D). The permeability is μ_0 for all configurations. The excitation is a Gaussian voltage pulse with $\tau = 0.5$ ns and $t_1 = 4\tau$.*

and (B) the time difference between the second negative peak and the second positive peak is $\Delta t = 8.96 - 5.6 = 3.36$ ns and $\Delta t = 22.24 - 12.16 = 10.08$ ns, respectively. This shows that the current along the wire in (A) travels approximately $10.08/3.36 = 3$ times faster then the one along the wire in (C), which is exactly the square root of the quotient $\epsilon_{1,C}/\epsilon_{1,A} = 9/1$. For (B) and (D) the same observation is made. The conductivity of the embedding has no effect on the travel time of the current along the wire because the contribution in k_1 is not real-valued. In Hallén's equation, the conductivity does have an

attenuating effect on the current. Because of this attenuating effect, the current along the wire will vanish quicker as can be observed from comparing (A) with (B) and (C) with (D).

After approximately 35 ns, the shape of the current in (A) behaves as a damped oscillation. This can be explained from the fact that the dominant mode of the current along the wire attenuates slower than the other modes. The current travels along the wire and reflects at the end faces of the wire, see also the next section. After a certain time, only the dominant mode contributes to the current along the wire which has a fixed travel time (depending on the medium parameters). Therefore, the current will act as an oscillation. The attenuating effect follows directly from the fact that the wire is radiating and therefore loses power as time passes. If the embedding also has a conductivity σ_1, the current along the wire attenuates quicker.

3.4   Approximate solution of Hallén's equation

As described above, the current along a single thin wire has a traveling-wave nature. In 1961, Altshuler [13] described a traveling-wave linear antenna. This new look inspired many authors to find approximate expressions of the current along the wire in terms of traveling waves. In the next section, this approximation is derived. The purpose of this section is to give some insight in the behavior of the current along a wire.

Inspired by the first-order approximation given by Bouwkamp [44] and earlier published results [37, 51, 52, 53], a traveling-wave model is derived to describe the current along a wire [35]. In [35], the parameters that are used in the derivation as given below were found by fitting the current to a reference current.

To describe the current by a traveling-wave model, Hallén's equation in the frequency domain (3.51) is used to derive a first order approximate expression for the current along the wire. The wire is embedded in a homogeneous medium with $\varepsilon_1(\mathbf{r}) = \varepsilon_1$ and $\mu_1(\mathbf{r}) = \mu_0$ and only a voltage excitation is considered. Then Hallén's equation can be written as

$$
\int_0^L \frac{I(x', \omega) \exp(ik_1 R_a)}{4\pi R_a} dx'
$$
$$
= \int_0^L \frac{I(x', \omega) \exp(ik_1 R_a) - I(x, \omega) \exp(ik_1 a) + I(x, \omega) \exp(ik_1 a)}{4\pi R_a} dx'
$$
$$
= F_0(\omega) \exp\left(ik_1 x\right) + F_L(\omega) \exp\left(ik_1 (L - x)\right) + \frac{Y_1}{2} V(\omega) \exp(ik_1 |x - x_g|). \quad (3.64)
$$

The left-hand side of (3.64) can be written as

$$\int_0^L \frac{I(x',\omega)\exp(ik_1 R_a) - I(x,\omega)\exp(ik_1 a)}{4\pi R_a}dx' + I(x,\omega)\exp(ik_1 a)\int_0^L \frac{dx'}{4\pi R_a}. \quad (3.65)$$

The last integral in the right hand side of (3.65) can be calculated analytically as follows

$$\int_0^L \frac{1}{R_a}dx' = \int_0^x \frac{dx'}{\sqrt{(x-x')^2 + a^2}} + \int_x^L \frac{dx'}{\sqrt{(x-x')^2 + a^2}} = \Omega(x)$$

$$= 2\log\left(\frac{L}{a}\right) + \log\left(\frac{x + \sqrt{x^2 + a^2}}{L}\right) + \log\left(\frac{L - x + \sqrt{(L-x)^2 + a^2}}{L}\right). \quad (3.66)$$

The first-order approximation consists of neglecting the first integral in (3.65) [35, 54]. The remaining current belongs to the approximated equation and will therefore be denoted as $I_f(x,\omega)$.

With the substitution of $\Omega(x)$ into (3.51), the first order approximate solution of Hallén's equation is given by

$$I_f(x,\omega) = \frac{2\pi Y_1}{\Omega(x)}V(\omega)\exp(ik_1(|x - x_g| - a))$$

$$+ \frac{4\pi}{\Omega(x)}\left[F_0(\omega)\exp\left(ik_1(x-a)\right) - F_L(\omega)\exp\left(ik_1((L-x)-a)\right)\right]. \quad (3.67)$$

By using the boundary conditions $I_f(0,\omega) = I_f(L,\omega) = 0$, the factors $F_0(\omega)$ and $F_L(\omega)$ are found as

$$F_0(\omega) = \frac{Y_1}{2}V(\omega)\frac{\exp[ik_1(2L - x_g)] - \exp[ik_1 x_g]}{1 - \exp(2ik_1 L)}, \quad (3.68)$$

$$F_L(\omega) = \frac{Y_1}{2}V(\omega)\frac{\exp[ik_1(L + x_g)] - \exp[ik_1(L - x_g)]}{1 - \exp(2ik_1 L)}. \quad (3.69)$$

Substituting (3.68) and (3.69) in (3.67) results in

$$I_f(x,\omega) = \frac{2\pi Y_1}{\Omega(x)}V(\omega)\left[\exp(ik_1(|x - x_g| - a)) - \sum_{m=0}^{\infty}\exp\left(ik_1(x + x_g + 2mL)\right)\right.$$

$$- \sum_{m=0}^{\infty}\exp\left(ik_1(2L - x - x_g + 2mL)\right) + \sum_{m=0}^{\infty}\exp\left(ik_1(2L + x - x_g + 2mL)\right)$$

$$\left. + \sum_{m=0}^{\infty}\exp\left(ik_1(2L - x + x_g + 2mL)\right)\right], \quad (3.70)$$

where the fact has been used that for $\text{Im}\, k_1 > 0$

$$\frac{1}{1 - \exp(2ik_1 L)} = \sum_{m=0}^{\infty}\exp(2ik_1 mL). \quad (3.71)$$
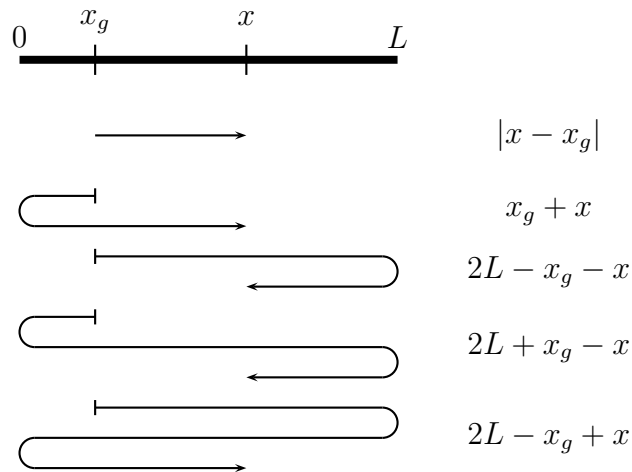
Figure 3.7: *The various possibilities for current waves originating from x_g to arrive at the observation point x.*

From the series approximation, the traveling-wave nature can easily be seen. For $m = 0$, the various contributions have been visualized in Figure 3.7. It is observed that the first and second series represent the contributions with $2m + 1$ reflections. The third and fourth series represent the contributions with $2m + 2$ reflections. All contributions, except for the direct contribution, repeat themselves after traveling over a distance $2L$. Note that in that case the current wave has reflected at least twice.

Since the current wave is fully reflected at the end faces of the wire in the model above, the sign of the current changes. This is related with a reflection coefficient that equals -1. The admittance function in (3.70) equals

$$Y(x) = \frac{2\pi Y_1}{\Omega(x)}. \tag{3.72}$$

A closer look at the traveling-wave model (3.70) shows that the current is now fully described by an admittance times a superposition of delayed voltage pulses. That this is a first-order model follows from the fact that the reflection coefficient does not attenuate the voltage. In free space, k_1 is real-valued and therefore the current will never attenuate. The frequency-domain series representation then does not converge. From a physical point of view this is unacceptable and therefore a higher-order approximation is required.

At the end faces of the wire, the current wave normally does not reflect immediately [35, 52]. Therefore an extra time delay should be incorporated in the solution to describe the current along the wire. In general, the reflection coefficient does not equal -1 [45]. The admittance is known to be frequency dependent while the expression (3.72) is not. By ap-

proximating the reflection coefficient and the admittance more accurately, a higher-order approximation of the traveling-wave current based on (3.70) can be constructed. For the sake of completeness, a short derivation of the higher-order model is given below. In [35], the higher-order approximation is given in the time domain. The parameters involved with this approximation are found by fitting the current on the current calculated with Hallén's equation. It was shown that the radiated electric field was better approximated with the fitted model than with the direct frequency-domain model. A more detailed description can be found in [35].

3.4.1   Higher-order approximation

A short derivation of a higher-order approximation to describe the current along the wire in terms of traveling waves will be given. As a guideline, the first order approximation given by (3.70) will be used to incorporate the generalized admittance found by Shen *et al.* [46] and the reflection coefficient found by Ufimtsev [45]. The time delay for reflection at the end faces of the wire will be included in the reflection coefficient. Note that for the derivation of generalized admittance and the reflection coefficient, the constraint that $|k_1 a| < 0.2$ is assumed.

Shen *et. al.* [46] approximated the admittance of an infinitely long wire antenna excited at $x_g = 0$ by describing first the current along that wire. The current along the infinitely long wire is described by

$$I_\infty(x, \omega) = iY_0 V(\omega) \exp(ik_1|x|)$$
$$\cdot \log\left(1 + \frac{2i\pi}{2\log(k_1 a) + \gamma - \log\left(k_1|x| + \sqrt{(k_1 x)^2 + \exp(-2\gamma)}\right) - i\frac{3\pi}{2}}\right), \quad (3.73)$$

where $\gamma \approx 0.577215664...$ is Euler's constant. The factor $\exp(ik_1|x|)$ shows the traveling-wave nature of the current along the wire in Shen's approximation. The admittance is then found as

$$Y_f(x) = \frac{I_\infty(x - x_g, \omega)}{V(\omega)\exp(ik_1|x - x_g|)}. \quad (3.74)$$

The current represented by (3.73) is excited by a delta-gap voltage at $x_g = 0$. In the present model of a finite wire, the point of excitation is $x_g > 0$. Thus a current wave traveling away from x_g in both directions has the value $I(x, \omega) = I_\infty(x - x_g, \omega)$ for $0 < x < L$.

The admittance from (3.74) is plotted in Figure 3.8.   Plots A and B are given for the arguments $x = x_g$ and $|x - x_g| = L/2$, respectively. The frequency range is up to 10 GHz.
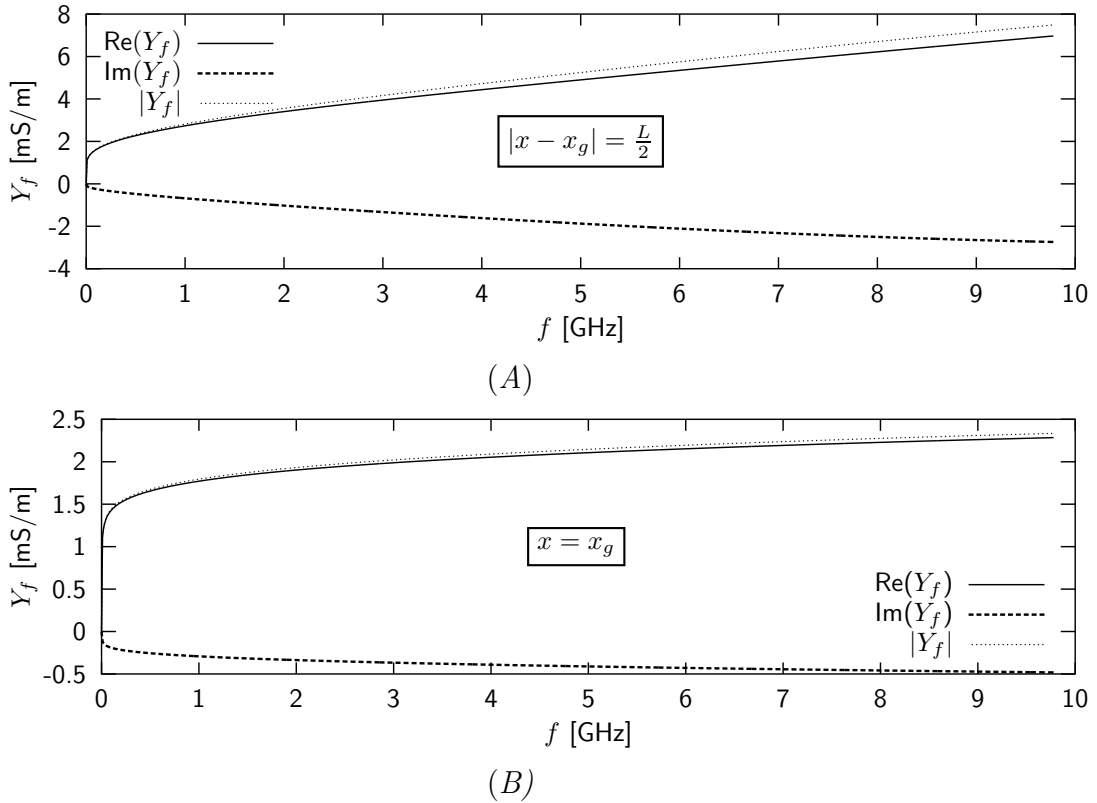
Figure 3.8: *The generalized admittance Y_f for $|x - x_g| = L/2$ (A) and $x = x_g$ (B).*

From both plots, it is observed that $\mathrm{Re}(Y_f)$ dominates the behavior of the absolute value of the generalized admittance.

Since the time delay will be incorporated into the reflection coefficient, the real or absolute value of the generalized admittance may be chosen. If the complex admittance would be chosen, additional, unwanted time delays could be introduced. The generalized admittance is therefore redefined according to

$$Y_f(x) = \left| \frac{I_\infty(x - x_g, \omega)}{V(\omega) \exp(ik_1 |x - x_g|)} \right|. \tag{3.75}$$

In the first-order approximate traveling wave model, the current waves reflect at $x = 0$ and $x = L$ with a reflection coefficient $R_f = -1$. A current wave which has been reflected at $x = 0$ has a generalized admittance $Y_f(x_g)$. A current wave which has reflected at least once at $x = L$ has a generalized admittance $Y_f(L - x_g)$ and a current wave traveling from $x = x_g$ without having been reflected has a generalized admittance $Y_f(|x - x_g|)$. What remains is a better approximation of the reflection coefficient R_f.

In 1962, Ufimtsev [45] derived an approximation of the reflection coefficient for a thin cylindrical conductor. The work of Ufimtsev is based on earlier work by Vainshtein [55].

The high-frequency approximate reflection coefficient at the end of a thin-wire antenna is found as

$$R_f = \frac{i\pi - 2\log\left(\exp(\gamma)k_1 a\right)}{\log\left(\dfrac{2iL}{\exp(\gamma)k_1 a^2}\right) - E(2k_1 L)\exp(-2ik_1 L)}, \tag{3.76}$$

where

$$E(2k_1 L) = -\int_{2k_1 L}^{\infty} \frac{\cos(t)}{t}dt + i\int_{0}^{2k_1 L} \frac{\sin(t)}{t}dt - i\frac{\pi}{2}. \tag{3.77}$$

In Figure 3.9, the reflection coefficient is plotted as a function of frequency.   It is observed
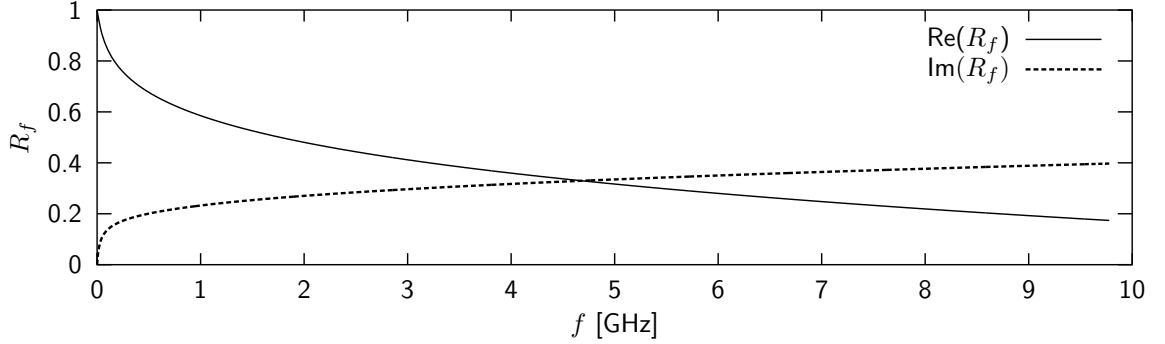
Figure 3.9: *The reflection coefficient R_f versus frequency f.*

that the reflection coefficient equals 1 only at frequency $f = 0$. With the definition of the reflection coefficient and the generalized admittance, the higher-order approximation of Hallén's solution is readily found as

$$
\begin{aligned}
I_f(x,\omega) =\ & Y_f(|x - x_g|)V(\omega)\exp(ik_1|x - x_g|) \\
& -Y_f(x_g)V(\omega)\sum_{m=0}^{\infty} R_f^{2m+1}\exp[ik_1(x + x_g + 2mL)] \\
& -Y_f(L - x_g)V(\omega)\sum_{m=0}^{\infty} R_f^{2m+1}\exp[ik_1(2L - x - x_g + 2mL)] \\
& +Y_f(x_g)V(\omega)\sum_{m=0}^{\infty} R_f^{2m+2}\exp[ik_1(2L - x + x_g + 2mL)] \\
& +Y_f(L - x_g)V(\omega)\sum_{m=0}^{\infty} R_f^{2m+2}\exp[ik_1(2L + x - x_g + 2mL)].
\end{aligned}
\tag{3.78}
$$

The latter equation can be further simplified to

$$
I_f(x, \omega) = Y_f(|x - x_g|)V(\omega)\exp(ik_1|x - x_g|)
$$

$$
+Y_f(x_g)V(\omega)\left[-\exp[ik_1(x + x_g - L)]\frac{R_f\exp(ik_1L)}{1 - R_f^2\exp(2ik_1L)} \right.
$$

$$
\left. +\exp[ik_1(x_g - x)]\frac{R_f^2\exp(2ik_1L)}{1 - R_f^2\exp(2ik_1L)} \right]
$$

$$
+Y_f(L - x_g)V(\omega)\left[-\exp[ik_1(L - x - x_g)]\frac{R_f\exp(ik_1L)}{1 - R_f^2\exp(2ik_1L)} \right.
$$

$$
\left. +\exp[ik_1(x - x_g)]\frac{R_f^2\exp(2ik_1L)}{1 - R_f^2\exp(2ik_1L)} \right]. \tag{3.79}
$$

In most examples, the point of observation equals the point of excitation $x = x_g = L/2$. In this case, (3.79) reduces to

$$
I_f(x = x_g = L/2, \omega) = Y_f(0)V(\omega)
$$

$$
+Y_f(L/2)V(\omega)\left[-2\sum_{m=0}^{\infty} R_f^{2m+1}\exp[ik_1((2m+1)L)] \right.
$$

$$
\left. +2\sum_{m=0}^{\infty} R_f^{2m+2}\exp[ik_1((2m+2)L)] \right]
$$

$$
= Y_f(0)V(\omega) - 2Y_f(L/2)V(\omega)\frac{R_f\exp(ik_1L)}{1 + R_f\exp(ik_1L)}. \tag{3.80}
$$

Apart from the approximate reflection coefficient, the current can now easily be evaluated. The reflection coefficient R_f can be determined numerically for each frequency before the summations are carried out. When the current I_f is calculated for a number of frequencies, the time-domain results are obtained after an inverse temporal Fourier transformation.

As an example, the current along a wire with length $L = 1$ m and radius $a = 0.002$ m will be calculated with the higher-order approximation and Hallén's equation from the previous section. The wire is excited by a Gaussian voltage pulse as defined in Section 3.3.2. The results are visualized in Figure 3.10. It is observed that the first pulse is well approximated by the higher-order model. In fact, until 20 ns, the pulses are well approximated. After 20 ns, the amplitude of the higher-order model current is larger than in Hallén's version of the current. In the frequency-domain approximation, the lowest possible mode of the current is not represented accurately. This mode is dominant in the late-time behavior of the total current.
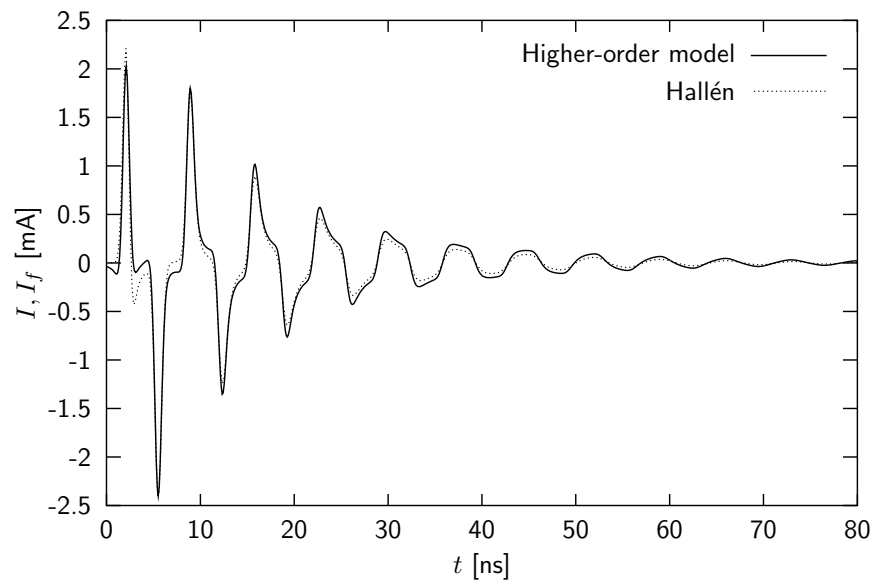
Figure 3.10: *The induced current at the center of a wire with length $L = 1$ m, radius $a = 0.002$ m, $M = 30$ and $N = 1024$. The wire is embedded in a homogeneous medium with parameters ε_0 and μ_0. The excitation is a Gaussian voltage pulse with $\tau = 0.5$ ns and $t_1 = 4\tau$.*

Chapter 4

Various configurations with thin wires

In the previous chapter, Hallén's equation was derived for a single thin wire in a homogeneous embedding which was referred to as medium 1. This equation will now be used to generalize thin-wire problems in various configurations. In each configuration one new element will be added. The configurations are depicted In Figure 4.1. The dots represent the cross sections of wires. In the various configurations, an interaction can be recognized from a pair of arrows. It is seen that each addition, whether that is an extra wire or an extra medium, increases the number of interactions between the elements of a configuration. The computational complexity therefore increases with each additional wire since all currents are coupled and they are calculated simultaneously. Configuration I has already been examined in the previous section and the results will be used for other configurations.

The goal of this chapter is to model a buried wire with a transmitting and receiving wire system above the ground (configuration IV). This last configuration is formed by adding various elements to the initial configuration (configuration I) in a natural order. As can be seen, in configuration II, the space is divided in two half spaces comprising different media. The difference in medium parameters of the half spaces causes a part of the radiated field from the wire to be reflected at the interface between these two half spaces. In configuration III, a second wire is added to the upper half space. Wire 1 is the transmitting wire and wire 2 is the receiving wire. This gives two extra interactions, one directly and one via the interface. With the addition of a third wire in the lower half space, configuration IV has been reached. Wire 3 is the buried wire. In this configuration, one more interaction is added to wire 1 and wire 2 in the form of a transmitted field through the interface between two half spaces. The transmitted field interaction takes place between wire 1 and wire 3
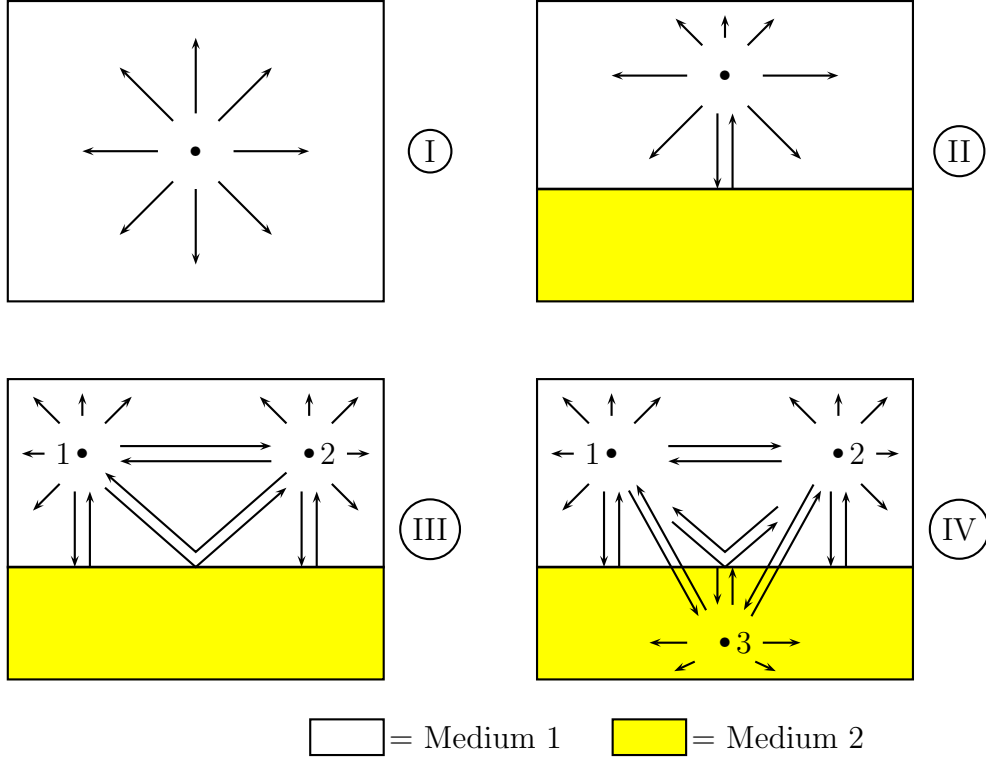
Figure 4.1: *Various configurations involving thin wires.*

as well as between wire 2 and wire 3.

The additional terms in Hallén's equation for increasing complexity of the configuration will be introduced according to an interaction table (see Table 4.1). The section number refers to the section pertaining to a configuration. Until configuration IV, the results can be verified from the literature [24, 25].

At the end of the chapter, the calculation times of a number of configurations are discussed.

4.1   Hallén's equation for a single thin wire above an interface between two half spaces

In the previous section, Hallén's equation for a single thin wire with a delta-gap source in a homogeneous medium, see (3.51), was derived as

$$\int_0^L \frac{I(x',\omega)\exp(ik_1 R_a)}{4\pi R_a}dx' = F_0(\omega)\exp\left(ik_1 x\right) + F_L(\omega)\exp\left(ik_1(L-x)\right)$$

$$+\frac{Y_1}{2}\left[V(\omega)\exp(ik_1|x-x_g|) + \int_0^L E_x^i(x'\mathbf{u}_x,\omega)\exp(ik_1|x-x'|)dx'\right], \tag{4.1}$$

Configuration	Section	Interactions
I	3.3	· None
II	4.1	· Wire and Interface
III	4.2	· Wire 1 and Interface
		· Wire 2 and Interface
		· Wire 1 and Wire 2
		· Wire 1, Wire 2 and Interface
IV	4.3	· Wire 1 and Interface
		· Wire 2 and Interface
		· Wire 1 and Wire 2
		· Wire 1, Wire 2 and Interface
		· Wire 3 and Interface
		· Wire 1, Wire 3 and Interface
		· Wire 2, Wire 3 and Interface

Table 4.1: *Interaction table for various configurations involving thin wires, see Figure 4.1.*

with $R_a = \sqrt{(x-x')^2 + a^2}$ and $k_1 = \omega\sqrt{\mu_0\varepsilon_1}$. As in the previous chapter, the interface between medium 1 and medium 2 is located at $z = 0$. The upper half space, $z < 0$, is denoted as medium 1 while the lower half space, $z > 0$, is denoted as medium 2. Instead of a current dipole source, a wire antenna with a circular cross section is located at $z = z_1 < 0$. The complex permittivities are ε_1 and ε_2 for medium 1 and medium 2, respectively. The permeability is μ_0 for both media. The wire is again of length L and radius a. The excitation is a delta-gap voltage source at $x = x_g$. For an overview of the configuration, see Figure 4.2. For visualization purposes, the limit $\Delta x \downarrow 0$ has not been carried out yet here. In this configuration, there is no incident field from an external source. However, the difference in dielectric properties between the two media adds a contribution from the interface to the current along the wire. This contribution finds its origin in a reflection from a part of the radiated field from the wire at the interface. This reflected field can be seen as a secondary incident field on the wire. The field incident on the wire can in that interpretation be written as [24]

$$E_x^i(x\mathbf{u}_x + z_1\mathbf{u}_z, \omega) = E_x^r(x\mathbf{u}_x + z_1\mathbf{u}_z, \omega) \tag{4.2}$$

where the superscript r denotes a reflected field due to the interface between the two media. To interrelate the current on the wire with the reflected field by the interface, the current
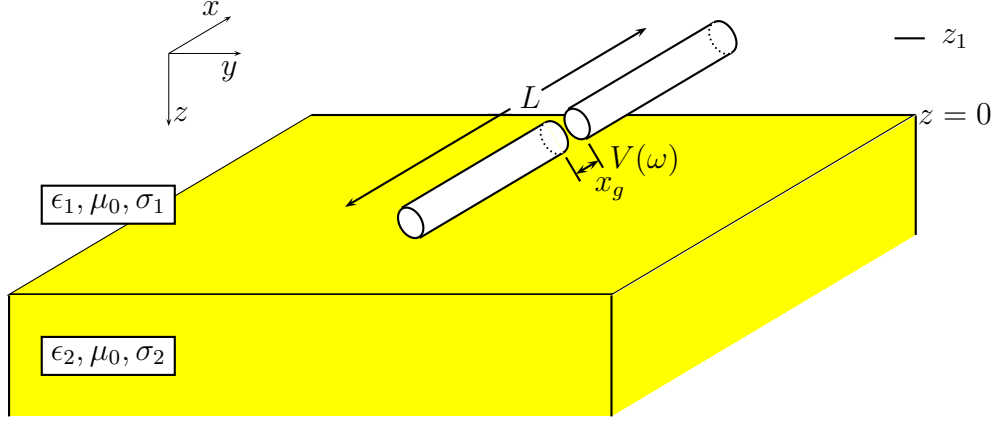
Figure 4.2: *A wire above an interface.*

is written as

$$I(x,\omega) = \int_0^L I(x'',\omega)\delta(x-x'')dx''. \tag{4.3}$$

Using superposition of the rewritten current on the reflected field at $\mathbf{r}$ from a current point source which is given by (2.107) yields

$$E_x^r(x'\mathbf{u}_x + z_1\mathbf{u}_z, \omega) = \frac{i\omega^2 Z_0}{8\pi}\int_0^L I(x'',\omega)\int_0^\infty \zeta^r((x'-x'')\mathbf{u}_x + z_1\mathbf{u}_z, \nu, \omega)d\nu dx'', \tag{4.4}$$

with

$$\zeta^r((x'-x'')\mathbf{u}_x + y\mathbf{u}_y + z_1\mathbf{u}_z, \nu, \omega) = \nu \exp(2k_0 u_1 z_1)$$
$$\cdot \left\{ J_0\left(k_0\nu|(x'-x'')\mathbf{u}_x + y\mathbf{u}_y|\right)\left[\frac{u_1}{\varepsilon_{1r}}R_{12}^E + \frac{1}{u_1}R_{12}^H\right]\right.$$
$$\left. + J_2\left(k_0\nu|(x'-x'')\mathbf{u}_x + y\mathbf{u}_y|\right)\cos(2\phi)\left[\frac{1}{u_1}R_{12}^H - \frac{u_1}{\varepsilon_{1r}}R_{12}^E\right]\right\}, \tag{4.5}$$

where $u_1 = (\nu^2 - \varepsilon_{1,r})^{\frac{1}{2}}$, $k_0 = \omega/c_0$ and $F(\omega)$ specified in (2.49) has been chosen such that $-i\omega F(\omega) = 1$. Note that in this configuration, $y = 0$ and $\cos(2\phi) = 1$. The reflected field due to the interface is now defined for every point along the wire. With the wire located at $\mathbf{r} = x\mathbf{u}_x + z_1\mathbf{u}_z$, with $0 < x < L$, the reflected-field term can be incorporated in (4.1)

$$\int_0^L \frac{I(x',\omega)\exp(ik_1 R_a)}{4\pi R_a}dx' - F_0(\omega)\exp(ik_1 x) - F_L(\omega)\exp(ik_1(L-x))$$
$$= \frac{Y_1}{2}\left[V(\omega)\exp(ik_1|x-x_g|) + \int_0^L E_x^r(x'\mathbf{u}_x + z_1\mathbf{u}_z, \omega)\exp(ik_1|x-x'|)dx'\right], \tag{4.6}$$

with E_x^r as defined in (4.4). In the next section, the discretized version of the reflected-field term will be given. The remaining parts of Hallén's equation (4.6) are discretized according to (3.60).

4.1.1 Discretization of the reflected field term

In the previous chapter, it was stated that the integral over ν is calculated with the aid of a composite Gaussian quadrature rule [24]. The integral over ν in (4.4) is approximated according to

$$\int_0^\infty \zeta^r((x' - x'')\mathbf{u}_x + z_1\mathbf{u}_z, \nu, \omega)d\nu \approx \sum_{k=1}^K \alpha_k \zeta^r((x' - x'')\mathbf{u}_x + z_1\mathbf{u}_z, \nu_k, \omega), \qquad (4.7)$$

where K is the number of points needed for the composite Gaussian quadrature rule. The weights $\{\alpha_k\}$ and abscissa $\{\nu_k\}$ are again calculated with the aid of the subroutine D01BCF of the NAG numerical library. Note that the weights $\{\alpha_k\}$ do not depend on the frequency. The integral from 0 to L is approximated with the aid of a trapezoidal rule [24].

As a result, the discretized reflected field term is obtained as

$$\int_0^L E_x^r(x'\mathbf{u}_x + z_1\mathbf{u}_z, \omega) \exp(ik_1|x_m - x'|)dx' \approx \frac{i\omega^2 Z_0 \Delta x}{8\pi} \sum_{m'=0}^M v_{m'} \exp(ik_1|x_m - x_{m'}|)$$

$$\cdot \sum_{m''=1}^{M-1} I_{m''}(\omega) \sum_{k=1}^K \alpha_k \zeta^r \left(x_{|m'-m''|}\mathbf{u}_x + z_1\mathbf{u}_z, \nu_k, \omega\right), \qquad (4.8)$$

for $m = 0, \ldots, M$ and where

$$v_m = \begin{cases} \Delta x, & \text{for } m = 1, \ldots, M-1, \\ \frac{\Delta x}{2} & \text{for } m = 0, M. \end{cases} \qquad (4.9)$$

Combining (3.60) with the discretized reflected field term results in the following discretized Hallén's equation for a wire above an interface between two half spaces:

$$\sum_{m'=1}^{M-1} w_{m-m'} \exp\left(ik_1 R_{m-m'}^a\right) I_{m'}(\omega) - F_0(\omega) \exp\left(ik_1 x_m\right) - F_L(\omega) \exp\left(ik_1(L - x_m)\right)$$

$$= \frac{Y_1}{2} \Bigg[\exp\left(ik_1|x_m - x_g|\right) V(\omega)$$

$$+ \frac{i\omega^2 Z_0 \Delta x}{8\pi} \sum_{m'=0}^M v_{m'} \exp(ik_1|x_m - x_{m'}|) \cdot \sum_{m''=1}^{M-1} I_{m''}(\omega)\xi^r(m' - m'', z_1) \Bigg], \quad (4.10)$$

with

$$\xi^r(m' - m'', z_1) = \sum_{k=1}^K \alpha_k \zeta^r \left(x_{|m'-m''|}\mathbf{u}_x + z_1\mathbf{u}_z, \nu_k, \omega\right), \qquad (4.11)$$

for $m = 0, \ldots, M$. The summation for $\xi^r(m' - m'', z_1)$ is carried out only once per frequency.

4.1.2   Results

A single thin wire is excited by a Gaussian voltage pulse as specified in Section 3.3.2. The current along the wire is calculated using the parameters $L = 1$ m and $a = 0.002$ m. The spatial discretization is given by $M = 30$ and the number of time steps is again $N = 1024$. The medium parameters of both half spaces as well as the height z_1 are varied.

The results have been compared to results from Rubio-Bretones *et al.* [24] where a frequency-domain Hallén technique was used as well. The results from [24] will be referred to as "Ref." In Figure 4.3, the currents at the center of the wire have been plotted for $z_1 = -0.25$ m.

(A)   (B)
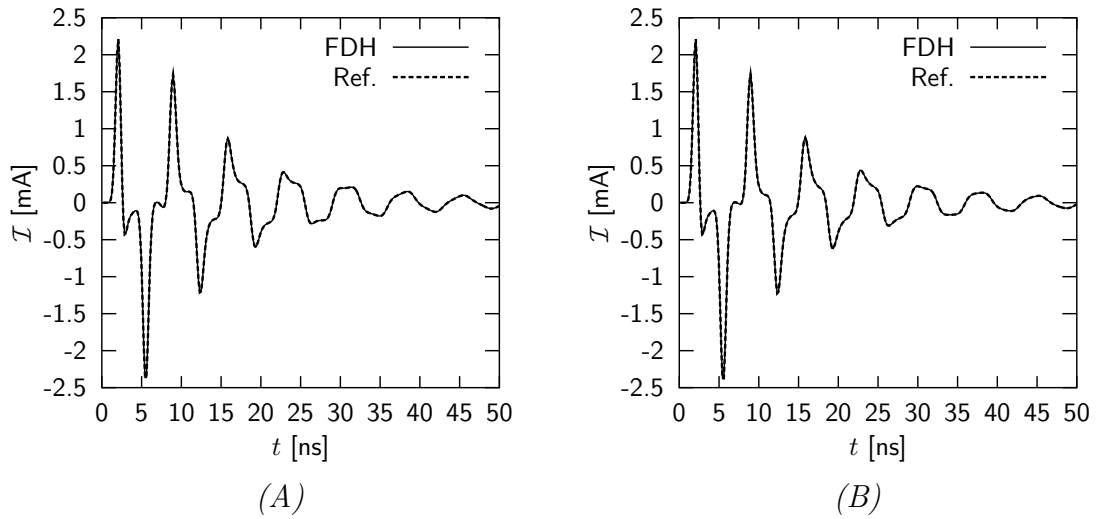
Figure 4.3:   *The induced current at the center of a wire with length $L = 1$ m, radius $a = 0.002$ m, $z_1 = -0.25$ m, $M = 30$ and $N = 1024$. The medium properties are $\epsilon_{1r} = 1$, $\sigma_1 = \sigma_2 = 0$, $\epsilon_{2r} = 9$ (A) and $\epsilon_{2r} = 3$ (B). The permeability is μ_0 in all cases. The excitation is a Gaussian voltage pulse with $\tau = 0.5$ ns and $t_1 = 4\tau$.*

The medium parameters are $\epsilon_{1r} = 1$, $\sigma_1 = 0$ and $\sigma_2 = 0$ for $\epsilon_{2r} = 9$ and $\epsilon_{2r} = 3$, respectively. It is observed that the results from the present frequency-domain Hallén method (FDH) are in perfect agreement with the reference results.

In Figure 4.4, the current at the center of the wire has been plotted for different heights z_1 and various complex permittivities of the lower half space. The free-space case is added for comparison. The currents are slightly affected by the presence of the interface. The effect of the interface on the current increases when the distance z_1 to the interface decreases. The conductivity σ_2 hardly influences the current in (B). In (D), the magnitude of the current is slightly higher due to the conductivity σ_2 because the magnitude of both the electric and magnetic reflection coefficient increases with increasing σ_2. However, the difference between the currents in case of an interface and free space is not dramatic.
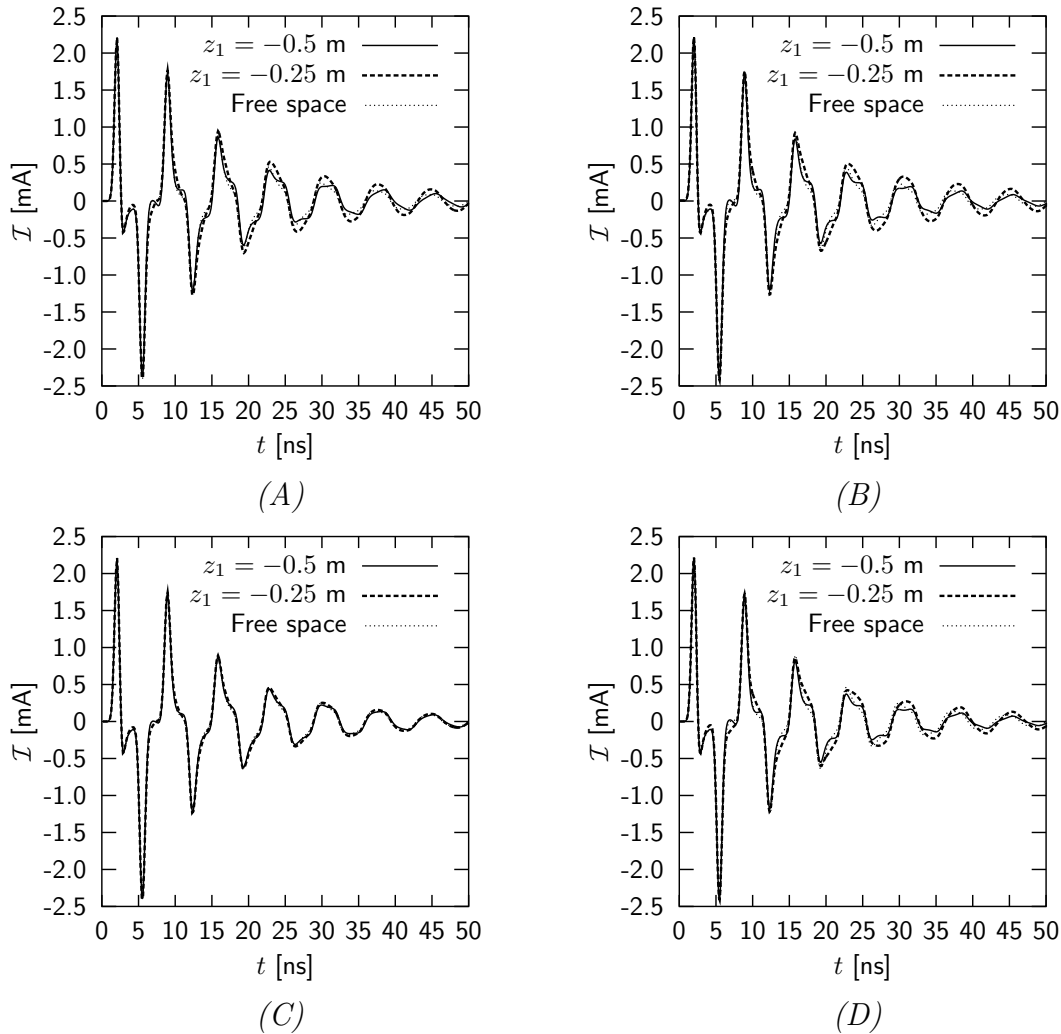
Figure 4.4: *The induced current at the center of a wire with length $L = 1$ m, radius $a = 0.002$ m, $M = 30$ and $N = 1024$ for different heights z_1. The medium properties are $\epsilon_{1r} = 1, \sigma_1 = 0$ for the upper half space. The properties of the lower half space are varied as $\epsilon_{2r} = 9, \sigma_2 = 0$ (A), $\epsilon_{2r} = 9, \sigma_2 = 0.05$ S/m (B), $\epsilon_{2r} = 3, \sigma_2 = 0$ (C) and $\epsilon_{2r} = 3, \sigma_2 = 0.05$ S/m (D). The excitation is a Gaussian voltage pulse with $\tau = 0.5$ ns and $t_1 = 4\tau$.*

The explanation is quite simple. In Figure 4.5, the wire is located above an interface. The wire radiates in all directions. The incident field on the wire is a part of the field reflected at the interface. This only takes place directly under the wire and is indicated by a wave A. The rest of the radiated field reflects at the interface as the waves B and does not return to the wire. In other words, only a very small portion of the radiated field affects the wire through a reflection at the interface when the radius of the wire is small.
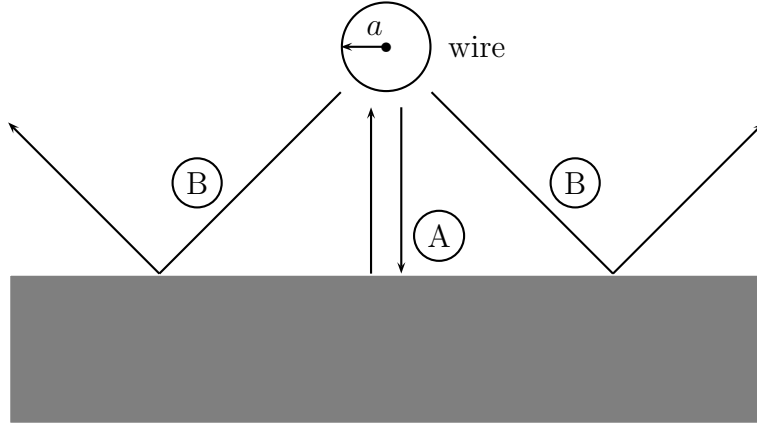
Figure 4.5: *The reflected field components at the interface.*

In Figure 4.6, the current at the center of the wire has been plotted for the case where the lower half space is perfectly electrically conducting (PEC). The height is $z_1 = -0.25$ m. In the case of a PEC interface, the conductivity $\sigma_2 \to \infty$, therefore the following limiting values of the reflection coefficients can be used

$$\lim_{\sigma_2 \to \infty} R_{12}^E = 1, \quad \lim_{\sigma_2 \to \infty} R_{12}^H = -1. \tag{4.12}$$

The oscillating behavior of the current that was observed in other configurations is now
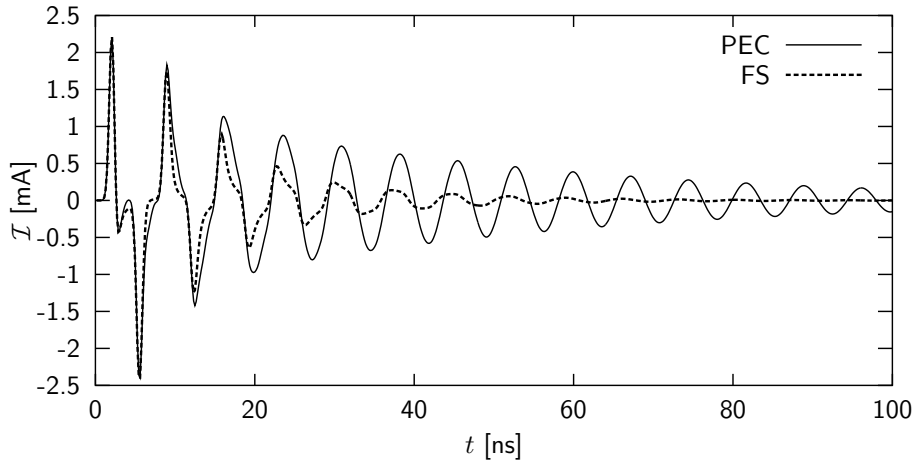
Figure 4.6: *The induced current at the center of a wire with length $L = 1$ m, radius $a = 0.002$ m, $z_1 = -0.25$ m, $M = 30$ and $N = 1024$ for $\sigma_2 \to \infty$ (PEC). The other medium properties are $\epsilon_{1r} = 1$, $\mu_{1r} = 1$ and $\sigma_1 = 0$. The free space case (FS) has been added for comparison. The excitation is a Gaussian voltage pulse with $\tau = 0.5$ ns and $t_1 = 4\tau$.*

much stronger and attenuates very slowly. The oscillatory behavior is no longer restricted to the wire. The wire and the PEC interface form a "waveguide" that allows a TEM mode. In Figure 4.7, the current at the center of the wire has been plotted for a height $z_1 = -0.25$ m and for various complex permittivities of the upper half space. The medium parameters of the lower half space are $\epsilon_{2r} = 1$ and $\sigma_2 = 0$. The same observations are
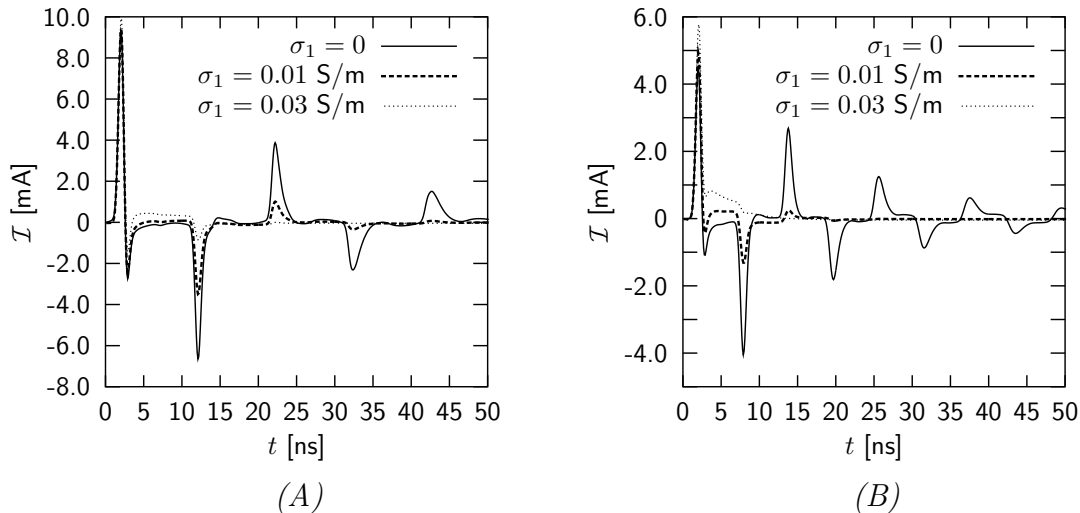
Figure 4.7: *The induced current at the center of a wire with length $L = 1$ m, radius $a = 0.002$ m, $z_1 = -0.25$ m, $M = 30$ and $N = 1024$ for various conductivities σ_1. The other medium properties are $\epsilon_{2r} = 1$, $\sigma_2 = 0$, $\epsilon_{1r} = 9$ (A) and $\epsilon_{1r} = 3$ (B). The excitation is a Gaussian voltage pulse with $\tau = 0.5$ ns and $t_1 = 4\tau$.*

made as in the previous results. The current is hardly influenced by the reflection at the interface. When the conductivity of the upper half space increases, the current along the wire is affected severely for both choices of the permittivity ϵ_{1r}. This is mainly due to the additional attenuation introduced by the conducting embedding and not by the interface.

4.2 Two wires above an interface between two half spaces

In this section, the configuration of the previous section is extended with a second wire as depicted in Figure 4.8. The wires are denoted as wire 1 and wire 2, respectively. In this configuration, wire 1 is driven by a delta-gap voltage at $x = x_g$. As a result of mutual coupling, a current will flow along both wires. To make a clear distinction between transmitter and receiver, the limit $\Delta x \downarrow 0$ has not been carried out in Figure 4.8. The wires
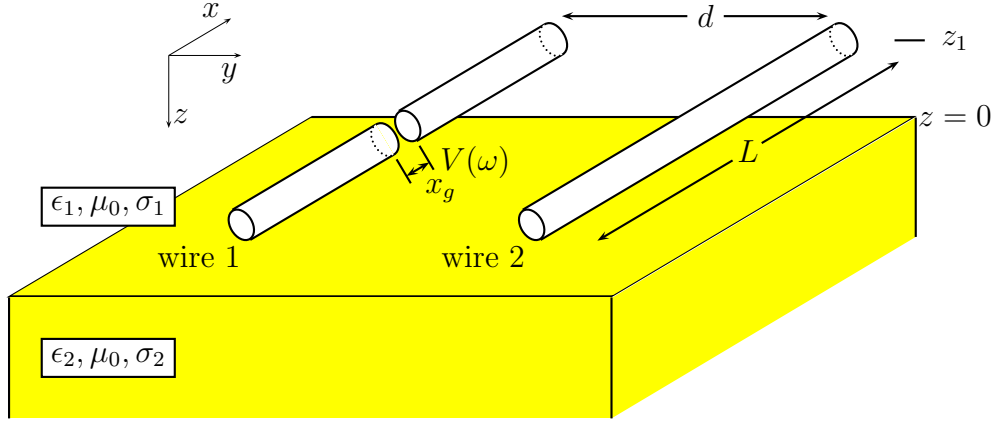
Figure 4.8: *Two wires above an interface.*

are located at $z = z_1 < 0$ above the interface at $z = 0$ between medium 1 and medium 2 with complex permittivities ε_1 and ε_2, respectively. The permeability is again μ_0 for both media. The distance between the wires is denoted as d, and the central axes of the wires are chosen $\mathbf{r}_1 = x\mathbf{u}_x + z_1\mathbf{u}_z$ and $\mathbf{r}_2 = x\mathbf{u}_x + d\mathbf{u}_y + z_1\mathbf{u}_z$ where $0 < x < L$ and the subscripts 1 and 2 refer to wire 1 and wire 2, respectively.

From the interaction table, Table 4.1, it follows that the currents along both wires influence each other. Wire 1 is considered to demonstrate the influence of the other wire. In addition to the reflection of a part of the radiated field from wire 1 at the interface, the field incident on wire 1 has now two extra contributions. In particular, the scattered field from wire 2 acts as a part of the incident field on wire 1 directly through medium 1 and also via a reflection at the interface at $z = 0$. Hence, the incident electric field in Hallén's equation for wire 1 can be written as

$$E_x^{i,1} = E_x^{r,1} + E_x^{r,2} + E_x^{d,2}, \tag{4.13}$$

where the superscripts i, r and d denote the incident field, the reflected field and the direct field, respectively. The additional superscripts 1 and 2 refer to the sources of the field terms, wire 1 and wire 2, respectively.

The term direct field is introduced here. The scattered field from wire 2 gives two contributions to wire 1 as stated above. The scattered field of wire 2 is a reaction to the scattered field from wire 1. Analogous to wire 1, the scattered field from wire 1 arrives at wire 2 in two ways, one directly trough medium 1 and one via a reflection at the interface. Therefore, the so-called scattered field is split up in two contributions which are referred to as the direct field and the reflected field.

The first term in the right-hand side of the latter equation can be described by (4.4) where

$I(x'', \omega) = I_1(x'', \omega)$ and $\mathbf{r} = \mathbf{r}_1$ are chosen. For the reflected field due to the current along wire 2, a similar contribution as (4.4) can be used where $I(x'', \omega) = I_2(x'', \omega)$ and $\mathbf{r} = \mathbf{r}_2$ are chosen.

The direct field can be derived elegantly in a manner that is similar to the derivation of Hallén's equation. Therefore, consider (3.41) for wire 2. The point of observation $\mathbf{r}$ is chosen on the axis of wire 1. Assume that the current density for wire 2 is given by $\mathbf{J}_2(\mathbf{r}', \omega)$. After using the null-field condition, (3.41) is generalized to

$$
\begin{aligned}
i\omega\varepsilon_1 \cdot (E_x^s(\mathbf{r}, \omega) &- \mathcal{S}_{\mathbf{\mathcal{D}}}(\mathbf{r})E_x(\mathbf{r}, \omega)) \\
&= \partial_x \nabla \cdot \boldsymbol{A}(\mathbf{r}, \omega) + k_1^2 \oint_{\mathbf{r}' \in \partial\mathbf{\mathcal{D}}} G(R, \omega)J_{2x}(\mathbf{r}', \omega)d\mathbf{r}',
\end{aligned}
\tag{4.14}
$$

with

$$
\boldsymbol{A}(\mathbf{r}, \omega) = \oint_{\mathbf{r}' \in \partial\mathbf{\mathcal{D}}} G(R, \omega)\mathbf{J}_2(\mathbf{r}', \omega)d\mathbf{r}',
$$

where $\partial\mathbf{\mathcal{D}}$ is the surface of wire 2. This equation is valid in a homogeneous space. Since in a homogeneous space an interface is absent, the scattered field E_x^s in (4.14) is equal to the direct field $E_x^{d,2}$ in (4.13). Following the same procedure as in Section 3.2, the $\nabla\cdot$ operator in the latter equation is broken up into a longitudinal and a transversal component. With the point of observation $\mathbf{r}$ on the central axis of wire 1 and the source point on the surface of wire 2, it follows that

$$
\begin{aligned}
R &= |(x - x')\mathbf{u}_x + d\mathbf{u}_y + a\mathbf{u}_{\rho'}(\phi')| \\
&= \sqrt{(x - x')^2 + d^2 + a^2 + 2ad\,(\mathbf{u}_y \cdot \mathbf{u}_{\rho'}(\phi'))} \\
&= R_d\sqrt{1 + \frac{2ad\,(\mathbf{u}_y \cdot \mathbf{u}_{\rho'}(\phi'))}{R_d^2} + \frac{a^2}{R_d^2}},
\end{aligned}
\tag{4.15}
$$

with $R_d = \sqrt{(x - x')^2 + d^2}$. After carrying out a Taylor expansion of the square root in the latter equation, the distance R is written as

$$
R \approx R_d\left[1 + \frac{ad\,[\mathbf{u}_y \cdot \mathbf{u}_{\rho'}(\phi')]}{R_d^2} + \mathcal{O}\left(\frac{a^2}{R_d^2}\right)\right],
\tag{4.16}
$$

where $\mathcal{O}(a^2/R_d^2)$ vanishes when the argument approaches 0. The second term in the right-hand side of (4.16) vanishes after the integration over ϕ'. Since $d \gg a$ and therefore $R_d \gg a$, the $\nabla\cdot$ operator is written as

$$
\nabla \cdot \boldsymbol{A}(\mathbf{r}, \omega) = \partial_x \oint_{\mathbf{r}' \in \partial\mathbf{\mathcal{D}}} G(R_d, \omega)J_{2x}(\mathbf{r}', \omega)d\mathbf{r}'.
\tag{4.17}
$$

If the currents at the end faces are neglected, (4.14) can be written as

$$i\omega\varepsilon_1 E_x^{d,2}(\mathbf{r},\omega) = \left(\partial_x^2 + k_1^2\right) \oint_{\mathbf{r}'\in\partial\mathcal{D}} G(R_d,\omega) J_{2x}(\mathbf{r}',\omega)d\mathbf{r}'. \tag{4.18}$$

Because $G(R_d,\omega)$ again does not depend on ϕ', the integral in (4.18) can be simplified analogous to (3.45). This results in

$$i\omega\varepsilon_1 E_x^{d,2}(\mathbf{r},\omega) = \left(\partial_x^2 + k_1^2\right) \int_0^L G(R_d,\omega) I_2(\mathbf{r}',\omega)dx'. \tag{4.19}$$

In a similar fashion as in Section 3.3, the differential operator in the latter equation can be handled elegantly to finally arrive at a special form of Hallén's equation.

The combination of the special form of Hallén's equation and the results from the previous section together with choosing $\mathbf{r} = x\mathbf{u}_x + d\mathbf{u}_y$ results in the generalized version of Hallén's equation for wire 1:

$$\int_0^L \left[\frac{I_1(x',\omega)\exp(ik_1R_a)}{4\pi R_a} + \frac{I_2(x',\omega)\exp(ik_1R_d)}{4\pi R_d} \right] dx'$$

$$= F_0(\omega)\exp\left(ik_1x\right) + F_L(\omega)\exp\left(ik_1(L-x)\right)$$

$$+ \frac{Y_1}{2}\left[V(\omega)\exp(ik_1|x-x_g|) + \int_0^L E_x^{r,1}(x'\mathbf{u}_x + z_1\mathbf{u}_z,\omega)\exp(ik_1|x-x'|)dx' \right.$$

$$\left. + \int_0^L E_x^{r,2}(x'\mathbf{u}_x + d\mathbf{u}_y + z_1\mathbf{u}_z,\omega)\exp(ik_1|x-x'|)dx' \right]. \tag{4.20}$$

For the second wire, a similar equation can be found.

From (4.20), it is easily seen that the current along wire 2 influences the current along wire 1. Since a similar equation is found for wire 2, the influence is mutual. The mutual influence is referred to as "mutual coupling". As far as the discretization is concerned, the only term that needs attention is the scattered field term from wire 2 in the case that the current on wire 1 is evaluated. The discretization for the remaining terms has already been discussed in previous sections.

4.2.1   Discretization of the direct field term

Since the distance d has already been assumed to be much larger than the radius a of the wire, the term R_d does not become singular when $x = x'$. Therefore the complete integrand can be approximated by a piecewise-linear expansion which results in the trapezoidal rule. The scattered field term can thus be approximated as

$$\int_0^L \frac{I_2(x',\omega)\exp(ik_1R_d)}{4\pi R_d} \approx \sum_{m'=0}^{M-1} u_{m-m'} I_{2,m'}(\omega)\exp(ik_1R_{m-m'}^d), \ m = 0,\ldots,M, \tag{4.21}$$

with

$$u_m = \frac{\Delta x}{4\pi R_m^d}, \quad R_m^d = \sqrt{(m\Delta x)^2 + d^2}. \tag{4.22}$$

Again, the boundary condition $I_2(0) = I_2(L) = 0$ is accounted for. With this result, the total discretized Hallén equation for wire 1 can be written as

$$\sum_{m'=1}^{M-1} \left[w_{m-m'} \exp\left(ik_1 R_{m-m'}^a\right) I_{1,m'}(\omega) + u_{m-m'} \exp\left(ik_1 R_{m-m'}^d\right) I_{2,m'}(\omega) \right]$$

$$= F_0(\omega) \exp\left(ik_1 x_m\right) + F_L(\omega) \exp\left(ik_1(L - x_m)\right)$$

$$+ \frac{Y_1}{2} \left\{ V(\omega) \exp\left(ik_1 |x_m - x_g|\right) + \frac{i\omega^2 Z_0 \Delta x}{8\pi} \sum_{m'=0}^{M} v_{m'} \exp(ik_1 |x_m - x_{m'}|) \right.$$

$$\left. \cdot \left[\sum_{m''=1}^{M-1} I_{1,m''}(\omega) \xi^{r,1}(m' - m'', z_1) + \sum_{m''=1}^{M-1} I_{2,m''}(\omega) \xi^{r,2}(m' - m'', d, z_1) \right] \right\},$$

$$m = 0, \ldots, M, \tag{4.23}$$

with

$$\xi^{r,1}(m' - m'', z_1) = \sum_{k=1}^{K} \alpha_k \zeta^r \left(x_{|m'-m''|} \mathbf{u}_x + z_1 \mathbf{u}_z, \nu_k, \omega\right), \tag{4.24}$$

$$\xi^{r,2}(m' - m'', d, z_1) = \sum_{k=1}^{K} \alpha_k \zeta^r \left(x_{|m'-m''|} \mathbf{u}_x + d\mathbf{u}_y + z_1 \mathbf{u}_z, \nu_k, \omega\right). \tag{4.25}$$

4.2.2 Results

In Section 4.1.2, the current along a single thin wire for a number of configurations was calculated. In this section, some examples will be shown for the configuration with two wires above an interface.

In the examples given in this section, the calculation was carried out for $L = 1$ m, $a = 0.002$ m, $M = 30$ and $N = 1024$. The excitation is again the Gaussian pulse as given in Section 3.3.2.

In Figure 4.9, the current at the center of both wires has been calculated for a height of $z_1 = -0.25$ m. The medium parameters are $\epsilon_{1r} = 1$, $\sigma_1 = \sigma_2 = 0$ and $\epsilon_{2r} = 9$. The permeability is again μ_0. The results have been compared to results from Rubio-Bretones *et al.* [25] which will be referred to as "Ref.". The free-space case (FS) had been added for comparison.
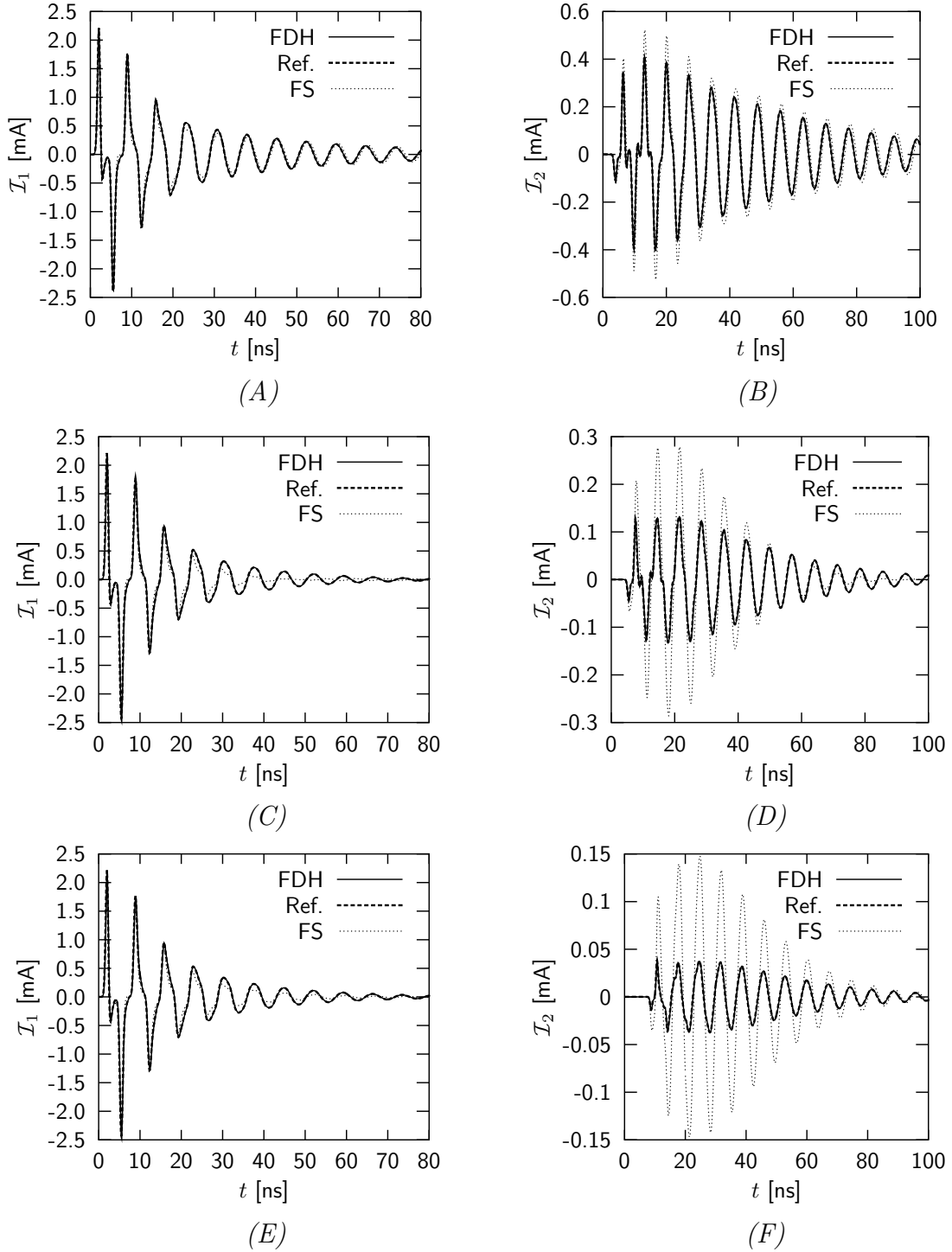
Figure 4.9: *The induced current at the center of wire 1 and 2. Both wires have a length $L = 1$ m and radius $a = 0.002$ m. The distance between the wires is $d = 0.5$ m for (A) and (B), $d = 1$ m for (C) and (D) and $d = 2$ m for (E) and (F). The height is $z_1 = -0.25$ m. The medium properties are $\epsilon_{1r} = 1$, $\sigma_1 = 0$, $\epsilon_{2r} = 9$ and $\sigma_2 = 0$ for all configurations. The excitation is a Gaussian voltage pulse with $\tau = 0.5$ ns and $t_1 = 4\tau$. The reference results (Ref.) are taken from [25] and the free space (FS) case has been added for comparison.*

The results are in good agreement with the reference results, as can be easily seen from all plots. Comparing (B), (D) and (F) with each other shows that the amplitude of the current along wire 2 is much higher when the distance d decreases. In the free-space (FS) case the amplitude is directly related to the distance; when the distance becomes two times smaller, the amplitude increases approximately with a factor of two. After approximately 20 ns, the current along wire 2 in (A) acts as a damped oscillation. When the distance between the wires is increased to 1 m, this damped oscillation effect starts after approximately 30 ns and also vanishes much quicker. The delay between the first negative peaks in (D) and (B) is exactly 1.67 ns which is expected from the difference in distance $((1-0.5)/c_0 = 1.67$ ns). For the current along wire 1, a similar oscillatory behavior is observed.

It is interesting to see that, for $d = 1$ m, the oscillatory behavior of the current along wire 1 attenuates much quicker than for the other distances d. The current along wire 2 produces a direct field to wire 1. This direct field results in a current along wire 1 that is of opposite sign compared to the current that was excited by the original voltage pulse for $d = 1$ m. For $d = 0.5$ m, the current along wire 1 due to $\mathcal{E}_x^{d,2}$ has the same sign as the current that is already traveling along the wire. The current along wire 2 is similar to the current along a single thin wire which means that the distance $d = 2$ m is large enough to ensure that mutual coupling has little effect.

For (A), (C) and (E), it is observed that the early-time behavior of the current ($t < 20$ ns) is hardly influenced by the presence of wire 2. The reason for this is that the voltage pulse still dominates over the coupling contribution from wire 2. After 30 ns, the magnitudes of the currents along wire 1 and wire 2 for $d = 1$ m are almost the same resulting in the oscillatory behavior of both currents. In (A) this happens slightly earlier because the initial magnitude of the current in (B) is larger than in (D). Because of this larger magnitude in current, which is a direct effect of the smaller distance between the wires, the oscillation vanishes at a slower rate. In general, the oscillation strongly depends on the coupling between the wires.

The influence from the reflection at an interface on the current along a single thin wire was observed to be negligible. In (A), (C) and (E), this observation is confirmed. However, the currents along wire 2 are affected by the presence of an interface, as can be easily observed from (B), (D) and (F). When the coupling between wire 1 and wire 2 is stronger, the presence of the interface has less effect on the current along wire 2. After approximately 30 ns, the damped oscillation starts in (D), and the amplitude of the current along wire 2 is reduced heavily until 50 ns. In (F) this reduction of the current along wire 2 is after approximately 80 ns. The oscillatory behavior of both wires is influenced by the direct coupling but also by the coupling to the interface.

To demonstrate this effect, a PEC interface has been used. The wire parameters are the same as in previous configurations. The distance between the wires is $d = 1$ m and the height is $z_1 = -0.25$ m. The results are visualized in Figure 4.10. It is observed that the
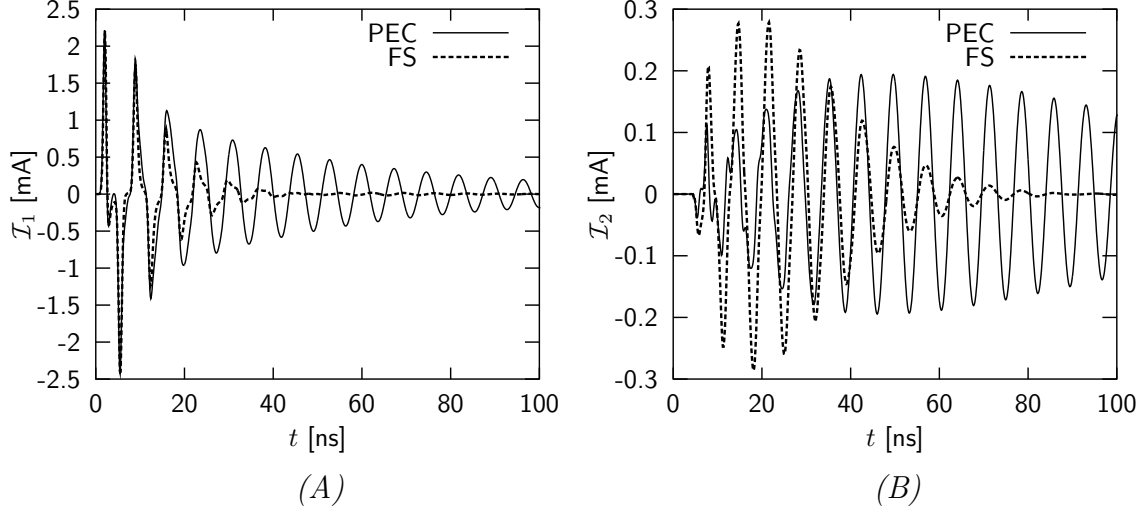
Figure 4.10: *The induced current at the center of wire 1 and 2. Both wires have a length $L = 1$ m and radius $a = 0.002$ m. The distance between the wires is $d = 1$ m and the height is $z_1 = -0.25$ m. The lower half space is perfectly conducting (PEC). The medium properties of the upper half space are $\epsilon_{1r} = 1$ and $\sigma_1 = 0$. The excitation is a Gaussian voltage pulse with $\tau = 0.5$ ns and $t_1 = 4\tau$. The free space (FS) case has been added for comparison.*

current along both wires oscillates heavily and attenuates very slowly. For the single wire above the PEC interface from Figure 4.6, it was observed that the oscillatory behavior of the current starts after approximately 20 ns. In plot (A) of Figure 4.10, the same observation is made. This means that, also in the PEC interface case, wire 2 has little influence on the current along wire 1. The presence of the PEC interface has an attenuating effect on the current along wire 2 until approximately 30 ns. After that, the presence of the PEC interface results in a slowly attenuated, oscillating current along both wires.

It is clear that the presence of the interface has an attenuating effect on the current along wire 2. Since the current along wire 1 is hardly influenced by the presence of wire 2 and the interface, in the remainder of this section, only currents along wire 2 will be shown. This applies when the conductivity of the lower half space is kept fairly small. For increasing conductivity, the lower half space will behave more like a PEC half space and in that case, a strong oscillatory behavior of the current along both wires can be expected.

To investigate the effects of choosing a shorter and larger distance to the interface, the
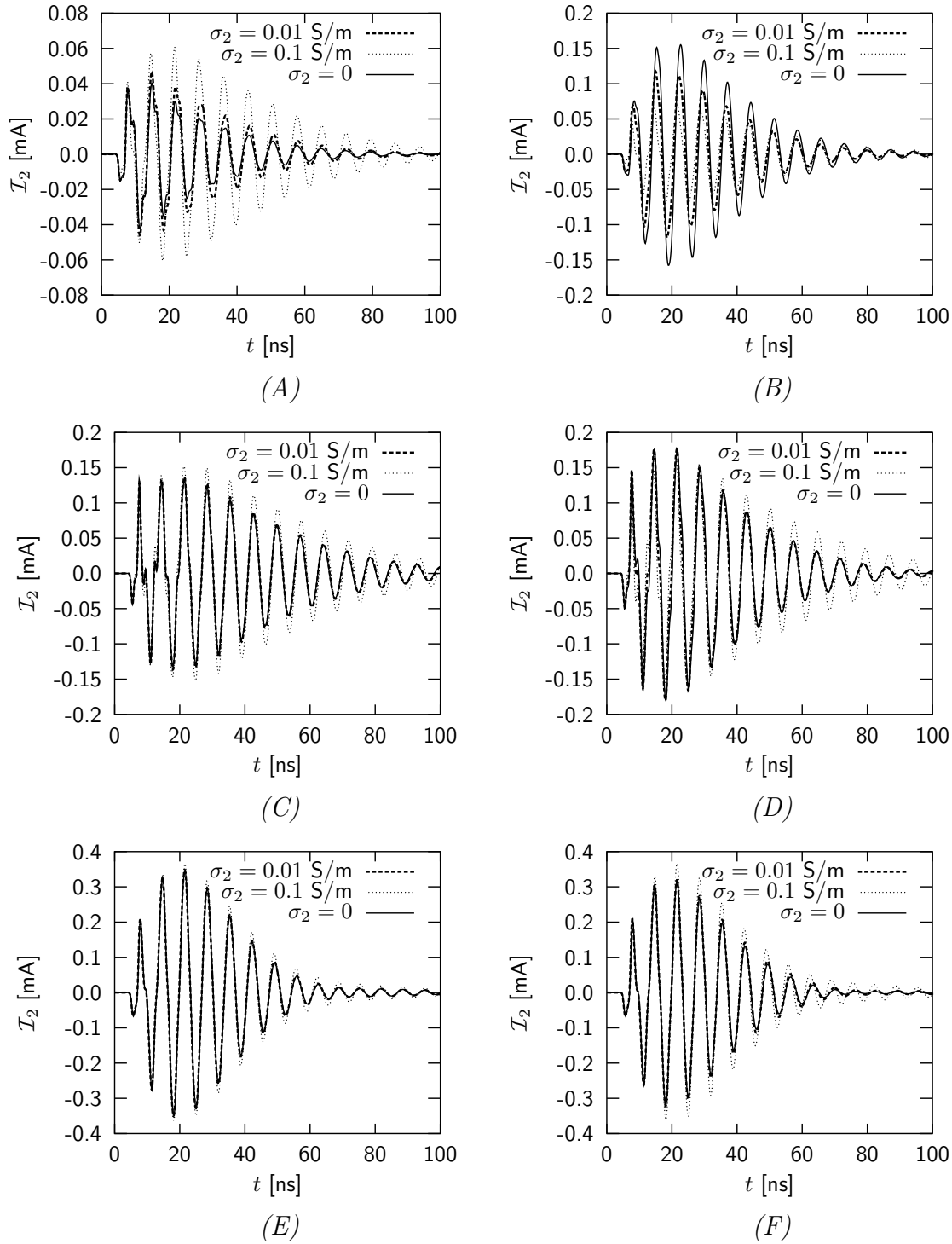
Figure 4.11: *The induced current at the center of wire 2 with length $L = 1$ m and radius $a = 0.002$ m for different conductivities σ_2. The distance is $d = 1$ m and $z_1 = -0.1$ m for (A) and (B), $z_1 = -0.25$ m for (C) and (D) and $z_1 = -1$ m for (E) and (F). The medium properties are $\epsilon_{r,1} = 1$, $\sigma_1 = 0$ and $\epsilon_{r,2} = 9$ for (A), (C) and (E) and $\epsilon_{r,2} = 3$ for (B), (D) and (F). The permeability is μ_0 for all configurations. The excitation is a Gaussian voltage pulse with $\tau = 0.5$ ns and $t_1 = 4\tau$.*

previous configuration is used with heights $z_1 = -0.1$ m, $z_1 = -0.25$ m and $z_1 = -1$ m. The distance between the wires is kept fixed at $d = 1$ m. The currents along wire 2 have been plotted for various conductivities σ_2 of the lower half space. The relative permittivity is $\epsilon_{2r} = 9$ for the plots on the left and $\epsilon_{2r} = 3$ for the plots on the right (see Figure 4.11). The remaining medium parameters are $\mu_1 = \mu_2 = \mu_0$ and $\sigma_1 = 0$ for all configurations. It is immediately observed from (E) and (F) that the conductivity of the lower half space has hardly any influence on the current along wire 2 at $z_1 = -1$ m, even for a fairly high conductivity σ_2. This means that the direct influence between wire 1 and wire 2 dominates over the reflection at the interface. The conductivity though, has a slightly stronger effect when ϵ_{2r} is lower. When the height is $z_1 = -0.25$ m, (C) and (D), the currents are still not much affected by the conductivity σ_2 for $t < 30$ ns. After this time, the damped oscillation starts as was observed earlier. The magnitude of the oscillating current increases for higher conductivity. For $z_1 = -0.1$ m, the magnitude is approximately 4 times lower for $\epsilon_{2r} = 9$ and $\sigma_2 = 0$ compared to $\epsilon_{2r} = 3$ and $\sigma_2 = 0$. For increasing σ_2, the magnitudes of the currents in (A) and (B) are almost the same. Compared to the free-space current along wire 2, the presence of the interface has an attenuating effect on the current along wire 2 provided that the conductivity is not too high. When σ_2 increases, its influence in the complex permittivity ϵ_{2r} increases. Therefore, the currents in the plots on the left and right for $z_1 = -0.1$ m are almost the same when $\sigma_2 = 0.1$ S/m.

4.3   Three coupled wires in a half space configuration

In this section, the configuration of the previous section is extended with a third wire as depicted in Figure 4.12. The wires are denoted as wire 1, wire 2 and wire 3, respectively. In this configuration, wire 1 is driven by a delta-gap voltage source. Again, to make the distinction between transmitter and receivers, the delta gap is clearly indicated in the figure. Wire 1 and wire 2 are located at $z = z_1 < 0$ above the interface at $z = 0$, and wire 3 is located at $z = z_2 > 0$ below the interface. The complex permittivities are ε_1 and ε_2, for the upper half space and the lower half space, respectively. The permeability is again μ_0 for both half spaces. The distance between wire 1 and wire 2 is denoted as d. The central axes of the wires are chosen $\mathbf{r}_1 = x\mathbf{u}_x + z_1\mathbf{u}_z$ and $\mathbf{r}_2 = x\mathbf{u}_x + d\mathbf{u}_y + z_1\mathbf{u}_z$ for $0 < x < L$. The subscripts 1 and 2 refer to wire 1 and wire 2, respectively. The distance in the y-direction between wire 1 and wire 3 is denoted as d_2 and the depth of wire 3 is denoted as z_2. The central axis of wire 3 is chosen as $\mathbf{r}_3 = x\mathbf{u}_x + d_2\mathbf{u}_y + z_2\mathbf{u}_z$ for $0 < x < L$. The subscript 3 refers to wire 3. From the interaction table (Table 4.1), it follows that the
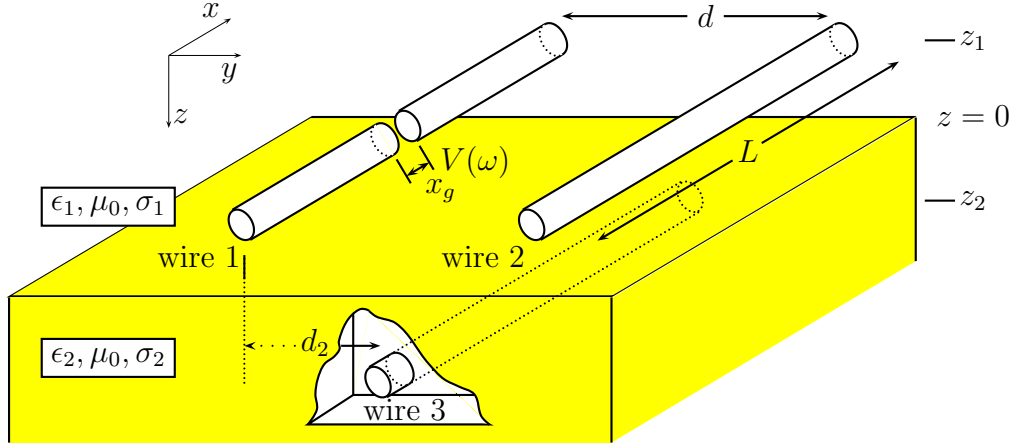
Figure 4.12: *Two wires above an interface between two half spaces and one buried wire.*

fields incident on wire 1 and wire 2 have an extra contribution in the form of a transmitted field from wire 3 through the interface. Wire 3 has three contributions in its incident field. Namely the transmitted fields through the interface from wires 1 and 2, respectively and a reflected field from the interface due to the scattered field from wire 3. To demonstrate the influence of the transmitted-field contribution, Hallén's equation for wire 3 is discussed. The incident field along wire 3 can be written as a sum of the three contributions as follows

$$E_x^{i,3} = E_x^{r,3} + E_x^{t,1} + E_x^{t,2}, \tag{4.26}$$

where the superscript t denotes the transmitted field and the additional superscript 3 refers to wire 3. The other superscripts have been defined in previous sections. The reflected-field term is, in principle, again the one described in (4.4). To obtain the correct expression in medium 2, merely ε_1 is replaced by ε_2, $-z_1$ is replaced by z_2 and the current is chosen as $I(x'',\omega) = I_3(x'',\omega)$. Note that the complex wavenumber is now k_2. The reflected field term for wire 3 is then found as

$$E_x^{r,3}(x'\mathbf{u}_x + d_2\mathbf{u}_y + z_2\mathbf{u}_z, \omega) = \frac{i\omega^2 Z_0}{8\pi} \int_0^L I_3(x'',\omega) \int_0^\infty \nu \, d\nu \exp\left[-2k_0 u_2 z_2\right]$$

$$\cdot \left\{ J_0\left(k_0\nu|x'-x''|\right) \left[\frac{u_2}{\varepsilon_{2r}} R_{21}^E + \frac{1}{u_2} R_{21}^H \right] \right.$$

$$\left. + J_2\left(k_0\nu|x'-x''|\right) \cos(2\phi) \left[\frac{1}{u_2} R_{21}^H - \frac{u_1}{\varepsilon_{2r}} R_{21}^E \right] \right\} dx'', \tag{4.27}$$

with

$$R_{21}^E = \frac{\varepsilon_1 u_2 - \varepsilon_2 u_1}{\varepsilon_1 u_2 + \varepsilon_2 u_1}, \quad R_{21}^H = \frac{u_2 - u_1}{u_2 + u_1},$$

the electric and magnetic reflection coefficients in medium 2, respectively. Note that in the reflected field term again $\cos(2\phi) = 1$. With this result, the expressions for the transmitted fields from wires 1 and 2 can be easily found with the aid of the substitutions above and (2.108). This yields the transmitted field from wire 1:

$$
E_x^{t,1}(x'\mathbf{u}_x + d_2\mathbf{u}_y + z_2\mathbf{u}_z, \omega) = \frac{i\omega^2 Z_0}{8\pi} \int_0^L I_1(x'', \omega) \int_0^\infty \nu \, d\nu \exp\left[k_0(u_1 z_1 - u_2 z_2)\right]
$$

$$
\cdot \left\{ J_0 \left(k_0\nu|(x'-x'')\mathbf{u}_x + d_2\mathbf{u}_y|\right) \left[\frac{1}{u_1}T_{12}^H - \frac{u_2}{\varepsilon_{2r}}T_{12}^E\right] \right.
$$

$$
\left. + J_2 \left(k_0\nu|(x'-x'')\mathbf{u}_x + d_2\mathbf{u}_y|\right) \left[\frac{1}{u_1}T_{12}^H + \frac{u_2}{\varepsilon_{2r}}T_{12}^E\right] \right\} dx'', \tag{4.28}
$$

with

$$
T_{12}^E = \frac{2\varepsilon_2 u_1}{\varepsilon_2 u_1 + \varepsilon_1 u_2}, \qquad T_{12}^H = \frac{2u_1}{u_2 + u_1}. \tag{4.29}
$$

The expression for the transmitted field from wire 2 is similar to (4.28). Hallén's equation to describe the current along wire 3 is written as

$$
\int_0^L I_3(x', \omega)\frac{\exp(ik_2 R_a)}{4\pi R_a}dx' = F_0(\omega)\exp\left(ik_2 x\right) + F_L(\omega)\exp\left(ik_2(L-x)\right)
$$

$$
+\frac{Y_2}{2}\left[\int_0^L E_x^{r,3}(x'\mathbf{u}_x + d_2\mathbf{u}_y + z_2\mathbf{u}_z, \omega)\exp(ik_2|x-x'|)dx'\right.
$$

$$
+\int_0^L E_x^{t,1}(x'\mathbf{u}_x + d_2\mathbf{u}_y + z_2\mathbf{u}_z, \omega)\exp(ik_2|x-x'|)dx'
$$

$$
\left.+\int_0^L E_x^{t,2}(x'\mathbf{u}_x + d_2\mathbf{u}_y + z_2\mathbf{u}_z, \omega)\exp(ik_2|x-x'|)dx'\right]. \tag{4.30}
$$

For wires 1 and 2 similar equations are found. The discretization of these three coupled equations has already been discussed in previous sections. The actual new item is the transmitted field, which is obtained in exactly the same manner as the reflected-field term in previous sections.

4.3.1   Results

In the previous section, the currents along wire 1 and wire 2 were calculated for a number of configurations. In this section the results from a few examples with the presence of a third wire will be discussed and compared to the currents obtained in the previous section. The excitation is again the Gaussian pulse specified in Section 3.3.2. In all examples, the

points of excitation and observation are chosen at the centers of the wires. The current along the wires has been calculated for $L = 1$ m, $a = 0.002$ m, $d = 1$ m, $d_2 = d/2$, $M = 30$ and $N = 1024$. In the different examples, the depth of the wire z_2, the height z_1 of wire 1 and wire 2 and the medium parameters of the lower half space ϵ_{2r} and the conductivity σ_2 are varied. The remaining medium parameters are $\epsilon_{1r} = 1$, $\sigma_1 = 0$ and $\mu_1 = \mu_2 = \mu_0$ in all examples. In Figure 4.13, the currents at the centers of wire 1 and wire 2 are plotted. The solid lines represent a current with the influence of a buried wire and the dotted lines represent a current without a buried wire. The height is varied as $z_1 = -0.1$ m for (A), (B), (E) and (F) and $z_1 = -0.25$ m for (C), (D), (G) and (H). The relative permittivity of the lower half space is $\epsilon_{2r} = 9$ for (A) through (D) and $\epsilon_{2r} = 3$ for (E) through (H). The conductivity of the lower half space is $\sigma_2 = 0$ for all configurations. The depth of the buried wire is kept fixed at $z_2 = 0.1$ m.

It is again observed that the current along wire 1 is hardly affected by the presence of the buried wire. Therefore in the remaining examples, only the current along wire 2 will be plotted.

For $z_1 = -0.25$ m, the presence of wire 3 hardly contributes to the current along wire 2 for both permittivities of the lower half space, see (D) and (H). For $z_1 = -0.1$ m, the influence of wire 3 can be easily observed from plots (B) and (F). For $\epsilon_{2r} = 9$, the current along wire 2 is affected stronger by the presence of wire 3. The magnitude of the current along wire 2 in (B) is lower than in (F) due to the higher reflection coefficient at the interface. It was shown in previous examples that the presence of the interface has a negative effect on the current as long as the conductivity is fairly small. The transmission coefficient T_{12}^E will be lower for a high relative permittivity ϵ_{2r}, thus the induced current on wire 3 will be lower when $\epsilon_{2r} = 9$. But the transmission coefficient T_{21}^E will be higher for $\epsilon_{2r} = 9$. Combination of these effects results in a larger contribution from wire 3 to the current along wire 2 when $\epsilon_{2r} = 9$. Further on in this section, the different electric field contributions arriving at wire 2 will be examined.

In the next two examples, the same configuration is used. In Figure 4.14, the permittivity of the lower half space is $\epsilon_{2r} = 9$. The conductivity is varied as $\sigma_2 = 0$ for (A) and (B), $\sigma_2 = 0.01$ S/m for (C) and (D) and $\sigma_2 = 0.03$ S/m for (E) and (F). The height is varied as $z_1 = -0.1$ m for (A), (C) and (E) and $z_1 = -0.25$ m for (B), (D) and (F). The distance between wires 1 and 2 is $d = 1$ m. The depth of the buried wire is again $z_2 = 0.1$ m. For $z_1 = -0.1$ m, the influence of σ_2 is considerable. In all cases the presence of wire 3 can be easily observed. For $z_2 = -0.25$ m, the presence of wire 3 cannot be observed clearly. The conductivity does not make a difference here.

For a lower permittivity, namely $\epsilon_{2r} = 3$, the effect of σ_2 at the heights $z_1 = -0.1$ m
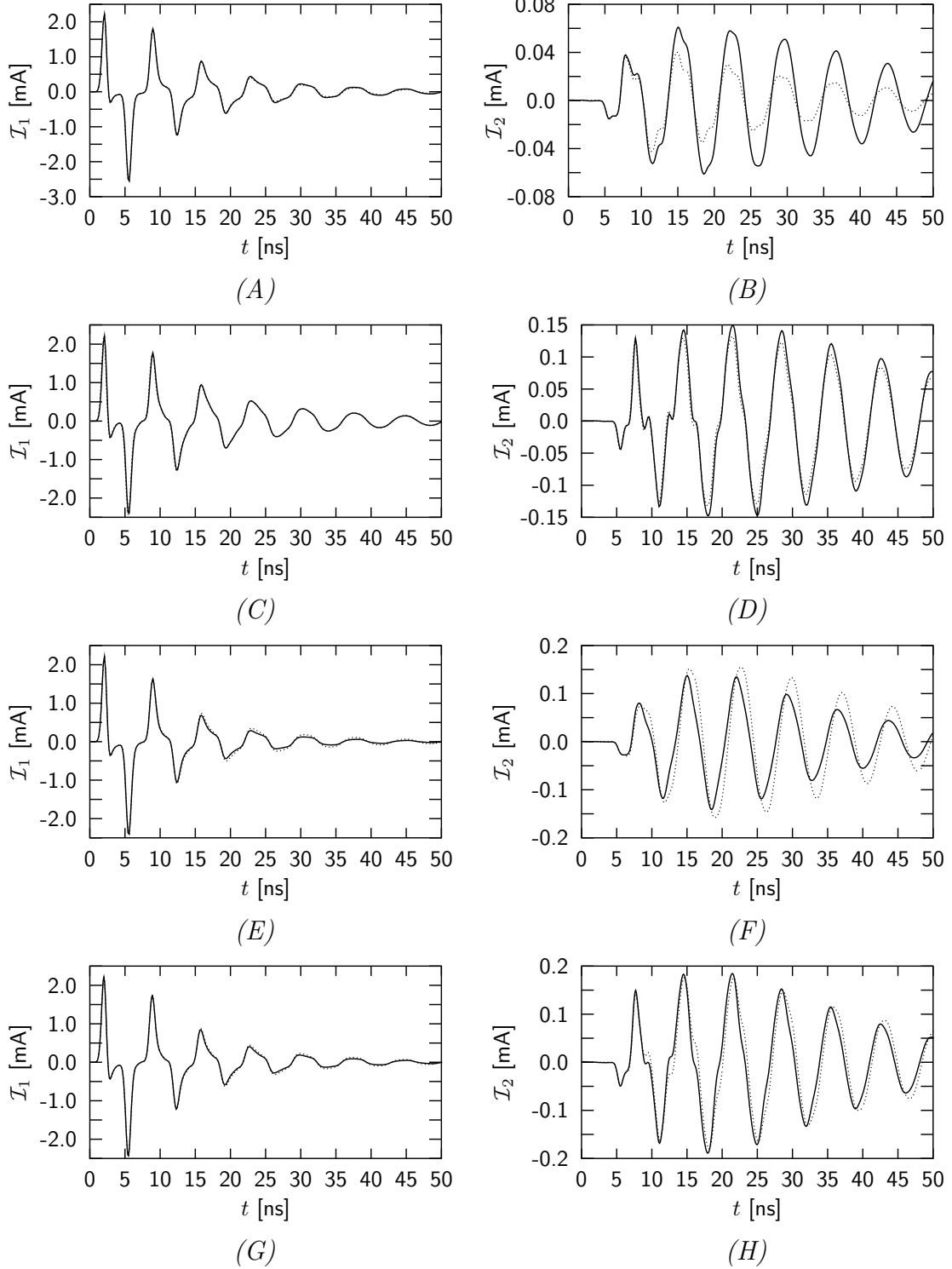
Figure 4.13: *The induced currents at the centers of wire 1 (A,C,E,G) and wire 2 (B,D,F,H) both with length $L = 1$ m and radius $a = 0.002$ m. The distance between wire 1 and 2 is $d = 1$ m, the height of wire 1 and 2 is $z_1 = -0.1$ m for (A), (B), (E) and (F) and $z_1 = -0.25$ m for (C), (D), (G) and (H). The medium properties are $\epsilon_{2r} = 9$ for (A) to (D) and $\epsilon_{2r} = 3$ for (E) to (H). The remaining parameters are $\epsilon_{1r} = 1, \sigma_1 = \sigma_2 = 0, \mu_1 = \mu_2 = \mu_0$ and $z_2 = 0.1$ m for all configurations. The excitation is a Gaussian voltage pulse with $\tau = 0.5$ ns and $t_1 = 4\tau$. The solid lines represent "with wire 3" and the dotted lines "without wire 3".*
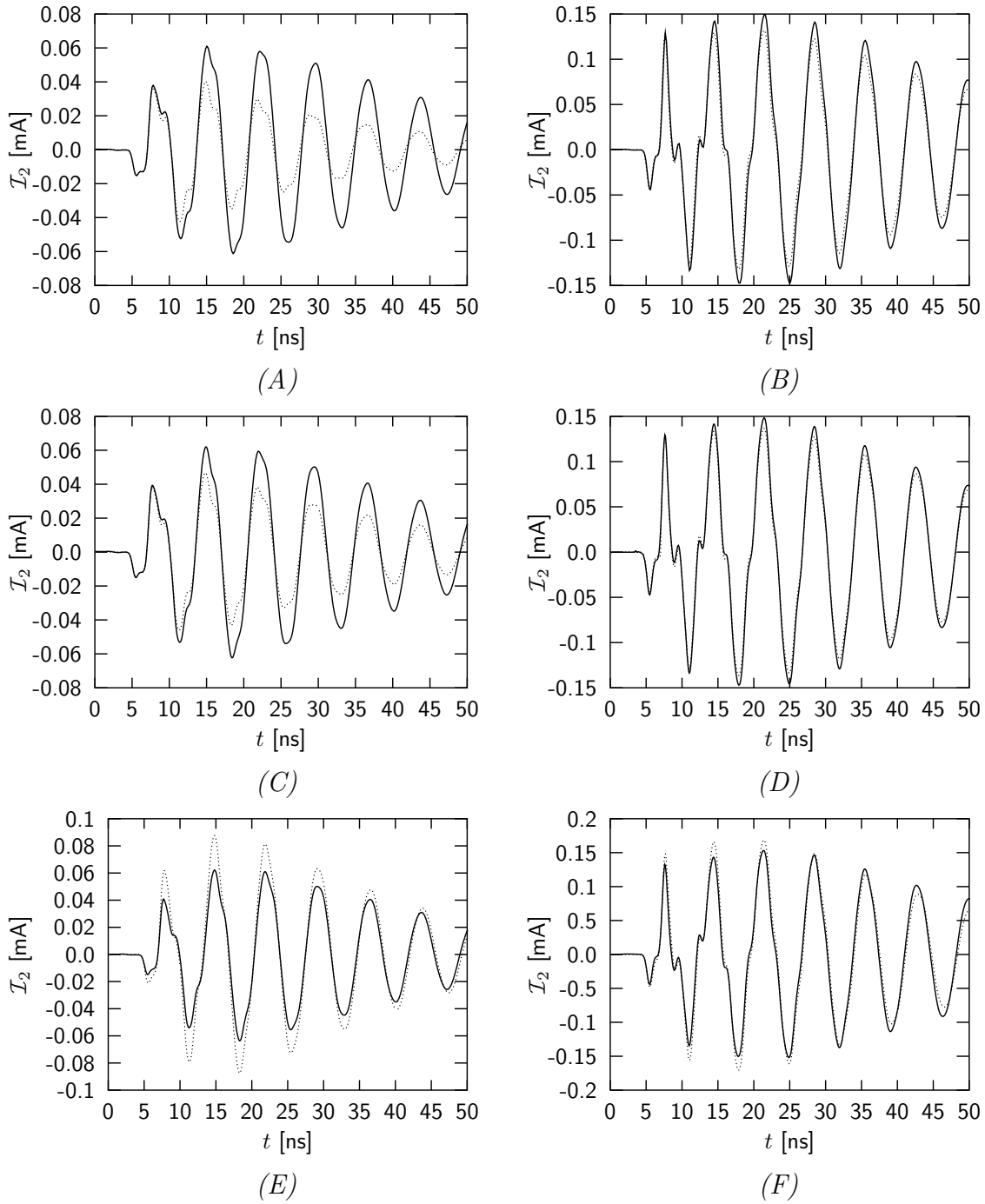
Figure 4.14: *The induced current at the center of wire 2 with length $L = 1$ m and radius $a = 0.002$ m. The distance is $d = 1$ m, the depth of wire 3 is $z_2 = 0.1$ m. The height of wires 1 and 2 is $z_1 = -0.1$ m for plots (A), (C) and (E) and $z_1 = -0.25$ m for plots (B), (D) and (F). The medium parameters are $\epsilon_{1r} = 1$, $\sigma_1 = 0$, $\epsilon_{2r} = 9$ and $\sigma_2 = 0$ for (A) and (B), $\sigma_2 = 0.01$ S/m for (C) and (D) and $\sigma_2 = 0.03$ S/m for (E) and (F). The permeability is μ_0 for all configurations. The excitation is a Gaussian voltage pulse with $\tau = 0.5$ ns and $t_1 = 4\tau$. The solid lines represent "with wire 3" and the dotted lines represent "without wire 3".*
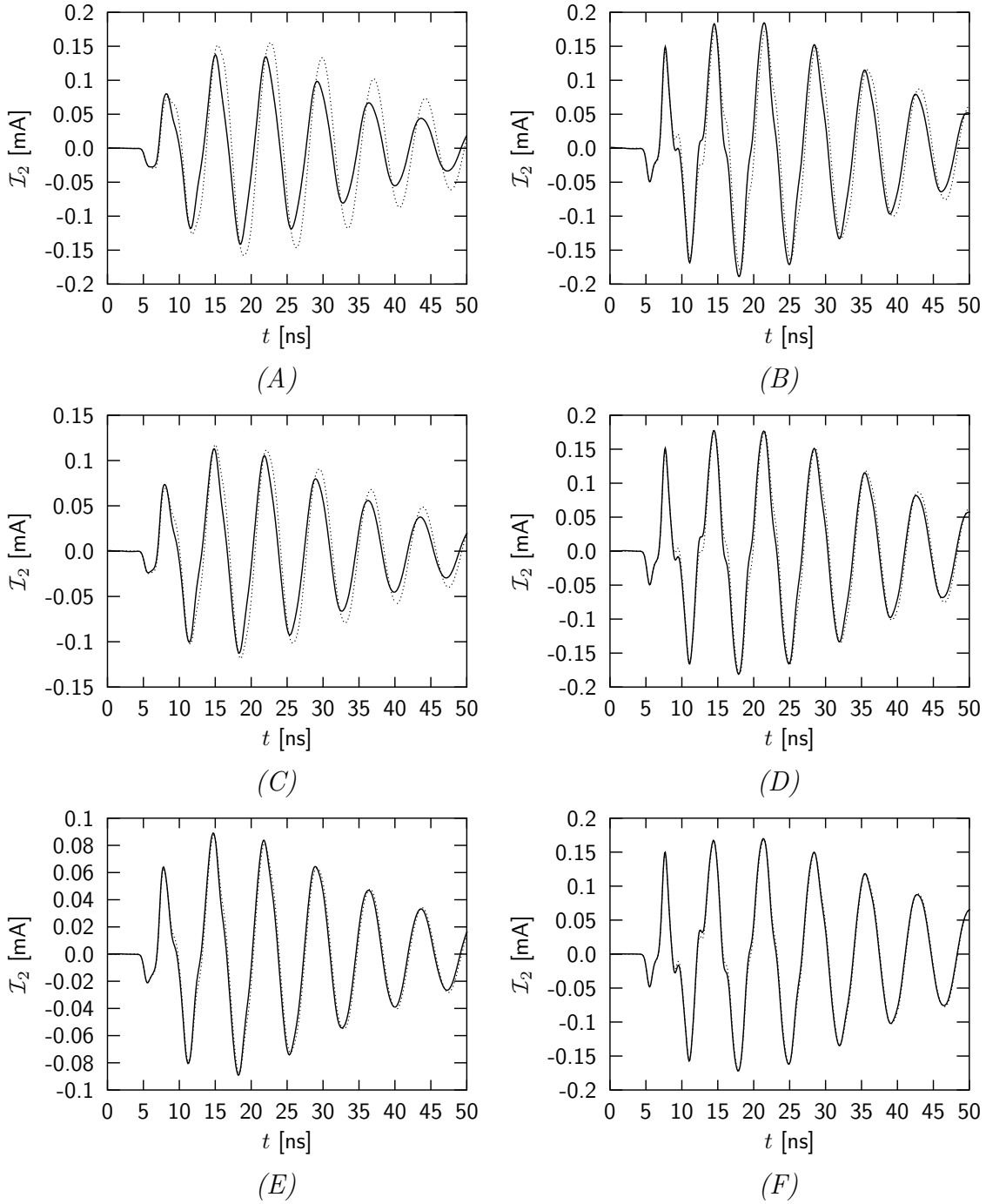
Figure 4.15: *The induced current at the center of wire 2 with length $L = 1$ m and radius $a = 0.002$ m. The distance is $d = 1$ m, the depth of wire 3 is $z_2 = 0.1$ m. The height of wires 1 and 2 is $z_1 = -0.1$ m for plots (A), (C) and (E) and $z_1 = -0.25$ m for plots (B), (D) and (F). The medium parameters are $\epsilon_{1r} = 1$, $\sigma_1 = 0$, $\epsilon_{2r} = 3$ and $\sigma_2 = 0$ for (A) and (B), $\sigma_2 = 0.01$ S/m for (C) and (D) and $\sigma_2 = 0.03$ S/m for (E) and (F). The permeability is μ_0 for all configurations. The excitation is a Gaussian voltage pulse with $\tau = 0.5$ ns and $t_1 = 4\tau$. The solid lines represent "with wire 3" and the dotted lines represent "without wire 3".*

and $z_1 = -0.25$ m, respectively, is visualized in Figure 4.15. In general, the presence of a buried wire cannot be distinguished easily from the current along wire 2. For increasing conductivity σ_2, the effect of wire 3 on the current along wire 2 decreases. For $\sigma_2 = 0.03$ S/m, the presence of wire 3 can no longer be observed any more.

To conclude this chapter, the different electric fields contributing to the incident field term in Hallén's equation for wire 2 are plotted in Figure 4.16. The incident field term is given by

$$\mathcal{E}_x^{i,2} = \mathcal{E}_x^{d,1} + \mathcal{E}_x^{r,1} + \mathcal{E}_x^{r,2} + \mathcal{E}_x^{t,3}.$$

Since a wire antenna radiates stronger near the end faces of the wire, the end face at $\mathbf{r} = d\mathbf{u}_y + z_1\mathbf{u}_z$ is chosen as the point of observation. The wires in the configuration are the same as in previous examples. The medium parameters are $\epsilon_{1r} = 1, \sigma_1 = 0, \sigma_2 = 0$ and $\mu_1 = \mu_2 = \mu_0$ for $\epsilon_{2r} = 9$ (A) and (B) and $\epsilon_{2r} = 3$ (C) and (D). The height is $z_1 = -0.1$ m and the depth is again $z_2 = 0.1$ m. It is observed from (A) and (C), which are both responses from wire 1, that the direct field $\mathcal{E}_x^{d,1}$ is almost the same. The reflected field in (A) is larger than in (C), as could be expected from the larger reflection coefficient in (A). It is interesting to see that the direct field and the reflected field at the interface from wire 1 in (A) have almost the same magnitude but are of opposite sign for $t > 10$ ns. In (C), the reflected field is still of opposite sign but not of the same magnitude anymore for $t > 10$ ns. The direct contribution will therefore be more dominant when $\epsilon_{2r} = 3$. This was already observed in previous examples. From (B) and (D), it is observed that the reflected field at the interface from wire 2 is smaller for $\epsilon_{2r} = 9$. This is due to the smaller initial current along wire 2. Furthermore, it is observed that the transmitted field from wire 3 is much smaller for $\epsilon_{2r} = 9$. From the electric fields in Figure 4.16, it can be concluded that the contribution from wire 1 to wire 2 is smaller for a larger permittivity. The reflected field from wire 2 and the transmitted field from wire 3 are smaller for increasing permittivity. The improved visibility of the buried wire for $\epsilon_{2r} = 9$ comes from the fact that the contribution of wire 1 is smaller for increasing permittivity.

In general, it is observed that the buried wire cannot be detected from the shape of the current directly. This is due to the mutual coupling between wire 1 and wire 2. The strong mutual coupling is a direct effect of the oscillatory behavior of the currents along both wires. This oscillating behavior is the result from the traveling-wave nature of the current. If the height z_1 is small, the amplitude of the current along wire 2 due to the presence of wire 3 changes. For larger distances z_1, a difference in amplitude can no longer be observed directly. Of course, a number of standard signal processing tools exist to enhance the output signal of wire 2 for detection purposes. In Chapters 6 and 7, two techniques
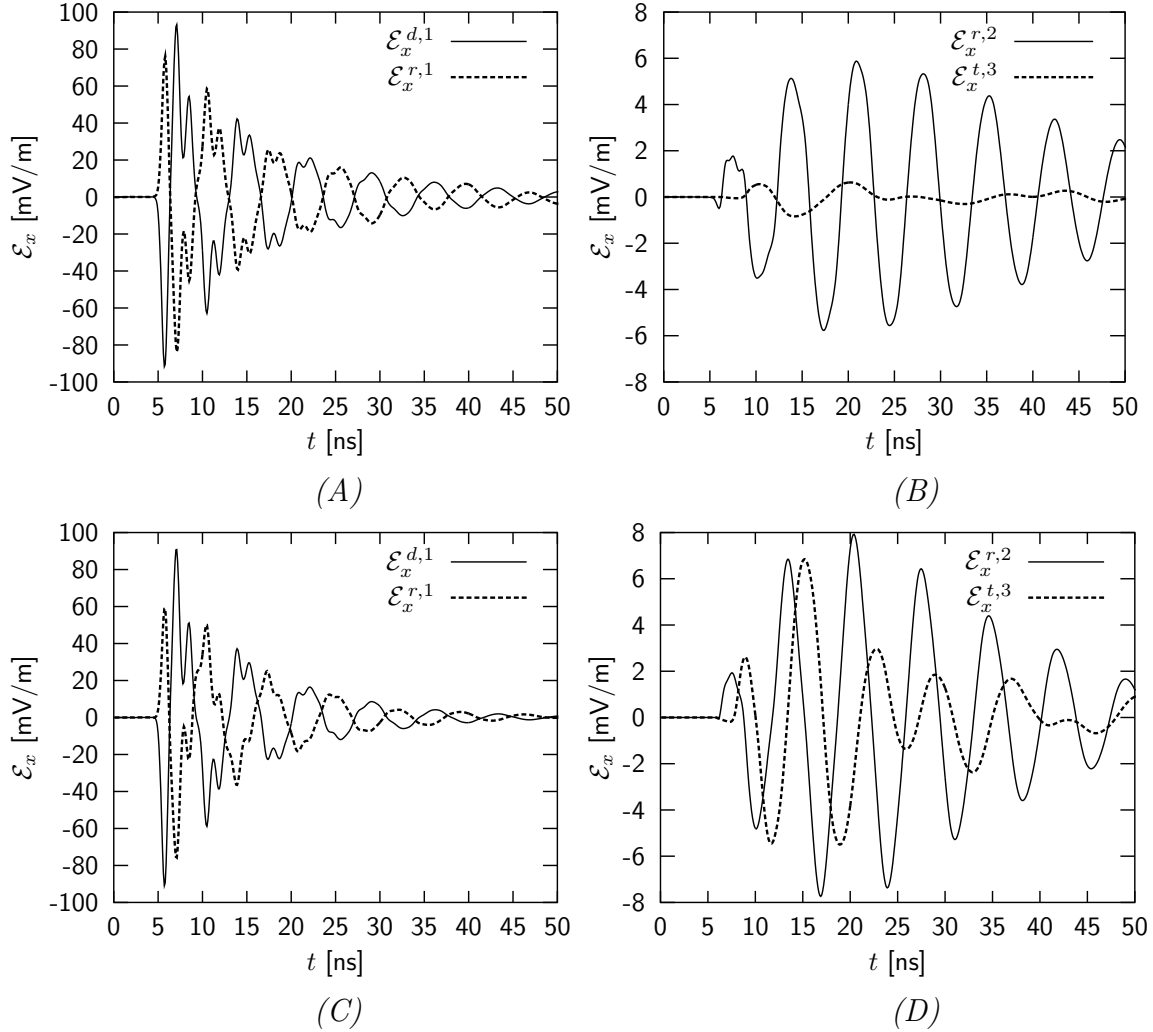
Figure 4.16: *The electric field strengths originating from the various wires in the configuration incident on wire 2 at position* $\mathbf{r} = d\mathbf{u}_y + z_1\mathbf{u}_z$. *The wires are of length* $L = 1$ *m and have a radius* $a = 0.002$ *m. The height and depth are* $z_1 = -0.1$ *m and* $z_2 = 0.1$ *m, respectively. The medium parameters are* $\epsilon_{1r} = 1, \sigma_1 = \sigma_2 = 0$ *and* $\epsilon_{2r} = 9$ *for (A) and (B) and* $\epsilon_{2r} = 3$ *for (C) and (D).*

are introduced to eventually enhance the detection.

4.4   Computation times

At the end of this chapter, the computation times from a few configurations from previous sections are gathered. The configurations consist of one, two and three wires. All wires are of length $L = 1$ m and have radius $a = 0.002$ m. The excitation is again the Gaussian

voltage pulse specified in Section 3.3.2.

The single wire is embedded in free space (FS) and in a configuration with two half spaces. The lower half space has a relative permittivity of $\epsilon_{2r} = 3$ and $\epsilon_{2r} = 9$, respectively. The other material parameters are equal to those of free space. The height of the wire is $z_1 = -0.1$ m.

In the configuration with two wires, the embedding is free space (FS) and a configuration with two half spaces. The lower half space has a relative permittivity of $\epsilon_{2r} = 3$ and $\epsilon_{2r} = 9$, respectively. The other material parameters are equal to those of free space. The height of both wires is $z_1 = -0.1$ m. The distance between the wires is $d = 1$ m.

In the case where 3 wires are considered, the embedding is a configuration with two half spaces. The lower half space has a relative permittivity of $\epsilon_{2r} = 3$ and $\epsilon_{2r} = 9$, respectively. Wire 1 and 2 are located in the upper half space at a height $z_1 = -0.1$ m. The third wire is a buried wire and is located at a depth of $z_2 = 0.1$ m. The distance between wire 1 and wire 2 is $d = 1$ m and the distance between wire 1 and wire 3 in the y-direction is $d_2 = d/2 = 0.5$ m.

The computation times that have been recorded are the total computation time t_{tot} and the time to calculate the spectral integral involved with the reflected and transmitted field terms t_{spec}. The number of time steps for which all calculations were done are $N = 1024$, $N = 2048$ and $N = 4096$, respectively. The computation times refer to a personal computer with an AMD Athlon 1800 processor and 512 MBytes DDR266 memory. The results are tabulated in Table 4.2

From the column FS in Table 4.2 it can be concluded that adding a wire to the configuration results in $2\sqrt{2}$ times the computation time for each value of N. This is expected from the use of CGFFT. Increasing the number of time steps with a factor of two and four, respectively, results in an increase of t_{tot} approximately with the same factor. In general, for one and two wires it is observed that the calculation of the spectral integral is more time consuming than the actual calculation of the currents along the wires. In the case where three wires are embedded in a half space configuration, this is only partly true. Depending on the permittivity, the spectral integral is the dominant factor in the calculation. Here, for $\epsilon_{2r} = 3$, the spectral integral is dominant in t_{tot} while for $\epsilon_{2r} = 9$ it is not.

		FS	$\epsilon_{2r} = 3$		$\epsilon_{2r}=9$	
N	# of wires	t_{tot} [s]	t_{spec} [s]	t_{tot} [s]	t_{spec} [s]	t_{tot} [s]
	1	1.28	6.96	8.45	7.29	8.85
1024	2	3.50	17.14	21.47	17.46	21.70
	3	NA	44.82	71.90	47.18	97.62
	1	2.56	14.16	17.51	14.38	17.57
2048	2	7.06	35.16	43.61	34.82	43.49
	3	NA	89.93	144.77	92.73	194.40
	1	5.11	28.14	34.90	28.91	35.41
4096	2	14.14	69.90	86.63	70.06	87.15
	3	NA	179.92	289.31	181.12	380.70

Table 4.2: *CPU times for the spectral integral and the total computation time. The timings are considered for 1, 2 and 3 wires. The relative permittivities of the lower half space are free space (FS), $\epsilon_{2r} = 3$ and $\epsilon_{2r} = 9$, respectively. The number of time steps is $N = 1024$, $N = 2048$ and $N = 4096$, respectively. The free space situation is not available (NA) for configurations with 3 wires.*

Chapter 5

Wires with arbitrary orientation and length

In previous chapters, coupled integral equations were derived for several configurations to describe the currents along the wires in the respective cases. The configurations, so far, were restricted to parallel wires of equal length. To dispose of extra parameters for optimizing the detection of a buried wire, it is interesting to study configurations with wires of arbitrary length and arbitrary orientation with respect to a reference coordinate system.

In this section, rotated and translated coordinate systems with respect to a reference coordinate system will be introduced. Subsequently, Hallén's equation for a single thin wire pointing in the x-direction of an arbitrary coordinate system is subjected to this transformation. All transformations are considered with respect to the reference coordinate system $(\mathbf{O}_r, \mathbf{u}_{x_r}, \mathbf{u}_{y_r}, \mathbf{u}_{z_r})$. A wire can thus be arbitrarily positioned in space. If in the new coordinate system the wire is oriented along the x-axis, only the pertaining incident field term needs to be considered.

Next, the coupling between two, now arbitrarily oriented, wires in free space is studied again. This coupling exists because the radiated field of one wire may be regarded as a part of the incident field on the other wire. When the radiated field is also written in terms of the reference coordinate system, mutual coupling can be described.

The organization of this chapter is as follows. First, the transformation from the reference coordinate system to an arbitrary coordinate system and vice versa is introduced. Next, the transformation is applied to Hallén's equation for a single thin wire and a transformation is applied to Hallén's equation for a second thin wire in another arbitrary coordinate system. With these three steps, wires can be arbitrarily positioned with respect to a reference

coordinate system.

5.1   Coordinate transformations

The currents along a set of straight wires are coupled via the radiated field and the incident-field term in Hallén's equation pertaining to each wire. As described earlier, for an arbitrarily oriented wire as in Figure 5.1, the incident-field term in coordinate system $(\mathbf{O}_1, \mathbf{u}_{x_1}, \mathbf{u}_{y_1}, \mathbf{u}_{z_1})$ is transformed to the reference system. In a later stage, the currents along other wires can be related to the current along the wire displayed in Figure 5.1. Before the
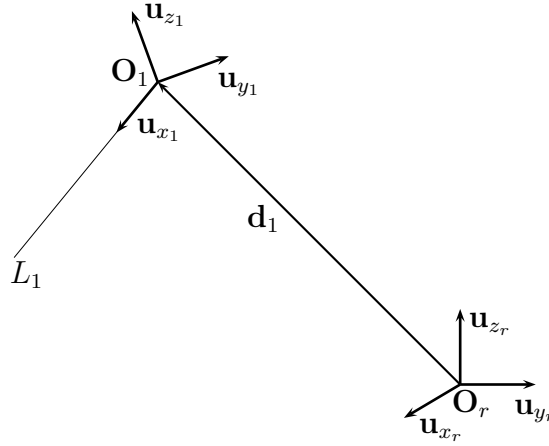
Figure 5.1:   *An arbitrarily oriented thin wire with respect to the reference system* $(\mathbf{O}_r, \mathbf{u}_{x_r}, \mathbf{u}_{y_r}, \mathbf{u}_{z_r})$.

incident field term is transformed to the reference system for every point along the wire, first an arbitrary point $\mathbf{r} = x_1\mathbf{u}_{x_1} + y_1\mathbf{u}_{y_1} + z_1\mathbf{u}_{z_1}$ in coordinate system $(\mathbf{O}_1, \mathbf{u}_{x_1}, \mathbf{u}_{y_1}, \mathbf{u}_{z_1})$ will be expressed in terms of the unit vectors of the reference system $(\mathbf{O}_r, \mathbf{u}_{x_r}, \mathbf{u}_{y_r}, \mathbf{u}_{z_r})$. The transformation involves the following steps.

(A) Translation of the system $(\mathbf{O}_r, \mathbf{u}_{x_r}, \mathbf{u}_{y_r}, \mathbf{u}_{z_r})$ over a displacement vector $\mathbf{d}_1$ resulting in $\left(\mathbf{O}_1, \mathbf{u}_x^{(1)}, \mathbf{u}_y^{(1)}, \mathbf{u}_z^{(1)}\right)$.

(B) Rotation of $\left(\mathbf{O}_1, \mathbf{u}_x^{(1)}, \mathbf{u}_y^{(1)}, \mathbf{u}_z^{(1)}\right)$ around the z-axis over an angle ϕ_1 resulting in $\left(\mathbf{O}_1, \mathbf{u}_x^{(2)}, \mathbf{u}_y^{(2)}, \mathbf{u}_z^{(2)}\right)$.

(C) Rotation of system $\left(\mathbf{O}_1, \mathbf{u}_x^{(2)}, \mathbf{u}_y^{(2)}, \mathbf{u}_z^{(2)}\right)$ around the y-axis over a second angle θ_1 resulting in $(\mathbf{O}_1, \mathbf{u}_{x_1}, \mathbf{u}_{y_1}, \mathbf{u}_{z_1})$.

In Figure 5.2, each step is visualized. The extra superscripts (1) and (2) indicate that the first and the second step have been carried out, respectively. The two intermediate coordinate systems are only introduced for the derivation of the transformation. Note that
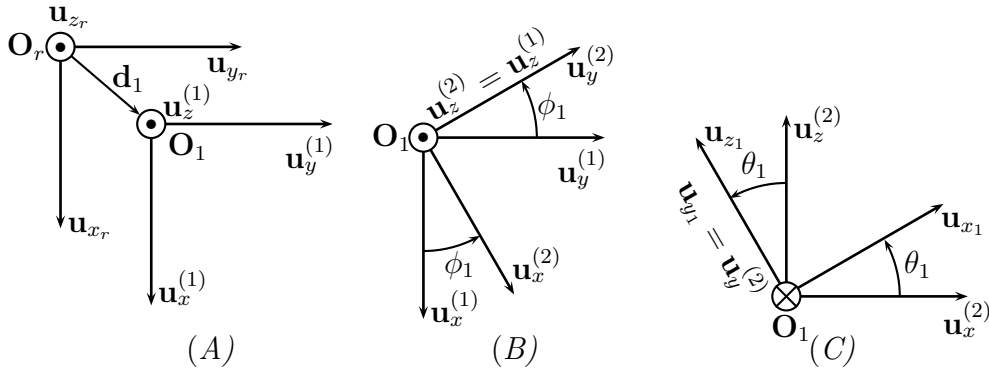
Figure 5.2: *Translation over $\mathbf{d}_1$ (A), rotation over ϕ_1 around the z-axis (B), and rotation over θ_1 around the y-axis (C), respectively.*

the subscript 1 refers to coordinate system 1.

An arbitrary vector $\mathbf{r}$ can be written as

$$
\begin{aligned}
\mathbf{r} &= x_r\mathbf{u}_{x_r} + y_r\mathbf{u}_{y_r} + z_r\mathbf{u}_{z_r} = x^{(1)}\mathbf{u}_x^{(1)} + y^{(1)}\mathbf{u}_y^{(1)} + z^{(1)}\mathbf{u}_z^{(1)} \\
&= x^{(2)}\mathbf{u}_x^{(2)} + y^{(2)}\mathbf{u}_y^{(2)} + z^{(2)}\mathbf{u}_z^{(2)} = x_1\mathbf{u}_{x_1} + y_1\mathbf{u}_{y_1} + z_1\mathbf{u}_{z_1}.
\end{aligned} \tag{5.1}
$$

The derivation of the transformation formulas is carried out by composition of at most three individual steps whose mathematical description is given below.

The transformation of the reference system to system 1 is then as follows

(A) Translation over $\mathbf{d}_1 = d_{1x}\mathbf{u}_{x_r} + d_{1y}\mathbf{u}_{y_r} + d_{1z}\mathbf{u}_{z_r}$:

$$
\mathbf{r} = x_r\mathbf{u}_{x_r} + y_r\mathbf{u}_{y_r} + z_r\mathbf{u}_{z_r} = x^{(1)}\mathbf{u}_x^{(1)} + y^{(1)}\mathbf{u}_y^{(1)} + z^{(1)}\mathbf{u}_z^{(1)}, \tag{5.2}
$$

with

$$
\begin{pmatrix} x^{(1)} \\ y^{(1)} \\ z^{(1)} \end{pmatrix} = \begin{pmatrix} x_r \\ y_r \\ z_r \end{pmatrix} - \begin{pmatrix} d_{1x} \\ d_{1y} \\ d_{1z} \end{pmatrix}, \quad \text{and} \quad \begin{pmatrix} \mathbf{u}_x^{(1)} \\ \mathbf{u}_y^{(1)} \\ \mathbf{u}_z^{(1)} \end{pmatrix} = \begin{pmatrix} \mathbf{u}_{x_r} \\ \mathbf{u}_{y_r} \\ \mathbf{u}_{z_r} \end{pmatrix}. \tag{5.3}
$$

(B) Rotation around the z-axis over ϕ_1:

$$
\mathbf{r} = x^{(1)}\mathbf{u}_x^{(1)} + y^{(1)}\mathbf{u}_y^{(1)} + z^{(1)}\mathbf{u}_z^{(1)} = x^{(2)}\mathbf{u}_x^{(2)} + y^{(2)}\mathbf{u}_y^{(2)} + z^{(2)}\mathbf{u}_z^{(2)}, \tag{5.4}
$$

with

$$\begin{pmatrix} x^{(2)} \\ y^{(2)} \\ z^{(2)} \end{pmatrix} = \underline{\mathbf{T}}^{(1)} \begin{pmatrix} x^{(1)} \\ y^{(1)} \\ z^{(1)} \end{pmatrix}, \quad \begin{pmatrix} \mathbf{u}_x^{(2)} \\ \mathbf{u}_y^{(2)} \\ \mathbf{u}_z^{(2)} \end{pmatrix} = \underline{\mathbf{T}}^{(1)} \begin{pmatrix} \mathbf{u}_x^{(1)} \\ \mathbf{u}_y^{(1)} \\ \mathbf{u}_z^{(1)} \end{pmatrix}, \tag{5.5}$$

$$\text{and} \quad \underline{\mathbf{T}}^{(1)} = \begin{pmatrix} \cos\phi_1 & \sin\phi_1 & 0 \\ -\sin\phi_1 & \cos\phi_1 & 0 \\ 0 & 0 & 1 \end{pmatrix}.$$

(C) Rotation around the y-axis over θ_1:

$$\mathbf{r} = x^{(2)}\mathbf{u}_x^{(2)} + y^{(2)}\mathbf{u}_y^{(2)} + z^{(2)}\mathbf{u}_z^{(2)} = x_1\mathbf{u}_{x_1} + y_1\mathbf{u}_{y_1} + z_1\mathbf{u}_{z_1}, \tag{5.6}$$

with

$$\begin{pmatrix} x_1 \\ y_1 \\ z_1 \end{pmatrix} = \underline{\mathbf{T}}^{(2)} \begin{pmatrix} x^{(2)} \\ y^{(2)} \\ z^{(2)} \end{pmatrix}, \quad \begin{pmatrix} \mathbf{u}_{x_1} \\ \mathbf{u}_{y_1} \\ \mathbf{u}_{z_1} \end{pmatrix} = \underline{\mathbf{T}}^{(2)} \begin{pmatrix} \mathbf{u}_x^{(2)} \\ \mathbf{u}_y^{(2)} \\ \mathbf{u}_z^{(2)} \end{pmatrix}, \tag{5.7}$$

$$\text{and} \quad \underline{\mathbf{T}}^{(2)} = \begin{pmatrix} \cos\theta_1 & 0 & \sin\theta_1 \\ 0 & 1 & 0 \\ -\sin\theta_1 & 0 & \cos\theta_1 \end{pmatrix}.$$

With these three steps the following composed transformation formula from the reference system to coordinate system 1 can be constructed:

$$\begin{pmatrix} x_1 \\ y_1 \\ z_1 \end{pmatrix} = \underline{\mathbf{T}}^{(2)} \begin{pmatrix} x^{(2)} \\ y^{(2)} \\ z^{(2)} \end{pmatrix} = \underline{\mathbf{T}}^{(2)} \cdot \underline{\mathbf{T}}^{(1)} \begin{pmatrix} x^{(1)} \\ y^{(1)} \\ z^{(1)} \end{pmatrix} = \underline{\mathbf{T}}_1 \left[\begin{pmatrix} x_r \\ y_r \\ z_r \end{pmatrix} - \begin{pmatrix} d_{1x} \\ d_{1y} \\ d_{1z} \end{pmatrix} \right], \tag{5.8}$$

and

$$\begin{pmatrix} \mathbf{u}_{x_1} \\ \mathbf{u}_{y_1} \\ \mathbf{u}_{z_1} \end{pmatrix} = \underline{\mathbf{T}}_1 \begin{pmatrix} \mathbf{u}_{x_r} \\ \mathbf{u}_{y_r} \\ \mathbf{u}_{z_r} \end{pmatrix}, \tag{5.9}$$

with

$$\underline{\mathbf{T}}_1 = \underline{\mathbf{T}}^{(2)} \cdot \underline{\mathbf{T}}^{(1)} = \begin{pmatrix} \cos\phi_1\cos\theta_1 & \sin\phi_1\cos\theta_1 & \sin\theta_1 \\ -\sin\phi_1 & \cos\phi_1 & 0 \\ -\cos\phi_1\sin\theta_1 & -\sin\phi_1\sin\theta_1 & \cos\theta_1 \end{pmatrix}. \tag{5.10}$$

Because $\underline{\mathbf{T}}_1\underline{\mathbf{T}}_1^T = \mathbf{I}$, the transformation matrix $\underline{\mathbf{T}}_1$ is orthogonal and hence the inverse transformation matrix can be written as

$$\underline{\mathbf{T}}_1^{-1} = \underline{\mathbf{T}}_1^T = \begin{pmatrix} \cos\phi_1\cos\theta_1 & -\sin\phi_1 & -\cos\phi_1\sin\theta_1 \\ \sin\phi_1\cos\theta_1 & \cos\phi_1 & -\sin\phi_1\sin\theta_1 \\ \sin\theta_1 & 0 & \cos\theta_1 \end{pmatrix}, \tag{5.11}$$

where the superscript T stands for "transposed" [56, page 39]. The transformation from coordinate system $(\mathbf{O}_1, \mathbf{u}_{x_1}, \mathbf{u}_{y_1}, \mathbf{u}_{z_1})$ to the reference system is found as

$$\begin{pmatrix} x_r \\ y_r \\ z_r \end{pmatrix} = \underline{\mathbf{T}}_1^T \begin{pmatrix} x_1 \\ y_1 \\ z_1 \end{pmatrix} + \begin{pmatrix} d_{1x} \\ d_{1y} \\ d_{1z} \end{pmatrix}, \quad \begin{pmatrix} \mathbf{u}_{x_r} \\ \mathbf{u}_{y_r} \\ \mathbf{u}_{z_r} \end{pmatrix} = \underline{\mathbf{T}}_1^T \begin{pmatrix} \mathbf{u}_{x_1} \\ \mathbf{u}_{y_1} \\ \mathbf{u}_{z_1} \end{pmatrix} \tag{5.12}$$

The subscript 1 in the transformation matrix indicates that the transformation pertains to coordinate system 1. Since all transformations are from and to the reference coordinate system, no extra indication is made. In general, a transformation from coordinate system $n = 1, 2, \ldots$ to the reference system is described by a transformation matrix $\underline{\mathbf{T}}_n$ and a translation vector $\mathbf{d}_n$. Note that the components of the vector $\mathbf{d}_n$ are found with respect to the reference coordinate system.

5.2   Transformation of the incident-field term in Hallén's equation

With the coordinate transformations that are found, the electric field in a certain coordinate system can be transformed to the reference system and vice versa. Once the transformed electric field from a coordinate system is known in the reference system, the transformation to a second coordinate system can be carried out. If these electric fields originate from wire antennas, the mutual coupling between wires, each in their own coordinate system, can be described.

In terms of the notation of previous chapters, the radiated electric field originating from a wire antenna will be referred to as the direct field $\mathbf{E}^d(\mathbf{r})$ of a wire.

The transformation as described in the previous section will be applied to the incident field term in Hallén's equation for a thin wire in coordinate system 1 and length L_1, see Figure 5.1.

The incident field term at position $\mathbf{r}$ can be written as

$$E_{x_1}^i(\mathbf{r})\mathbf{u}_{x_1} + E_{y_1}^i(\mathbf{r})\mathbf{u}_{y_1} + E_{z_1}^i(\mathbf{r})\mathbf{u}_{z_1} = E_{x_r}^i(\mathbf{r})\mathbf{u}_{x_r} + E_{y_r}^i(\mathbf{r})\mathbf{u}_{y_r} + E_{z_r}^i(\mathbf{r})\mathbf{u}_{z_r}, \tag{5.13}$$

with

$$\mathbf{r} = x_1\mathbf{u}_{x_1} + y_1\mathbf{u}_{y_1} + z_1\mathbf{u}_{z_1} = x_r\mathbf{u}_{x_r} + y_r\mathbf{u}_{y_r} + z_r\mathbf{u}_{z_r}. \tag{5.14}$$

The position $\mathbf{r}$ can be described in terms of the reference system as well as in terms of coordinate system 1 as was shown earlier. For the incident electric field vector, the transformation is limited to the orientation and magnitude of the three field components. The value of the field vector is already determined by the position $\mathbf{r}$ which is a parameter of the incident electric field. This can be easily shown by introducing the start and end points of the incident field vector as

$$\mathbf{p} = (p_{x_1}, p_{y_1}, p_{z_1}) \begin{pmatrix} \mathbf{u}_{x_1} \\ \mathbf{u}_{y_1} \\ \mathbf{u}_{z_1} \end{pmatrix} = (p_{x_r}, p_{y_r}, p_{z_r}) \begin{pmatrix} \mathbf{u}_{x_r} \\ \mathbf{u}_{y_r} \\ \mathbf{u}_{z_r} \end{pmatrix}, \tag{5.15}$$

$$\mathbf{q} = (q_{x_1}, q_{y_1}, q_{z_1}) \begin{pmatrix} \mathbf{u}_{x_1} \\ \mathbf{u}_{y_1} \\ \mathbf{u}_{z_1} \end{pmatrix} = (q_{x_r}, q_{y_r}, q_{z_r}) \begin{pmatrix} \mathbf{u}_{x_r} \\ \mathbf{u}_{y_r} \\ \mathbf{u}_{z_r} \end{pmatrix}, \tag{5.16}$$

respectively. The incident field vector as such is then defined by $\mathbf{q} - \mathbf{p}$. When the coordinate transformation is carried out on the right-hand sides of (5.15) and (5.16) as follows

$$\begin{pmatrix} p_{x_r} \\ p_{y_r} \\ p_{z_r} \end{pmatrix} = \mathbf{\underline{T}}_1^T \begin{pmatrix} p_{x_1} \\ p_{y_1} \\ p_{z_1} \end{pmatrix} + \begin{pmatrix} d_{1x} \\ d_{1y} \\ d_{1z} \end{pmatrix}, \quad \begin{pmatrix} q_{x_r} \\ q_{y_r} \\ q_{z_r} \end{pmatrix} = \mathbf{\underline{T}}_1^T \begin{pmatrix} q_{x_1} \\ q_{y_1} \\ q_{z_1} \end{pmatrix} + \begin{pmatrix} d_{1x} \\ d_{1y} \\ d_{1z} \end{pmatrix},$$

$$\text{and} \quad \begin{pmatrix} \mathbf{u}_{x_r} \\ \mathbf{u}_{y_r} \\ \mathbf{u}_{z_r} \end{pmatrix} = \mathbf{\underline{T}}_1 \begin{pmatrix} \mathbf{u}_{x_1} \\ \mathbf{u}_{y_1} \\ \mathbf{u}_{z_1} \end{pmatrix}, \tag{5.17}$$

it is seen that the translation vector $\mathbf{d}_1$ cancels in the subtraction $\mathbf{q} - \mathbf{p}$. Hence, the translation has no effect in the transformation of a field vector.

With this result, the transformation of the incident electric field term in Hallén's equation from the reference system to system 1 is found as

$$\left(E_{x_1}^i(\mathbf{r}), E_{y_1}^i(\mathbf{r}), E_{z_1}^i(\mathbf{r}) \right) \begin{pmatrix} \mathbf{u}_{x_1} \\ \mathbf{u}_{y_1} \\ \mathbf{u}_{z_1} \end{pmatrix} = \left(E_{x_r}^i(\mathbf{r}), E_{y_r}^i(\mathbf{r}), E_{z_r}^i(\mathbf{r}) \right) \begin{pmatrix} \mathbf{u}_{x_r} \\ \mathbf{u}_{y_r} \\ \mathbf{u}_{z_r} \end{pmatrix}, \tag{5.18}$$

with

$$
\begin{pmatrix} x_r \\ y_r \\ z_r \end{pmatrix} = \underline{\mathbf{T}}_1^T \begin{pmatrix} x_1 \\ y_1 \\ z_1 \end{pmatrix} + \begin{pmatrix} d_{1x} \\ d_{1y} \\ d_{1z} \end{pmatrix}, \quad \begin{pmatrix} E_{x_r}^i \\ E_{y_r}^i \\ E_{z_r}^i \end{pmatrix} = \underline{\mathbf{T}}_1^T \begin{pmatrix} E_{x_1}^i \\ E_{y_1}^i \\ E_{z_1}^i \end{pmatrix},
$$

$$
\text{and} \quad \begin{pmatrix} \mathbf{u}_{x_r} \\ \mathbf{u}_{y_r} \\ \mathbf{u}_{z_r} \end{pmatrix} = \underline{\mathbf{T}}_1^T \begin{pmatrix} \mathbf{u}_{x_1} \\ \mathbf{u}_{y_1} \\ \mathbf{u}_{z_1} \end{pmatrix}. \tag{5.19}
$$

What remains is to write the electric field in the reference system in terms of the electric field in system 1. With the incident field term as defined in (5.18), the transformation from system 1 to the reference system is determined by

$$
\begin{pmatrix} x_1 \\ y_1 \\ z_1 \end{pmatrix} = \underline{\mathbf{T}}_1 \left[\begin{pmatrix} x_r \\ y_r \\ z_r \end{pmatrix} - \begin{pmatrix} d_{1x} \\ d_{1y} \\ d_{1z} \end{pmatrix} \right], \quad \begin{pmatrix} E_{x_1}^i \\ E_{y_1}^i \\ E_{z_1}^i \end{pmatrix} = \underline{\mathbf{T}}_1 \begin{pmatrix} E_{x_r}^i \\ E_{y_r}^i \\ E_{z_r}^i \end{pmatrix},
$$

$$
\text{and} \quad \begin{pmatrix} \mathbf{u}_{x_1} \\ \mathbf{u}_{y_1} \\ \mathbf{u}_{z_1} \end{pmatrix} = \underline{\mathbf{T}}_1 \begin{pmatrix} \mathbf{u}_{x_r} \\ \mathbf{u}_{y_r} \\ \mathbf{u}_{z_r} \end{pmatrix}. \tag{5.20}
$$

In the previous chapter, a special form of Hallén's equation is used to describe the mutual coupling between two wires. In this equation, the wires have to be kept parallel to each other. Since the wires may now be arbitrarily oriented, an extension of this special form is needed.

In the next section, the electric field from an electric point dipole will be derived in the frequency domain. The result can then be used to find an expression for the direct field of a wire. This direct field is used to describe the mutual coupling between two wires.

5.3 The electric field of a line current in a homogeneous medium

To determine the direct field of a thin wire, first the electric field of a line current is considered. With the result obtained in this section and superposition, the direct field from a wire can be described.

An electric current source $\mathbf{J}_1$ is located in a homogeneous medium with complex permittivity ε_1 and permeability μ_1. The source only differs from zero inside a bounded volume $\mathcal{D}$. The subscript 1 refers to an arbitrary coordinate system 1.

According to (2.21) and (2.22), Maxwell's equations in the frequency domain are given by

$$\nabla \times \mathbf{E} - i\omega\mu_1\mathbf{H} = \mathbf{0}, \tag{5.21}$$

$$\nabla \times \mathbf{H} + i\omega\varepsilon_1\mathbf{E} = \mathbf{J}_1. \tag{5.22}$$

The first equation yields $\nabla \cdot \mathbf{H} = 0$ provided that $\omega \neq 0$, i.e., that static fields are excluded. This result implies that the solution for $\mathbf{H}$ can be written as

$$\mathbf{H} = \nabla \times \mathbf{A}_m, \tag{5.23}$$

where $\mathbf{A}_m$ is the magnetic vector potential. Substituting the magnetic vector potential (5.23) in (5.21) gives

$$\nabla \times (\mathbf{E} - i\omega\mu_1\mathbf{A}_m) = \mathbf{0}. \tag{5.24}$$

From (5.24), it follows that an arbitrary electric scalar potential Φ exists and that the electric field can be written as

$$\mathbf{E} = i\omega\mu_1\mathbf{A}_m + \nabla\Phi. \tag{5.25}$$

Substituting (5.25) and (5.23) in (5.22) yields

$$\nabla \times (\nabla \times \mathbf{A}_m) - k_1^2\mathbf{A}_m + i\omega\varepsilon_1\nabla\Phi = \mathbf{J}_1, \tag{5.26}$$

where $k_1 = \omega\sqrt{\varepsilon_1\mu_1}$. After substitution of $\nabla \times (\nabla \times \mathbf{A}_m) = \nabla(\nabla \cdot \mathbf{A}_m) - \nabla^2\mathbf{A}_m$ in (5.26) and choosing

$$\nabla \cdot \mathbf{A}_m = -i\omega\varepsilon_1\Phi, \tag{5.27}$$

the following equation for the magnetic vector potential is found:

$$\left(\nabla^2 + k_1^2\right)\mathbf{A}_m = -\mathbf{J}_1. \tag{5.28}$$

The solution for the magnetic vector potential should satisfy the radiation conditions. These radiation conditions imply that the solution must decay to zero or represent outgoing waves when $|\mathbf{r}| \to \infty$. The magnetic vector potential is readily found as

$$\mathbf{A}_m(\mathbf{r},\omega) = \int_{\mathbf{r}' \in \mathcal{D}} \frac{\exp(ik_1|\mathbf{r} - \mathbf{r}'|)}{4\pi|\mathbf{r} - \mathbf{r}'|}\mathbf{J}_1(\mathbf{r}',\omega)d\mathbf{r}'. \tag{5.29}$$

Substitution of (5.27) in (5.25) gives

$$\mathbf{E} = i\omega\mu_1\mathbf{A}_m + \frac{i}{\omega\varepsilon_1}\nabla\nabla \cdot \mathbf{A}_m = \frac{i}{\omega\varepsilon_1}\left[k_1^2 + \nabla\nabla\cdot\right]\mathbf{A}_m. \tag{5.30}$$

The electromagnetic field from a current source in a homogeneous medium is now fully determined by (5.23) and (5.30), which are both expressed in terms of the magnetic vector potential.

To obtain an expression for the electric field of a current source in a homogeneous medium, the electric current density is defined as

$$\mathbf{J}_1(\mathbf{r}_1, \omega) = I_1(x_1, \omega)\delta(y_1)\delta(z_1)\left[U(x_1) - U(x_1 - L_1)\right]\mathbf{u}_{x_1}, \tag{5.31}$$

where $U(x_1)$ is the Heaviside step function and $I_1(x_1, \omega)$ is the current at position x_1. The magnetic vector potential (5.29) can then be simplified to

$$\mathbf{A}_m(\mathbf{r}_1, \omega) = \frac{1}{4\pi}\int_0^{L_1} \frac{\exp(ik_1 R_1)}{R_1} I_1(x_1', \omega)\mathbf{u}_{x_1}dx_1', \tag{5.32}$$

with $R_1 = \sqrt{(x_1 - x_1')^2 + y_1^2 + z_1^2}$.

To obtain the electric field, first the $\nabla\cdot$ operator is carried out. This yields

$$\nabla \cdot \mathbf{A}_m = \frac{1}{4\pi}\int_0^{L_1} I_1(x_1', \omega)\partial_{x_1}\psi\, dx_1' \tag{5.33}$$

where

$$\psi = \frac{\exp(ik_1 R_1)}{R_1}. \tag{5.34}$$

Evaluating the partial derivative with respect to x_1 gives

$$\nabla \cdot \mathbf{A}_m = \frac{1}{4\pi}\int_0^{L_1} I_1(x_1', \omega)\partial_{x_1}\psi dx_1'$$

$$= \frac{1}{4\pi}\int_0^{L_1} (ik_1 R_1 - 1)\frac{\exp(ik_1 R_1)}{R_1^3}(x_1 - x_1')I_1(x_1', \omega)dx_1'. \tag{5.35}$$

With this result the last term of (5.30) is found as

$$\nabla\nabla \cdot \mathbf{A}_m = \frac{1}{4\pi}\int_0^{L_1} I_1(x_1', \omega)\nabla\left[\phi(x_1 - x_1')\right]dx_1', \tag{5.36}$$

where

$$\phi = (ik_1 R_1 - 1)\frac{\exp(ik_1 R_1)}{R_1^3}. \tag{5.37}$$

If the ∇ operator in the right-hand side of (5.36) is carried out, (5.36) can be elaborated as

$$\nabla\nabla \cdot \mathbf{A}_m = \frac{1}{4\pi}\int_0^{L_1} \left((x_1 - x_1')\nabla\phi + \phi\mathbf{u}_{x_1}\right)I_1(x_1'\mathbf{u}_{x_1}, \omega)dx_1'$$

$$= \frac{1}{4\pi}\int_0^{L_1} \Bigg[\left((ik_1 R_1)^2 - 3ik_1 R_1 + 3\right)\frac{\exp(ik_1 R_1)}{R_1^5}(x_1 - x_1')\mathbf{R}_1$$

$$+ (ik_1 R_1 - 1)\frac{\exp(ik_1 R_1)}{R_1^3}\mathbf{u}_{x_1}\Bigg]I_1(x_1', \omega)dx_1', \tag{5.38}$$

with $\mathbf{R}_1 = (x_1 - x_1')\mathbf{u}_{x_1} + y_1\mathbf{u}_{y_1} + z_1\mathbf{u}_{z_1}$.

Finally, the electric field due to an arbitrary line current source is obtained as

$$\mathbf{E}(\mathbf{r}_1, \omega) = \frac{i}{4\pi\omega\varepsilon_1} \int_0^{L_1} \left[\left((ik_1R_1)^2 - 3ik_1R_1 + 3\right) \frac{\exp(ik_1R_1)}{R_1^5} (x_1 - x_1') \mathbf{R}_1 \right.$$
$$\left. - \left((ik_1R_1)^2 - ik_1R_1 + 1\right) \frac{\exp(ik_1R_1)}{R_1^3} \mathbf{u}_{x_1} \right] I_1(x_1', \omega) dx_1'. \tag{5.39}$$

Now that all ingredients are known to formulate expressions that describe the mutual coupling between wire antennas in arbitrary Cartesian coordinate systems, a system of equations is set up to describe the mutual coupling between two arbitrarily oriented wires.

5.3.1   Two mutually coupled, arbitrarily oriented wires in a homogeneous medium

The mutual coupling between wires can be described by using the direct field from one wire as an incident field on the other wire and vice versa. As an example, the configuration depicted in Figure 5.3 is studied. As can be seen, a wire with length L_1 is considered in
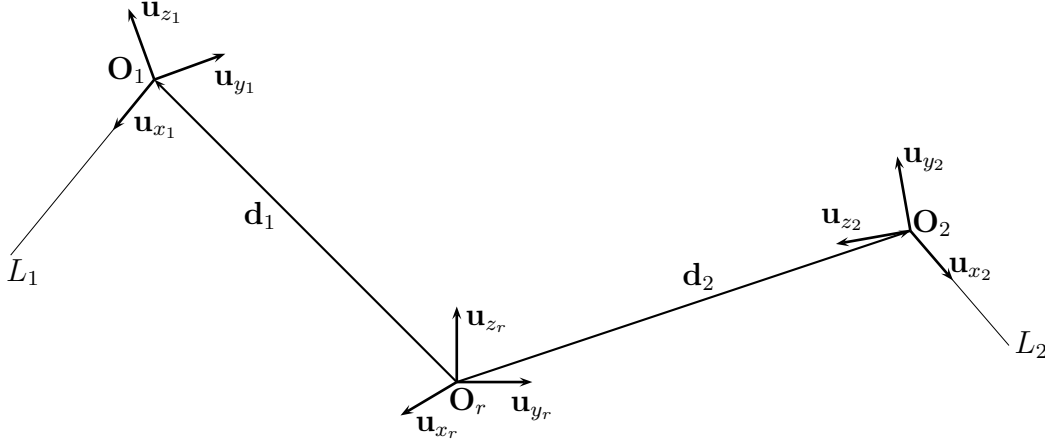
Figure 5.3:   *Two arbitrarily oriented wires with respect to the reference system* $(\mathbf{O}_r, \mathbf{u}_{x_r}, \mathbf{u}_{y_r}, \mathbf{u}_{z_r})$.

system 1 and a second wire with length L_2 is considered in system 2. Both wires have radius a. The wires will be referred to as wire 1 and wire 2, respectively. The total configuration is embedded in a homogeneous medium with complex permittivity ε_1 and permeability μ_1. Wire 1 is related to the reference system through $\mathbf{d}_1$ and transformation matrix $\underline{\mathbf{T}}_1$ and wire 2 through $\mathbf{d}_2$ and $\underline{\mathbf{T}}_2$.

To describe the mutual coupling, the direct field of wire 1 is treated as part of the incident field on wire 2 and vice versa. In that way, the currents along wire 1 and wire 2 are related

to each other. As an example, the direct field from wire 2 will be transformed to system 1 via the reference system to demonstrate the influence of wire 2 on wire 1. The direct field from wire 2 is given by

$$\mathbf{E}_2^d(x_2\mathbf{u}_{x_2} + y_2\mathbf{u}_{y_2} + z_2\mathbf{u}_{z_2}, \omega) = \frac{i}{4\pi\omega\varepsilon_1}\int_0^{L_2}\left[\left((ik_1R_2)^2 - 3ik_1R_2 + 3\right)\frac{\exp(ik_1R_2)}{R_2^5}x_2\mathbf{R}_2\right.$$

$$\left. - \left((ik_1R_2)^2 - ik_1R_2 + 1\right)\frac{\exp(ik_1R_2)}{R_2^3}\right]I_2(x_2', \omega)dx_2', \tag{5.40}$$

with $\mathbf{R}_2 = (x_2 - x_2')\mathbf{u}_{x_2} + y_2\mathbf{u}_{y_2} + z_2\mathbf{u}_{z_2}$ and $R_2 = |\mathbf{R}_2|$.

First (5.20) is used to transform the direct field from wire 2 to the reference system. Applying (5.20) to (5.40) gives

$$\left(E_{x_r}^i(\mathbf{r}), E_{y_r}^i(\mathbf{r}), E_{z_r}^i(\mathbf{r})\right)\begin{pmatrix}\mathbf{u}_{x_r}\\\mathbf{u}_{y_r}\\\mathbf{u}_{z_r}\end{pmatrix} = \left(E_{x_2}^d(\mathbf{r}), E_{y_2}^d(\mathbf{r}), E_{z_2}^d(\mathbf{r})\right)\begin{pmatrix}\mathbf{u}_{x_2}\\\mathbf{u}_{y_2}\\\mathbf{u}_{z_2}\end{pmatrix}, \tag{5.41}$$

with

$$\begin{pmatrix}E_{x_2}^d\\E_{y_2}^d\\E_{z_2}^d\end{pmatrix} = \underline{\mathbf{T}}_2\begin{pmatrix}E_{x_r}^i\\E_{y_r}^i\\E_{z_r}^i\end{pmatrix}, \quad \begin{pmatrix}x_2\\y_2\\z_2\end{pmatrix} = \underline{\mathbf{T}}_2\left[\begin{pmatrix}x_r\\y_r\\z_r\end{pmatrix} - \begin{pmatrix}d_{2x}\\d_{2y}\\d_{2z}\end{pmatrix}\right],$$

$$\text{and} \quad \begin{pmatrix}\mathbf{u}_{x_2}\\\mathbf{u}_{y_2}\\\mathbf{u}_{z_2}\end{pmatrix} = \underline{\mathbf{T}}_2\begin{pmatrix}\mathbf{u}_{x_r}\\\mathbf{u}_{y_r}\\\mathbf{u}_{z_r}\end{pmatrix}. \tag{5.42}$$

Then (5.19) is used to transform $\mathbf{E}_r^i$ from the reference system to system 1. This yields

$$\left(E_{x_1}^i(\mathbf{r}), E_{y_1}^i(\mathbf{r}), E_{z_1}^i(\mathbf{r})\right)\begin{pmatrix}\mathbf{u}_{x_1}\\\mathbf{u}_{y_1}\\\mathbf{u}_{z_1}\end{pmatrix} = \left(E_{x_r}^i(\mathbf{r}), E_{y_r}^i(\mathbf{r}), E_{z_r}^i(\mathbf{r})\right)\begin{pmatrix}\mathbf{u}_{x_r}\\\mathbf{u}_{y_r}\\\mathbf{u}_{z_r}\end{pmatrix}, \tag{5.43}$$

with

$$\begin{pmatrix}E_{x_r}^i\\E_{y_r}^i\\E_{z_r}^i\end{pmatrix} = \underline{\mathbf{T}}_1^T\begin{pmatrix}E_{x_1}^i\\E_{y_1}^i\\E_{z_1}^i\end{pmatrix}, \quad \begin{pmatrix}x_r\\y_r\\z_r\end{pmatrix} = \underline{\mathbf{T}}_1^T\begin{pmatrix}x_1\\y_1\\z_1\end{pmatrix} + \begin{pmatrix}d_{1x}\\d_{1y}\\d_{1z}\end{pmatrix},$$

$$\text{and} \quad \begin{pmatrix}\mathbf{u}_{x_r}\\\mathbf{u}_{y_r}\\\mathbf{u}_{z_r}\end{pmatrix} = \underline{\mathbf{T}}_1^T\begin{pmatrix}\mathbf{u}_{x_1}\\\mathbf{u}_{y_1}\\\mathbf{u}_{z_1}\end{pmatrix}. \tag{5.44}$$

Substitution of (5.41) in (5.43) and (5.42) in (5.44) gives

$$
\left(E_{x_1}^i(\mathbf{r}), E_{y_1}^i(\mathbf{r}), E_{z_1}^i(\mathbf{r})\right)
\begin{pmatrix} \mathbf{u}_{x_1} \\ \mathbf{u}_{y_1} \\ \mathbf{u}_{z_1} \end{pmatrix}
=
\left(E_{x_2}^d(\mathbf{r}), E_{y_2}^d(\mathbf{r}), E_{z_2}^d(\mathbf{r})\right)
\begin{pmatrix} \mathbf{u}_{x_2} \\ \mathbf{u}_{y_2} \\ \mathbf{u}_{z_2} \end{pmatrix},
\tag{5.45}
$$

with

$$
\begin{pmatrix} E_{x_2}^d \\ E_{y_2}^d \\ E_{z_2}^d \end{pmatrix}
= \underline{\mathbf{T}}_2 \underline{\mathbf{T}}_1^T
\begin{pmatrix} E_{x_1}^i \\ E_{y_1}^i \\ E_{z_1}^i \end{pmatrix}, \quad
\begin{pmatrix} x_2 \\ y_2 \\ z_2 \end{pmatrix}
= \underline{\mathbf{T}}_2 \left[\underline{\mathbf{T}}_1^T \begin{pmatrix} x_1 \\ y_1 \\ z_1 \end{pmatrix} + \underline{\mathbf{D}} \right],
$$

$$
\underline{\mathbf{D}} = \mathbf{d}_2 - \mathbf{d}_1, \quad \text{and} \quad
\begin{pmatrix} \mathbf{u}_{x_2} \\ \mathbf{u}_{y_2} \\ \mathbf{u}_{z_2} \end{pmatrix}
= \underline{\mathbf{T}}_2 \underline{\mathbf{T}}_1^T
\begin{pmatrix} \mathbf{u}_{x_1} \\ \mathbf{u}_{y_1} \\ \mathbf{u}_{z_1} \end{pmatrix}
\tag{5.46}
$$

The incident field for wire 2 can easily be found by interchanging the subscripts 1 and 2 in the latter equation.

Hallén's equation for wire 1 then becomes

$$
\int_0^{L_1} \frac{I(x_1')\exp(ik_1 R_a)}{4\pi R_a} dx_1' - F_0^1 \exp(ik_1 x_1) - F_L^1 \exp(ik_1(L_1 - x_1))
$$
$$
= \frac{Y_1}{2} \left[V \exp(ik_1|x_1 - x_{g1}|) + \int_0^{L_1} E_{x_1}^i(x_1' \mathbf{u}_{x1}) \exp(ik_1|x_1 - x_1'|) dx_1' \right],
\tag{5.47}
$$

where only the x-component of the incident electric field $\mathbf{E}_1^i$ needs to be taken. For wire 2, a similar equation is found.

5.4   Results

In this section, the transformation matrix will be applied to a two-wire configuration in free space as depicted in Figure 5.3. The arbitrary orientation of the wires results in a significant increase of the computational effort due to the loss of the possibility to use FFT's for the calculation of the spatial convolutions. As a reference, the method-of-moments code called Numerical Electromagnetics Code (NEC) will be used [36, 57].

NEC is a computer code for the analysis of the electromagnetic response of antennas and other metallic structures. The source can be a voltage source or an external incident field, i.e., a plane wave. Structures are modeled with wire segments, and surfaces are modelled with patches. The segments that NEC uses are always straight and short. To obtain accurate results, a proper choice of the spatial discretization is of the utmost importance.

The number of segments should be sufficient to produce accurate results for the highest frequency occurring in the calculation. However, the dimension and the number of segments with respect to the wavelength λ are limited. In general, the size Δx of the segments on a wire should not be larger than 0.1λ. On the other hand, shorter segments may be needed to accurately model a critical region of the antenna. In the NEC code, wire segments shorter than 0.001λ should be avoided to ensure numerical stability. The first modeling rule for NEC is thus given as

$$0.001 < \frac{\Delta x}{\lambda} < 0.1. \tag{5.48}$$

The wire radius a relative to the wavelength is limited by the approximation used for the kernel in the electric field integral equation. In NEC, the user can choose between two different kernels, namely the exact kernel and the reduced kernel. By choosing the first kernel, the current will be calculated as if it is concentrated on the central axis of the wire in NEC. In calculations with the exact kernel, the current is assumed to be uniformly distributed around the surface of each wiresegment. The NEC user's guide [57] recommends to keep $2\pi a \ll \lambda$. A more convenient rule is found in [58] as

$$0 < a < 0.01\lambda. \tag{5.49}$$

Last but not least, the accuracy of the results also depends on the quotient $\Delta x/a$. The NEC user's guide guarantees errors less than 1% if

$$\frac{\Delta x}{a} > 2, \quad \text{for the exact kernel,} \tag{5.50}$$

$$\frac{\Delta x}{a} > 8, \quad \text{for the reduced kernel.} \tag{5.51}$$

The geometry of a wire is given by the coordinates of the end faces of the wire and the radius a. The length of a wire is calculated from those coordinates. By giving the coordinates of the end faces of a wire, the user is able to position a wire completely arbitrarily. The current is always flowing along the x-axis of a certain coordinate system. The coordinates of wire n are represented as

$$W_n = \{(x_b, y_b, z_b), (x_e, y_e, z_e)\}, \tag{5.52}$$

where the subscripts b and e represent the begin and end point of a wire. In all examples given below, the reduced kernel is used. With the examples given in this section, the steps A, B and C of the transformation are introduced successively.

In the first example, the coordinates of two wires with radius $a = 0.002$ m in free space are given by $W_1 = \{(0,0,0), (1,0,0)\}$ and $W_2 = \{(0,1,0), (1,1,0)\}$. The lengths of both wires

is thus 1 m and the wires are still parallel oriented. The excitation is a delta-gap voltage with an amplitude of 1 V. This voltage source will be used in the rest of this chapter. The calculation is carried out for a frequency of 300 MHz, which means that $\lambda = 1$ m. In Figure 5.4 the absolute values of the currents in the frequency domain along wire 1 and wire 2 is plotted. It is immediately seen that the currents match the results from NEC
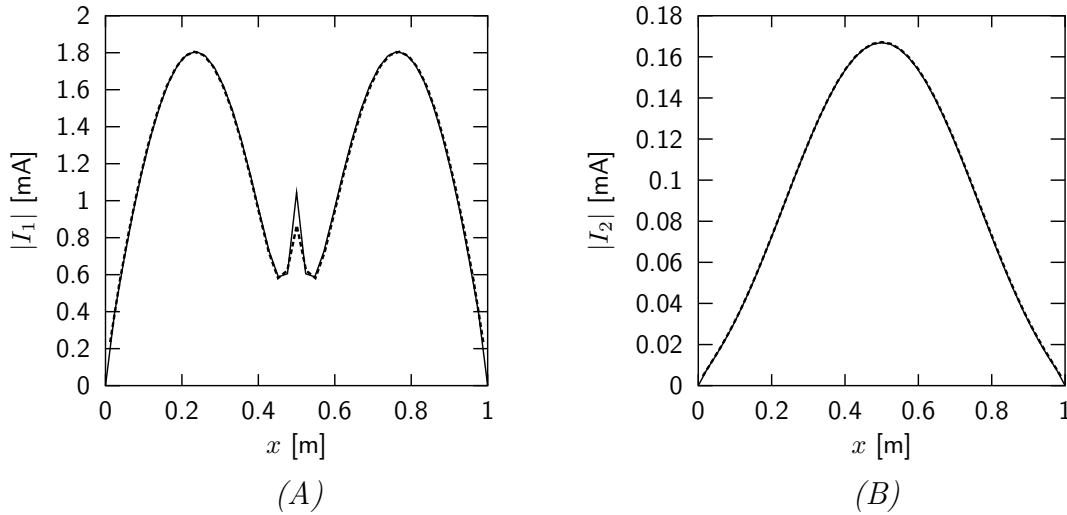
Figure 5.4: *The induced currents along wire 1 and wire 2. The radius of both wires is $a = 0.002$ m. The coordinates of the end faces of the wires are given by $W_1 = \{(0,0,0),(1,0,0)\}$ and $W_2 = \{(0,1,0),(1,1,0)\}$. The wires are located in free space. Wire 1 is excited with a delta-gap voltage at the center of the wire with an amplitude of 1V. The frequency of operation is $f = 300$ MHz. The solid lines represent results obtained with Hallén's equation. The dotted lines represent results obtained with NEC.*

very accurately. The larger peak at the center of wire 1 can be explained from the different approaches used for the calculation of both results. The currents are symmetrical around the center of the wires. The fact that the current along wire 2 matches perfectly shows that the direct field from wire 1 incident on wire 2 is calculated accurately. The shape of the current is not the same for wire 1 and wire 2. The distance d is already large enough for the radiated field from wire 1 to behave as a far field which is incident on wire 2 [59]. Therefore, the current along wire 1 follows as the current which is induced by a plane wave. Also in the frequency domain results, the magnitude of the current along wire 2 is about 10 times less than along wire 1. This was already observed in the time domain in previous chapters. Along wire 1, two peaks can be recognized. The current along a wire behaves as a sinusoidal function [14, 44, 60, 61]. Since the wire is λ long, exactly one period of a sine and/or cosine fits on the wire. Therefore, the absolute value shows two peaks. On wire

2, there is only one peak visible but the behavior of the current near the end faces of the wire shows that there is more than half a period of a sinusoidal present.

In the next example, again two wires in free space are considered. The coordinates are given by $W_1 = \{(0,0,0), (1,0,0)\}$ and $W_2 = \{(0.9,1,0), (1.9,1,0)\}$. The wires have again a length of 1 m and are parallel. The difference with the previous configuration is the offset in the x-direction of 0.9 m and the frequency, which is now $f = 600$ MHz. The absolute values of the currents along both wires are depicted in Figure 5.5. It is observed that

(A) (B)
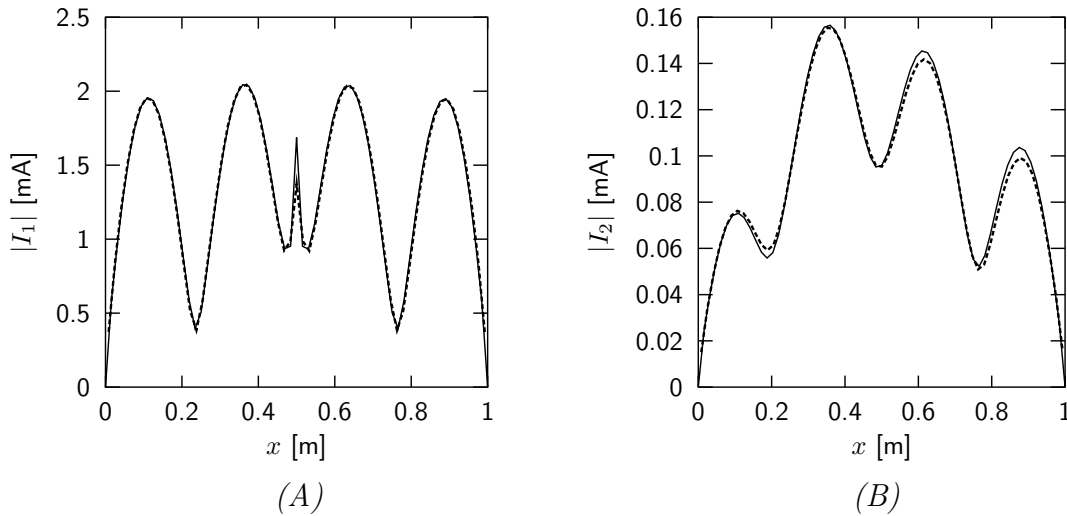
Figure 5.5: *The induced currents along wire 1 and wire 2. The radius of both wires is $a = 0.002$ m. The coordinates of the end faces of the wires are given by $W_1 = \{(0,0,0), (1,0,0)\}$ and $W_2 = \{(0.9,1,0), (1.9,1,0)\}$. The wires are located in free space. Wire 1 is excited with a delta-gap voltage at the center of the wire with an amplitude of 1V. The frequency of operation is $f = 600$ MHz. The solid lines represent results obtained with Hallén's equation. The dotted lines represent results obtained with NEC.*

the results are similar. The symmetry around the center of wire 2 is no longer observed. The behavior of the currents along both wires is described by two periods of a sinusoidal. The current along wire 1 is almost symmetrical. Therefore it can be concluded that the presence of wire 2 has hardly any effect on the current along wire 1. It is clear that step A of the transformation process performs well.

In the previous example, the length of wire 2 is 1 m. Now, the length of wire 2 is decreased to 0.5 m. The wires have the coordinates $W_1 = \{(0,0,0), (1,0,0)\}$ and $W_2 = \{(0.85,1,0), (1.35,1,0)\}$. The absolute values of the currents along both wires are depicted in Figure 5.6. It is immediately observed that the current along wire 2 is described by a single period of a sinusoidal. Because of the offset in the x-direction, the current is not
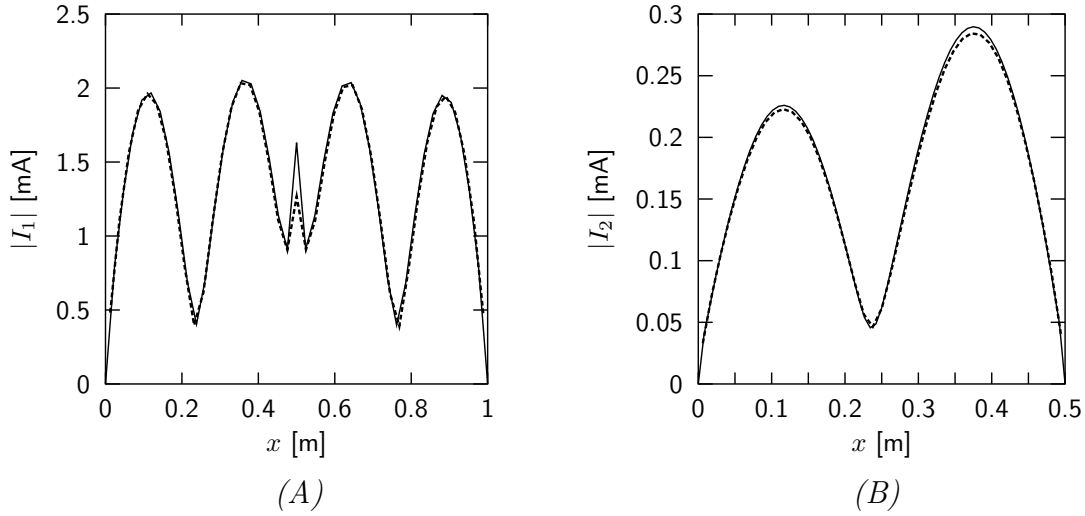
Figure 5.6: *The induced currents along wire 1 and wire 2. The radius of both wires is $a = 0.002$ m. The coordinates of the end faces of the wires are given by $W_1 = \{(0,0,0),(1,0,0)\}$ and $W_2 = \{(0.85,1,0),(1.35,1,0)\}$. The wires are located in free space. Wire 1 is excited with a delta-gap voltage at the center of the wire with an amplitude of 1V. The frequency of operation is $f = 600$ MHz. The solid lines represent results obtained with Hallén's equation. The dotted lines represent results obtained with NEC.*

symmetrical around the center of the wire. In general, the result is in good agreement with the reference result. Step A of the transformation is performing well. Again, the current along wire 1 is hardly affected by the presence of wire 2.

To demonstrate the next step in the transformation process, two wires in free space with coordinates $W_1 = \{(0,0,0),(1,0,0)\}$ and $W_2 = \{(0.2,0.5,0),(0.2,1.5,0)\}$ are considered. The frequency is again $f = 600$ MHz. The absolute values of the currents along both wires are depicted in Figure 5.7. It is observed that the results are similar. This means that step B of the transformation process performs well.

Next, two wires in free space with coordinates $W_1 = \{(-0.5,0,0),(0.5,0,0)\}$ and $W_2 = \{(-4.33,1,-0.25),(4.33,1,0.25)\}$, respectively, are considered. The frequency is again $f = 600$ MHz and the wires are located in free space. The absolute values of the currents along wire 1 and wire 2 are plotted in Figure 5.8.

The currents are in perfect agreement with the reference results. Therefore it may be concluded that step C of the transformation process is accurate. The current along both wires can again be described by two periods of a sinusoidal. Because the rotation over θ is at the center of both wires, the current along wire 2 is again fully symmetrical. Once more, the current along wire 1 does not change significantly due to the presence of wire 2.
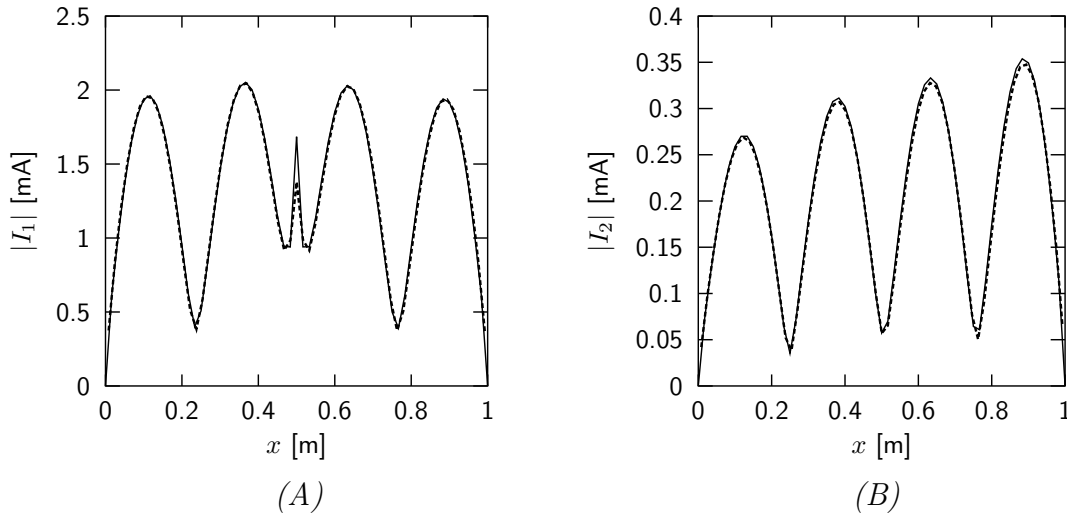
Figure 5.7: *The induced currents along wire 1 and wire 2. The radius of both wires is* $a =$ *0.002 m. The coordinates of the end faces of the wires are given by* $W_1 = \{(0,0,0),(1,0,0)\}$ *and* $W_2 = \{(0.2,0.5,0),(0.2,1.5,0)\}$. *The wires are located in free space. Wire 1 is excited with a delta-gap voltage at the center of the wire with an amplitude of 1V. The frequency of operation is* $f = 600$ *MHz. The solid lines represent results obtained with Hallén's equation. The dotted lines represent results obtained with NEC.*

In the last example, two wires with coordinates $W_1 = \{(-0.5, 0.2, -0.4), (0.4, 0.3, 0.2)\}$ and $W_2 = \{(0.25, 1, 0.1), (0.65, 0.82, 0.47)\}$ are considered. The frequency is again $f = 600$ MHz and the wires are located in free space. The absolute values of the currents along both wires are depicted in Figure 5.9. The coordinates were chosen completely arbitrarily for this example. Wire 1 is approximately 1.1 m long. Slightly more than two periods of a sinusoidal describe the behavior of the current along wire 1. The other wire is approximately 0.57 m long. This means that half a period of a sinusoidal describes the behavior of the current along wire 2. This is indeed observed. The second wire has offsets in all three directions. Moreover, it is rotated over both ϕ and θ. The transformation process thus performs well. In general, the magnitude of the current is lower when wire 2 rotates over ϕ and θ with respect to wire 1. This can be easily seen when the results in Figure 5.6 are compared to those in Figure 5.9. A similar observation is made concerning Figure 5.5 and Figure 5.8. The first plot shows a maximum current of 160 μA while the latter shows a maximum current of 90 μA. When the second wire does not have an offset in the x-direction in Figure 5.5, the maximum current is found to be 110 μA. It may be concluded that the transformation works accurately. Another important observation is that the effects of mutual coupling are still important.
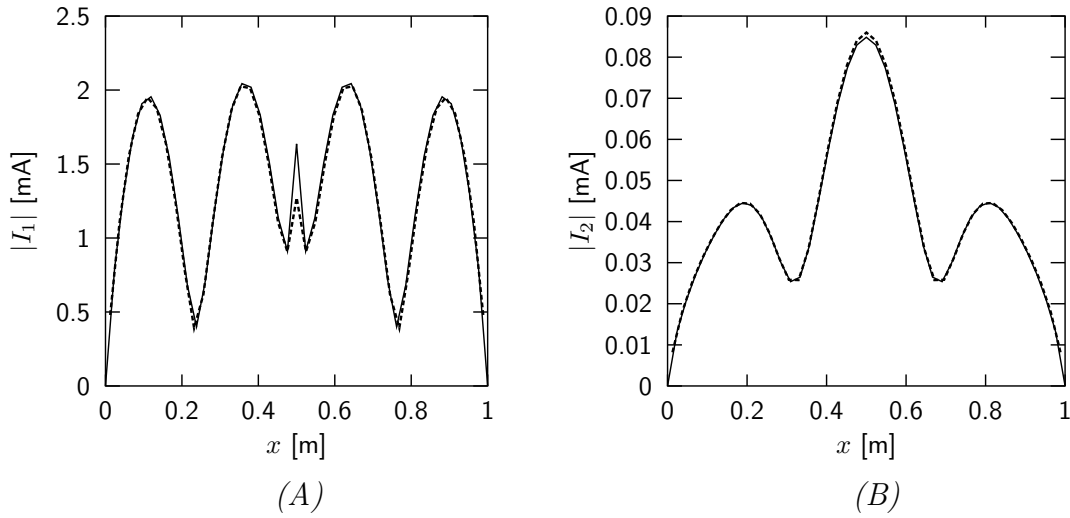
Figure 5.8: *The induced currents along wire 1 and wire 2. The radius of both wires is $a = 0.002$ m. The coordinates of the end faces of the wires are given by $W_1 = \{(-0.5, 0, 0), (0.5, 0, 0)\}$ and $W_2 = \{(-4.33, 1, -0.25), (4.33, 1, 0.25)\}$. The wires are located in free space. Wire 1 is excited with a delta-gap voltage at the center of the wire with an amplitude of 1V. The frequency of operation is $f = 600$ MHz. The solid lines represent results obtained with Hallén's equation. The dotted lines represent results obtained with NEC.*
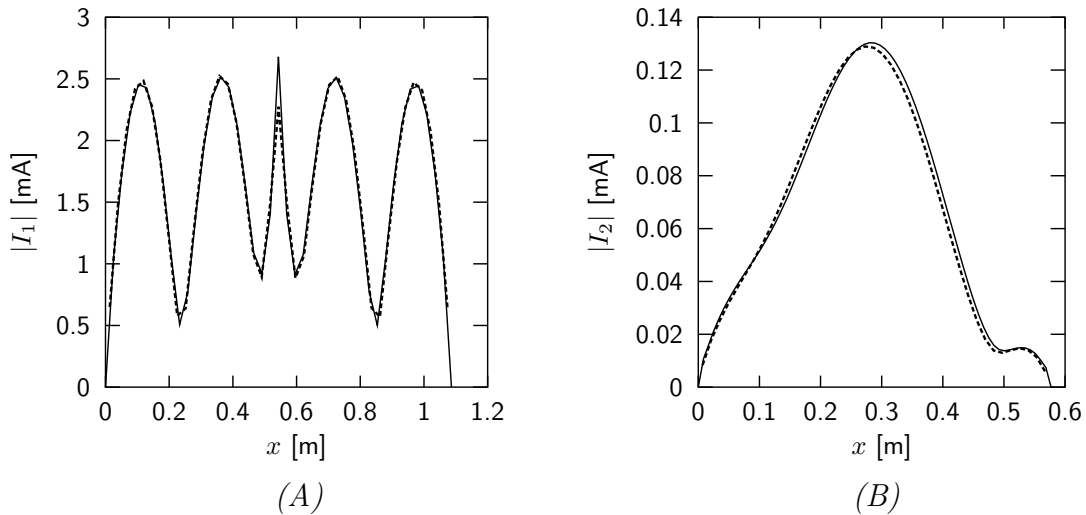
Figure 5.9: *The induced currents along wire 1 and wire 2. The radius of both wires is $a = 0.002$ m. The coordinates of the end faces of the wires are given by $W_1 = \{(-0.5, 0.2, -0.4), (0.4, 0.3, 0.2)\}$ and $W_2 = \{(0.25, 1, 0.1), (0.65, 0.82, 0.47)\}$. The wires are located in free space. Wire 1 is excited with a delta-gap voltage at the center of the wire with an amplitude of 1V. The frequency of operation is $f = 300$ MHz. The solid lines represent results obtained with Hallén's equation. The dotted lines represent results obtained with NEC.*

Chapter 6

Suppression of repeated reflections

The presence of a buried wire may have an influence on the current along the wires in the detection set up. To recognize this response directly from the current along wire 2 is quite complicated due to repeated reflections at the end faces of both wires in the detection set up and of the buried wire. The currents along the wires 1 and 2 can be subjected to a variety of signal processing tools to enhance the detection. These enhancements filter the information about the buried object from the current along wire 2. In other words, effects of the buried wire that are already present in the current along wire 2 become better visible.

Instead of signal processing or post processing, it is also possible to modify the wires 1 and 2 before using them for detection purposes. In this chapter, two possible modifications are introduced and discussed.

The first modification to the wires is the application of a so-called Wu-King profile. The current along a wire has a slowly attenuating late-time response because of the repeated reflections of the traveling current wave at the end faces of the wire. If these repeated reflections can be suppressed by attenuating the current wave towards the end faces of the wire, it is possible to see the influence of secondary incident fields on the current along a wire. In 1965, Wu and King proposed a resistance profile along the wire which attenuates the current towards the end faces of a wire [17].

The second modification to reduce the repeated reflections is pulse compensation. With pulse compensation, a second pulse with a carefully chosen amplitude and time delay is generated from the original first voltage pulse at wire 1. Combining the responses from both pulses on wire 1 causes a significant reduction of the oscillatory behavior of the current along wire 1. For the compensation of the current along wire 2, a similar procedure can be followed.

6.1   The Wu-King resistive loading

In this section, the current along a perfectly conducting thin wire in a homogeneous space is considered, see Figure 3.3. The wire has a length L and a radius a. The material parameters of the homogeneous space are given as $\varepsilon_1(\mathbf{r}) = \varepsilon_1$ and $\mu(\mathbf{r}) = \mu_0$. The current along such a wire is repeatedly reflected at the end faces of the wire. To avoid the repeated current reflections, Wu and King [17] derived a resistance distribution that attenuates the current towards the end faces of the wire. With their particular distribution, a current wave originating from the center of the wire travels along the antenna and is fully attenuated when it reaches the end faces of the wire. Therefore, the current wave does not return any more from the end faces. The derivation will be demonstrated with a generalization of the resistance profile as was found in [17]. In 1967, Shen and Wu [62] derived an expression to describe a resistance distribution with a variable degree of loading. Several authors [62, 63, 64] have used this adjustable profile in theory and experiment. They all come to the same conclusion that the degree of loading is not very critical for the field pattern from the antenna as long as the degree of loading is between 90% and 110% of the resistive profile Z^{WK} proposed by Wu and King [17]. It has also been demonstrated that the theory complies with experiments [22, 29, 62, 63].

When the total current along the wire is given by $I(x, \omega)$, and the wire has the internal impedance per unit length $Z^i(x) = Z^{\mathrm{WK}}(x - L/2)$, the total tangential electric field on the axis is given by

$$E_x(x\mathbf{u}_x, \omega) = Z^i(x)I(x, \omega) + V(\omega)\delta(x - L/2) + E_x^i(x\mathbf{u}_x, \omega), \quad 0 < x < L, \tag{6.1}$$

where $x_g = L/2$ is chosen. The point of excitation is chosen at the center of the wire and the resistance profile is chosen symmetrical around the driving point. With the aid of (6.1), Pocklington's equation (3.48) can be extended to

$$(\partial_x^2 + k_1^2) \int_0^L G(R_a, \omega)I(x', \omega)dx'$$
$$= -i\omega\varepsilon_1 \left[V(\omega)\delta(x - L/2) + Z^i(x)I(x, \omega) + E_x^i(x\mathbf{u}_x, \omega) \right], \, 0 < x < L, \tag{6.2}$$

where

$$G(R_a, \omega) = \frac{\exp(ik_1R_a)}{4\pi R_a}, \quad R_a = \sqrt{(x - x')^2 + a^2},$$

Following the notation of Wu and King [17] and Shen and Wu [62], (6.2) is written as

$$(\partial_x^2 + k_1^2)\int_{-L/2}^{L/2} G(R_a, \omega)I(x', \omega)dx' = -i\omega\varepsilon_1 \left[V(\omega)\delta(x) + Z^i(x)I(x, \omega) + E_x^i(x\mathbf{u}_x, \omega) \right], (6.3)$$

for $-L/2 < x < L/2$. Further on, x will be replaced by $x - L/2$ again to return to the original notation from previous chapters. The next step in the derivation is to approximate the integral in (6.3) by

$$\int_{-L/2}^{L/2} \frac{\exp(ik_1 R_a)}{R_a} I(x',\omega)dx' \approx I(x,\omega)\Psi, \tag{6.4}$$

where the factor Ψ remains to be determined [17]. Since Ψ varies slowly with respect to x and ω, the arguments of Ψ are omitted. Substitution of (6.4) into (6.3) gives

$$(\partial_x^2 + k_1^2)I(x,\omega) = -\frac{4\pi i\omega\varepsilon_1}{\Psi}\left[V(\omega)\delta(x) - Z^i(x)I(x,\omega) + E_x^i\left((x + L/2)\mathbf{u}_x,\omega\right)\right]. \tag{6.5}$$

The latter equation can be rewritten as

$$\left[\partial_x^2 + k_1^2 + ik_1 f(x)\right]I(x,\omega) = -\frac{4\pi i\omega\varepsilon_1}{\Psi}\left[V(\omega)\delta(x) + E_x^i\left((x + L/2)\mathbf{u}_x,\omega\right)\right], \tag{6.6}$$

with

$$f(x) = \frac{4\pi Z^i(x)}{Z_1 \Psi}, \tag{6.7}$$

which is a so-called distribution function [61] and Z_1 is the characteristic impedance of the homogeneous medium. This function describes the distribution of the resistance along the wire. The resistance should go to infinity at the end faces of the wire to fully attenuate the current at those positions. In [62], $f(x)$ is chosen as

$$f(x) = \frac{2\alpha}{L/2 - |x|}, \tag{6.8}$$

where the dimensionless constant α represents the degree of loading with $0 \le \alpha \le 1$. When $\alpha = 0$, the resistance profile is absent, hence the current in (6.6) behaves as a current distribution along a perfectly conducting wire. In [17], the constant $\alpha = 1$. At this point the derivation of the resistance profile therefore deviates from the one followed by Wu and King, hence $0 \le \alpha \le 1$.

With the choice of $f(x)$, the internal impedance per unit length $Z^i(x)$ can be determined. The only unknown is the factor Ψ. To find an expression for Ψ, the current along the wire is represented as [15]:

$$I(x,\omega) = A\exp(ik_1|x|)(L/2 - |x|)\Phi(\beta), \tag{6.9}$$

where $\beta = 2ik_1(L/2 - |x|)$ and A is an arbitrary constant which does not depend on x. The factor $\exp(ik_1|x|)$ describes the traveling-wave nature. The factor $(L/2 - |x|)$ ensures that the current is zero at the end faces of the wire.

The functional Φ can be obtained by substituting (6.9) in (6.6). Since the distribution is symmetrical around $x = 0$, the derivation can be restricted to the interval $0 < x < L/2$. For $x > 0$, first the derivatives with respect to x in (6.6) are found as follows

$$
\begin{aligned}
\partial_x^2 I(x,\omega) &= \partial_x^2 \left[A \exp(ik_1|x|)(L/2 - |x|)\Phi(\beta) \right] \\
&= A\partial_x [ik_1 \exp(ik_1 x)(L/2 - x)\Phi(\beta) - \exp(ik_1 x)\Phi(\beta) + \exp(ik_1 x)(L/2 - x)\partial_x\Phi(\beta)] \\
&= A\exp(ik_1 x)\bigg[\left[(ik_1)^2(L/2 - x) - 2ik_1 \right] \Phi(\beta) + [2ik_1(L/2 - x) - 2]\,\partial_x\Phi(\beta) \\
&\quad + (L/2 - x)\partial_x^2\Phi(\beta)\bigg].
\end{aligned}
\tag{6.10}
$$

When $\partial_x\Phi(\beta)$ is rewritten as

$$
\partial_x\Phi(\beta) = -2ik_1\partial_\beta\Phi(\beta),
\tag{6.11}
$$

and (6.9) and (6.10) are substituted in (6.6), the following equation is obtained

$$
\beta\partial_\beta^2\Phi(\beta) + (2 - \beta)\partial_\beta\Phi(\beta) + (\alpha - 1)\Phi(\beta) = 0,
\tag{6.12}
$$

for $x > 0$. This equation is recognized as Kummer's equation [41, 13.1.1] with the general solution

$$
\Phi(\beta) = BM(b, c, \beta),
\tag{6.13}
$$

where $b = 1 - \alpha$ and $c = 2$. In the latter equation, B is an arbitrary constant and $M(b, c, \beta)$ is known as Kummer's function.

Kummer's function has the following integral representation [41, 13.2.1]

$$
M(b, c, \beta) = \frac{\Gamma(c)}{\Gamma(c - b)\Gamma(b)} \int_0^1 \exp(\beta u)(1 - u)^{c-b-1} u^{b-1} du.
\tag{6.14}
$$

For the given b and c, this function becomes

$$
M(1 - \alpha, 2, \beta) = \frac{\Gamma(2)}{\Gamma(1 - \alpha)\Gamma(1 + \alpha)} \int_0^1 \exp(\beta u)\left(\frac{1 - u}{u}\right)^\alpha du.
\tag{6.15}
$$

Because of the singularity at $u = 0$, it is convenient to modify the integration path to a contour C such that it fully encloses the interval $0 < u < 1$ [65, Chapter 6] and [66, Chapter 4]. With the integral representation as given above, (6.13) can be rewritten as

$$
\Phi(\beta) = B\frac{\Gamma(2)}{\Gamma(1 - \alpha)\Gamma(1 + \alpha)} \int_C \exp(\beta u)\left(\frac{1 - u}{u}\right)^\alpha du,
\tag{6.16}
$$

where the integration path is modified to the contour C mentioned above. Now that $\Phi(\beta)$ has been determined, (6.9) is substituted in (6.4). At $x = 0$, Ψ is found as

$$\Psi = \frac{2}{\Phi(\beta_0)} \int_0^{L/2} \frac{\exp(ik_1 R_0)}{R_0} \exp(ik_1 x') \left(1 - \frac{2x'}{L}\right) \Phi(\beta') dx', \tag{6.17}$$

with $R_0 = \sqrt{x'^2 + a^2}$, $\beta' = 2ik_1(L/2 - x')$ and $\beta_0 = ik_1 L$. Interchanging the order of the integrations over x' and u gives

$$\Psi = \frac{2}{\int_C \left(\frac{1-u}{u}\right)^\alpha \exp(ik_1 Lu) du} \int_C \left\{ \left(\frac{1-u}{u}\right)^\alpha \exp(ik_1 Lu) \right.$$

$$\left. \cdot \int_0^{L/2} \left[\frac{\exp(ik_1 R_0)}{R_0} - \frac{2x'}{L}\frac{\exp(ik_1 R_0)}{R_0}\right] \exp[ik_1 x'(1 - 2u)]dx' \right\} du. \tag{6.18}$$

When R_0 is approximated by $R_0 \approx x'$, the latter expression can be written as

$$\Psi = \frac{2}{\int_C \left(\frac{1-u}{u}\right)^\alpha \exp(ik_1 Lu) du} \int_C \left(\frac{1-u}{u}\right)^\alpha \exp(ik_1 Lu)$$

$$\cdot \left[\underbrace{\int_0^{L/2} \frac{\exp\left(2ik_1 R_0(1-u)\right)}{R_0}dx'}_{g(x,u)} - \underbrace{\frac{2}{L}\int_0^{L/2} \exp\left(2ik_1 x'(1-u)\right)dx'}_{h(x,u)} \right] du. \tag{6.19}$$

It is observed that the approximation cannot be used for $g(x,u)$. The integral $h(x,u)$ in (6.19) can be evaluated in closed form:

$$h(x,u) = \frac{2}{L} \int_0^{L/2} \exp\left[2ik_1 x'(1-u)\right] dx' = \frac{i}{k_1 L(1-u)} \left[1 - \exp(ik_1 L(1-u))\right]. \tag{6.20}$$

The integral $g(x,u)$ in the right-hand side of (6.19) is solved as follows

$$g(x,u) = \int_0^{L/2} \frac{\exp\left(2ik_1 R_0(1-u)\right)}{R_0}dx'$$

$$= \int_0^{L/2} \left[\frac{1}{R_0} - \frac{1 - \cos[2k_1 R_0(1-u)]}{R_0} + i\frac{\sin[2k_1 R_0(1-u)]}{R_0}\right] dx'$$

$$= \sinh^{-1}\left(\frac{L}{2a}\right) - C(2A, H) + iS(2A, H), \tag{6.21}$$

where $A = k_1 a(1 - u)$, $H = k_1 L(1 - u)$, and where

$$C(p, q) = \int_0^q \frac{1 - \cos W}{W}du, \ S(p, q) = \int_0^q \frac{\sin W}{W}du, \ W = \sqrt{u^2 + p^2},$$

are the generalized cosine and sine integrals [61, chapter II.19]. The total function Ψ is then obtained as

$$
\Psi = 2\sinh^{-1}\left(\frac{L}{2a}\right) - \frac{2}{\int_C \left(\frac{1-u}{u}\right)^\alpha \exp(ik_1 Lu)du} \int_C \left(\frac{1-u}{u}\right)^\alpha \exp(ik_1 Lu)
$$

$$
\cdot \left[C(2A, H) - iS(2A, H) + \frac{i}{H}[1 - \exp(iH)]\right] du. \tag{6.22}
$$

As stated earlier, the constant $\alpha = 1$ gives the solution from Wu and King [17]. Evaluating (6.22) for $\alpha = 1$ gives

$$
\Psi = 2\left[\sinh^{-1}\left(\frac{L}{2a}\right) - C\left(2k_1 a, k_1 L\right) + iS\left(2k_1 a, k_1 L\right)\right] - \frac{i}{k_1 L}[1 - \exp(ik_1 L)]. \tag{6.23}
$$

Now that the factor Ψ has been found, the internal impedance per unit length can easily be found by combining (6.7) and (6.8). Before that step is carried out, x is replaced again by $x - L/2$ in accordance with (6.2). Now, (6.8) is redefined as

$$
f(x) = \frac{2}{L/2 - |x - L/2|}, \tag{6.24}
$$

for $0 < x < L$ and $\alpha = 1$. With the redefinition of $f(x)$, the following expression for Z^i is obtained

$$
Z^i(x) = \frac{Z_1 \Psi}{\pi(L - |2x - L|)}. \tag{6.25}
$$

In Figure 6.1, the internal impedance per unit length is plotted as a function of the position along the wire (A) and the parameter Ψ is plotted as a function of frequency, respectively. The length of the wire is $L = 1$ m and the radius is $a = 0.002$ m. In the calculations of the current along a single thin wire, the results between computations with the real part or the absolute value of Ψ did no deviate much from each other. Because of this and the fact that $\text{Re}(\Psi)$ can be used in the time domain, the real part of Ψ is used for the resistive profile. In addition, a real valued resistance profile is easier to construct in practical situations. The Wu-King resistive profile can thus be written as

$$
Z^i(x) = \frac{Z_1 \text{Re}(\Psi)}{\pi(L - |2x - L|)} \tag{6.26}
$$

Hallén's equation for a single thin wire with the Wu-King profile can thus be written as

$$
\int_0^L G(R_a, \omega)I(x', \omega)dx' - F_0(\omega)\exp(ik_1 x) - F_L(\omega)\exp(ik_1(L - x))
$$

$$
= \frac{Y_1}{2}\left[V(\omega)\exp(ik_1|x - L/2|) + \int_0^L Z^i(x')I(x', \omega)\exp(ik_1|x - x'|)dx'\right.
$$

$$
\left. + \int_0^L E_x^i(x'\mathbf{u}_x, \omega)\exp(ik_1|x - x'|)dx'\right], \tag{6.27}
$$
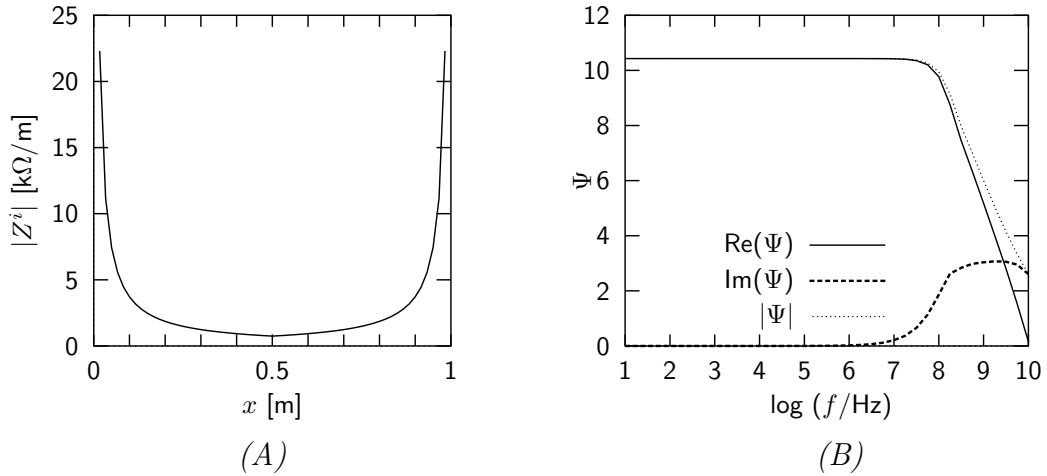
Figure 6.1: *The internal impedance per unit length $Z^i(x)$ and the parameter Ψ. The length is $L = 1$ m and the radius is $a = 0.002$ m. The internal impedance is calculated at a frequency of $f = 300$ MHz.*

for $0 < x < L$. Note that the point of excitation is chosen in the center of the wire, i.e., at $x_g = L/2$.

6.1.1 Results

In the previous section, a resistance profile to attenuate the current towards the end faces of a wire was derived. In this section, a few examples will illustrate the potential of the resistance profile.

First a single thin wire is excited by the voltage pulse as given in Section 3.3.2. The current along the wire is calculated for $L = 1$ m, $a = 0.002$ m, $M = 60$ and $N = 512$. The surrounding medium is free space. In Figure 6.2, the current along the wire has been plotted for $0 < x < L$ as a function of time. The left plot shows the current along a perfectly conducting thin wire and the right plot shows the current along a wire with the Wu-King profile. It is immediately observed that the current along the perfectly conducting thin wire oscillates heavily at all points along the wire and vanishes very slowly, see also Section 3.3.2. Along the Wu-King loaded wire, the current attenuates towards the end faces of the wire and the oscillating behavior of current along the wire is fully suppressed. To examine the effect of the oscillating current along the wire a bit further, the input impedance at the center of the wire is studied. The input voltage is a delta-gap voltage. The spectrum of the source is $V(\omega) = 1$. Again, the wire has a length $L = 1$ m and a
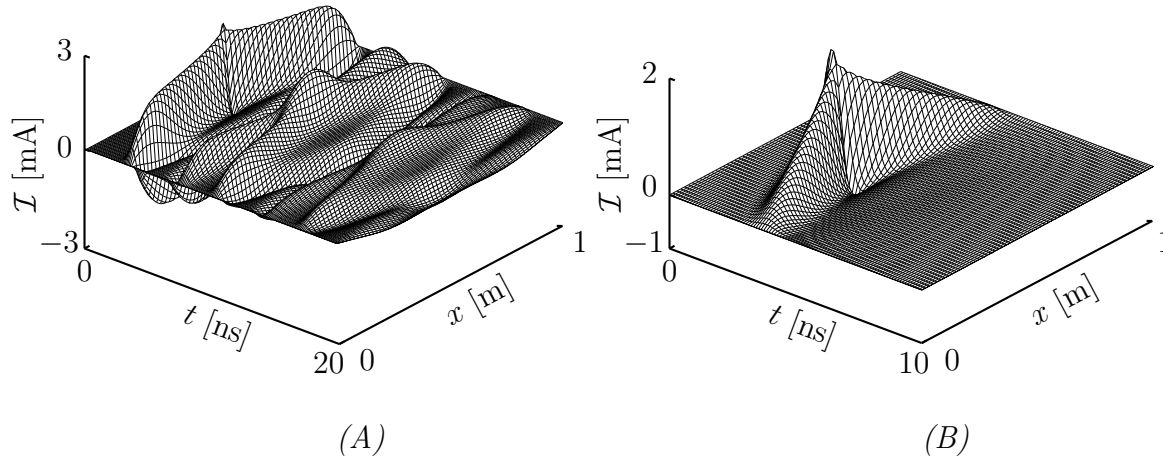
Figure 6.2: The induced current along a single thin wire with length $L = 1$ m and radius $a = 0.002$ m, $M = 60$ and $N = 512$ in free space. The currents along a perfectly conducting thin wire and along a Wu-King loaded wire are visualized in (A) and (B), respectively. The excitation is a Gaussian voltage pulse with $\tau = 0.5$ ns and $t_1 = 4\tau$.

radius $a = 0.002$ m. The frequency range is $0 < f < 2$ GHz. The cell size should be smaller than half the smallest wavelength. In this case, the wavelength is $\lambda = c_1/f_{\max} \approx 0.15$ m. This means that on a wire of length $L = 1$ m, there should be at least $2L/\lambda \approx 15$ cells.

In Figure 6.3, the magnitude and phase of the impedance at the center of the wire are plotted. The solid lines represent a perfectly conducting wire and the dashed lines represent the Wu-King loaded wire. It is immediately seen that the impedance of the Wu-King loaded wire is a very smooth function of the frequency. It is observed that the behavior of the impedance of the perfectly conducting wire oscillates around the impedance of the Wu-King loaded wire. In other words, the Wu-King profile averages the impedance of the wire over a broad frequency range. The smooth input impedance over a wide frequency range ensures that the wire is capable of measuring transient signals without pulse distortion.

As an illustrative example, two wires in free space are considered. Both wires have length $L = 1$ m and radius $a = 0.002$ m. The number of space steps is $M = 30$ and the number of time steps is $N = 1024$. The distance between the wires has been varied as $d = 0.5$ m, $d = 1$ m and $d = 2$ m. Both wires are loaded with the Wu-King resistance profile. The currents at the center of wire 1 *(A)* and wire 2 *(B)* are plotted in Figure 6.4. It is immediately observed that the current along wire 1 is not at all affected by the presence of wire 2. The first maximum is about 0.8 times the magnitude when compared to the response of a perfectly conducting wire, see Figure 4.9. For the magnitude of the first minimum, this factor is 0.3. After the first minimum, the current along the wire is almost
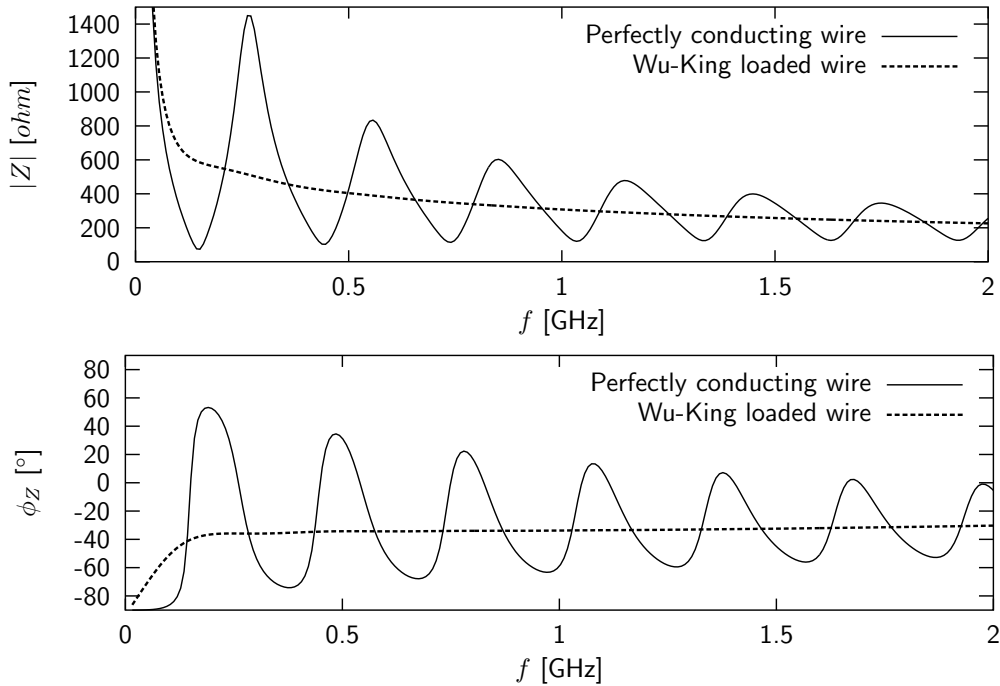
Figure 6.3: *The magnitude and phase of the input impedance at the center of a wire with length $L = 1$ m and radius $a = 0.002$ m, $M = 60$. The input voltage is a delta-gap voltage.*
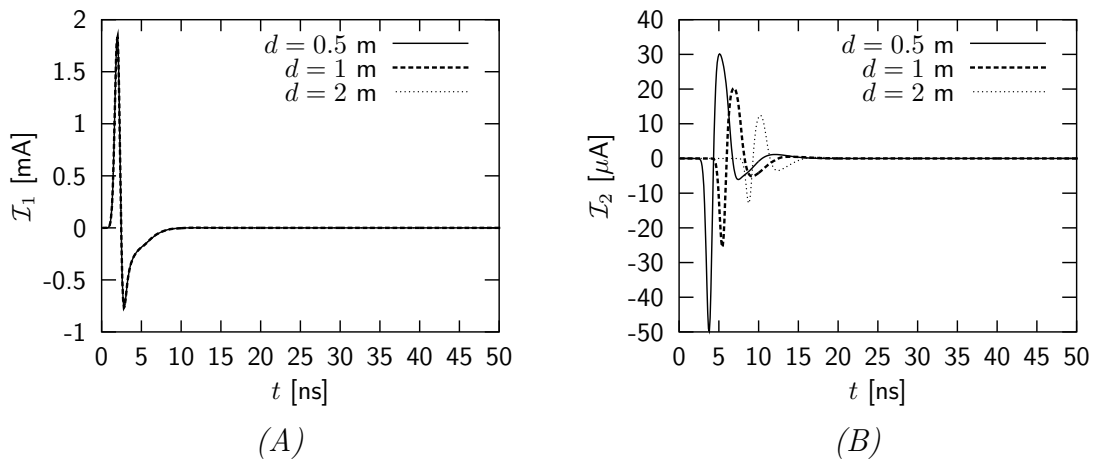
Figure 6.4: *The induced current in the center of wire 1 and wire 2 with length $L = 1$ m and radius $a = 0.002$ m, $M = 30$ and $N = 1024$ for various distances d. Both wires are loaded with the Wu-King resistance profile. The embedding is free space. The excitation is a Gaussian voltage pulse with $\tau = 0.5$ ns and $t_1 = 4\tau$.*

negligible.

The behavior of the current along wire 2 depends similarly on the distance between the wires as perfectly conducting wire antennas in a similar configuration, see Figure 4.9. The arrival time of the electric field is proportional to the distance d. The magnitude of the current for the first minimum is inversely proportional to the distance d. For wire 2, the magnitude of the current is approximately 2.4 times smaller in comparison with the current pulse on the unloaded wires. The first maximum of the current no longer relies directly on the changes in the distance between the wires. The magnitude of the second minimum of the current along wire 2 again changes with a different factor in relation to the distance. After this second minimum, the current along wire 2 is quickly attenuated.

6.2   Pulse compensation

In the previous section, the results obtained for wires with a resistance profile demonstrated that the reflections at the end faces of the wire can be suppressed. A disadvantage is the considerable power loss. Therefore, a different approach will be employed to avoid the unwanted reflections at the end faces of the wires.

In this section, pulse compensation will be considered as an alternative to the Wu-King resistance profile. The feasibility of pulse compensation can be understood from the traveling-wave model for the current described in Chapter 3. The pulse compensation for suppressing the reflections at the end faces of the wire is carried out in two steps. First, the reflections of the current at the end faces of wire 1 are compensated. Second, the reflections of the current at the end faces of wire 2 are compensated.

Pulse compensation amounts to generating a second pulse with a carefully chosen amplitude and time delay from the original first voltage pulse at wire 1. The combined response to both pulses on wire 1 causes a significant reduction of the oscillatory behavior of the current along wire 1. The current along wire 2 is compensated in a similar way. To find the proper shape of the compensation pulse, the data obtained from previous sections is used. Pulse compensation can be used as a pre-processing technique as well.

6.2.1   Compensation of the end face reflections

In this section, pulse compensation will be used to suppress the repeated reflections of the current at the end faces of a single wire. The pulse will be compensated with an additional Gaussian voltage pulse at the point of excitation x_g. Since the process of compensation is easier to visualize in the time domain, the discussion will take place in the time domain.

If the current is written as a function of the voltage, the current can be symbolically written as

$$\mathcal{I}(t) = f(\mathcal{V}(t)), \tag{6.28}$$

where the argument x is omitted. This function is envisaged in Figure 6.5 by the square containing V/I. The voltage $\mathcal{V}$ is the input and the current $\mathcal{I}$ is the output.
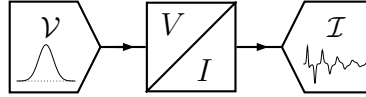
Figure 6.5: *Schematic view of $\mathcal{I}(t) = f(\mathcal{V}(t))$.*

If a second voltage pulse with amplitude A_1 and time delay T_1 is applied, the total current along the wire can be written as

$$\mathcal{I}_{\text{tot}}(t) = f(\mathcal{V}(t)) + A_1 f(\mathcal{V}(t - T_1)) = \mathcal{I}(t) + A_1\mathcal{I}(t - T_1). \tag{6.29}$$

The total process is depicted schematically in Figure 6.6. For the compensation, it is
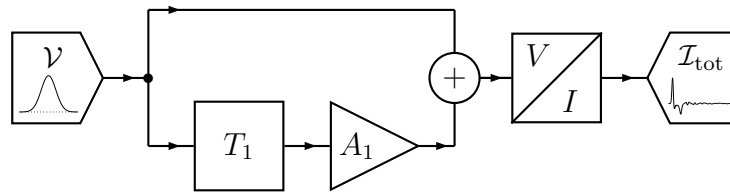
Figure 6.6: *Schematic view of $\mathcal{I}_{\text{tot}}(t) = \mathcal{I}(t) + A_1\mathcal{I}(t - T_1)$.*

required that the total current $\mathcal{I}_{\text{tot}}(t > t(1)) = 0$, where $t(1)$ represents the time it takes for the first reflected current wave to reach the point $x = x_g = L/2$. In Figure 6.7, these reflected current waves are shown. It is easily seen that the current waves that have
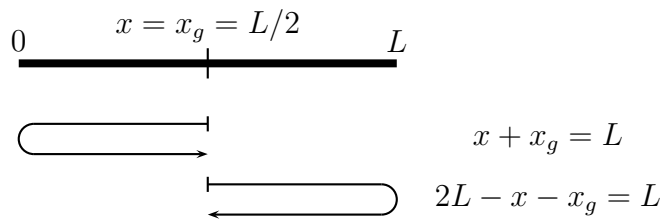
Figure 6.7: *The current waves arriving at $x = x_g = L/2$ that have been reflected once.*

been reflected once, both travel over a distance L. Therefore, the typical travel time for

$x = x_g = L/2$ is found as $t(1) = L/c_1$ where the time delay that occurs during reflection at the end faces as mentioned in Section 3.4.1 is not incorporated.

In the frequency-domain model, the current is given by

$$I_{\text{tot}}(\omega) = (1 + A_1 \exp(ik_1 T_1)) I(\omega). \tag{6.30}$$

Since the data from previous calculations is used, a sampled version of (6.29) is needed. This means that the compensation for the total current is then written as

$$\mathcal{I}_{\text{tot}}(i\Delta t) = \mathcal{I}(i\Delta t) + A_1 \mathcal{I}((i - j)\Delta t), \quad i = 0, \ldots, N, \tag{6.31}$$

where j is a fixed integer and N is the number of samples with time step Δt. The time delay is given by $T_1 = j\Delta t$. Of course, the time delay can also be found by interpolating between the discrete steps but this option is not used here since the time step is chosen very small.

The data sets from previous calculations all have the observation point at $x = x_g$. The unknown parameters A_1 and T_1 are found with an error minimization procedure.

Determination of the parameters

In this section, the unknown parameters A_1 and T_1 will be determined for $x = x_g$. To this end, the following squared error is introduced

$$\Lambda(\mathbf{p}) = \int_{t_{\min}}^{t_{\max}} [\mathcal{I}(t) + A_1 \mathcal{I}(t - T_1)]^2 \, dt = \int_{t_{\min}}^{t_{\max}} \mathcal{I}_{\text{tot}}^2(t) dt, \tag{6.32}$$

where $\mathbf{p} = [A_1, T_1]$ and $t_{\max}$ can in principle be chosen freely. When the compensation is accurate, the pulse will tend to zero rapidly for $t > t_{\min}$ so $t_{\max}$ can be fairly small to accomplish an accurate determination of the amplitude and the time delay, typically $t_{\max} = 10 t_{\min}$. This choice of $t_{\max}$ allows the current waves to be reflected at the end faces of the wire at least ten times before they reach the center of the wire again. The value $t_{\min}$ is chosen as $t(1) < t_{\min} < t(2)$, where $t(2) = 2(t(1) + \tau_d)$, where τ_d represents the additional delay time during which the current wave is being reflected at the end faces of the wire, see Section 3.4.1. The choice of $t_{\min}$ is based on the fact that the current waves reflect at the end faces of the wire at least one time before they reach the center of the wire again. The parameters are found by minimizing $\Lambda(\mathbf{p})$. To keep the option of adding additional parameters for the minimization, Powell's quadratic convergence method [67] will be used. With Powell's algorithm, multiple search directions can be employed simultaneously. The number of directions depends on the number of unknowns. In the Numerical Recipes Library [67], the search directions are cast into a matrix $\mathbf{X}$. The only real requirement for

using Powell's method is a good initial estimate $\mathbf{p} = \mathbf{p}_0$ and an initial set of search directions in $\mathbf{X}$. The unit matrix $\mathbf{X} = \mathbf{I}$ is used as the initial estimate for the search direction matrix. The minimization stops when a given tolerance is reached. To compensate the total current as accurately as possible, two options will be examined. First, the time delay T_1 is chosen fixed as the difference in time between the first local maximum of the current and the second local minimum of the current at the center of the wire. Between these instants, the current then has travelled from the point of excitation to $x = x_g$ and has been reflected once at the end faces of the wire. The amplitude A_1 is then the only parameter which needs to be optimized. The other option is to minimize with both parameters at the same time. It will be shown that this option is advantageous in comparison with the first option. Since $\tau = 0.5$ ns for the Gaussian voltage as given in Section 3.3.2, the first local maximum of the current is at the time instant $t = 4\tau = 2$ ns. The second local minimum is found from the data set to be at $t = 5.47$ ns. The initial estimates of A_1 and T_1 for both methods are chosen according to Table 6.1. The boundaries in the determination of Λ are chosen

	Initial estimates		Results after minimization	
Option	A_1	T_1 [ns]	A_1	T_1 [ns]
T_1 fixed	0.75	3.47	0.7582	3.4700
T_1 not fixed	0.75	$L/c_1 = 3.33$	0.7590	3.4637

Table 6.1: *Initial estimate and minimized values for the amplitude A_1 and time delay T_1 for both minimization options.*

as $t_{\min} = 7$ ns and $t_{\max} = 80$ ns. The parameters are determined for a wire with length $L = 1$ m and radius $a = 0.002$ m. The value for A_1 follows from the fact that the negative peak at $t(1)$ has to compensate the positive peak at $t(2)$ when the total current is zero for $t > t_{\min}$. The ratio between the amplitudes of the peaks at $t(1)$ and $t(2)$ is approximately 0.75.

After minimization, the following values for A_1 and T_1 are obtained, see Table 6.1. These results show that the amplitude, as well as the time delay have almost the same values for both choices. The total current $\mathcal{I}_{\text{tot}}(t)$ for these values of the compensation parameters is plotted in Figure 6.8. The uncompensated current is included as a reference. Comparing the three currents clearly shows that an extra compensation pulse reduces the current substantially. For the first reflection, the reduction is $20 \log(2.400/0.925) = 8.3$ dB. This is fairly good considering that the first reflection cannot be suppressed completely, see Section 1 of this chapter. For the third peak, the suppression of the current amounts
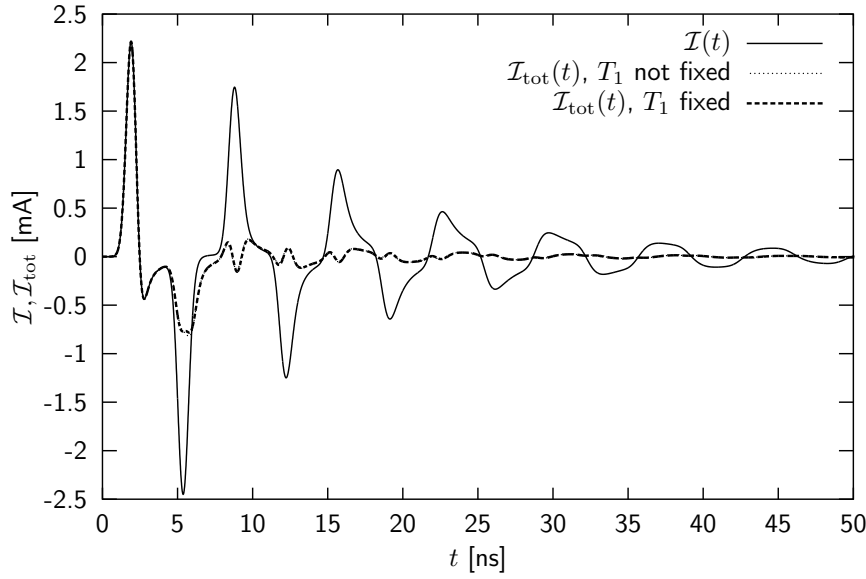
Figure 6.8: *Current at the center of a wire with length $L = 1$ m and radius $a = 0.002$ m in free space. The compensation parameters are $A_1 = 0.7582$ and $T_1 = 3.4700$ ns for T_1 fixed and $A_1 = 0.7590$ and $T_1 = 3.4637$ ns for T_1 not fixed.*

to $20 \log(1.801/0.189) = 19.6$ dB. When the current after 10 ns is zoomed in on, the compensation with T_1 not fixed reduces the current slightly better. Despite the small difference in amplitude and time delay, the option where T_1 is not fixed is preferred over the one with T_1 fixed.

Until now, the amplitude A_1 is considered real-valued. The amplitude may be complex-valued in the frequency domain. When the current is treated as a so-called dual-analytic signal, the imaginary part of the complex-valued amplitude has consequences for the time domain current. The significance of a complex amplitude A_1 for the pulse compensation can be explained with the aid of the theory of dual analytic signals [42, 68, 69]. Therefore a short discussion about such a signal is given below.

In Chapter 2, the inverse temporal Fourier transformation was defined as

$$\mathcal{F}(t) = \frac{1}{\pi} \text{Re} \int_0^\infty F(\omega) \exp(-i\omega t) d\omega, \text{ for } t \in \mathbb{R}. \tag{6.33}$$

The dual analytic signal associated with $\mathcal{F}(t)$ is then given by

$$\mathcal{F}_1(t) = \frac{1}{\pi} \int_0^\infty F(\omega) \exp(-i\omega t) d\omega \text{ for } \text{Im}(t) \leq 0. \tag{6.34}$$

With this definition, the inverse Fourier transformation for real-valued t can be written as

$$\mathcal{F}(t) = \text{Re} \left(\mathcal{F}_1(t) \right) = \text{Re} \left(\mathcal{F}_1(t - i0) \right), \tag{6.35}$$

where the notation $t - i0$ denotes the limit for Im $t \uparrow 0$. With the definition of the Hilbert transform $\mathcal{F}_H(t)$ of $\mathcal{F}(t)$, which is given by

$$\mathcal{F}_H(t) = \frac{1}{\pi} \text{PV} \int_{-\infty}^{\infty} \frac{\mathcal{F}(t')}{t - t'} dt', \tag{6.36}$$

where PV stands for the Cauchy principal value, the dual analytic signal can be written as

$$\mathcal{F}_1(t) = \mathcal{F}(t) - i\mathcal{F}_H(t). \tag{6.37}$$

Now, assume that A_1 in (6.30) is a complex-valued quantity. In that case the inverse Fourier transformation can be written as

$$\mathcal{I}_{\text{tot}}(t) = \frac{1}{\pi} \int_0^{\infty} [1 + (A_1' - iA_1'') \exp(-i\omega T_1)] I(\omega) \exp(-i\omega t) d\omega, \tag{6.38}$$

where A_1' and $-A_1''$ represent the real and imaginary part of A_1, respectively. With (6.35), the total current is found as

$$\begin{aligned} \mathcal{I}_{\text{tot}}(t) = \text{Re}(\mathcal{I}_{\text{tot},1}(t)) = \frac{1}{\pi} \Bigg\{ &\text{Re} \left(\int_0^{\infty} I(\omega) \exp(-i\omega t) d\omega \right) \\ &+ A_1' \text{Re} \left(\int_0^{\infty} I(\omega) \exp(-i\omega(t - T_1)) d\omega \right) \\ &+ A_1'' \text{Im} \left(\int_0^{\infty} I(\omega) \exp(-i\omega(t - T_1)) d\omega \right) \Bigg\} \\ = &\mathcal{I}(t) + A_1' \mathcal{I}(t - T_1) - A_1'' \mathcal{I}_H(t - T_1). \end{aligned} \tag{6.39}$$

Note that, in the frequency-domain calculations, the inclusion of the Hilbert transform does not require any significant extra computational effort.

Minimizing the squared error given by (6.32) gives the desired amplitude $A_1 = A_1' - iA_1''$ and the time delay T_1. The initial estimates are given in Table 6.2. The parameters are

	Initial estimates			Results after minimization		
Option	A_1'	A_1''	T_1 [ns]	A_1'	A_1''	T_1 [ns]
T_1 fixed	0.75	0	3.470	0.7596	0.0327	3.470
T_1 not fixed	0.75	0	$L/c_1 = 3.33$	0.7538	0.1315	3.384

Table 6.2: *Initial estimate and minimized values for the complex amplitude A_1 and time delay T_1 for both minimization options.*

again determined for a wire with length $L = 1$ m and radius $a = 0.002$ m. The boundaries in the determination of Λ are chosen as $t_{\min} = 7$ ns and $t_{\max} = 80$ ns. After minimization,
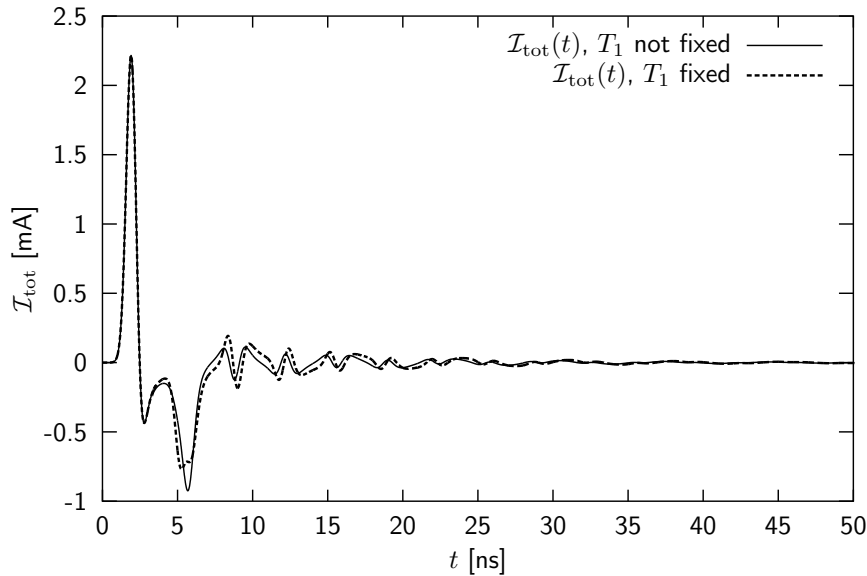
Figure 6.9: *Current at the center of a wire with length $L = 1$ m and radius $a = 0.002$ m in free space. The compensation parameters are given in Table 6.2.*

the values for A_1 and T_1 are obtained as in Table 6.2. The total current $\mathcal{I}_{\text{tot}}(t)$ is plotted for these parameters in Figure 6.9. As can be seen, the option with T_1 not fixed compensates the first reflected current wave better when compared to T_1 fixed. For later reflections, the option where T_1 is minimized performs better. As mentioned earlier, the current wave is not immediately reflected when it arrives at the end faces [35], see also Section 3.4.1. An additional time delay τ_d exists between arrival and reflection at the end faces. Therefore the fixed value for T_1 is more accurate for the first reflection but not for later reflections. Since the value of the calculated time delay T_1 comes closer to the initial estimate for T_1, it follows that A_1'' governs part of τ_d.

A comparison of Figure 6.8 with Figure 6.9 shows that the complex-valued amplitude A_1 is preferred over the real-valued amplitude.

From now on, compensation of the current will take place with a complex value of A_1. The minimized version of the time delay T_1 is chosen in the case of a single wire.

6.2.2   Compensation for a single thin wire

In the previous section, the compensation parameters have been determined by using previously generated data sets. Since the current in Hallén's equation depends linearly on the input voltage, pulse compensation can be employed on the excitation as well. The only modification of Hallén's equation is to multiply the voltage $V(\omega)$ with a factor of

$1 + A_1 \exp(ik_1 T_1)$. Hallén's equation for a single wire then reads

$$\int_0^L \frac{I(x', \omega) \exp(ik_1 R_a)}{4\pi R_a} dx' - F_0(\omega) \exp(ik_1 x) - F_L(\omega) \exp(ik_1(L-x))$$
$$= \frac{Y_1}{2} [1 + A_1 \exp(ik_1 T_1)] V(\omega) \exp(ik_1 |x - x_g|), \tag{6.40}$$

for $0 \leq x \leq L$. Pulse compensation is used on the data of the uncompensated wire of Figure 6.2.

The wire is again of length $L = 1$ m and radius $a = 0.002$ m. The spatial discretization is $M = 60$ and the number of time steps is $N = 512$. The wire is excited by the Gaussian voltage as given in Section 3.3.2. The result for $A_1 = 0.7538 - i0.1315$ and $T_1 = 3.3784$ is shown in Figure 6.10(B). The current along a perfectly conducting wire is added for comparison in Figure 6.10(A). It is observed that the current in (B) does not attenuate towards the end points as nicely as in the Wu-King case, see Figure 6.2 (B). This is a direct result from the compensation delay time T_1. The resistive profile has an effect immediately at the time of excitation. With pulse compensation, the second voltage pulse can only be applied when the current wave has reflected at least once. The effects of pulse compensation start from $t > T_1$. After the first positive and negative peak in plot (B), the current is effectively attenuated.

(A) (B)
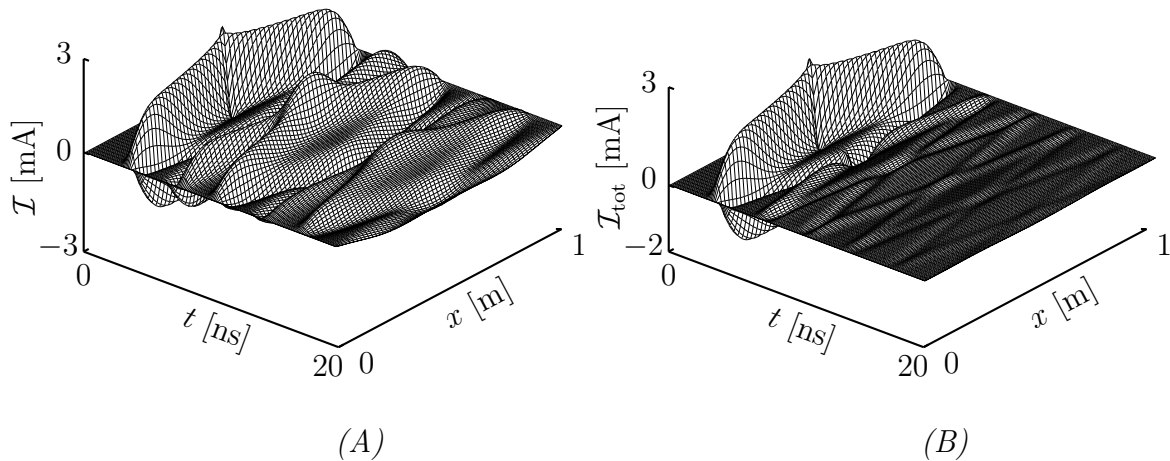
Figure 6.10: *The induced current along a single thin wire with length $L = 1$ m and radius $a = 0.002$ m, $M = 60$ and $N = 512$ in free space. The current along a perfectly conducting wire is visualized in plot (A). The current along a pulse-compensated thin wire with $A_1 = 0.7538 - i0.1315$ and $T_1 = 3.3784$ ns is visualized in plot (B).*

6.2.3   Compensation for two coupled thin wires

Now that the current along a single thin wire can be compensated satisfactorily, a second wire is added to study the effect of pulse compensation of a transmitting wire on the current along a receiving wire. These wires are again denoted as wire 1 and wire 2, respectively. Both wires have length $L = 1$ m and radius $a = 0.002$ m. The distance between the wires is $d = 1$ m. Both wires are embedded in free space. The initial estimates are given in Table 6.2 for T_1 not fixed.

When the influence of wire 2 is taken into account, the compensation parameters for the current along wire 1 are found as $A_1 = 0.7417 - i0.1196$ and $T_1 = 3.3786$ ns when T_1 is optimized and $A_1 = 0.7461 - i0.02$ and $T_1 = 3.47$ ns when T_1 is fixed. The presence of wire 2 does not change the parameters drastically in comparison with the case of a single thin wire in free space.

The total current along wire 2 with the compensation parameters from wire 1 is given by

$$\mathcal{I}_2'(t) = \mathcal{I}_2(t) + A_1'\mathcal{I}_2(t - T_1) - A_1''\mathcal{I}_{2,H}(t - T_1), \tag{6.41}$$

where $\mathcal{I}_2(t)$ is the current along wire 2 in the case of an uncompensated wire 1. The coupling from the current along wire 1 to the current along wire 2 is depicted schematically in Figure 6.11. It can be seen that the voltage pulse is the source for the total, compensated current along wire 1 and subsequently a direct field originating from wire 1. In the second schematic view, this direct field is the source for the current along wire 2.
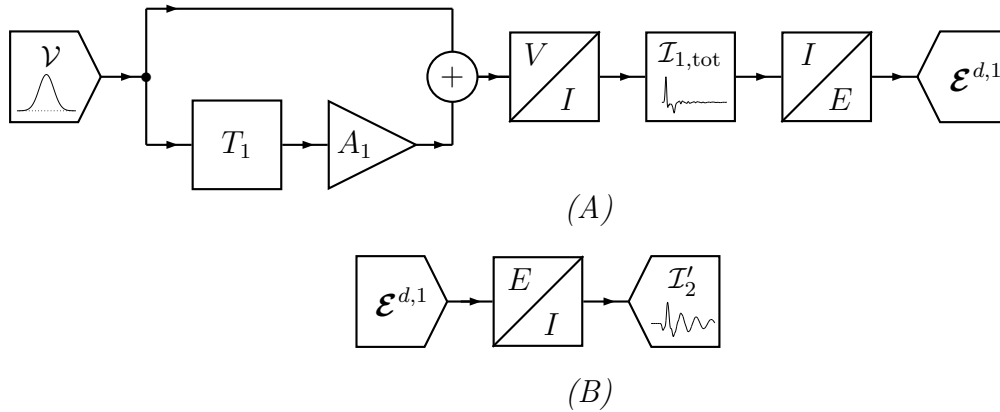
Figure 6.11: *Schematic visualization of the current functions along wires 1 (A) and 2 (B), respectively.*

In Figure 6.12, the current at the center of both wires has been plotted for both compensation parameters. The compensated current along a single thin wire is included in (A) and the uncompensated current along wire 2 is included in (B).
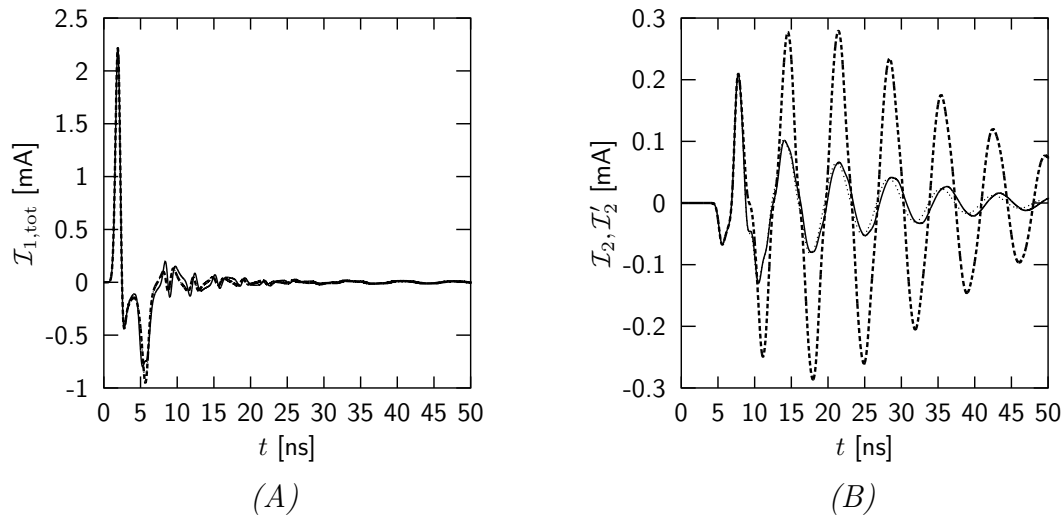
Figure 6.12: *Current at the centers of wire 1 and wire 2. Both wires have length $L = 1$ m and radius $a = 0.002$ m. The embedding is free space. The current along wire 1 is compensated with parameters $A_1 = 0.7461 - i0.02$ and $T_1 = 3.47$ ns when T_1 is fixed (solid lines) and $A_1 = 0.7417 - i0.1196$ and $T_1 = 3.3786$ ns when T_1 is optimized (dotted lines). In plot (A), the compensated current for a single wire is added for comparison (dashed line in left plot). In plot (B), the uncompensated current along wire 2 has been added for comparison (dashed line).*

From (A) in Figure 6.12, it is observed that the compensation where T_1 is optimized results in a slightly better compensation. The compensated current along a single wire in free space is similar to the result where T_1 is optimized. It is also seen that in general, the current along wire 1 is hardly affected by the presence of wire 2. On the other hand, the current along wire 2 is heavily affected by the compensation of wire 1. The attenuation for the second negative peak is about 6 dB. The first two peaks are not affected because these are mainly caused by the first maximum of the current along wire 1, which is not compensated. The compensation on wire 1 has an effect from about 3 ns after the start of the first current peak. The current along wire 2 shows the same time delay before the shape of the current changes. The oscillatory behavior of the current did not vanish. The compensation for T_1 optimized gives a slightly better reduction of the magnitude of the current when compared to the compensation with T_1 fixed. Therefore, the optimized version of T_1 is used in future calculations.

6.2.4 Pulse compensation of wire 2

Although the current along wire 2 is already attenuated considerably, pulse compensation is also applied to reduce the current along wire 2 even further after some time instant $t > T_2$, where T_2 is the time delay for the compensation of the current along wire 2. In the previous chapter, it was demonstrated that wire 1 is not affected by the presence of another wire. Therefore, wire 1 can be regarded as an impressed source for wire 2.

Since wire 2 is excited by a secondary field and not by a voltage pulse, the compensation works on the secondary incident field. The determination of the compensation parameters for wire 1 is based on the fact that the source is located at the center of the wire. For wire 2, the secondary field impinges along the whole wire. To ensure that both current waves have the same time delay, the current waves are reflected at least twice before they reach the point of excitation again, see Figure 6.13. The current along wire 2 depends linearly
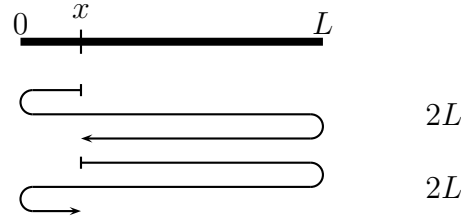
Figure 6.13: *The current waves arriving at a point x that have been reflected twice.*

on these secondary fields. The compensation parameters for wire 1 are already determined in the previous section. These parameters are directly related to the wire geometry.

The total currents along wire 1 and wire 2 with the compensation pulse are now defined as

$$\mathcal{I}_{1,\mathrm{tot}}(t) = \mathcal{I}_1(t) + A_1'\mathcal{I}_1(t - T_1) - A_1''\mathcal{I}_{1,H}(t - T_1),$$
$$\mathcal{I}_{2,\mathrm{tot}}(t) = \mathcal{I}_2'(t) + A_2'\mathcal{I}_2'(t - T_2) - A_2''\mathcal{I}_{2,H}'(t - T_2),$$

with

$$\mathcal{I}_2'(t) = \mathcal{I}_2(t) + A_1'\mathcal{I}_2(t - T_1) - A_1''\mathcal{I}_{2,H}(t - T_1),$$
$$\mathcal{I}_{2,H}'(t) = \mathcal{I}_{2,H}(t) + A_1'\mathcal{I}_{2,H}(t - T_1) + A_1''\mathcal{I}_2(t - T_1),$$

and where the subscripts 1 and 2 refer to the wires that are compensated. The currents with the prime represent the results as given in (6.41). The Hilbert transform $\mathcal{I}_{2,H}'(t)$ is obtained in a similar way as (6.39). The total current along wire 2 is shown schematically in Figure 6.14. Both wires again have a length $L = 1$ m and radius $a = 0.002$ m. The distance between the wires is $d = 1$ m. Since the wires are of equal length, the time delay is
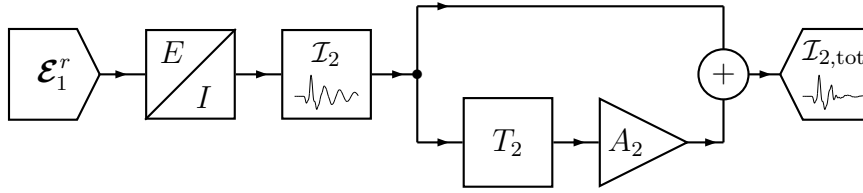
Figure 6.14: *Schematic visualization of the total current function along wire 2*

chosen as $T_2 = 2T_1$ and the amplitude as $A_2 = -A_1^2$. The wires are again embedded in free space. In Figure 6.15, the current at the center of wire 2 is plotted for the compensation parameters as given above.

From the results, it is seen that the current along wire 2 is reduced heavily by the compensation. Between 15 ns and 30 ns the current is not fully attenuated after compensation. The current along wire 1 is also not fully attenuated in this time interval but oscillates slightly and has almost the same magnitude as the current along wire 2 (dotted line). The oscillation of the current along wire 2 is maintained by the mutual coupling between the wires, see Chapter 4. After 30 ns, the current is fully attenuated. The magnitude of the current along the pulse compensated wires is about 10 times higher than in the Wu-King case.

Since the coupling between the wires affects the compensation of the current along wire 2, the parameters A_2 and T_2 are optimized in a similar way as A_1 and T_1 were found. In previous sections, the currents along both wires have been calculated for various configurations. These data are again used for the determination of optimized compensation parameters for wire 2. The initial estimates are given by $A_2 = -(0.75)^2 = -0.5625$ and $T_2 = 2L/c_1 = 6.67$ ns, see Figure 6.13. After minimization, the optimized compensation parameters for wire 2 are found as

$$A_2' = -0.5961, \quad A_2'' = -0.2491, \quad T_2 = 6.6643 \text{ ns}.$$

The current at the center of wire 2, $\mathcal{I}_{2,\text{tot}}$, is plotted in Figure 6.16 for two sets of compensation parameters. In the first case, the parameters obtained for wire 1 are used, i.e. $A_2 = -A_1^2$ and $T_2 = 2T_1$. In the second case, the optimized parameters are used. The current along wire 2 is already heavily influenced by the compensation of the current along wire 1. The current along wire 2 is compensated after approximately 20 ns. In comparison, the optimized parameters result in a better attenuation between 15 ns and 30 ns. After 30 ns, the other set of parameters gives better results.

It has been shown that the current along the wire can be compensated in a similar way as the current along wire 1. This is explained from the fact that wire 1 is identical to wire 2. Because the excitation of the current along wire 2 is more complicated in comparison to the current along wire 1, the time delay T_2 is larger.
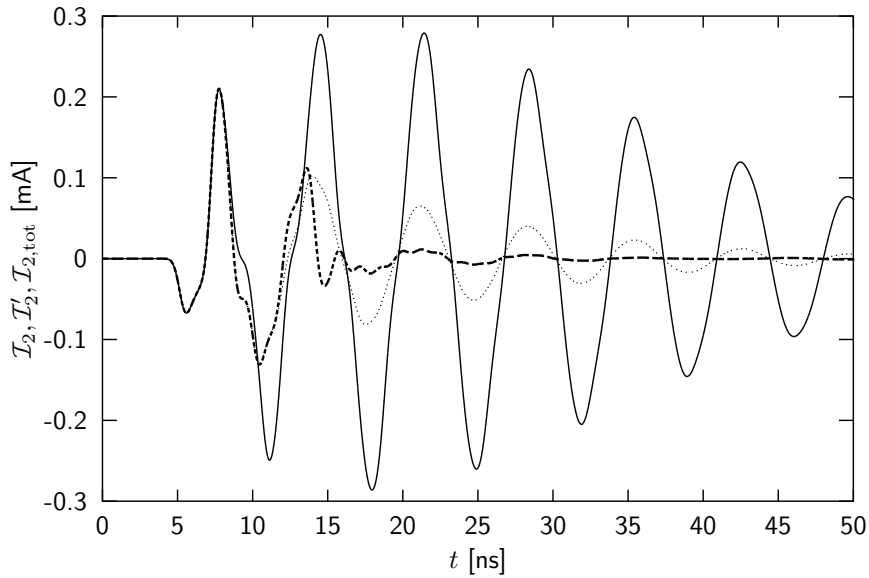
Figure 6.15: *Current at the center of wire 2 in free space. The length of the wire is $L = 1$ m and the radius $a = 0.002$ m. The solid line represents $\mathcal{I}_2$ when wire 1 is not compensated. The dotted line represents $\mathcal{I}_2$ when wire 1 is compensated with $A_1 = 0.7417 - i0.1196$, $T_1 = 3.3786$ ns and wire 2 is not compensated. The dashed line represents $\mathcal{I}_2$ when wire 1 is compensated with $A_1 = 0.7417 - i0.1196$, $T_1 = 3.3786$ ns and wire 2 with $A_2 = -A_1^2$ and $T_2 = 2T_1$.*
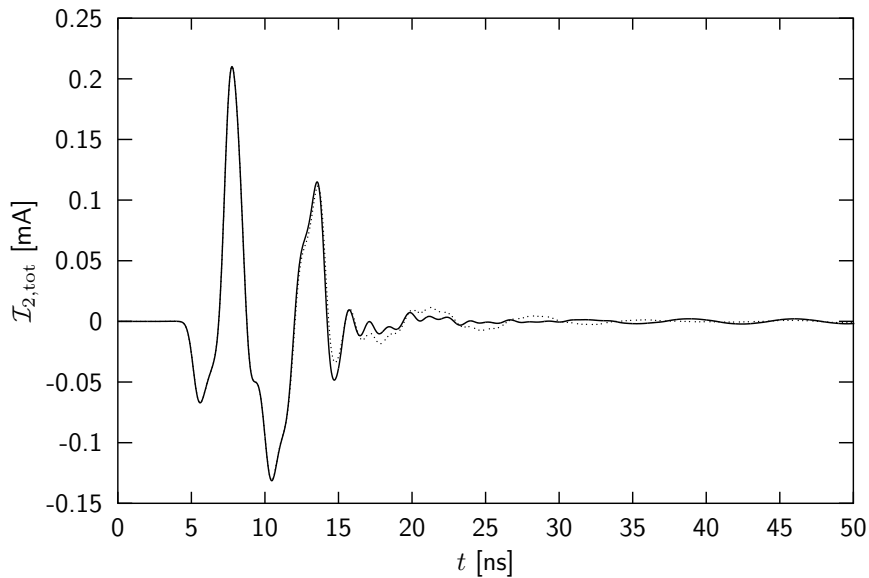
Figure 6.16: *Current at the center of wire 2 with length $L = 1$ m and radius $a = 0.002$ m in free space. Wire 1 is compensated with $A_1 = 0.7417 - i0.1196$, $T_1 = 3.3786$ ns. The dotted line represents represents $\mathcal{I}_2$ when wire 2 is compensated with $A_2 = -A_1^2$ and $T_2 = 2T_1$. The solid line represents $\mathcal{I}_2$ when wire 2 is compensated with the optimized values $A_2 = -0.5961 + i0.2491$ and $T_2 = 6.6643$ ns.*

Chapter 7

Enhanced detection of a buried wire

In this chapter a simple two-wire detection set up is considered to detect a buried wire with a minimum of post-processing techniques. The high direct coupling between the two wires, whether or not in the presence of an interface, turned out to be the major problem in detecting the buried wire directly from the current along wire 2. By suppressing the late-time reflections of the current along the wire, the effects of mutual coupling can be reduced as was shown in the previous chapter.

In Chapter 6, a Wu-King resistance profile and pulse compensation were shown to attenuate the late time response of the current along a wire. Both techniques are used to enhance the detection of a buried wire.

First, the resistively loaded wires are used in a half-space configuration as depicted in Figure's 4.8 and 4.12. Then, pulse compensation is used for the wires of the detection set up in a similar configuration. The compensation parameters are calculated for the same configuration in absence of the buried wire.

At the end of this chapter, the influence of various parameters of the configuration on the compensation parameters is examined.

7.1   A detection set up with resistively loaded wires

In this section, the wires of the detection set up are loaded with the Wu-King resistance profile.

The first configuration that is considered is the two-wire configuration that is depicted in Figure 4.8. The wires have a length $L = 1$ m and radii $a = 0.002$ m. The distance between the wires is $d = 1$ m. The relative complex permittivity of the upper half space is $\varepsilon_{1r} = 1$. The permeability is μ_0 for both half spaces. In Figure 7.1, the currents at the centers of

(A)

(B)

(C)

(D)

(E)

(F)
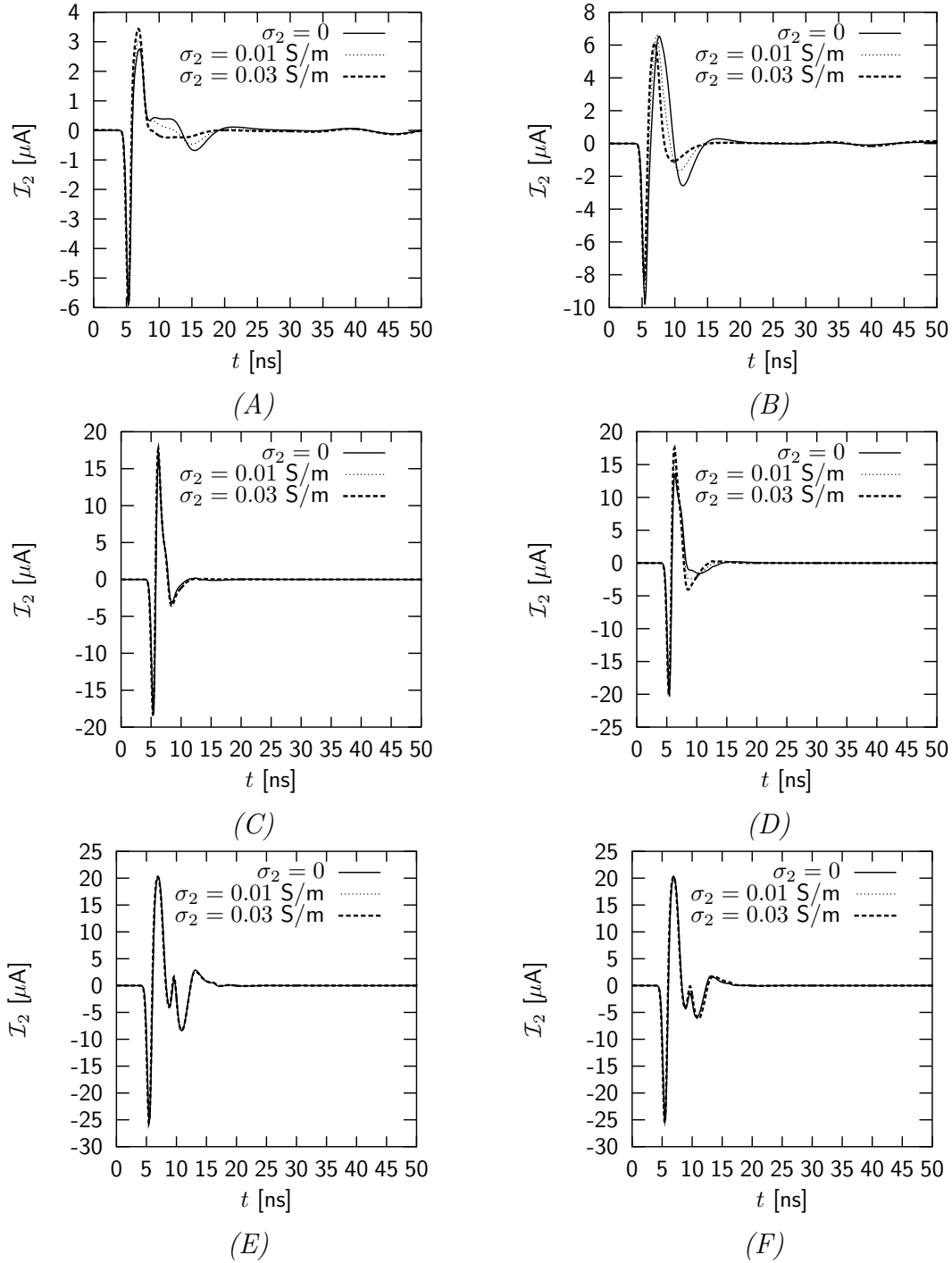
Figure 7.1:   *The induced currents at the center of wire 2 with length $L = 1$ m and radius $a = 0.002$ m for different conductivities σ_2. The distance is $d = 1$ m and $z_1 = -0.1$ m for (A) and (B), $z_1 = -0.25$ m for (C) and (D) and $z_1 = -1$ m for (E) and (F). The medium properties are $\epsilon_{1r} = 1$, $\epsilon_{2r} = 9$ for (A), (C) and (E) and $\epsilon_{1r} = 1$, $\epsilon_{2r} = 3$ for (B), (D) and (F). The permeability is μ_0 for all configurations. The excitation is a Gaussian voltage pulse with $\tau = 0.5$ ns and $t_1 = 4\tau$.*

wire 2 are plotted for various permittivities of the lower half space. The height is varied
as $z_1 = -0.1$ m, $z_1 = -0.25$ m and $z_1 = -1$ m. The current at the center of wire 1 for all
these configurations can be found in Figure 7.2.

The relative permittivity of the lower half space is $\epsilon_{2r} = 9$ for all plots on the left and
$\epsilon_{2r} = 3$ for all plots on the right. The conductivity of the lower half space is varied as
$\sigma_2 = 0$, $\sigma_2 = 0.01$ S/m and $\sigma_2 = 0.03$ S/m.

(A)   *(B)*
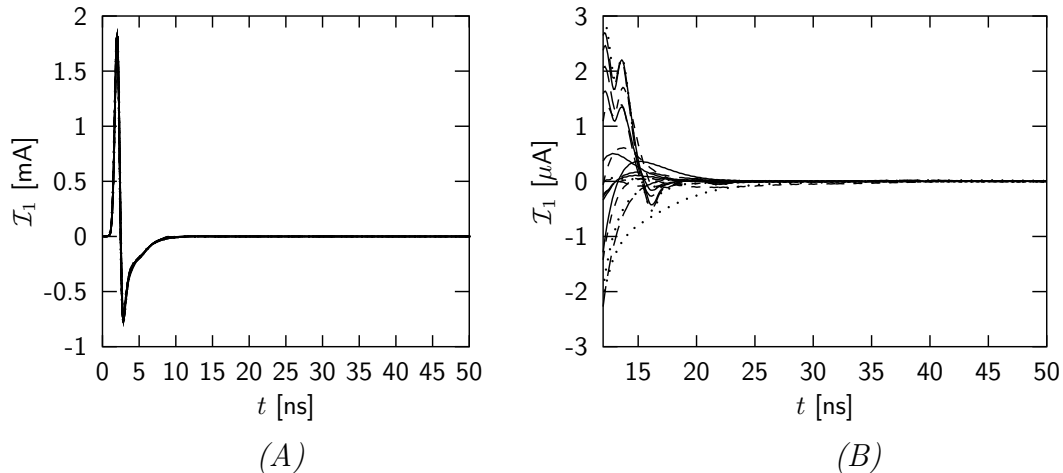
Figure 7.2: *The induced current at the center of wire 1 with length $L = 1$ m and radius
$a = 0.002$ m for different conductivities σ_2, permittivities ϵ_{2r} and heights z_1. The distance
between the wires is $d = 1$ m and $\varepsilon_{1r} = 1$. The permeability is μ_0 for all configurations.
The excitation is a Gaussian voltage pulse with $\tau = 0.5$ ns and $t_1 = 4\tau$.*

From Figure 7.2(A), it is immediately seen that regardless of the configuration, the current
along wire 1 is hardly influenced. That the current along wire 1 is still slightly affected by
the presence of the interface can be seen in (B).

The currents along wire 2 in Figure 7.1 are affected by the presence of the interface when
the detection set up is located close to the interface, see (A) and (B). The influence of
the conductivity in these successive plots can easily be noticed. The conductivity has an
effect within the time span from $5 < t < 20$ ns. For lower permittivity, (B), the effect
of the conductivity is bigger. The influence of the conductivity increases with decreasing
relative permittivity. This can also be observed from (C) and (D) where the height is
increased to $z_1 = -0.25$ m. The current in (D) is still affected by the conductivity while,
in (C), the current is no longer affected for the presented conductivities. In the plots
where $z_1 = -1$ m, the currents are no longer affected by the conductivity of the lower half
space. It is clear that an interface is present because of the small additional waveform
between 9 ns and 15 ns. The magnitude of the additional waveform is smaller when the
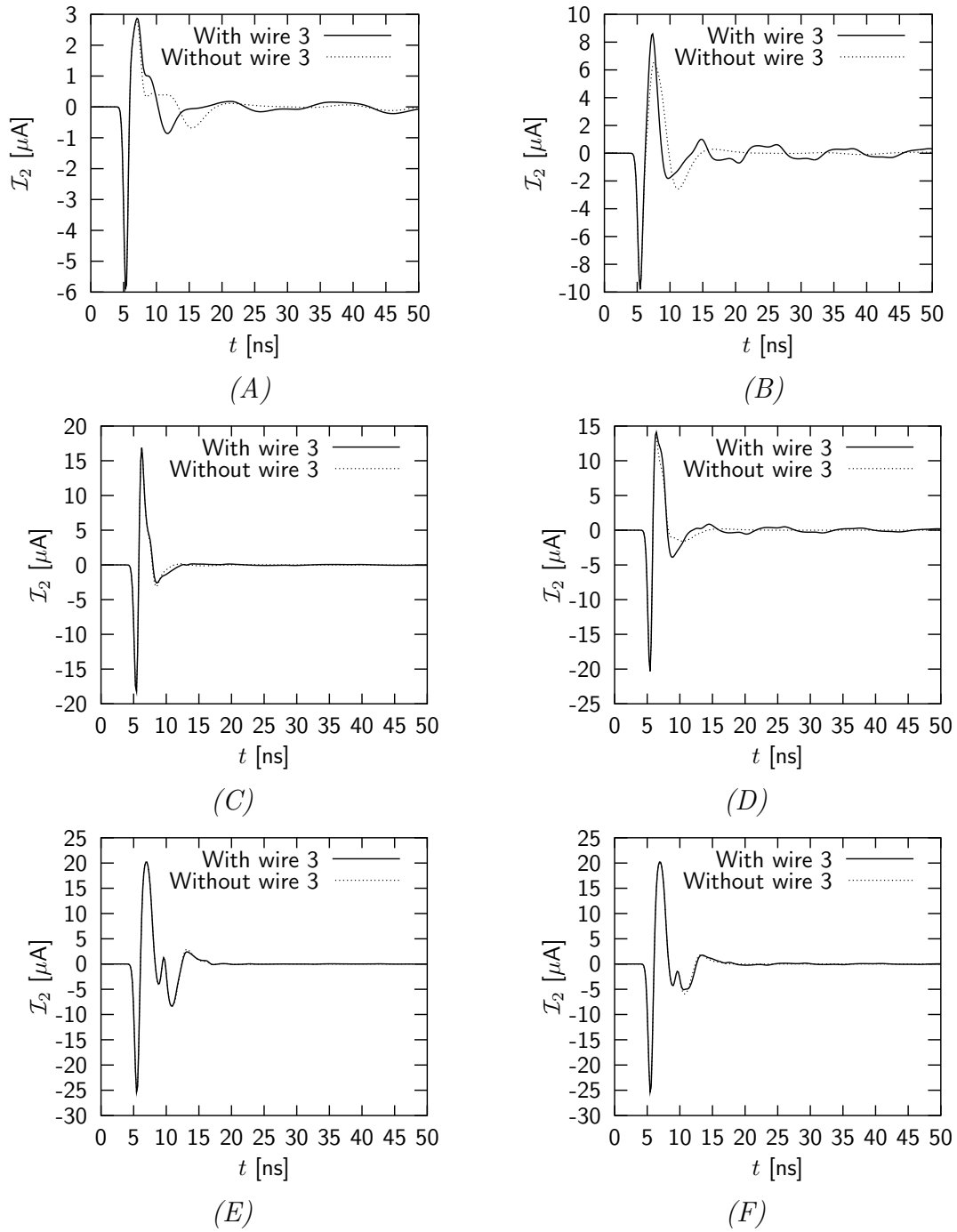
Figure 7.3: *The induced currents at the center of wire 2 with length $L = 1$ m and radius $a = 0.002$ m. The distance is $d = 1$ m and $z_1 = -0.1$ m for (A) and (B), $z_1 = -0.25$ m for (C) and (D) and $z_1 = -1$ m for (E) and (F). The medium properties are $\epsilon_{1r} = 1$, $\sigma_1 = \sigma_2 = 0$, $\mu_1 = \mu_2 = \mu_0$ and $\epsilon_{2r} = 9$ for (A), (C) and (E) and $\epsilon_{r,2} = 3$ for (B), (D) and (F). The buried wire has length $L = 1$ m, radius $a = 0.002$ m and is positioned at $z_2 = 0.1$ m. The excitation is a Gaussian voltage pulse with $\tau = 0.5$ ns and $t_1 = 4\tau$.*

relative permittivity is lower. The direct effect of a lower permittivity is a smaller reflection coefficient at the interface. Due to the reduced reflection at the interface, the current along wire 2 is less influenced when the permittivity is lower. Since wire 1 is not at all affected by its environment and the medium parameters of the upper half space are chosen equal to the ones from free space, in the remainder of this section, only plots of the current along wire 2 are given.

In Figure 7.3, the configuration as depicted in Figure 4.12 is considered. The medium parameters of the lower half space are $\epsilon_{2r} = 9$, $\sigma_2 = 0$ for all plots on the left and $\epsilon_{2r} = 3$, $\sigma_2 = 0$ for all plots on the right. Wire 3 with length $L = 1$ m and radius $a = 0.002$ m may be present in the lower half space at a depth of $z_2 = 0.1$ m. The lateral distance of wire 3 is given as $d_2 = 0.5$ m. At $z_1 = -1$ m, the current along wire 2 is hardly affected by the presence of wire 3. At $z_1 = -0.1$ m, there is a significant difference in the currents along wire 2 due to the presence of wire 3. In (B), the shape of the current clearly changes. In (A), the shape of the current also changes but to a lesser extent than in (B). At $z_1 = -0.25$ m, the current along wire 2 in (C) is hardly affected by the presence of the buried wire. When the permittivity is lower, see (D), the shape of the current still changes due to the presence of the buried wire. Looking at the late-time behavior of the current along wire 2, $t > 15$ ns, gives the impression that the shape of the current along wire 3 is visible. In Figure 7.4, the absolute value of the current at the center of wire 2 with and without wire 3, as well as the absolute value of the current at the center of wire 3 is plotted. The current along wire 2 indeed adapts to the current along wire 3. The shape of the current along wire 3 can be read immediately from the current along wire 2. The magnitude of the current along wire 3, when compared to the magnitude of the current along wire 2, is bigger. This is due to the fact that wire 3 is not loaded with the Wu-King profile.

To conclude this section, the effect of the conductivity σ_2 of the lower half space is studied. In Figure 7.5, the current at the center of wire 2 has been plotted for 3 different situations regarding wire 3. All three wires are again of length $L = 1$ m and radius $a = 0.002$ m. The height of the detection set up is $z_1 = -0.1$ m. The medium parameters are $\epsilon_{1r} = 1$, $\sigma_1 = 0$, $\epsilon_{2r} = 9$ for all plots on the left and $\epsilon_{2r} = 3$ for all plots on the right. The conductivity of the lower half space is varied as $\sigma_2 = 0$ in (A) and (B), $\sigma_2 = 0.01$ S/m in (C) and (D) and $\sigma_2 = 0.03$ S/m in (E) and (F). From (A) and (B), it follows that the transmitted field from wire 2 at a depth of $z_2 = 0.5$ m arrives 5.5 ns later in (A) than in (B). This is explained from the difference in optical path length divided by the respective wave speeds, which is exactly 5.5 ns. The difference between the arrival times of the transmitted field from wire 3 at $z_2 = 0.5$ m and $z_2 = 1$ m is approximately 9 ns
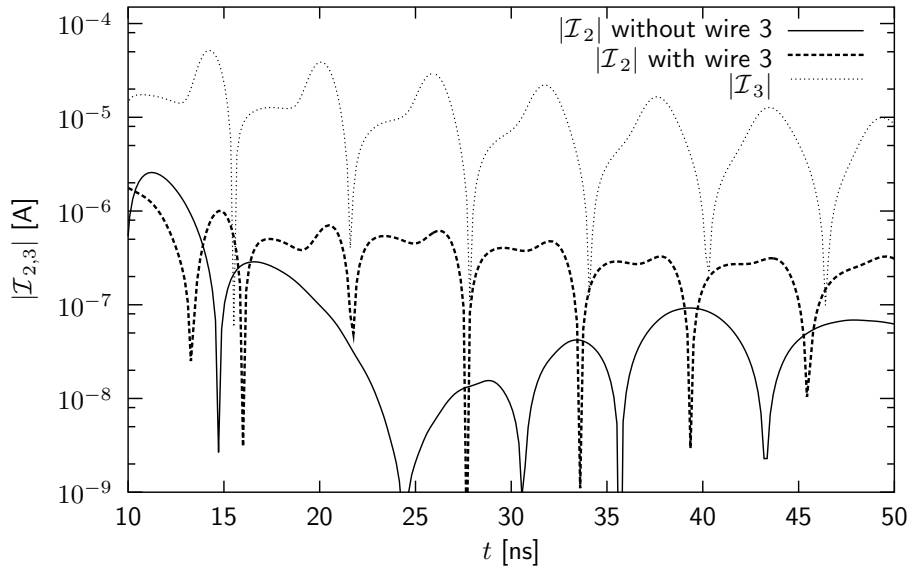
Figure 7.4: *The induced current at the center of wire 2 and wire 3 with lengths $L = 1$ m and radii $a = 0.002$ m. The distance is $d = 1$ m and height and depth are $z_1 = -0.1$ and $z_2 = 0.1$ m, respectively. The medium properties are $\epsilon_{1r} = 1$, $\sigma_1 = \sigma_2 = 0$, $\epsilon_{2r} = 3$ and the permeability is μ_0 for both half spaces. The excitation is a Gaussian voltage pulse with $\tau = 0.5$ ns and $t_1 = 4\tau$.*

for $\epsilon_{2r} = 9$ and 5 ns for $\epsilon_{2r} = 3$. The difference in travel times for the optical path length shows similar figures. Furthermore, it is noted that the presence of wire 3 shows up as a typical waveform in the current along wire 2. This waveform is almost the same for both permittivities and originates from the first current pulse induced on wire 3. Since the current along wire 2 adapts to the behavior of wire 3, the occurrence of peaks at later times gives additional information about both the depth of the wire and the lower half space provided that information about the type of buried object is known.

In (C), the presence of wire 3 still adds the typical waveform to the current along wire 2, but with a lower amplitude. The conductivity of the lower half space has a double effect on the transmitted field from wire 2. First, the fields in the lower half space are attenuated while travelling to and from wire 3. Second, the induced current along wire 3 is more rapidly attenuated for higher conductivities and for later times, see Figure 4.7. The consequences for the current along wire 2 are a reduced additional waveform due to the damping of the involved fields in the lower half space and a heavy attenuation of the late-time response of the current along wire 3. In (D), the current along wire 2 is hardly influenced by the presence of a buried wire. When the conductivity is increased further,
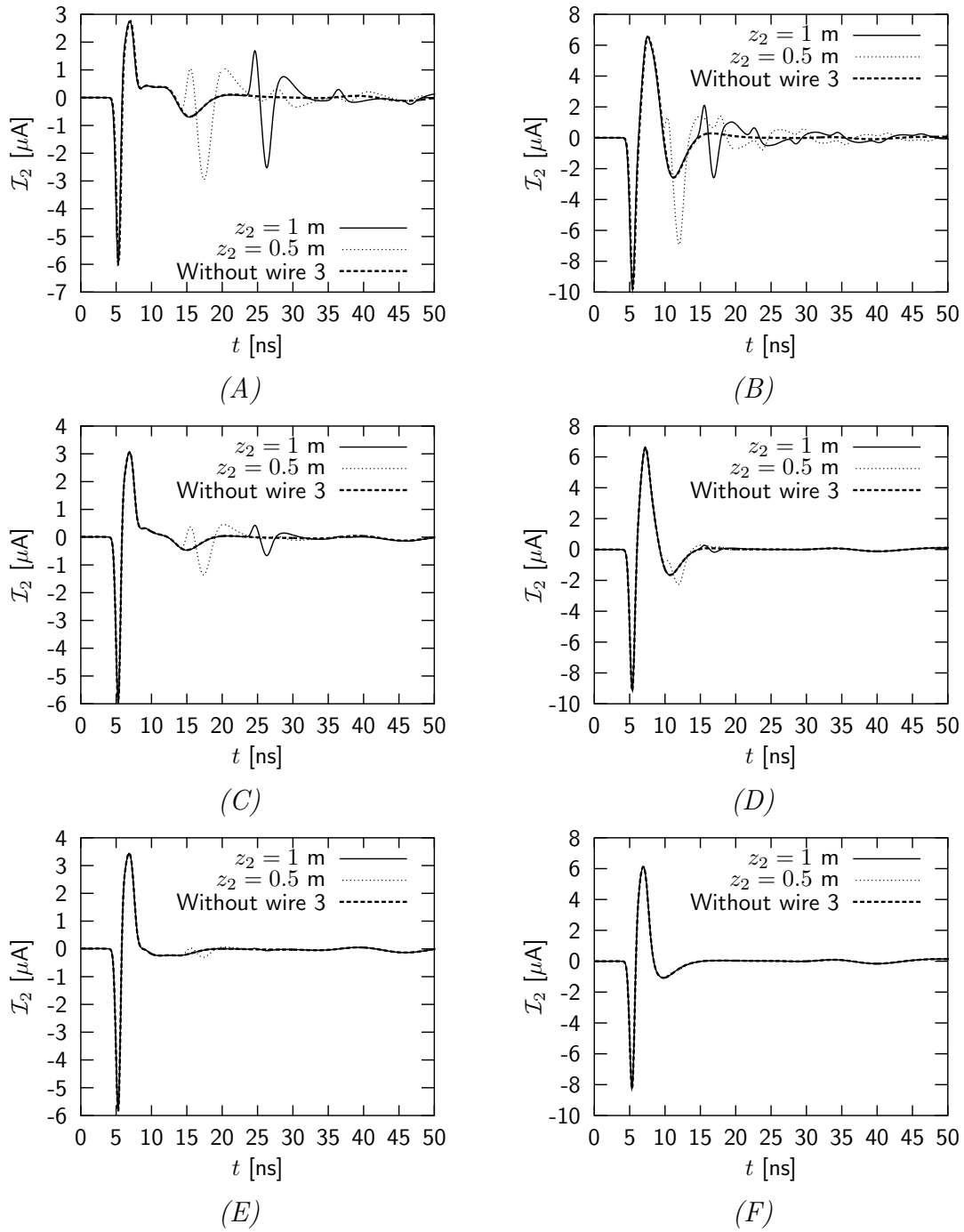
Figure 7.5: *The induced current at the center of wire 2 with length $L = 1$ m and radius $a = 0.002$ m for different depths z_2 of the buried wire. The distances are $d = 1$ m and $d_2 = 0.5$ m. The depth of wire 3 is varied as indicated in each plot. The medium properties are $\epsilon_{1r} = 1$, $\sigma_1 = 0$, $\epsilon_{2r} = 9$ for all plots on the left and $\epsilon_{2r} = 3$ for all plots on the right. The conductivity of the lower half space is varied as $\sigma_2 = 0$ in (A) and (B), $\sigma_2 = 0.01$ S/m in (C) and (D) and $\sigma_2 = 0.03$ S/m in (E) and (F). The permeability is μ_0 for all configurations. The excitation is a Gaussian voltage pulse with $\tau = 0.5$ ns and $t_1 = 4\tau$.*

see (E) and (F), the current along wire 2 is hardly affected by the presence of wire 3. In general, the influence of the conductivity is again more substantial when the permittivity is lower.

7.2   A detection set up with pulse-compensated wires

In this section, pulse-compensated wires are used in the detection set up. From previous results, it is observed that the detection set up should be positioned close to the interface. With pulse compensation, the effects of the interface on the current along wire 2 can be partly eliminated. This is achieved by adding a third compensation to the current along wire 2 as is depicted schematically in Figure 7.6. The direct field $\boldsymbol{\mathcal{E}}^{d,1}$ originates from wire
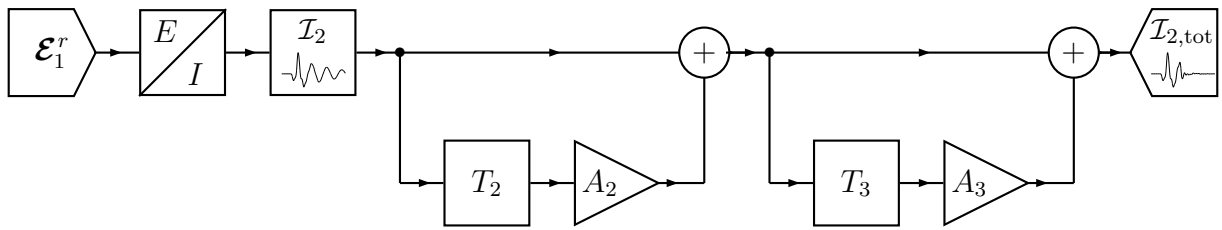
Figure 7.6: *Schematic visualization of the total current function along wire 2*

1 as depicted in Figure 6.11(A). This third compensation does not have fixed parameters but the compensation parameters depend on the medium properties of the lower half space. The first configuration that is considered is the two-wire configuration depicted in Figure 4.8. The wires have length $L = 1$ m, radius $a = 0.002$ m and the distance between the wires is $d = 1$ m. The height is $z_1 = -0.1$ m. The relative complex permittivity of the upper half space is $\epsilon_{1r} = 1$. The conductivity of the lower half space is $\sigma_2 = 0$. The permeability is μ_0 for both half spaces.

In Figure 7.7, the currents at the center of wire 2 are plotted for the relative permittivities $\epsilon_{2r} = 9$ and $\epsilon_{2r} = 3$ of the lower half space. The wires are compensated with the free-space parameters and with the parameters A_3, T_3 that have been optimized for the respective half spaces. The values of the compensation parameters for the different configurations are tabulated in Table 7.1.   In all cases, the additional compensation for wire 2 gives a better attenuation of the current along wire 2. When the height of the detection set up is $z_1 = -0.1$ m, the current is compensated very well after 25 ns.

ϵ_{2r}	$z_1[m]$	A_3'	A_3''	T_3 [ns]
3	-0.1	-0.084	-0.101	7.233
9	-0.1	-0.055	-0.027	7.281

Table 7.1: *The compensation parameters for different configurations.*

(A) $\qquad\qquad\qquad\qquad\qquad$ (B)
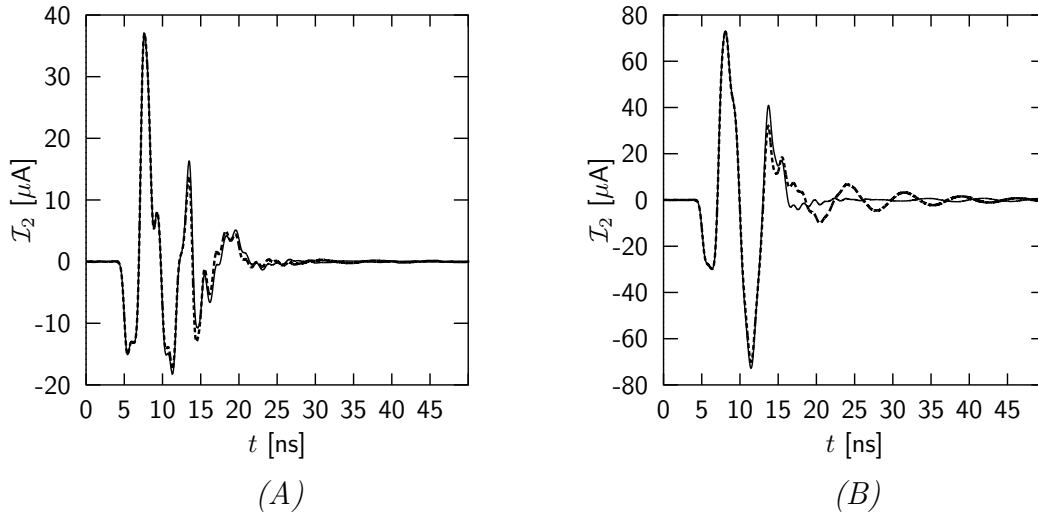
Figure 7.7: *The induced current at the center of wire 2 with length $L = 1$ m and radius $a = 0.002$ m. The distance between the wires is $d = 1$ m and the height is $z_1 = -0.1$ m. The medium properties are $\epsilon_{1r} = 1$, $\sigma_1 = \sigma_2 = 0$, $\epsilon_{2r} = 9$ (A) and $\epsilon_{2r} = 3$ (B). The permeability is μ_0 for all configurations. The currents are pulse compensated with optimized values (solid lines) and free-space values (dashed lines).*

7.2.1 The influence of various parameters on the pulse compensation

The presence of an interface has an influence on the currents of wire 1 and wire 2, which are both located at a height z_1 above the interface. It was observed that the presence of wire 2 affects the compensation parameters of wire 1 slightly. With a third compensation, effects from the lower half space can be partly eliminated. From previous results it was observed that the interface has a strong effect on the currents along the wires when z_1 is small. It is therefore interesting to see how the compensation parameters depend on the height z_1. In Table 7.2, the results are given for $0.1 \leq |z_1| \leq 1$ and the relative permittivities $\epsilon_{2r} = 3$, $\epsilon_{2r} = 9$ and $\epsilon_{2r} = 16$. In Figure 7.8, the real part of the amplitude A_3 is plotted as a function of the height z_1. The relative permittivity of the lower half space is varied as $\epsilon_{2r} = 3$, $\epsilon_{2r} = 9$ and $\epsilon_{2r} = 16$, respectively.

z_1 [m]	$\epsilon_{2r} = 3$			$\epsilon_{2r} = 9$			$\epsilon_{2r} = 16$		
	A_3'	A_3''	T_3 [ns]	A_3'	A_3''	T_3 [ns]	A_3'	A_3''	T_3 [ns]
-0.1	-0.084	-0.101	7.233	-0.055	-0.027	7.281	-0.154	-0.011	7.460
-0.2	-0.126	0.022	7.560	-0.192	0.066	7.581	-0.233	0.088	7.593
-0.3	-0.145	0.002	7.496	-0.229	-0.009	7.461	-0.266	-0.012	7.471
-0.4	-0.139	-0.004	7.469	-0.212	-0.007	7.500	-0.244	-0.008	7.539
-0.5	-0.098	0.071	8.779	-0.186	0.066	8.610	-0.211	0.086	8.700
-0.6	-0.086	0.040	8.893	-0.164	-0.005	8.678	-0.194	-0.033	8.555
-0.7	-0.005	0.051	10.481	-0.074	0.069	10.291	-0.100	0.074	10.279
-0.8	-0.008	0.008	10.271	-0.063	-0.019	10.171	-0.085	-0.033	10.181
-0.9	-0.013	-0.028	11.331	-0.078	-0.001	11.724	-0.103	0.012	11.760
-1.0	0.009	-0.061	11.112	-0.047	-0.100	11.260	-0.074	-0.113	11.315

Table 7.2: *Compensation parameters as a function of the height z_1 for various permittivities* ϵ_{2r}.
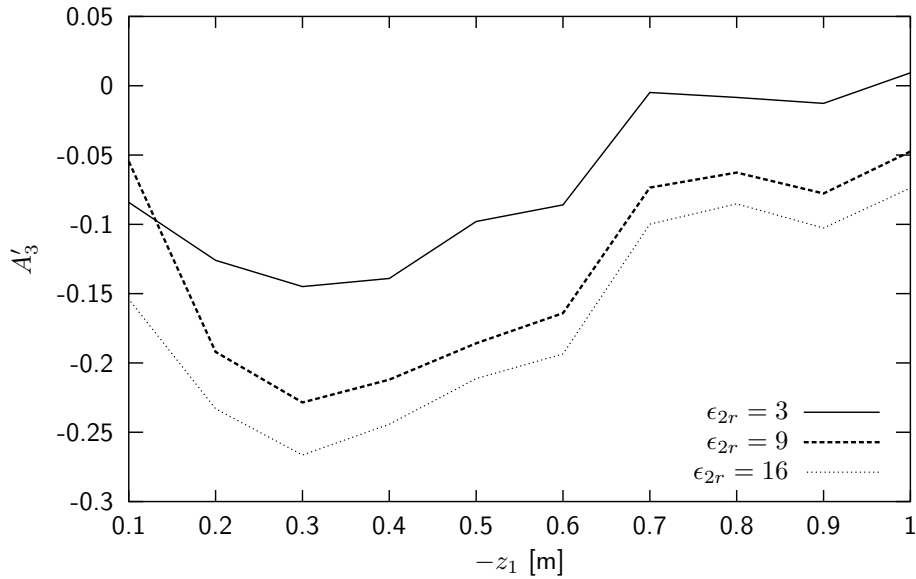
Figure 7.8: *The real part of the amplitude compensation factors from both wires as a function of the height z_1. The relative permittivity is chosen as $\epsilon_{2r} = 3$, $\epsilon_{2r} = 9$ and $\epsilon_{2r} = 16$.*
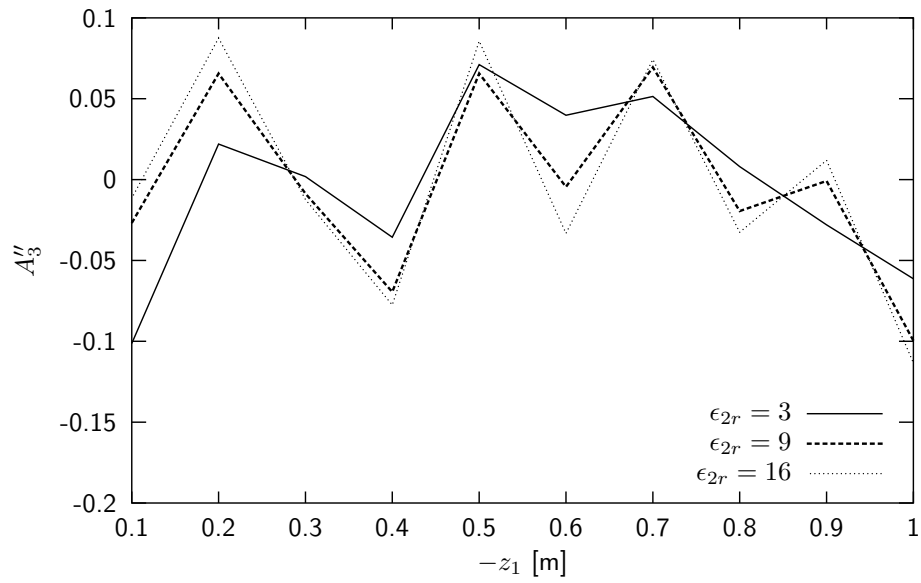
Figure 7.9: *The imaginary part of the amplitude compensation factors from both wires as a function of the height z_1. The relative permittivity is chosen as $\epsilon_{2r} = 3$, $\epsilon_{2r} = 9$ and $\epsilon_{2r} = 16$.*
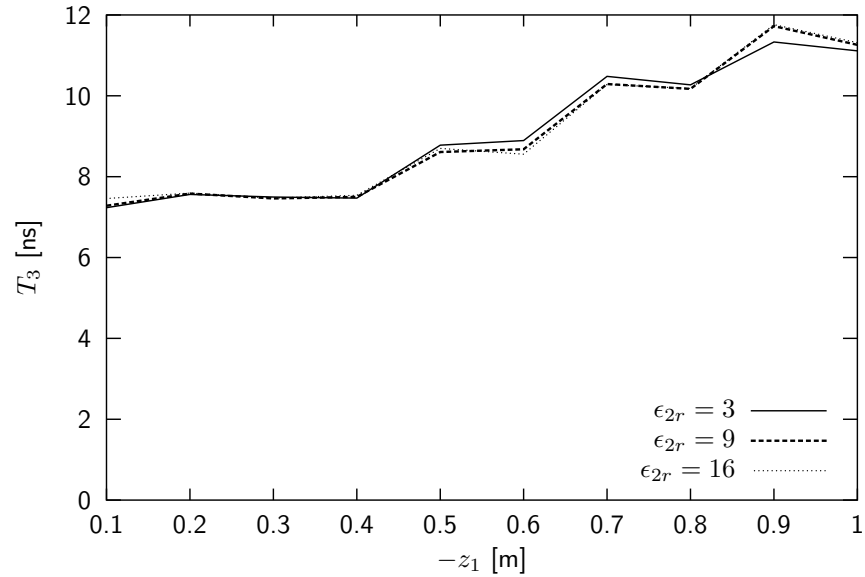
Figure 7.10: *The time delays for the pulse compensation of both wires as a function of the height z_1. The relative permittivity is chosen as $\epsilon_{2r} = 3$, $\epsilon_{2r} = 9$ and $\epsilon_{2r} = 16$.*

The imaginary part of A_3 is plotted in Figure 7.9 for the same configuration. The matching time delays T_3 for the pulse compensation are depicted in Figure 7.10.

From Figure 7.10, it is immediately observed that the time delay T_3 is more or less linearly dependent on the height z_1. This can be fully explained from the increasing travel time for an increasing height z_1. The plot for the real part of the compensation parameters A_3 shows a curve with a minimum at $z_1 = -0.3$ m. Furthermore, the curve is not smooth. The fact that standing waves may exist at certain heights z_1 probably causes this phenomenon. From Figure 7.9, it is observed that the imaginary part of the amplitude compensation parameter A_3 shows a similar behavior as the real part of A_3 but with a local maximum around $z_1 = -0.4$ m. For increasing permittivity of the lower half space the variation of A_3 is stronger.

Next, the dependence on ϵ_{2r} for a fixed z_1 of the compensation parameters is studied. The results are listed in Table 7.3. In Figure 7.11, the real part of A_3 is plotted for heights $z_1 = -0.1$ m and $z_1 = -0.25$ m and $2 \leq \epsilon_{2r} \leq 16$. The imaginary part of the amplitude

	$z_1 = -0.1$m			$z_1 = -0.25$m		
ϵ_{2r}	A_3'	A_3''	T_3 [ns]	A_3'	A_3''	T_3 [ns]
2	-0.090	-0.063	7.265	-0.113	0.013	0.752
3	-0.084	-0.101	7.233	-0.139	0.014	0.750
4	-0.074	-0.116	7.224	-0.157	0.019	7.518
5	-0.065	-0.116	7.216	-0.174	0.018	7.480
6	-0.026	-0.127	7.030	-0.187	0.026	7.515
7	-0.018	-0.124	7.050	-0.199	0.031	7.530
8	0.000	-0.089	7.080	-0.210	0.031	7.520
9	-0.055	-0.027	7.281	-0.220	0.033	7.514
10	-0.100	0.002	7.470	-0.228	0.033	7.511
11	-0.122	0.013	7.510	-0.235	0.034	7.511
12	-0.139	0.015	7.519	-0.241	0.035	7.512
13	-0.150	0.015	7.524	-0.247	0.033	7.501
14	-0.156	0.012	7.524	-0.252	0.036	7.513
15	-0.158	0.000	7.490	-0.257	0.037	7.511
16	-0.154	-0.011	7.460	-0.260	0.040	7.530

Table 7.3: Compensation parameters as a function of the permittivity ϵ_{2r} for heights $z_1 = -0.1$ m and $z_1 = -0.25$ m.
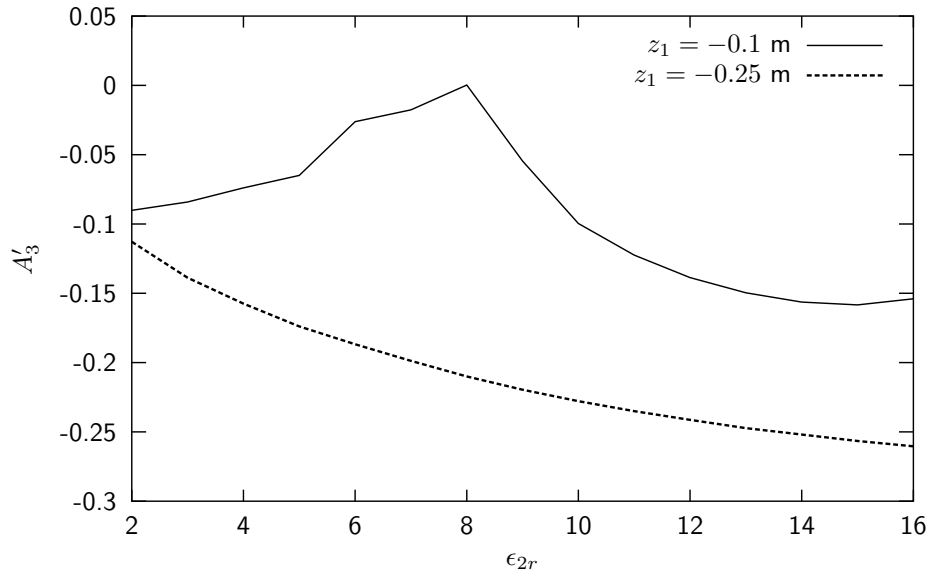
Figure 7.11: *The real part of the amplitude compensation factors from both wires as a function of the relative permittivity ϵ_{2r}. The height of the wires is chosen as $z_1 = -0.1$ m and $z_1 = -0.25$ m.*

A_3 is plotted in Figure 7.12. The appropriate time delay T_3 is depicted in Figure 7.13. It is observed that T_3 is hardly influenced by the increasing permittivity. Together with the height dependence of the time delay, it can be concluded that the time delay T_3 depends directly on the path length between the wires via the interface and thus on the height z_1. For $z_1 = -0.25$ m, the real and imaginary parts of A_3 are smooth functions of the permittivity ϵ_{2r}. From previous results, it was observed that the presence of an interface has a strong effect on the current along wire 2 when z_1 is small. This is in accordance with the observation that for $z_1 = -0.1$ m the amplitude A_3 changes rapidly as a function of the permittivity. For an increasing height z_1, indeed the influence of the presence of the interface on the compensation parameter A_3 is smaller.

In general, the choice of parameters for the third compensation demands proper attention. The current along wire 2 is strongly affected by the presence of an interface, especially when z_1 is small. In all cases, the time delays are less critical.

7.2.2 Detection of a buried wire

The currents that are shown in the examples in this section are calculated for the configuration depicted in Figure 4.12. The wires have length $L = 1$ m, radius $a = 0.002$ m and the
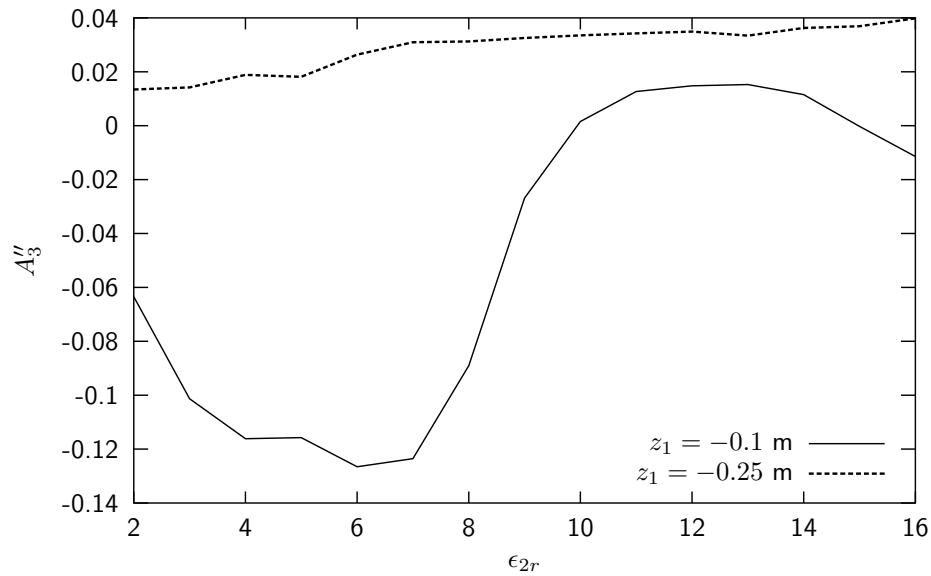
Figure 7.12: *The imaginary part of the amplitude compensation factors from both wires as a function of the relative permittivity ϵ_{2r}. The height of the wires is chosen as $z_1 = -0.1$ m and $z_1 = -0.25$ m.*
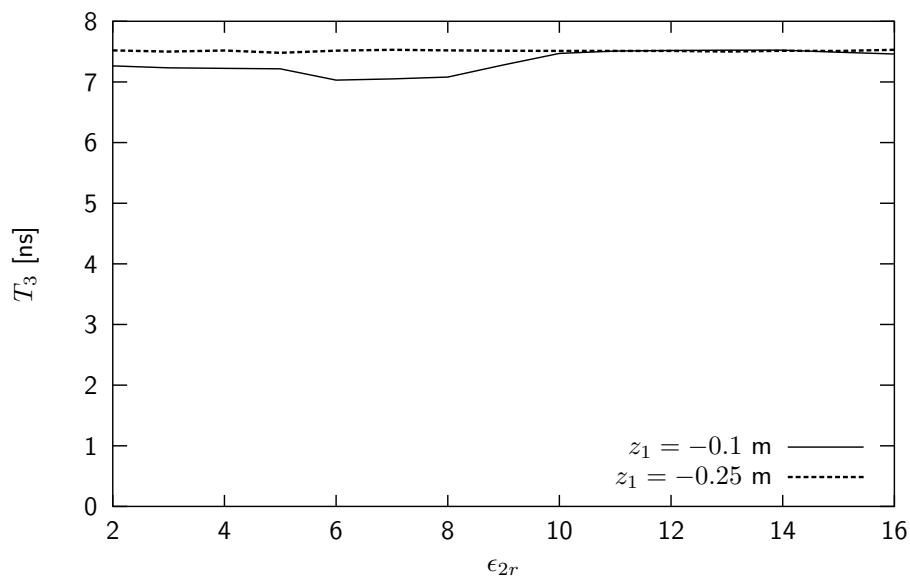
Figure 7.13: *The time delays for the pulse compensation of both wires as a function of the relative permittivity ϵ_{2r}. The height of the wires is chosen as $z_1 = -0.1$ m and $z_1 = -0.25$ m.*

distance between the wires is $d = 1$ m. The height is given by $z_1 = -0.1$ m. The relative permittivity of the upper half space is $\epsilon_{1r} = 1$. The conductivity and permeability of both half spaces is $\sigma_1 = \sigma_2 = 0$ and μ_0, respectively. In the calculation of the currents along the pulse-compensated wires in the detection set up, the free-space parameters are used. The current along wire 2 is compensated by the third compensation with the parameters from Table 7.1.

The relative permittivity of the lower half space is $\epsilon_{2r} = 9$ for all plots on the left and $\epsilon_{2r} = 3$ for all plots on the right. Wire 3 with length $L = 1$ m and radius $a = 0.002$ m may be present in the lower half space. The lateral distance from wire 3 to wire 1 is given as $d_2 = 0.5$ m.

In Figure 7.14, the currents at the center of wire 2 for $z_2 = 0.1$ m and $z_2 = 1$ m are plotted. From all results, it is seen that the presence of the buried wire has a strong effect on the current along wire 2. Especially after 20 ns, the current is heavily affected. In (A), the difference between the two currents is bigger than in the Wu-King case after $t = 15$ ns. The current in (B) is comparable to the Wu-King case. When the depth of wire 3 increases, the current in (C) is affected in a similar way as in the Wu-King case after $t \approx 23$ ns. However, the difference in the current is bigger for $t = 35$ ns. In the last plot, the influence of wire 3 starts around 10 ns. The pulse compensation has not started yet at that time. Therefore, the arrival of the transmitted field from wire 3 is not visible from the current along wire 2. After approximately 15 ns, the difference between the currents is comparable with the Wu-King case.
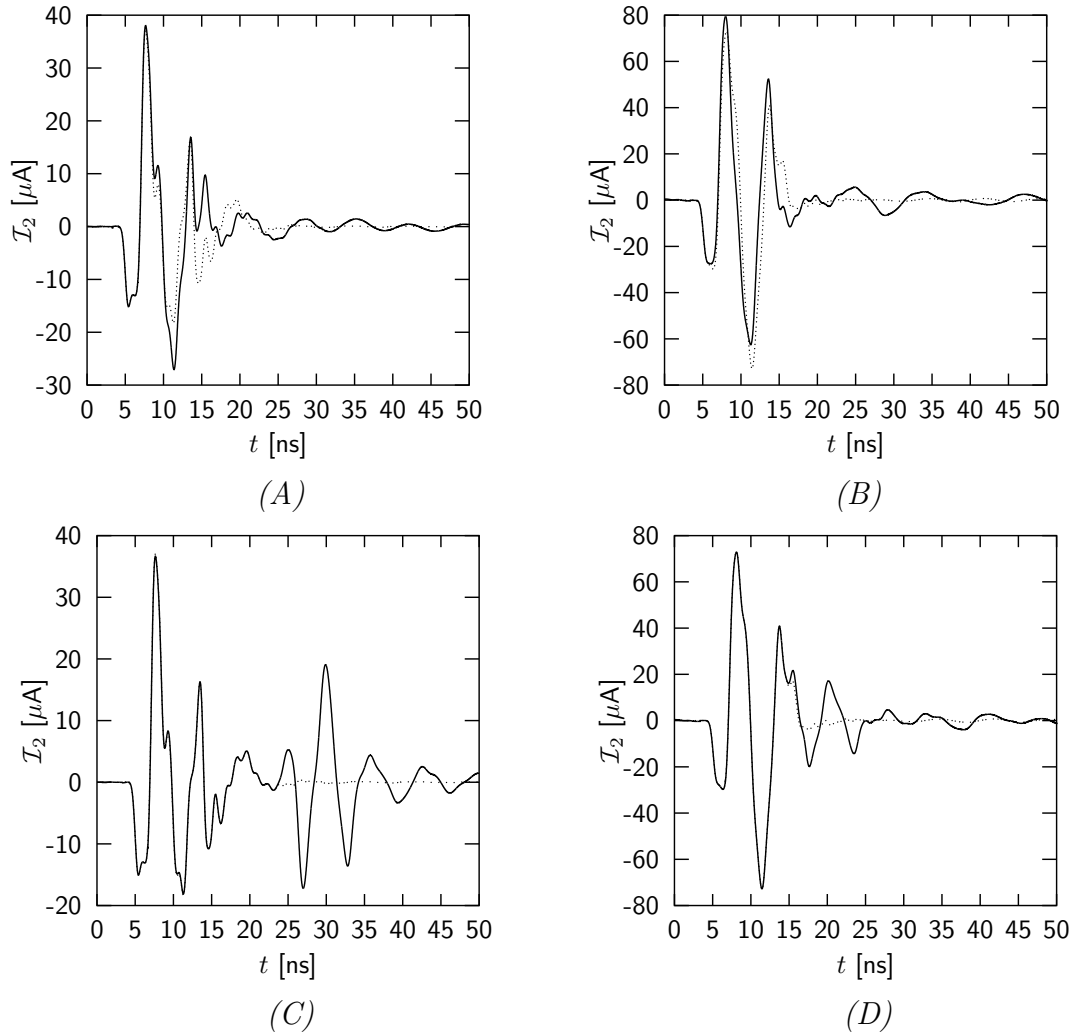
Figure 7.14: *The induced current at the center of wire 2 with length $L = 1$ m and radius $a = 0.002$ m. The length and radius of the buried wire is $L = 1$ m and $a = 0.002$ m, respectively. The distance between the wires is $d = 1$ m and the height is $z_1 = -0.1$ m. The medium properties are $\epsilon_{1r} = 1$, $\sigma_1 = \sigma_2 = 0$, $\epsilon_{2r} = 9$ for (A) and (C) and $\epsilon_{2r} = 3$ for (B) and (D). The permeability is μ_0 for all configurations. The currents are pulse compensated with optimized values. The depth of wire 3 is $z_2 = 0.1$ m for (A) and (B), and $z_2 = 1$ m for (C) and (D). The dotted lines represent the current in absence of wire 3 and the solid lines represent the current in presence of wire 3.*

Chapter 8

Scanning the lower half space

In the previous chapter, it was shown that a buried wire can in principle be detected by the detection set up. In this chapter, the currents along the wires of the detection set are calculated at different positions in the y-direction. The technical term for such a series of currents is a scan, and in this particular case a B-scan [12]. The presence of the buried wire affects the current along the wires in the detection set up. Since the travel time and the position with respect to the interface from the transmitted field from the transmitting wire to the receiving wire via the buried wire changes all the time, the current along the receiving wire changes. The variation in the current along the receiving wire makes it possible to see if a buried wire is present.

Both the Wu-King resistive profile and pulse compensation will be used on the wires of the detection set up. The pulse-compensation parameters are optimized for the respective configurations.

8.1   Introduction

The detection of objects is difficult with only a single time signal. The observation can be made only by comparing the time signal to a reference signal pertaining to the situation. The reference signal is defined as a signal without a buried object but with the presence of the homogeneous half space. When a series of calculations of the current along a wire is performed for different positions, a difference can easily be observed by plotting the various time signals next to each other. Such a series of time signals is usually referred to as a "scan". In the literature, see e.g. Daniels [12], three types of scans can be distinguished.

Consider the data to be of the form

$$A(x_i, y_j, t_k) \quad \text{for} \quad \begin{aligned} i &= 0, \ldots, I, \\ j &= 0, \ldots, J, \\ k &= 0, \ldots, K. \end{aligned} \qquad (8.1)$$

Then the three types of scans are defined as in Figure 8.1. From Figure 8.1, it follows that all previous plots are A-scans, namely one time signal at a fixed point. The B-scan is a series of time signals when the wire is moved in the x or y-direction. The C-scan is a series of measurements in both directions for a fixed value of z or a range of z-values.

With the detection set up formed by wire 1 and wire 2, a B-scan is carried out for a number of configurations. The detection set up is moving in the y-direction as depicted in Figure 8.2. Both wires have a length $L = 1$ m and radius $a = 0.002$ m and are directed parallel to each other and the interface. The distance between the wires of the detection set up is $d = 1$ m. The detection set up is located at a height z_1. The buried wire has a length L_3 and radius $a = 0.002$ m and is located at a depth $z_2 = 0.1$ m. The distance in the y-direction of wire 3 with respect to wire 1 is denoted by d_2. Since the reference coordinate system is chosen such that at wire 1, $y = 0$, the distance d_2 can have a negative value. So $d_2 < 0$ merely indicates that wire 3 is located to the left of wire 1. The length of wire 3 may be varied and the wire may also have an offset x_{off} in the x-direction. The permittivity and conductivity of the upper half space are $\epsilon_{1r} = 1$ and $\sigma = 0$, respectively, in all examples. The permeability of both half spaces is chosen as $\mu_1 = \mu_2 = \mu_0$ in all cases.

The depth of the buried wire is chosen fixed as $z_2 = 0.1$ m. When z_2 increases, the influence of the current along wire 3 shows up in a distinct waveform in the current along wire 2 at later times. This increases the detectability of wires that are located at larger depths, provided that the conductivity of the lower half space does not attenuate the current along wire 3 and the transmitted field too much.

In general, all scans will be performed over a range of $-1 < d_2 < 2$ m. The scan interval is divided into 75 steps, which yields a spatial discretization in the y-direction with a step of $\Delta d_2 = 0.04$ m. The current is then plotted versus time t and position d_2. Such a plot is referred to as a "synthetic seismogram". The effects of the buried wire on the local minima and maxima of the current at the center of wire 2 occur at different time instants as a result of the varying y-position. The relation between the varying time instants and the different y positions is described by hyperbolas [12]. Therefore, the presence of the buried wire results in hyperbolic spreading functions in the synthetic seismogram.
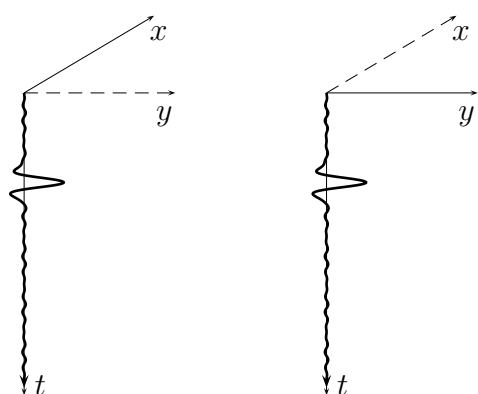
$$f(t_k) = A(x_i, y_j, t_k) \quad \text{for} \quad i = \text{constant},$$
$$j = \text{constant},$$
$$k = 0, \ldots, K.$$

(A)
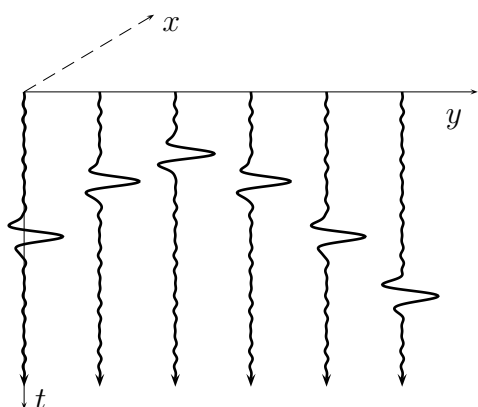
$$f(x_i, t_k) = A(x_i, y_j, t_k) \quad \text{for} \quad i = 0, \ldots, I,$$
$$j = \text{constant},$$
$$k = 0, \ldots, K,$$

or

$$f(y_j, t_k) = A(x_i, y_j, t_k) \quad \text{for} \quad i = \text{constant},$$
$$j = 0, \ldots, J,$$
$$k = 0, \ldots, K.$$

(B)
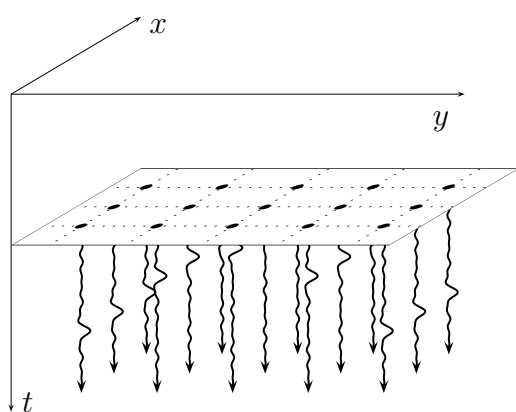
$$f(x_i, y_j, t_k) = A(x_i, y_j, t_k) \quad \text{for} \quad i = 0, \ldots, I,$$
$$j = 0, \ldots, J,$$
$$k = 0, \ldots, K.$$

(C)

Figure 8.1: *Definition of the A-scan (A), B-scan (B) and C-scan (C). The indices i, j and k refer to sampling in the x, y and t direction, respectively.*
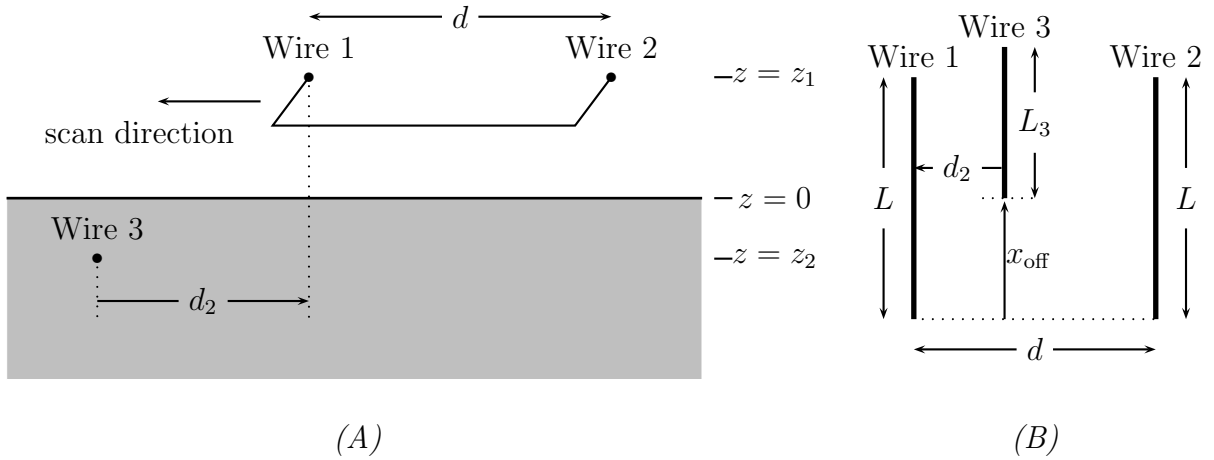
Figure 8.2: *Lateral view (A) and top view (B) for the B-scan.*

8.2 B-scan with Wu-King loaded wires in the detection set up

The wires of the detection set up are loaded with a resistance profile. This detection set up is then used to generate B-scans as discussed in the previous section. In all examples, the medium parameters of the upper half space are equal to those of vacuum. The length of the wires of the detection set up is $L = 1$ m and the radius is $a = 0.002$ m. The distance between the wires is $d = 1$ m. The excitation of wire 1 is again the Gaussian pulse as given in Section 3.3.2.

In the first example, wire 3 is absent. The rest of the configuration is as described in the previous section with $z_1 = -0.1$ m, $\epsilon_{2r} = 9$ and $\sigma_2 = 0$. The current along wire 2 is plotted in Figure 8.3. Obviously, the current does not change with d_2 when the same lower half space is scanned. For future use it is therefore sufficient to calculate only one reference result instead of an entire scan. From previous results it was observed that the first minimum of the current along wire 2 is not affected by the presence of a buried wire.

In the second example, two synthetic seismograms are presented to show the advantages of the Wu-King profile. The configuration is as described in the previous section with $L_3 = 1$ m, $x_{\text{off}} = 0$, $z_1 = -0.1$ m, $z_2 = 0.1$ m $\epsilon_{2r} = 3$ and $\sigma_2 = 0$. In Figure 8.4, plot (A) shows the current at the center of wire 2 without the resistance profile while plot (B) shows the current at the center of wire 2 with the resistance profile. It is immediately seen that the current along the perfectly conducting wire is oscillating heavily. In both plots,
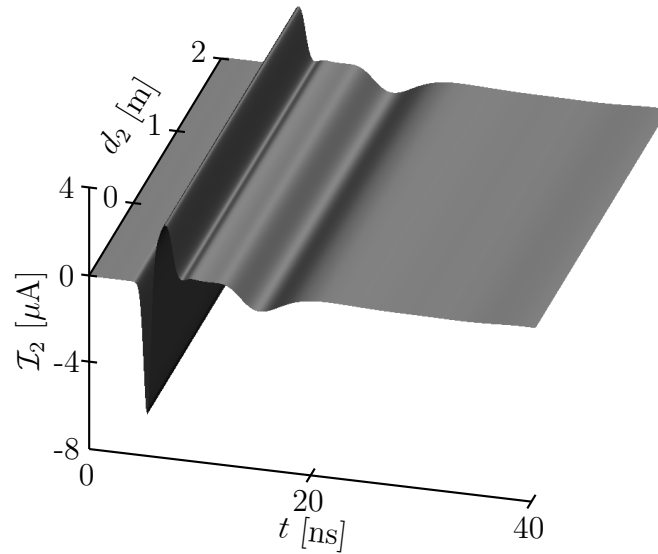
Figure 8.3: *The induced current at the center of wire 2 with length $L = 1$ m and radius $a = 0.002$ m. The buried wire is absent. The medium properties are $\epsilon_{1r} = 1, \sigma_1 = \sigma_2 = 0$, $\epsilon_{2r} = 9$ and the permeability is μ_0 in both half spaces. The wires of the detection set up are resistively loaded.*

(A)

(B)
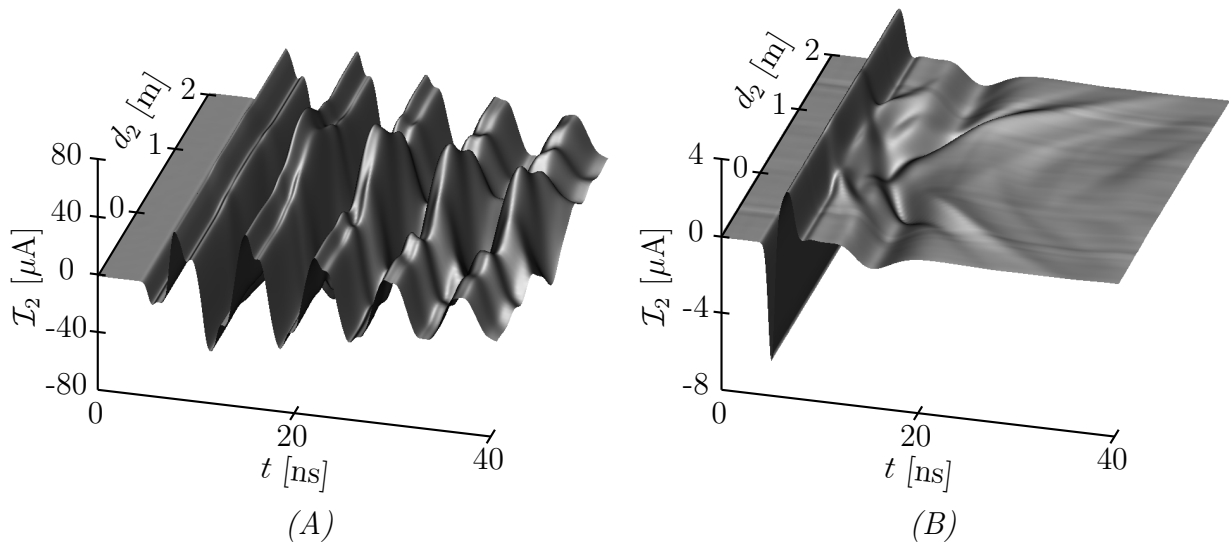
Figure 8.4: *The induced current at the center of wire 2 with length $L = 1$ m and radius $a = 0.002$ m. The depth of the buried wire with length $L_3 = 1$ m and radius $a = 0.002$ m is $z_2 = 0.1$ m. The offset is $x_{\text{off}} = 0$. The medium properties are $\epsilon_{1r} = 1$, $\sigma_1 = \sigma_2 = 0$, $\epsilon_{2r} = 3$ and the permeability is μ_0 for both half spaces. In (A), the wires of the detection set up are perfectly conducting while in (B), they are resistively loaded.*

the first maximum is visibly affected by the presence of the buried wire when it is located between $0 < d_2 < d$. For the perfectly conducting wire, this effect is observed during the entire scan. From the Wu-King loaded wire, a hyperbolic spreading function can be recognized directly from the current along wire 2. This means that the depth of the buried wire can be calculated directly from the signal detected by a Wu-King loaded wire.

Earlier, it was mentioned that only one calculation is necessary as a reference. This particular calculation contains information about the entire configuration without the presence of wire 3. In detection terminology, the reference calculation is referred to as a background calculation. Subtracting the reference calculation from the synthetic seismogram yields a second synthetic seismogram showing the difference between the two time signals. This technique is commonly known as "background subtraction".

As a first example of background subtraction, the detection set up is located at $z_1 = -0.1$ m and wire 3 is located at $z_2 = 0.1$ m. The offset is $x_{\text{off}} = 0$. In Figure 8.5, the current at the center of wire 2 has been plotted for $\epsilon_{2r} = 3$ and $\sigma_2 = 0$. The permittivity is changed to $\epsilon_{2r} = 9$ for the scan in Figure 8.6. The hyperbolic spreading functions can easily be observed. For $t \to \infty$, the hyperbolic spreading function approaches the asymptotes associated with the spreading function. In Figure 8.6, the angle of the asymptotes with a time axis through the point $d = 0.5$ m is smaller than in Figure 8.5. The asymptote is given by [12]:

$$d_2 = \frac{d}{2} \pm \frac{\Delta d_2}{\Delta t}(t - t_c), \tag{8.2}$$

where t_c is a constant. The factor $\Delta d_2/\Delta t$ is referred to as the relative speed v_r of the entire configuration. In Figure 8.5, the relative speed is found as:

$$v_r = \frac{2-1}{14-7.5}10^9 = 153.9 \ 10^6 \frac{\text{m}}{\text{s}}, \tag{8.3}$$

where the values for the dots have been obtained directly from the data set. The path length l_3 for a signal from wire 1 to wire 2 via wire 3 is given by $l_3 = 2\sqrt{(d/2)^2 + (z_2 - z_1)^2}$. Since the first arrival time and the relative speed are known, l_3 can be determined by multiplying the arrival time with the relative speed. The depth of the wire is then given as [12]:

$$z_2 = \sqrt{\left(\frac{v_r t_0}{2}\right)^2 - \left(\frac{d}{2}\right)^2} + z_1. \tag{8.4}$$

The first arrival time is $t_0 = 7$ ns. For Figure 8.5, the depth of wire 3 is then found as $z_2 = 0.099$ m. This value is in accordance with the input parameter.
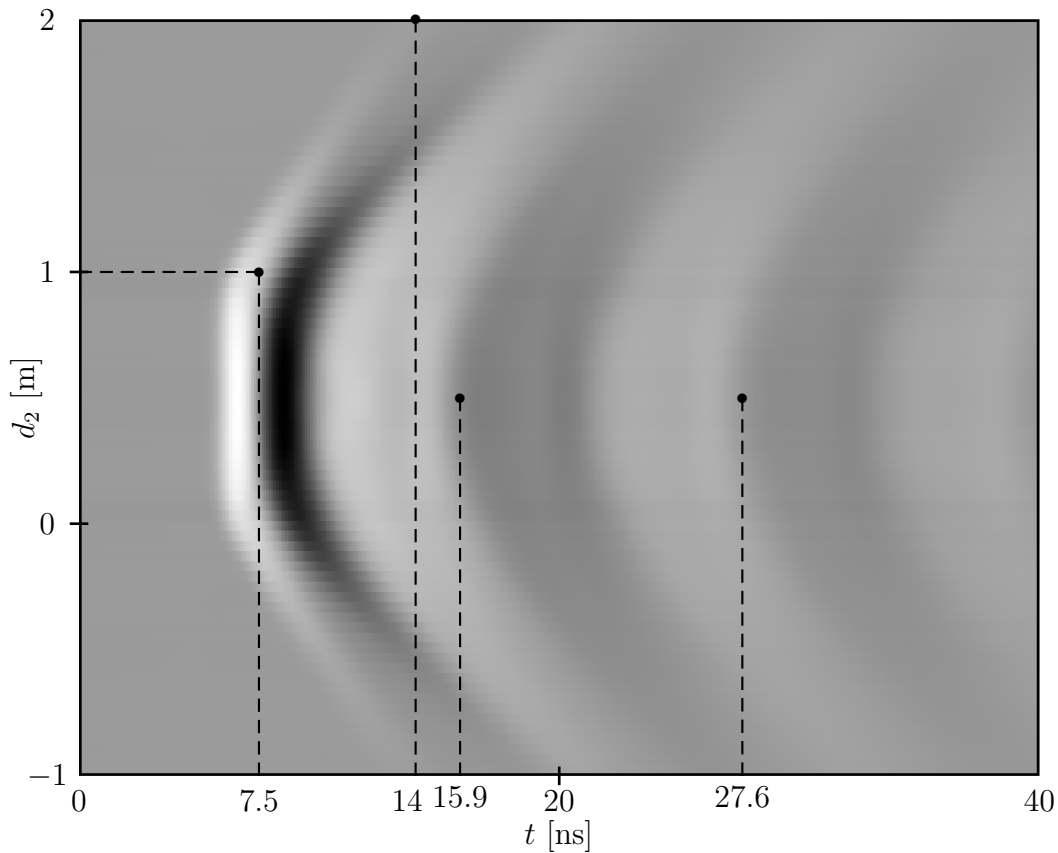
Figure 8.5: *The induced current at the center of wire 2 with length $L = 1$ m and radius $a = 0.002$ m. The depth of the buried wire with length $L_3 = 1$ m and radius $a = 0.002$ m is $z_2 = 0.1$ m. The offset is $x_{\text{off}} = 0$. The medium properties are $\epsilon_{1r} = 1$, $\sigma_1 = \sigma_2 = 0$, $\epsilon_{2r} = 3$. The permeability is μ_0 for both half spaces. The wires of the detection set up are resistively loaded.*

The arrival time can also be calculated by means of the respective speeds of the media and the distance that a wave has to travel from wire 1 to wire 2 via wire 3. Let t_1 be the time that the field travels through the upper half space with velocity $c_1 = c_0 = 3 \ 10^8$ m/s, and let t_2 be the time that the field travels trough the lower half space with speed c_2. Then the following relation is found for the arrival time

$$\tilde{t}_0 = t_1 + t_2 = 2 \left(-\frac{z_1 \sqrt{(d/2)^2 + (z_2 - z_1)^2}}{(z_2 - z_1)c_1} + \frac{z_2 \sqrt{(d/2)^2 + (z_2 - z_1)^2}}{(z_2 - z_1)c_2} \right). \tag{8.5}$$

From this equation, it is observed that all variables except c_2 are already known. Since the magnitude of the Gaussian voltage pulse reaches its maximum at 2 ns and the arrival time $\tilde{t}_0$ is taken at the first peak value that occurs in the synthetic seismogram, the arrival
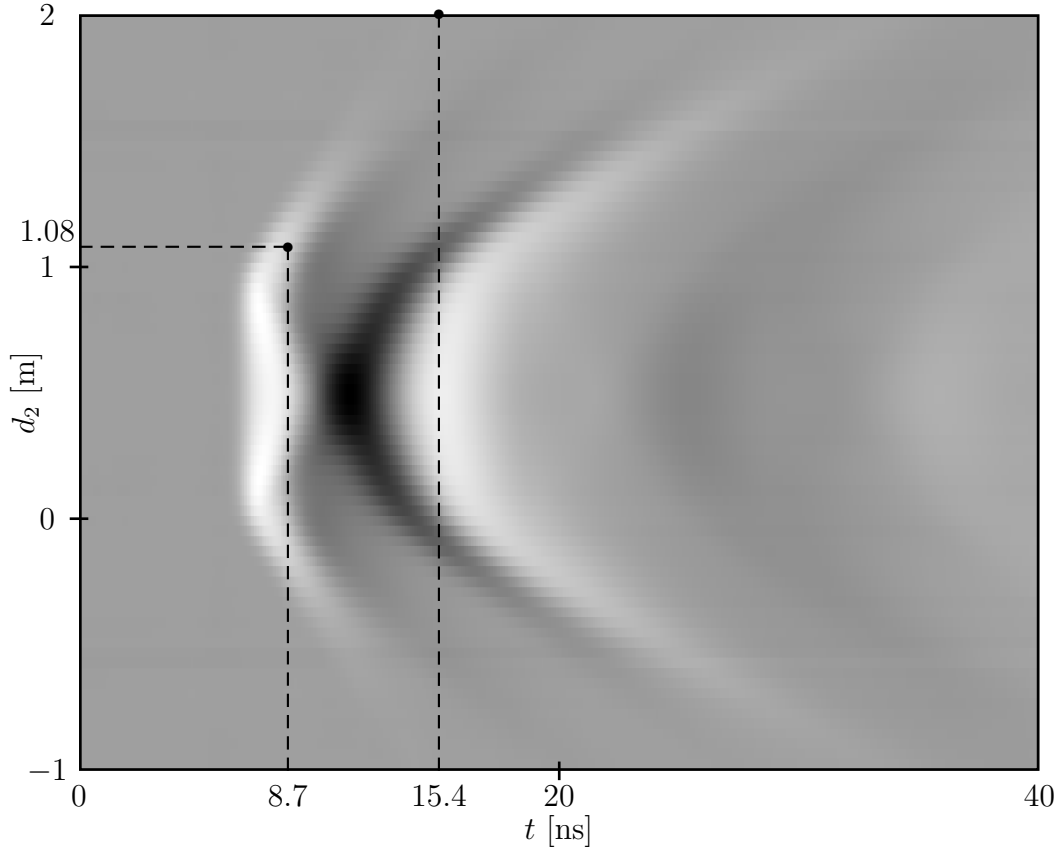
Figure 8.6: *The induced current at the center of wire 2 with length $L = 1$ m and radius $a = 0.002$ m. The depth of the buried wire with length $L_3 = 1$ m and radius $a = 0.002$ m is $z_2 = 0.1$ m. The offset is $x_{off} = 0$. The medium properties are $\epsilon_{1r} = 1$, $\sigma_1 = \sigma_2 = 0$, $\epsilon_{2r} = 9$. The permeability is μ_0 for both half spaces. The wires of the detection set up are resistively loaded.*

time lies at $\tilde{t}_0 = t - 2 = 5$ ns. With the given value for $\tilde{t}_0$, the speed in the lower half space is found as $c_2 = 168 \ 10^6$ m/s. The relative permittivity is then found as $\epsilon_{2r} = 3.2$. This value is also quite accurate when compared to the input parameters.

The last parameter that can be retrieved from the synthetic seismogram is the length of the wire. When the time delay parameter T_{delay} that can be observed from the synthetic seismogram is known, the length of the buried wire is determined by $L_3 = T_{delay} c_2 / 2$. From Figure 8.5 the time delay is found as $T_{delay} = 27.6 - 15.9 = 11.7$ ns. This yields for the length of the buried wire $L_3 = 0.98$ m, which is again an accurate representation of the input parameters.

From Figure 8.6, the relative speed is calculated as $v_r = 137.3 \ 10^6$ m/s. The first arrival time is found as $t_0 = 8$ ns. The depth is then $z_2 = 0.13$ m. This value is not as accurate

as in the previous example because the lines are less distinct in Figure 8.6 when compared to Figure 8.5. A small deviation in the time difference may cause inaccurate results.

In the next example, wire 3 is of length $L_3 = 0.5$ m and the offset is $x_{\text{off}} = 0.25$ m. In Figure 8.7, the current along wire 2 for this configuration has been plotted for $\epsilon_{2r} = 3$ and $\sigma_2 = 0$. A few interesting features can be seen immediately. The asymptotes from the
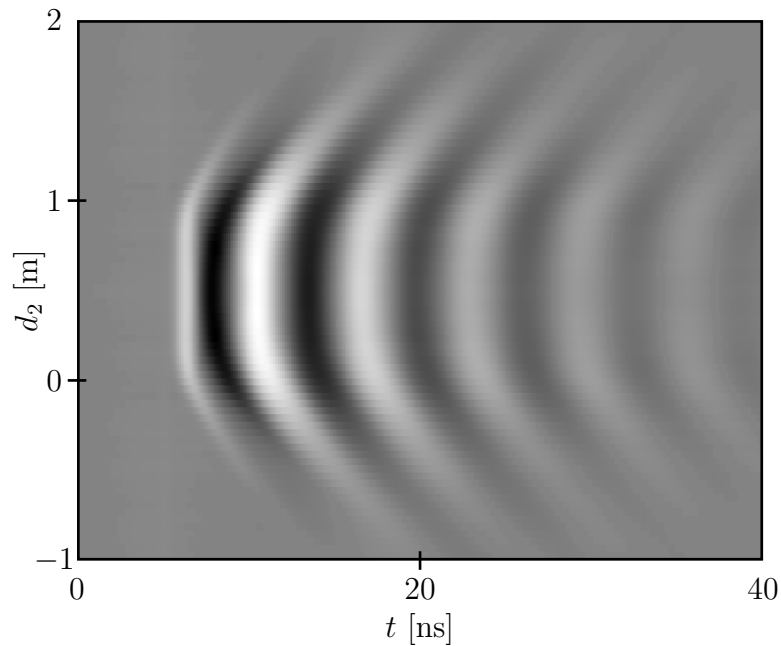
Figure 8.7: *The induced current at the center of wire 2 with length $L = 1$ m and radius $a = 0.002$ m. The depth of the buried wire with length $L_3 = 0.5$ m and radius $a = 0.002$ m is $z_2 = 0.1$ m. The offset is $x_{\text{off}} = 0.25$ m. The medium properties are $\epsilon_{1r} = 1$, $\sigma_1 = \sigma_2 = 0$, $\epsilon_{2r} = 3$. The permeability is μ_0 for both half spaces. The wires of the detection set up are resistively loaded.*

first hyperbola are exactly the same as the asymptotes in Figure 8.5. This actually shows that the angles of the asymptotes contain information about the medium properties of the lower half space rather than about the buried wire. The time delay between two distinctive points in the late-time behavior of the current along wire 2 shows that T_{delay} is exactly half the value that was found in Figure 8.5. This is expected because wire 3 is half the size of wire 3 in Figure 8.5. The elevated maxima and minima between $0 < d_2 < d$ are stronger here than for wire 3 with length $L_3 = 1$ m. It is also observed that the current along wire 3 is attenuated slower when the wire is shorter. This shows that the oscillating behavior of the current along wire 2 is determined by the repeated reflections of the current along the buried wire. The repeated reflections of the current along wire 3 cannot be suppressed

by the resistive profile along the wires of the detection set up.

In the last examples the length and the offset of the buried wire are varied as $L_3 = 1$ m and $x_{\text{off}} = 0.9$ m and $L_3 = 0.5$ m and $x_{\text{off}} = 0.75$ m. The currents at the centers of wire 2 have been plotted in Figure 8.8. From plot (A), it is observed that the first arrival time t_0
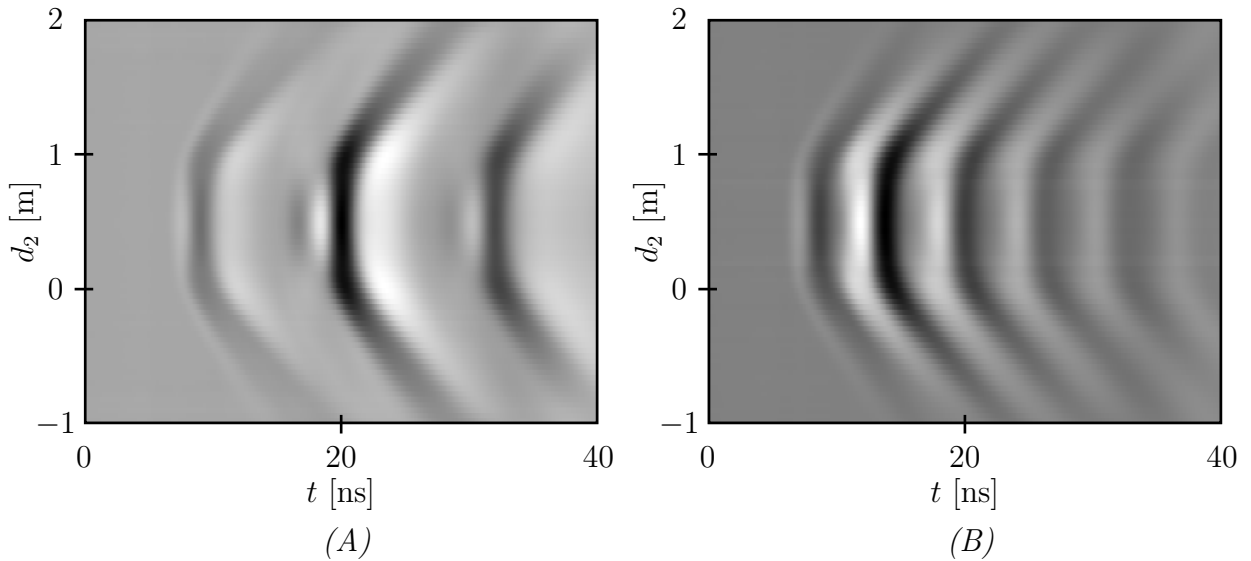
Figure 8.8: *The induced currents at the centers of wire 2 with length $L = 1$ m and radius $a = 0.002$ m. The depth of the buried wire with radius $a = 0.002$ m is $z_2 = 0.1$ m. The length and offset of the buried wire are varied as $L_3 = 1$ m and $x_{\text{off}} = 0.9$ m (A) and $L_3 = 0.5$ m and $x_{\text{off}} = 0.75$ m (B). The medium properties are $\epsilon_{1r} = 1$, $\sigma_1 = \sigma_2 = 0$, $\epsilon_{2r} = 3$. The permeability is μ_0 for both half spaces. The wires of the detection set up are resistively loaded.*

is smaller when compared to a buried wire with length $L_3 = 1$ m and $x_{\text{off}} = 0$. In plot (B), a similar observation can be made. The transmitted field from wire 1 reaches wire 3 later when an offset x_{off} between the centers of the wires of the detection set up and wire 3 is present. The angles of the asymptotes are the same again in both plots. This means that information about the lower half space is preserved. The length of wire 3 cannot easily be determined from these plots.

8.3 B-scan with pulse-compensated wires in the detection set up

The currents along the wires of the detection set up are pulse compensated with a carefully chosen set of complex amplitudes and time delays. Both parameters depend on the height of the detection set up and on the material parameters of the lower half space as was shown in Section 7.2.

The basic configuration is the same as in Section 8.2. In the examples that are shown in this section, the lengths of the wires of the detection set up are $L = 1$ m and the radii are $a = 0.002$ m. The height of the detection set up is $z_1 = -0.1$ m. The depth of wire 3 is $z_2 = 0.1$ m in all examples. The radius of wire 3 is $a = 0.002$ m. The length and offset of wire 3 may be varied. The medium parameters of the respective half spaces are $\epsilon_{1r} = 1$ and $\sigma_1 = \sigma_2 = 0$. The permeability is equal to μ_0 for all configurations. The compensation parameters for both wires are given in Table 7.1.

In general the maxima and minima of the currents along wire 2 are about ten times larger in magnitude for pulse compensation than the currents along the Wu-king loaded wires. In the first examples, wire 3 has a length $L_3 = 1$ m and the offset is $x_{\text{off}} = 0$. The relative permittivity is $\epsilon_{2r} = 3$ for Figure 8.9 and $\epsilon_{2r} = 9$ for Figure 8.10. The arrival time and angle of the asymptotes are the same as in the synthetic seismograms obtained with Wu-King loaded wires. After $t = 15$ ns, the influence from wire 3 on the current along wire 2 is clearly visible, especially around $d_2 = 0$ and $d_2 = 1$ m. For these values of d_2, wire 3 is in the same (x, z)-plane as wire 1 and wire 2, respectively. The mutual interaction at those points is at its maximum. In addition, the wire radiates the strongest around the end faces of a wire where the Wu-King profile attenuates the current. Therefore, the presence of wire 3 can be noticed by the "hot spots" in the synthetic seismogram for uncompensated wires. In the Wu-King case, the resistive profile spreads this effect out over time, see Figure 8.5. For $\epsilon_{2r} = 9$, the effects of wire 3 last longer with pulse compensation. Outside the region $0 < d_2 < d$, the current is fully attenuated after about 35 ns while in the Wu-King case it does not. This indicates that pulse compensation is more precise in scanning applications since it leads to a better discrimination outside the region $0 < d_2 < d$.

In the third configuration, wire 3 has a length $L_3 = 0.5$ m, radius $a = 0.002$ m and the offset is $x_{\text{off}} = 0.25$ m. The relative permittivity is $\epsilon_{2r} = 3$. The synthetic seismogram for this configuration is depicted in Figure 8.11. The influence of wire 3 on the current along wire 2 is stronger in comparison with Figure 8.9. The mutual interaction between the wires when wire 3 is present in the region $0 < d_2 < d$ is very strong. Outside this region, the
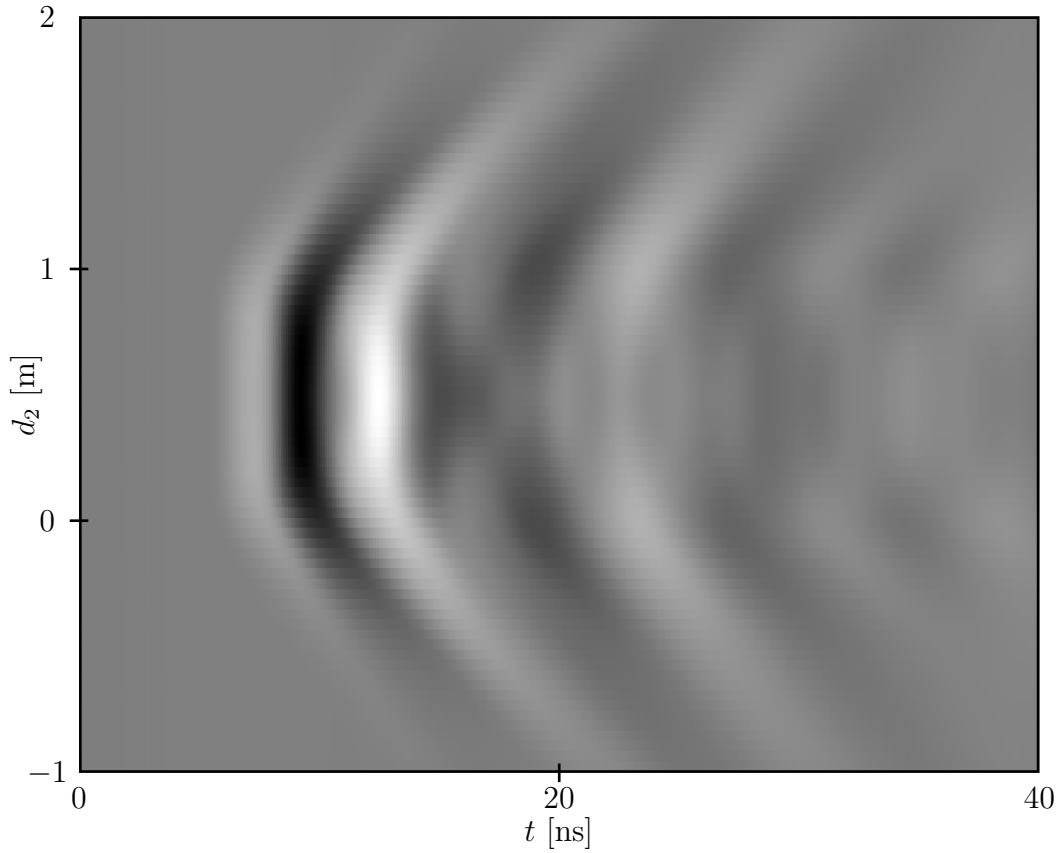
Figure 8.9: *The induced current at the center of wire 2 with length $L = 1$ m and radius $a = 0.002$ m. The depth of the buried wire with length $L_3 = 1$ m and radius $a = 0.002$ m is $z_2 = 0.1$ m. The offset is $x_{\text{off}} = 0$. The medium properties are $\epsilon_{1r} = 1$, $\sigma_1 = \sigma_2 = 0$, $\epsilon_{2r} = 3$. The permeability is μ_0 for both half spaces. The wires of the detection set up are pulse compensated.*

current is fully attenuated with pulse compensation after $t = 35$ ns. Again, hot spots are noticeable at later times.

In the final examples, the length and the offset of the buried wire are varied as $L_3 = 1$ m and $x_{\text{off}} = 0.9$ m and $L_3 = 0.5$ m and $x_{\text{off}} = 0.75$ m. The relative permittivity of the lower half space is $\varepsilon_{2r} = 3$. The currents at the centers of wire 2 have been plotted in Figure 8.12. The currents along the pulse-compensated wires are attenuated more rapidly outside the region $0 < d_2 < d$ in comparison with Figure 8.8. The hot spots as noted in previous figures are no longer present. Here, the center of the buried wire has an offset with respect to the centers of the wires of the detection set up. The current distribution along the wire is therefore no longer symmetrical. A comparison between the plots (A) of Figure 8.8 and Figure 8.12 shows that effects of the buried wire are stronger with pulse-compensation.
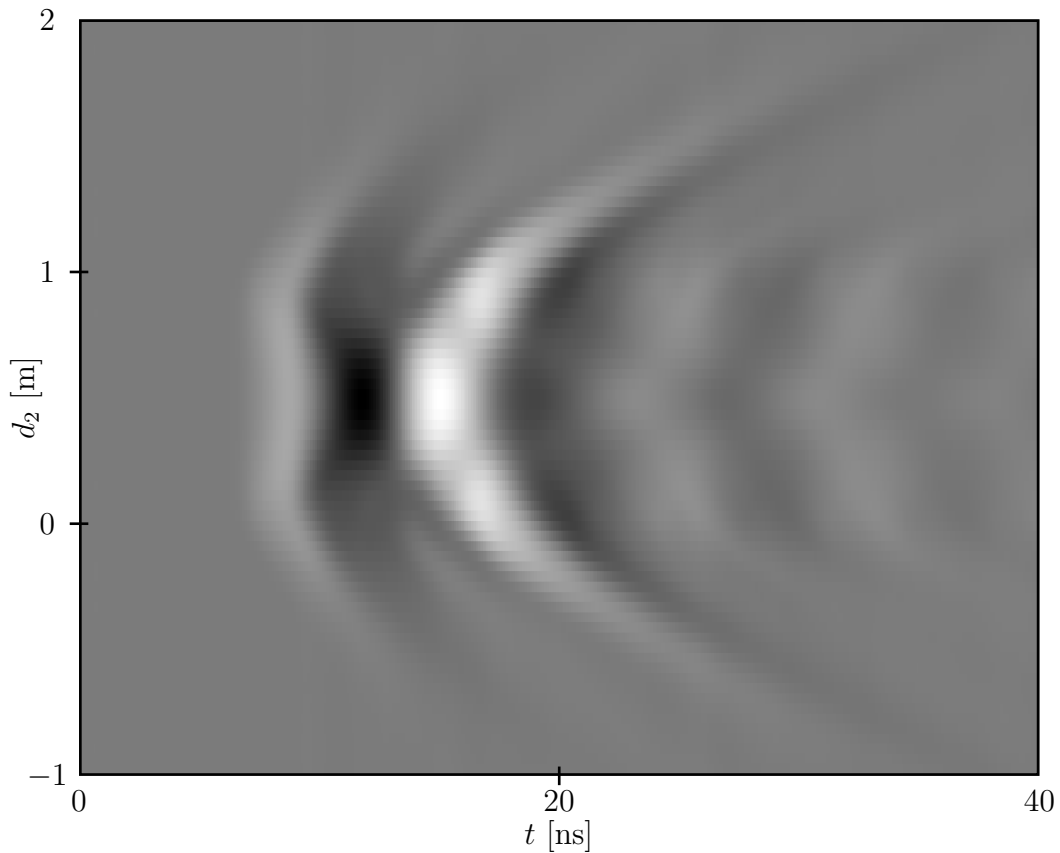
Figure 8.10: *The induced current at the center of wire 2 with length $L = 1$ m and radius $a = 0.002$ m. The depth of the buried wire with length $L_3 = 1$ m and radius $a = 0.002$ m is $z_2 = 0.1$ m. The offset is $x_{\text{off}} = 0$. The medium properties are $\epsilon_{1r} = 1$, $\sigma_1 = \sigma_2 = 0$, $\epsilon_{2r} = 9$. The permeability is μ_0 for both half spaces. The wires of the detection set up are pulse compensated.*

Again, it is observed from both plots that information about the object cannot be easily retrieved when an offset x_{off} is applied. Information about the lower half space is still retrievable from the synthetic seismogram.

When an offset between the center of the buried wire and the wires of the detection set up is present, more advanced signal processing will be needed to retrieve more information about the object. For this case, a C-scan should be made in order to tell something about the position of the wire. When the detection set up is also moved into the x-direction, the first arrival time will appear as a hot spot in a certain time slice. A time slice is a plot in x and y-direction for a given time instance. With this extra information, the depth of wire 3 should be retrievable.
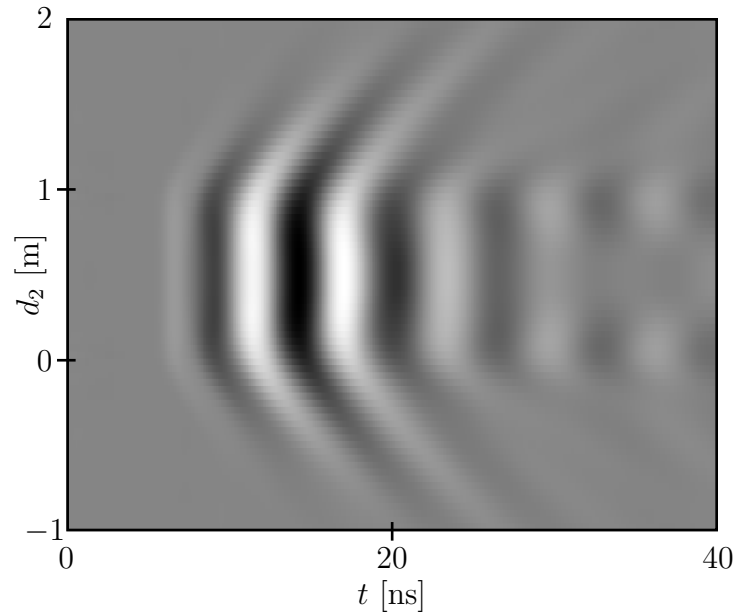
Figure 8.11: *The induced current at the center of wire 2 with length $L = 1$ m and radius $a = 0.002$ m. The depth of the buried wire with length $L_3 = 0.5$ m and radius $a = 0.002$ m is $z_2 = 0.1$ m. The offset is $x_{\text{off}} = 0.25$ m. The medium properties are $\epsilon_{1r} = 1$, $\sigma_1 = \sigma_2 = 0$, $\epsilon_{2r} = 3$. The permeability is μ_0 for both half spaces. The wires of the detection set up are pulse compensated.*
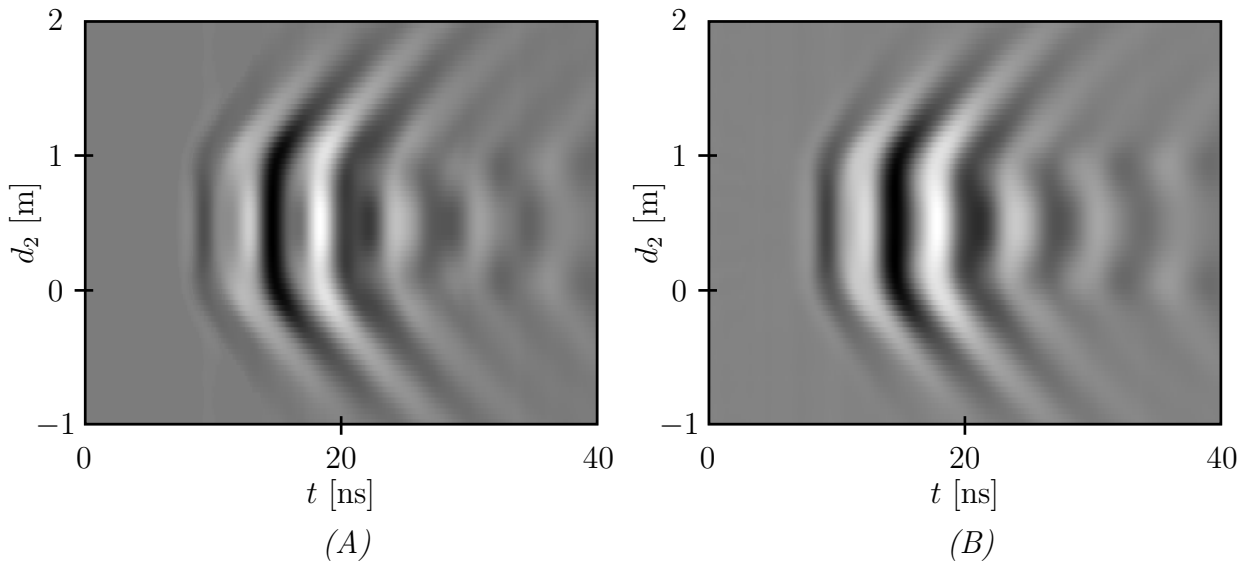
Figure 8.12: *The induced currents at the centers of wire 2 with length $L = 1$ m and radius $a = 0.002$ m. The depth of the buried wire with radius $a = 0.002$ m is $z_2 = 0.1$ m. The length and offset of the buried wire are varied as $L_3 = 1$ m and $x_{\text{off}} = 0.9$ m (A) and $L_3 = 0.5$ m and $x_{\text{off}} = 0.75$ m (B). The medium properties are $\epsilon_{1r} = 1$, $\sigma_1 = \sigma_2 = 0$, $\epsilon_{2r} = 3$. The permeability is μ_0 for both half spaces. The wires of the detection set up are pulse compensated.*

Chapter 9

The inhomogeneous slab

At the end of this thesis, one final configuration is studied. An inhomogeneous slab sandwiched between two homogeneous half spaces is analyzed by the detection set up, see Figure 9.1. In the literature, Rubio Bretones *et al* [32] described a similar case with resistively loaded wires in the detection set up. The goal of the study was to determine properties of the lower half space with a simple detection set up. With pulse compensated wires, similar results are expected.

With the introduction of the slab, the reflected-field terms become more complicated. An elegant solution to handle the reflected field terms for $z < 0$ and the inverse spatial Fourier transformation involved is presented in [27] and [32], respectively. With the resistively
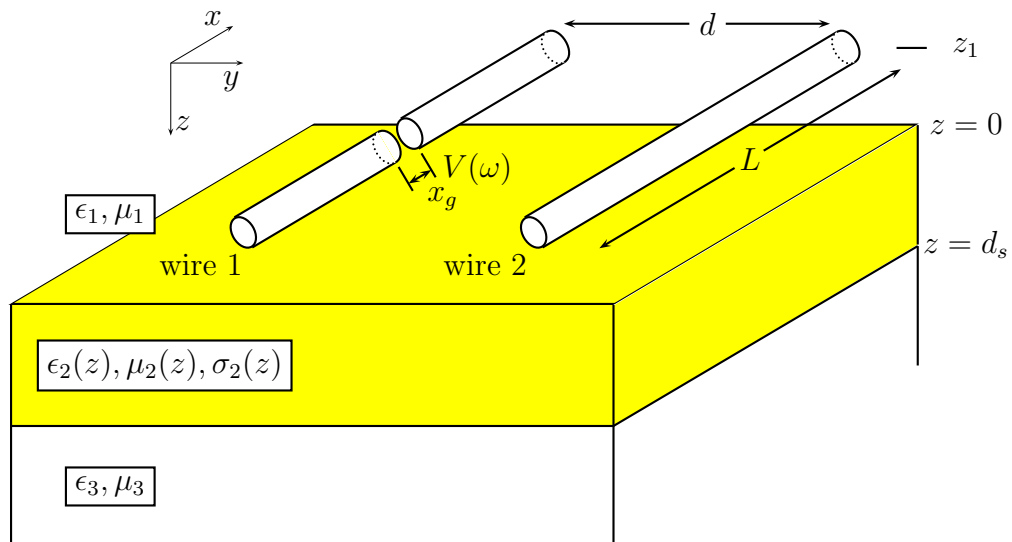
Figure 9.1: *An inhomogeneous slab configuration*

151

loaded wires, the slab properties can be understood better from the current at the center of wire 2 [32]. Again, wire 1 was hardly affected by the presence of the second medium. For the examples presented in this section, the computer code that generated the results of [32] is used. Calculations can be carried out for wires with or without the resistive loading. In all examples, the half spaces have a complex permittivity $\varepsilon_1 = \varepsilon_3 = \varepsilon_0$ and a permeability $\mu_1 = \mu_3 = \mu_0$. In [32], only the slab may have a conductivity as depicted in Figure 9.1. It was observed that the conductivity only attenuates the effects of the slab on the current along wire 2 [32]. Therefore, in all the examples given here, the conductivity $\sigma_2(z)$ of the slab is chosen zero. The length of the wires of the detection set up is again $L = 1$ m and their radius is $a = 0.002$ m. The height of the detection set up is chosen as $z_1 = -0.25$ m. The distance between the wires is $d = 1$ m and the width of the slab $d_s = 2$ m. The permittivity of the slab is varied as $\epsilon_{2r}(z) = 2 + 9z$, $\epsilon_{2r}(z) = 20$ and $\epsilon_{2r}(z) = 2$, respectively, while the permeability is $\mu_{2r} = \mu_0$. The results for the unloaded and loaded wires are repeated from [32, Figure 2] but for a slab width of 2 m, see Figure 9.2. For the sake of completeness, the currents at the center of wire 1 are plotted as well. To obtain the currents from (A) and (B), perfectly conducting wires are used. The plots (C) and (D) were obtained with resistively loaded wires. It is observed from (C) that the resistance profile is again effective in suppressing the end reflections of the wire and thus attenuating the current effectively. From both currents at the center of wire 1, it is not possible to visibly retrieve information about the slab. From (D), the waveforms added to the current along wire 2 by the reflected wave at $z = d_s$ can be easily observed for all three permittivity profiles. In (B), the additional waveform due to the slab with permittivity $\epsilon_{2r}(z) = 2$ is not visible in the current at the center of wire 2. In the waveform introduced by the permittivities $\epsilon_{2r}(z) = 20$ and $\epsilon_{2r}(z) = 2 + 9z$, only the first positive peaks as recognized from (D) are visible in the currents in (B). Since the first negative peaks are not clearly visible, the first arrival time is not known. By looking only at the currents in (B), the arrival times of the additional waveforms due to the slab cannot be retrieved.

In the remaining examples of this chapter, only the currents along wire 2 will be plotted. The resistively loaded wires show to be advantageous over the perfectly conducting wires, see Figure 9.2 and [32]. Based on the results from previous chapters, the perfectly conducting wires are pulse compensated. The compensation parameters are chosen equal to the ones obtained for a similar detection set up in free space. The compensation parameters are chosen this way because it is necessary to retrieve information about the slab and thus for the entire embedding. As a first test, the configurations from the previous example are used. In Figure 9.3, the current at the center of wire 2 is plotted. The additional waveforms added to the current along wire 2 by the slab with permittivities $\epsilon_{2r}(z) = 2 + 9z$ and
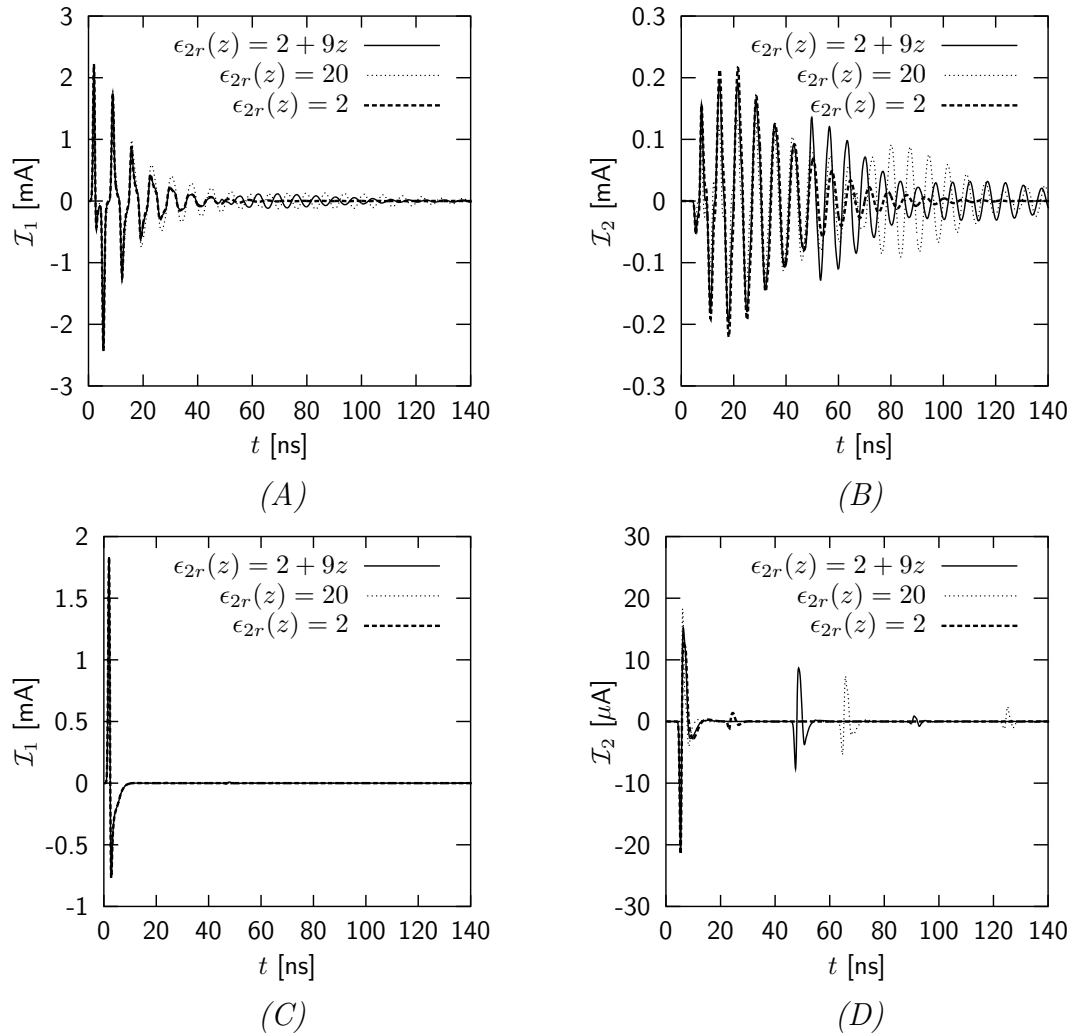
Figure 9.2: *The induced currents at the center of wire 1 and wire 2. Both wires are of length $L = 1$ m with radius $a = 0.002$ m. The height is chosen as $z_1 = -0.25$ m and the distance between the wires is $d = 1$ m. The half spaces have the material properties of vacuum. The permeability and conductivity of the slab are the same as for vacuum. The permittivity $\varepsilon_{2r}(z)$ of the slab is varied as indicated. The wires from (C) and (D) are loaded with the resistive profile from Chapter 6. The excitation is a Gaussian voltage pulse with $\tau = 0.5$ ns and $t_1 = 4\tau$.*

$\epsilon_{2r}(z) = 20$ are clearly visible. The first negative peak is more difficult to recognize from the additional waveform added by the slab with permittivity $\epsilon_{2r}(z) = 2$. From comparing the currents along the pulse compensated wires to the currents obtained for the same configuration with uncompensated PEC wires, see Figure 9.2, it is clearly observed that more information is retrieved with the pulse-compensated wires. Although pulse compensation
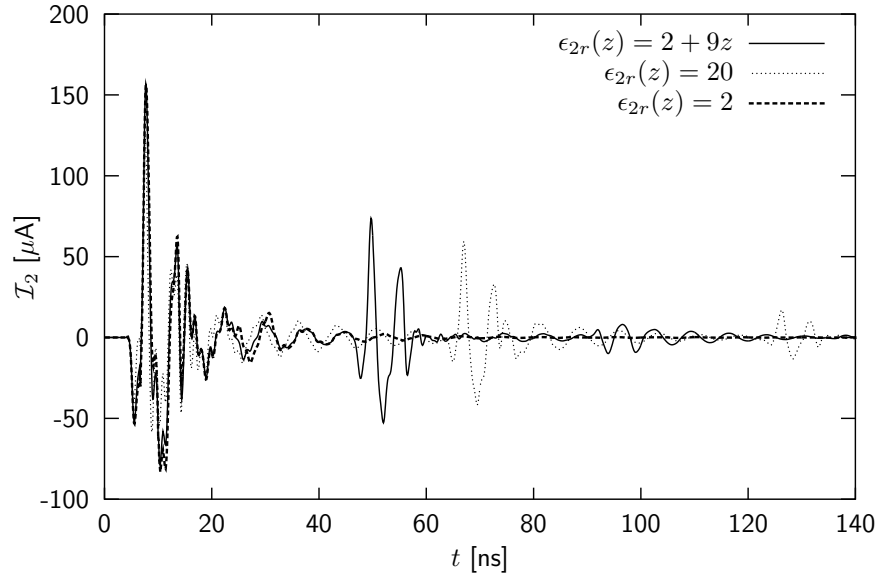
Figure 9.3: *The induced current at the center of wire 2. The wire is of length $L = 1$ m with radius $a = 0.002$ m. The height is chosen as $z_1 = -0.25$ m. The half spaces have the material properties of vacuum. The permeability and the conductivity of the slab are the same as for vacuum. The permittivity $\varepsilon_{2r}(z)$ of the slab is varied as indicated. The free-space compensation parameters for 2 wires are used. The excitation is a Gaussian voltage pulse with $\tau = 0.5$ ns and $t_1 = 4\tau$.*

allows the oscillating behavior of the current to some extent, the influence from the slab can now be clearly recognized as well as the first arrival time. Compared to the Wu-King loaded wires, a similar pulse shape is introduced to the current at the center of the pulse-compensated wires by the interface at $z = d_2$. The additional waveform is attenuated later in the latter case. This is a direct result from the fact that the current wave has to be allowed to travel twice along wire 2 before pulse compensation has any effect. Again, the most important difference is that the magnitude of the current is about 10 times higher in the pulse-compensated case. The arrival times from the reflected wave at $z = d_s$ are the same as in the Wu-King case.

In the next example, a linear permittivity and linear permeability profile in the slab are studied. The rest of the configuration, with the exception of the method for suppressing the end reflections, is the same as in the other examples. In Figure 9.4, the currents at the center of a Wu-King loaded wire, see (A), and of a pulse compensated wire 2, see (B), are plotted. The medium parameters of the slab are varied as $\epsilon_{2r}(z) = 2 + 9z$, $\mu_{2r}(z) = 1$ for the permittivity profile and $\epsilon_{2r}(z) = 1$, $\mu_{2r}(z) = 2 + 9z$ for the permeability profile. From
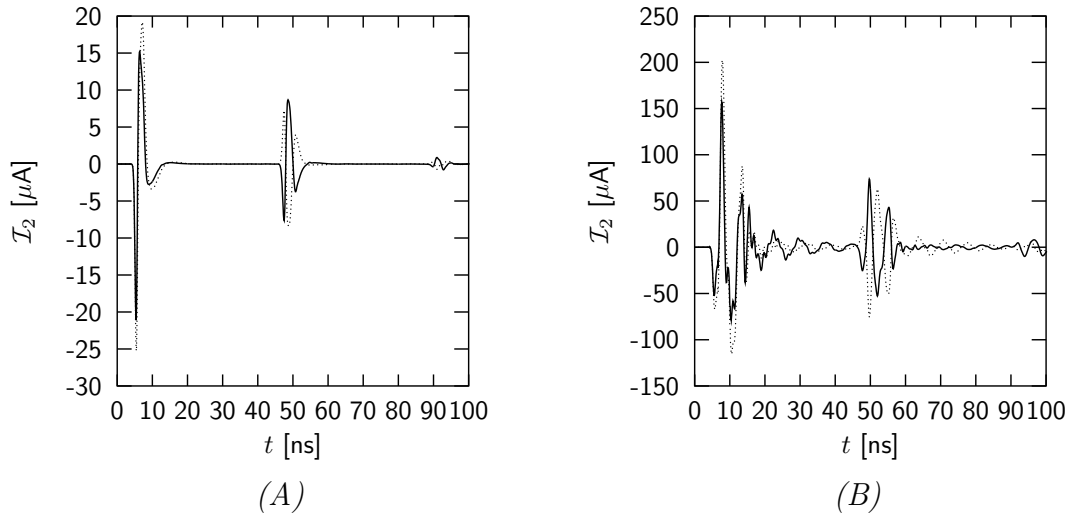
Figure 9.4: *The induced currents at the center of wire 2. The wire is of length $L = 1$ m with radius $a = 0.002$ m. The height is chosen as $z_1 = -0.25$ m and the distance between the wires is $d = 1$ m. The half spaces have the material properties of vacuum. The permittivity and permeability of the slab are varied as $\epsilon_{2r}(z) = 2 + 9z$, $\mu_{2r}(z) = 1$ (solid lines) and $\epsilon_{2r}(z) = 1$, $\mu_{2r}(z) = 2 + 9z$ (dotted lines). The conductivity of the slab is $\sigma(z) = 0$. The wires are loaded with the Wu-King profile in (A). The free-space compensation parameters for two wires are used in (B). The excitation is a Gaussian voltage pulse with $\tau = 0.5$ ns and $t_1 = 4\tau$.*

the plots it is observed that the additional waveform due to the reflected wave at $z = d_s$ occurs at the same time instant in both currents. The signs of the waveforms introduced by the slab are the same for both methods. Again, pulse compensation attenuates the effects a little later then the resistive profile.

Based on these results, it may be concluded that effects from the slab remain visible after pulse compensation. The additional waveform that occurs in the current is not removed by the pulse compensation scheme as it is used here. Besides the effects from the slab, the results show that the currents along wire 2 are not fully compensated by the free-space parameters. Between the additional pulses due to the reflected waves at $z = d_s$, the wire oscillates with a rather big amplitude. In previous chapters, it was seen that the interface at $z = 0$ plays an important role in the determination of the compensation parameters. Especially for the first 6 ns, the interface has a strong effect on the current along wire 2. Therefore, in the configuration as described above with $\epsilon_{2r}(z) = 20$ and $\mu_{2r}(z) = 1$, a third compensation will be applied. The compensation parameters from Table 7.3 are used. The results are presented in Figure 9.5. It is observed immediately
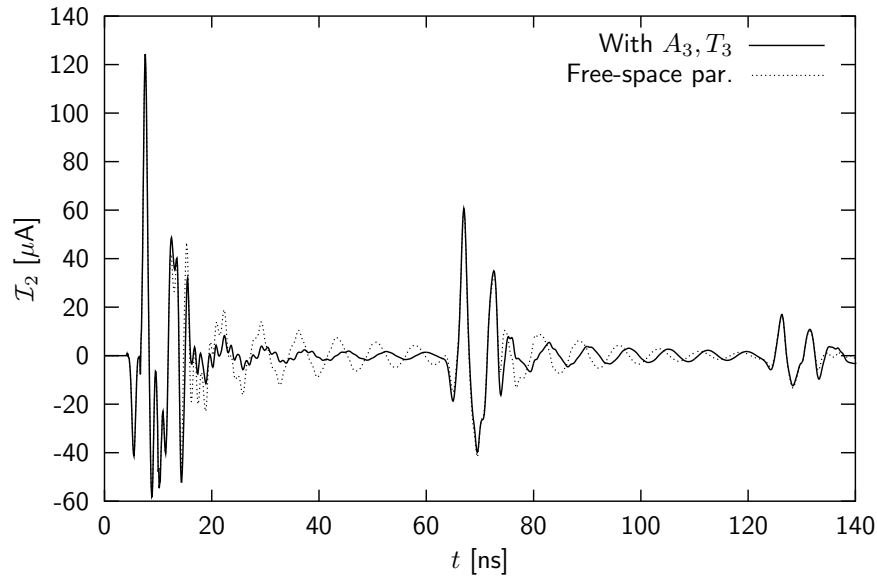
Figure 9.5: *The induced current at the center of wire 2. The wire is of length $L = 1$ m with radius $a = 0.002$ m. The height is chosen as $z_1 = -0.25$ m and the distance between the wires is $d = 1$ m. The half spaces have the material properties of vacuum. The permittivity, permeability and conductivity of the slab are $\epsilon_{2r}(z) = 20$, $\mu_{2r}(z) = 0$ and $\sigma(z) = 0$, respectively. The compensation parameters can be found in Table 7.3. The excitation is a Gaussian voltage pulse with $\tau = 0.5$ ns and $t_1 = 4\tau$.*

that the current is compensated better between the responses of the current to the first and second reflected wave at $z = d_s$. The additional waveform that is introduced to the current due to the reflection at $z = d_s$ is not affected by the third compensation. Even when the minimization is focused on the additional waveform due to the reflection at $z = d_s$, this waveform is not compensated by the third compensation. The effects from the slab are not compensated which means that the properties of the lower half space are not compensated either. Therefore, properties of the lower half space may be retrieved from the current along wire 2. Note that the additional compensation is carried out as a test only. It was not the aim of the analysis as such.

Chapter 10

Conclusions and recommendations

The work presented in this thesis studies the possibilities of a cheap and easy to build antenna system for the detection of buried objects. To simplify the analysis a wire antenna is used as a buried object. The antenna system for the detection of the buried object consists of two wire antennas. The study concerns the modeling and numerical computation of coupled integral equations that describe various configurations containing wire antennas.

The first part of the study focusses on the formulation of the general theory that is used for modeling different parts of the configuration under study. In Chapter 2, Maxwell's equations are formulated. From these equations, general reflected and transmitted field terms at an interface between two media are derived. An electric point dipole source serves as the source term in Maxwell's equations. The temporal and spatial Fourier transformations associated with the reflected and transmitted field terms are addressed.

Chapter 3 involves the derivation of several formulations to describe the current along a single thin wire. First the electric and magnetic field integral equation, EFIE and MFIE, respectively, for an electrically impenetrable object are derived from Maxwell's equations as given in Chapter 2. The integral representation associated with the EFIE is then used to find an equation that describes the current along a single, perfectly conducting thin wire. The result of this derivation is the integro-differential equation of Pocklington. The latter equation is rewritten to end up with a different formulation for the current along the wire. The integral equation obtained in this manner was first given by Hallén and is for that reason often referred to as Hallén's equation. At the end of Chapter 3, a traveling-wave model to describe the current along a wire is derived. The obtained approximate expression for the current provides insight into the behavior of the current along the wire. The results show that the current behaves as a damped oscillation along the wire. The oscillating effect is a result of the traveling-wave nature of the current along the wire. Namely, the current

reflects repeatedly at the end faces of a wire.

The second part of the study deals with the description of the desired configuration. This configuration consists of two half spaces with a two-wire antenna set up in the upper half space, and a third wire that is buried in the lower half space. The two wires in the upper half space are together referred to as the detection set up in which one wire serves as the transmitting wire and the other wire serves as the receiver. To arrive at a set of coupled integral equations that describe the currents along the three wires, a few increasingly complicated configurations are analyzed in Chapter 4. The building blocks for each step are derived in Chapters 2 and 3. The individual steps are tested and the results are compared to results from the literature. All intermediate configurations give accurate results.

After the description of the three-wire configuration, a method to describe the arbitrary orientation of a wire with respect to a second wire is derived in Chapter 5. Some results obtained with the aid of this method prove to be accurate.

The results of Chapter 4 show that a buried wire can in principle be detected by the detection set up. It is also demonstrated that the best visible detection is obtained when the detection setup is located close to the interface. The permittivity of the lower half space mainly has an effect on the current along the receiving wire. The conductivity of the lower half space, on the other hand, affects the current along both wires of the detection set up. The electric and magnetic reflection coefficients tend to ± 1 when the conductivity becomes high. Slowly attenuating, but heavily oscillating currents along both wires of the detection set up are the result. Since the conductivity of the lower half space has an attenuating effect on the current along the buried wire, as well as on the transmitted fields, the influence of the buried wire on the current along the receiving wire is heavily reduced for increasing conductivity. The contribution from the buried wire is limited to a small amplitude effect. In addition, the buried wire does not deform the general shape of the current along the receiving wire but merely raises or reduces its amplitude. Only after comparing the current to a reference current, a contribution from the buried wire can be noticed. The slowly attenuating, oscillating behavior of the current along the receiving wire is still present. This particular behavior of the current makes it difficult to detect a buried wire from the received signal directly.

To suppress this oscillating behavior, two methods are presented in Chapter 6. In the first method, Hallén's equation is used to model a resistance distribution along the wire. This resistive profile extinguishes the current wave towards the end faces of the wire. The oscillating effect of the current along the wire is fully suppressed, which results in a smooth frequency response of the wire.

The second method is pulse compensation. It is shown that with a carefully chosen time delay and complex amplitude, a second voltage pulse can be generated from the first voltage pulse. The combined response of both voltage pulses results in a single current pulse along the wire. However, the effects from the embedding on the current along the wire are exactly the same. After compensation of the transmitting and receiving wire, the current along the transmitting antenna becomes less sensitive to the influence of the receiving wire and the half space. This effect is observed as well for a resistively loaded wire. The current along the receiving wire, on the other hand, is very much affected by the presence of an interface. To reduce the effects of the interface, a third compensation with different parameters is used to attenuate the effects of the lower half space on the current along the receiving wire. The oscillating behavior of the current along the buried wire is not affected by both methods. Therefore, effects of the buried wire become visible in the current along the receiving wire.

While the first enhancement involves a physical change of the wire antenna, the second enhancement is carried out at the input and output of the wire directly. The technique can be applied after the current has been obtained or it can be applied on the input and output signals directly. Thus, pulse compensation can be either implemented in software or hardware while the Wu-King profile can only be realized in hardware.

It is shown in Chapters 6 and 7 that the transmitting and receiving characteristics of the detection set up are greatly enhanced by applying both methods. A buried wire changes the current along the receiving wire such that the presence of the buried wire can be observed visually from the shape of the current without any signal processing. In addition, features from the lower half space can be obtained from the current along the receiving wire.

The resistively loaded wires are used to perform a scan of the lower half space in Chapter 8. Since the buried wire should be allowed to be in an arbitrary position somewhere in the lower half space, results of Chapter 5 are used to facilitate this. However, there is a big disadvantage in calculating the currents along coupled, non-parallel thin wires. In previous computations, the fact that the wires were located parallel to each other offered the possibility of using FFT's for an efficient computation of the spatial convolutions. The direct computation of the convolution terms requires extra computational effort in both memory and time. To keep the computation times low, the wires of the detection set up are kept parallel to each other and the buried wire.

Certain features of the entire lower half space can be retrieved from the synthetic seismograms generated by the computational scan. At all times, the depth and relative speed to and from the buried wire can be found. The extraction of the length of the buried wire is only possible when the centers of the wires are located in the same plane perpendicular

to the axes of the wires. The detection set up can therefore not be used to retrieve the length of the buried wire. Although some of the features can be retrieved directly from the current along the receiving wire, the subtraction of a reference signal enhances the plot significantly. This reference signal holds information of the configuration without the buried wire. The first current wave along the receiving wire is much higher in magnitude than the effects of the other signals. Instead of this so-called background subtraction, zooming in on the current after the first current pulse enhances the plot as well. However, when the buried object is located close to the interface, it may not be possible to recognize the first arrival time of the electric field from that object in the current along the receiving wire directly in that case.

The pulse-compensated wires are also used for a scan of the lower half space in Chapter 8. The synthetic seismograms look similar to the ones obtained with the resistively loaded wires. The magnitude of the current pulse along the receiving wire is approximately 10 times higher than in the loaded case. This means that the pulse-compensated wires are far more efficient than resistively loaded wires. Features of the lower half space are more pronounced in the seismograms than with the loaded wires.

Compared to the unloaded wires, the current along the resistively loaded wires attenuates much quicker. A detection set up with resistively loaded antennas is therefore very suitable for scanning applications. The detection set up is capable of moving rapidly over the interface. The results obtained from the pulse compensation prove that the technique can be of a great practical use. The strength of the technique lies in the fact that the compensation parameters can easily be implemented in hardware. With both methods, the computational effort for post processing is reduced considerably.

In both cases, the presence of the buried wire adds a visibly detectable waveform to the current along the receiving wire. However, when the conductivity of the lower half space is bigger, the magnitude of the additional waveform becomes smaller. For the pulse-compensated wires this is only partly true. For low permittivities of the lower half space, the additional waveform due to the presence of a buried wire is obvious. When the permittivity increases, it is more difficult to distinguish whether or not an object is present in the lower half space.

For objects which are located at greater depths, the current along the receiving wire shows an additional waveform for both techniques. For a detection set up with pulse-compensated wires, the results are not influenced any more by a larger permittivity.

With pulse compensation, the influence of the lower half space on the current along the wires of the detection set up can be partly attenuated. However, when the permittivity increases, it also compensates partly the effects of the presence of a buried wire which is

close to the interface. This makes it harder to detect such a buried wire. For wires at greater depths, detection is no problem. Even the conductivity of the lower half space does not play an important role here. Of course, at much greater depths, the attenuation of the transmitted field into the lower half space makes detection very difficult.

At the end of the thesis, a slab configuration is probed with the detection set up. Both methods for enhancing the current distribution along the wire were employed. The results show that the methods are comparable. However, the current along the resistively loaded wire is again a factor of 10 lower than in the pulse-compensated case. Secondly, the pulse-compensated current along the receiving wire is slightly oscillating between the characteristic waveforms due to repeated reflections of the slab. Nevertheless, the current in the time interval between two of those waveforms can be attenuated efficiently when the parameters for a third compensation are optimized in that time interval.

Both methods are useful in the study of a lower half space. In both cases, a buried wire is observable directly from the current along the receiving wire. The pulse-compensated wires have a better energy efficiency than the resistively loaded wires. The current along the wire still oscillates visibly while the current along the resistively loaded wire does not. Because the resistive profile also attenuates the effects of the buried wire, the pulse-compensated wires perform better in the detection of the buried wire. This can also be concluded by looking at the synthetic seismograms.

The advantage of pulse compensation is that each individual contribution can be treated separately while the resistive profile attenuates all contributions. After dealing with the direct contribution from the transmitting wire, a third compensation can be applied to eliminate the current pulse due to interface reflections. This third compensation does not affect the response to the presence of the buried wire, which makes it easy to detect that buried wire. In the case of a slab, the third compensation network cannot compensate for the reflection at the interface between the slab and the lower half space. This is inherent to the choice of the starting point for the minimization procedure to determine the compensation parameters.

Finally, a few suggestions regarding interesting future research topics are made. It was demonstrated that a buried wire can be detected by a simple bi-static antenna set up. When the end reflections of the current wave at the end faces of the antenna are attenuated by either a resistive profile or pulse compensation, the detection of a buried wire is greatly enhanced. Results of the resistively loaded wires are comparable to results of pulse-compensated wires. But with one important difference, the magnitude of the current along the pulse-compensated receiving wire is about 10 times higher than in the resistively loaded case. It seems plausible that other antenna systems, such as resistively or capaci-

tively loaded bow-tie antennas [70, 71, 72] and vee dipoles [20], can be pulse compensated in a similar manner.

The ability for both techniques to quickly attenuate the current along a wire antenna makes it possible to increase the repetition rate of the input signal. Both types of wires are thus attractive for scanning applications. The pulse-compensated wires have the extra advantage that their power consumption is far less in comparison with the resistively loaded wires. Thinking about scanning applications, the pulse compensated wires could be used as a pre-scanning device in conjunction with a more advanced radar system. Because the pulse-compensated wires have the ability to handle short pulses, the wires could be rotated 90 degrees back and forth. In that way, the polarization of the electromagnetic waves is changed every second measurement. Of course, the data processing would require a little bit more effort.

Before any measurements are carried out, the determination of a criterion that links an optimal detection to certain parameters of the entire configuration would be very useful. A first attempt to formulate a criterion is made in [31].

The results presented in Chapters 7 and 8 should be verified by measurements. A measurement in a controlled environment with and without a homogeneous lower half space should validate that the pulse compensation indeed works and can be made with mostly passive components. The next test is then on actual ground. In both cases, a test measurement has to be carried out for obtaining the compensation parameters. In view of the measurements on an actual ground, it is beneficial when the reflected and transmitted field terms as described in Chapter 2 are adapted to handle real grounds.

Instead of the buried wire, a more realistic buried object should be considered. Therefore, the buried object can be generalized to a metallic object and subsequently to a dielectric object.

Bibliography

[1] K. Anderson. An overview of the global land mines crisis. In K.M. Cahill, editor, *Clearing The Fields: Solutions to The Global Landmines Crisis*, pages 17–23. Basic Books & The Council on Foreign Relations, 1995.

[2] B. Boutros-Ghali. The land mine crisis: A humanitarian disaster. *Foreign Affairs*, 73(5):8–13, 1994.

[3] C. Hülsmeyer. German patent number 165546, 1904.

[4] M. Dabas, C. Camerlynck, and P. Freixas. Simultaneous use of electrostatic quadrupole and GPR in urban context: investigation of the basement of the Cathedral of Girona (Catalunya-Spain). *Geophysics*, pages 1–7, 2000.

[5] J.L. Davis and A.P. Annan. Ground-penetrating radar for high resolution mapping of soil and rock stratigraphy. *Geophysical Prospecting*, 37:531–551, 1989.

[6] G.G. Schaber, J.F. McCauley, C.S. Breed, and G.R. Olhoeft. Shuttle imaging radar: Physical controls on signal penetration and subsurface scattering in the Eastern Sahara. *IEEE Transactions on Geoscience and Remote Sensing*, 24:603–623, 1986.

[7] L. Carin and S. Vitebskiy. Short-pulse scattering from and the resonances of buried and surface metal mines. In C.E. Baum, L. Carin, and A.P. Stone, editors, *Ultra-Wideband Short-Pulse Electromagnetics 3*. Plenum Press, 1997.

[8] L. Peters jr., J.J. Daniels, and J.D. Young. Ground penetrating radar as an environmental sensing tool. *Proc. IEEE*, 82:1802–1822, 1994.

[9] X. Zhu and L. Carin. Multi-resolution time-domain analysis of a ground-penetrating radar system. *IEEE Trans. Antennas and Propagation*. Submitted for publication.

[10] A.D. Hibbs. Man portable mine detector using nuclear quadrupole resonance - first year progress and test results. In *IEE Conf. Publ.: Detection of Abandoned Landmines*, pages 138–141. IEE Conf. Publ., 1998.

[11] A.D. Hibbs, G.A. Barrall, P.V. Czipott, A.J. Drew, D. Gregory, D.K. Lathrop, Y.K. Lee, E.E. Magnuson, R. Mathews, D.C. Skvoretz, S.A. Vierkotter, and D.O. Walsh. Detection of tnt and rdx landmines by stand-off quadrupole resonance. In *Proc. of SPIE: Detection and Remediation Technologies for Mines and Minelike Targets IV*, volume 3710, pages 454–465, 1999.

[12] D.J. Daniels. *Surface penetrating radar*. IEE, London, 1996.

[13] E.E. Altshuler. The traveling-wave linear antenna. *IRE Trans. Antennas and Propagation*, 9:324–329, 1961.

[14] E. Hallén. *Electromagnetic theory*. Chapman & Hall, 1962. Translated from the Swedish edition by R. Gåsström.

[15] L.C. Shen. An experimental study of the antenna with nonreflecting resistive loading. *IEEE Trans. Antennas and Propagation*, 15(5):606–611, 1967.

[16] C.D. Taylor. Cylindrical transmitting antenna: Tapered resistivity and multiple impedance loadings. *IEEE Trans. Antennas and Propagation*, 16(2):176–179, 1968.

[17] T.T. Wu and R.W.P. King. The cylindrical antenna with nonreflecting resistive loading. *IEEE Trans. Antennas and Propagation*, 13:369–373, 1965.

[18] L. Carin, N. Geng, M. McClure, J. Sichinaand, and L. Nguyen. Ultra-wideband synthetic-aperture-radar for mine-field detection. *Antennas and Propagation Magazine*, 41(1):18–33, 1999.

[19] R.W.P. King and G.S. Smith. *Antennas in matter*. MIT Press, 1981.

[20] T.P. Montoya and G.S. Smith. Land mine detection using a ground-penetrating radar based on resistively loaded vee dipoles. *IEEE Trans. Antennas and Propagation*, 47(12):1795–1806, 1999.

[21] Y. Chevalier, Y. Imbs, B. Beillard, J. Andrieu, M. Jouvet, B. Jecko, M. LeGoff, and E. Legros. A new broad band resistive wire antenna for ultra-wide-band applications. In E. Heyman, B. Mendelbaum, and J. Shiloh, editors, *Ultra-Wideband Short-Pulse Electromagnetics 4*. Kluwer Academic/Plenum Press, 1999.

[22] J.G. Malony and G.S. Smith. A study of transient radiation from the Wu-King resistive monopole- FDTD analysis and experimental measurements. *IEEE Trans. Antennas and Propagation*, 41(5):668–676, 1990.

[23] T.P. Montoya and G.S. Smith. A study of pulse radiation from several broad-band loaded monopoles. *IEEE Trans. Antennas and Propagation*, 44(8):1172–1182, 1996.

[24] A. Rubio Bretones and A.G. Tijhuis. Transient excitation of a straight thin wire segment over an interface bewteen two dielectric half spaces. *Radio Science*, 30(6):1723–1738, 1995.

[25] A. Rubio Bretones and A.G. Tijhuis. Transient excitation of two coupled wires over an interface between two dielectric half spaces. *Radio Science*, 32(1):25–41, 1997.

[26] S.N. Samaddar and E.L. Mokole. Transient behavior of radiated and received fields associated with a resistively loaded dipole. In E. Heyman, B. Mendelbaum, and J. Shiloh, editors, *Ultra-Wideband Short-Pulse Electromagnetics 4*. Kluwer Academic/Plenum Press, 1999.

[27] A.G. Tijhuis and A. Rubio Bretones. Transient excitation of a layered dielectric medium by a pulsed electric dipole. *IEEE Trans. Antennas and Propagation*, 48(10):1673–1684, 2000.

[28] M. Kanda. The time domain characteristics of a traveling wave linear antenna with linear and nonlinear parallel loads. *IEEE Trans. Antennas and Propagation*, 28(2):267–276, 1980.

[29] K.P. Essele and S.S. Stuchly. Pulse-receiving characteristics of resistively loaded dipole antennas. *IEEE Trans. Antennas and Propagation*, 38(10):1677–1683, 1990.

[30] Y.P. Liu and D.L. Sengupta. Transient radiation from a linear antenna with non-reflecting resistive loading. *IEEE Trans. Antennas and Propagation*, 22(2):212–220, 1974.

[31] S.H.J.A. Vossen, A.G. Tijhuis, E.S.A.M. Lepelaars, and A.P.M. Zwamborn. Detection of a buried wire with two resistively loaded wire antennas. *Radio Science*, pages 21–1–21–14, December, 2002.

[32] A. Rubio Bretones, A.G. Tijhuis, R. Gómez Martin, and S.H.J.A. Vossen. Transient excitation of two loaded wires above a half-space with a cover layer. *IEEE Trans. Antennas and Propagation*, 2002. To be published.

[33] P.C. Pocklington. Electrical oscillations in wires. *Proc. Cambridge Philosophical Society*, pages 324–332, 1897.

[34] E. Hallén. Theoretical investigation into the transmitting and receiving qualities of antennae. *Nova Acta Regiae Societatis Scientiarum Upsaliensis, Ser. IV*, 11(4):1–44, 1938.

[35] J. Bogerd, A.G. Tijhuis, and J.J.A. Klaasen. Electromagnetic excitation of a thin wire: A traveling-wave approach. *IEEE Trans. Antennas and Propagation*, AP-46(8):1202–1211, 1998.

[36] G.J. Burke and A.J. Poggio. Part I: Program description, theory. In *Numerical Electromagnetics Code (NEC-2), Method of Moments*. Lawrence Livermore Laboratory, 1981.

[37] A.G. Tijhuis, Z.Q. Peng, and A. Rubio Bretones. Transient excitation of a straight thin-wire segment: A new look at an old problem. *IEEE Trans. Antennas and Propagation*, AP-40(10):1132–1146, 1992.

[38] E.S.A.M. Lepelaars. *Transient electromagnetic excitation of biological media by circular loop antennas*. PhD thesis, Eindhoven University of Technology, Eindhoven, 1997.

[39] L.B. Felsen and N. Marcuvitz. *Radiation and scattering of waves*. Prentice-Hall, Inc., New Jersey, 1973.

[40] W.C. Chew. *Waves and fields in inhomogenous media*. Van Nostrand Reinhold, New York, 1990.

[41] M. Abramowitz and I.A. Stegun. *Handbook of mathematical functions*. Dover Publications, New York, 1972.

[42] E.F. Kuester and A.G. Tijhuis. A Weyl representation for two-dimensional time-domain wave functions and its application to scattering from inhomogeneous dielectric slabs. Technical Report 1982-17, Delft University of Technology, 1982.

[43] A.J. Poggio and E.K. Miller. Integral equation solutions of three-dimensional scattering problems. In R. Mittra, editor, *Computer Techniques for Electromagnetics*, chapter 4. Pergamon Press, 1973.

[44] C.J. Bouwkamp. Hallén's theory for a straight, perfectly conducting wire, used as a transmitting or receiving aerial. *Physica*, 9:609–631, 1942.

[45] P.Y. Ufimtsev. Diffraction of plane waves by a thin cylindrical conductor. *Radio Eng. Electron*, 7:241–249, 1962.

[46] L.C. Shen, T.T. Wu, and R.W.P. King. A simple formula of current in dipole antennas. *IEEE Trans. Antennas and Propagation*, 16(5):542–547, 1968.

[47] A.G. Tijhuis. Iterative techniques for the solution of integral equations in transient electromagnetic scattering. In J.A. Kong and T.P. Sarkar, editors, *PIER 5: Application of Conjugate Gradient Method to Electromagnetics and Signal Analysis*, pages 455–538. Elsevier Science Publishing Co., 1991.

[48] A.T. de Hoop. *Handbook of radiation and scattering of waves*. Academic Press, London, 1995.

[49] M.F. Cátedra, R.P. Torres, J. Basterrechea, and E. Gago. *The CG-FFT method: Application of signal processing techniques to electromagnetics*. Artech House, London, 1995.

[50] A. Rubio Bretones, R. Gómez Martin, and A. Salinas. DOTIG1, a time domain numerical code for the study of the interaction of electromagnetic pulses with thin-wire structures. *COMPEL*, 8(1):39–61, 1989.

[51] H.T. Shamansky, A.K. Domminek, and L. Peters jr. Electromagnetic scattering by a straight thin wire. *IEEE Trans. Antennas and Propagation*, 37:1019–1025, 1989.

[52] R. Gómez Martin, J.A. Morente, and A. Rubio Bretones. An approximate analysis of transient radiation from linear antennas. *Int. J. Electron.*, 61(3):343–353, 1986.

[53] E.K. Miller and J.A. Landt. Direct time-domain techniques for transient radiation and scattering from wires. *Proc. IEEE*, 68:1396–1423, 1980.

[54] R.J.C. Smets. Electromagnetic excitation of a thin wire: An analytical approach. Master's thesis, Eindhoven University of Technology, TTE division, 1994.

[55] L.A. Vainshtein. Current waves in a thin cylindrical conductor: I. currents and impedance of a transmitting antenna. *J. Tech. Phys. USSR*, 4:673–688, 1959.

[56] S. Lipschutz. *Linear algebra*. McGraw-Hill Book Company Inc., Singapore, 1968.

[57] G.J. Burke and A.J. Poggio. Part III: User's guide. In *Numerical Electromagnetics Code (NEC-2), Method of Moments*. Lawrence Livermore Laboratory, 1981.

[58] Bardarson and Just. Necdraw. In *9th Annual Review of Progress in Applied Computational Electromagnetics*, page 235, 1993.

[59] S.H.J.A. Vossen. Mutual coupling between a wire antenna of finite conductivity and a large object. Master's thesis, Eindhoven University of Technology, TTE division, 1997.

[60] G.J. Burke and E.K. Miller. Modeling antennas near to and penetrating a lossy interface. *IEEE Trans. Antennas and Propagation*, 32(10):1040–1049, 1984.

[61] R.W.P. King. *The theory of linear antennas*. Cambridge University Press, 1956.

[62] L.C. Shen and T.T. Wu. Cylindrical antenna with tapered resistive loading. *Radio Science*, 2(2):191–201, 1967.

[63] M. Kanda. A relatively short cylindrical antenna with tapered resistive loading for picosecond pulse measurements. *IEEE Trans. Antennas and Propagation*, 26(3):439–447, 1978.

[64] D.L. Sengupta and Y.P. Liu. Analytical investigation of waveforms radiated by a resistively loaded linear antenna excited by a Gaussian pulse. *Radio Science*, 6(9):621–630, 1974.

[65] A. Erdélyi. *Higher transcendental functions*, volume I. McGraw-Hill Book Company Inc., 1953.

[66] N.M. Temme. *Speciale functies in de mathematische fysica*. Epsilon Uitgaven, Utrecht, 1990. in Dutch.

[67] W.K. Press, S.A. Teukolsky, W.T. Vetterling, and B.P. Flannery. *Numerical recipes in Fortran, second edition*. University Press, Cambridge, 1992.

[68] M. Born and E. Wolf. *Principles of optics*. Pergamon Press, 1975.

[69] D. Gabor. Theory of communication (part I). *J. IEE*, 93:429–411, 1946.

[70] S.M. Booker, A.P. Lambert, and P.D. Smith. Calculation of surface impedance effects on transient antenna radiation. *Radio Science*, 31:1663–1669, 1996.

[71] A.A. Lestari, A.G. Yarovoy, and L.P. Ligthart. Capacitively-tapered bowtie antenna. In *Millennium Conference on Antennas and Propagation, conference proceedings on CD-ROM*, pages 9–14, 2000.

[72] K.L. Shlager, G.S. Smith, and J.G. Malony. Optimization of bow-tie antennas for pulse radiation. *IEEE Trans. Antennas and Propagation*, 42(7):975–982, 1994.

Summary

In this thesis, a theoretical study is carried out to investigate the feasibility of detecting a buried wire with a transmitting and receiving thin-wire antenna. Detection is primarily based on "electromagnetic coupling". This means that a primary current along an antenna induces a secondary current along a second antenna and vice versa. This takes places via an electromagnetic field that propagates through the medium in which the two antennas are located. The properties of that medium have an influence on this electromagnetic field and hence the currents along the antennas are influenced as well. As a representative configuration, two homogeneous half spaces are considered. The properties of each half space can be different. For the transmitting and receiving antenna, two thin-wire antennas are chosen. Both wire antennas are located in the upper half space. As an example of an object to be detected, a wire antenna is chosen that is buried in the lower half space. Reflected and transmitted fields will occur at the interface between the two half spaces. This complicates the coupling problem when compared to a similar problem in a homogeneous environment.

The mathematical description of the detection problem leads to a system of coupled integral equations that describes the currents along the three wires. The interface between the two half spaces is dealt with by taking into account the reflected and transmitted fields in the formulation. An impressed voltage source at the center of the transmitting wire serves as the source term. The system of equations is solved with the aid of the Conjugate-Gradient method; this method minimizes the squared error in the equality sign of the discretized integral equations. Important issues are the fixed spatial discretization of the wires, the use of a composite Gaussian quadrature rule to determine the reflected and transmitted fields and the use of a Fast Fourier Transformation to evaluate spatial convolutions.

The influence of a large number of parameters on the detection of the buried wire has been investigated by numerical calculations. Amongst the parameters that were varied are the distance between and the height of the transmitting and receiving wire, the depth at which the buried wire is located and the electromagnetic properties of both half spaces. Numerical

calculations demonstrate that the current along the receiving wire is influenced by the presence of a buried wire. However, compared to the effects of the repeated reflections of the currents at the end faces of the wires but also of mutual coupling between the transmitting and receiving wires and reflected fields at the interface, the additional contribution is small. Therefore, a direct interpretation of the received time signal is virtually impossible.

To enhance the detection, two techniques have been studied. First, a carefully chosen resistance profile has been implemented on the transmitting and receiving wire numerically. This suppresses repeated reflections of the currents at the end faces of the wires. The detection is greatly improved but the resistance profile has an adverse effect on the energy consumption of the wires. As a second technique, pulse compensation is studied. With pulse compensation, a simple passive pre or postprocessing is applied to the input and output signal, respectively. Numerical calculations show that, also in this case, the detection of the buried wire is improved. However, pulse compensation does not stress the energy consumption. Pulse compensation is new and it seems feasible to implement this idea on the transmitting and receiving wire in both software and hardware.

Both techniques have been used to simulate a scan of the subsurface containing a buried wire. The output of such a scan is a three-dimensional image which shows characteristic information about the subsurface and the buried wire.

Finally, a slab configuration is probed with both the resistively loaded and the pulse-compensated wire antennas.

Samenvatting

In dit proefschrift wordt een theoretische studie uitgevoerd naar de haalbaarheid van de detectie van een begraven draad m.b.v. een zend- en ontvangst dunne draadantenne. De detectie is gebaseerd op het verschijnsel "elektromagnetische koppeling". Dat wil zeggen dat een primaire stroom langs een antenne een secundaire stroom induceert langs een tweede antenne en vice versa. Dit gebeurt via het elektromagnetische veld dat zich in de omgeving van de twee antennes voortplant. De eigenschappen van die omgeving beïnvloeden dit elektromagnetische veld, waardoor ook de stromen langs de antennes worden beïnvloed. Als configuratie beschouwen we twee homogene halfruimten met verschillende materiaaleigenschappen. Als zend- en ontvangstantenne kiezen we draadantennes die zich in de bovenste halfruimte bevinden. Als voorbeeld van een te detecteren object kiezen we een draad die begraven is in de onderste halfruimte. Aan het grensvlak tussen de twee media ontstaan gereflecteerde en doorgelaten velden. Dit compliceert het koppelingsprobleem t.o.v. een vergelijkbaar probleem in een homogene omgeving.

De wiskundige beschrijving van dit probleem leidt tot een gekoppeld stelsel integraalvergelijkingen voor de stromen langs de drie draden. Om de medium-overgang te modelleren zijn gereflecteerde en doorgelaten velden in de formulering meegenomen. Als bron beschouwen we een opgedrukte spanning in het midden van de zenddraad. Dit koppelingsprobleem is opgelost m.b.v. de Conjugate Gradient methode; dit is een iteratieve methode die de kwadratische fout in het gelijkteken van de gediscretiseerde integraalvergelijkingen minimaliseert. Belangrijk hierbij is de constante stapgrootte in de ruimtelijke discretisatie van de draden, het gebruik van een samengestelde Gauss kwadratuur ter bepaling van de gereflecteerde- en doorgelaten velden en het gebruik van zogenaamde Fast Fourier Transformations om ruimtelijke convoluties te bepalen.

In de uitgevoerde berekeningen is de invloed van een groot aantal parameters op de detectie onderzocht, zoals de afstand tussen en de hoogte waarop de zend- en ontvangstdraad zich bevinden, de diepte waarop de begraven draad zich bevindt en de elektromagnetische eigenschappen van de verschillende media. Uit de resultaten blijkt dat de begraven draad

een waarneembare invloed heeft op de stroom langs de ontvangstdraad. Echter, die extra invloed is klein t.o.v. met name de herhaalde reflecties van de stromen aan de uiteinden van de draden maar ook t.o.v. de effecten van de onderlinge koppeling tussen de zend- en ontvangstdraad en de gevolgen van reflecties aan het grensvlak. Dit maakt een directe interpretatie van het ontvangen tijdsignaal bijna onmogelijk.

Om de detectie te verbeteren is een tweetal technieken bestudeerd. Ten eerste zijn in de gemodelleerde configuratie, de zend- en ontvangstdraad van een speciaal gekozen weerstandsprofiel voorzien. Hiermee worden herhaalde reflecties van de stroom aan de uiteinden van beide draden onderdrukt. Dit verbetert de detectie maar heeft een negatieve invloed op de benodigde energie. Als tweede techniek bekijken we pulscompensatie, een eenvoudige passieve pre- en postprocessing van respectievelijk het in- en uitgangssignaal. De berekende resultaten geven aan dat de begraven draad ook in dit geval beter detecteerbaar is, echter zonder dat er extra energie nodig is. Pulscompensatie is nieuw en het lijkt mogelijk om dit idee in een praktische situatie hard- dan wel softwarematig te implementeren bij zowel de zend- als de ontvangstdraad.

Beide technieken zijn gebruikt voor het simuleren van een scan van de ondergrond met een begraven draad. Hierdoor ontstaat een drie-dimensionaal beeld dat karakteristieke eigenschappen van de ondergrond en de begraven draad laat zien.

Ten slotte zijn beide technieken gebruikt om een slabconfiguratie te onderzoeken.

Curriculum Vitae

Stefan Henri Jean Antoin Vossen was born in Nederweert, The Netherlands, on October 15, 1970. After he graduated from secondary school at the St. Ursula comprehensive school in Horn, he enrolled as a student in Electrical Engineering at the Eindhoven University of Technology in 1990. In 1996, his interest in applied electromagnetic research took him to the Physics and Electronics Laboratory of the Dutch Organization for Applied Research (TNO-FEL). Under the joint supervision of Prof.Dr. A.G. Tijhuis and Prof.Dr.Ir. A.P.M. Zwamborn he conducted research after the mutual coupling between a wire antenna and a large object for his M.Sc. Thesis. In April 1997, he received the M.Sc. Degree in Electrical Engineering from the Eindhoven University of Technology. Subsequently, he carried out his Ph.D. project at TNO-FEL from May 1997 to December 2001 under the supervision of Prof.Dr. A.G. Tijhuis, Dr.Ir. E.S.A.M. Lepelaars and Prof.Dr.Ir. A.P.M. Zwamborn. During his Ph.D. project, he cooperated with Prof.Dr.Ir. Zwamborn and Prof.Dr. Tijhuis in supervising undergraduate students. In addition he advised colleagues and carried out minor tasks in research projects at TNO-FEL. From February 2002, he is employed at TNO-FEL as a research scientist and the technology manager of the Electromagnetic Effects group, respectively.

Acknowledgments